

---

# Applied Research Laboratory

## Technical Report

INVESTIGATION OF MECHANISMS THAT CAUSE  
CHANGES TO BOTTOM REVERBERATION  
FLUCTUATION STATISTICS

by

L. S. Deliman

PENNSTATE

---



20091130236

The Pennsylvania State University  
**APPLIED RESEARCH LABORATORY**  
P.O. Box 30  
State College, PA 16804

**INVESTIGATION OF MECHANISMS THAT CAUSE  
CHANGES TO BOTTOM REVERBERATION  
FLUCTUATION STATISTICS**

by

L. S. Deliman

Technical Report No. TR 98-001  
January 1998

L.R. Hettche  
Applied Research Laboratory

Approved for public release; distribution unlimited

# REPORT DOCUMENTATION PAGE

Form Approved  
OMB No. 0704-0188

Public reporting burden for this collection of information is estimated to average 1 hour per response, including the time for reviewing instructions, searching existing data sources, gathering and maintaining the data needed, and completing and reviewing the collection of information. Send comments regarding this burden estimate or any other aspect of this collection of information, including suggestions for reducing the burden, to Washington Headquarters Services, Directorate for Information Operations and Reports, 1215 Jefferson Davis Highway, Suite 1202, Arlington, VA 22202-4382, and to the Office of Management and Budget, Paperwork Reduction Project (0704-0188), Washington, DC 20503.

1. AGENCY USE ONLY (Leave blank)	2. REPORT DATE	3. REPORT TYPE AND DATES COVERED
	December 1997	Technical Report
4. TITLE AND SUBTITLE		5. FUNDING NUMBERS
Investigation of Mechanisms that Cause Changes to Bottom Reverberation Fluctuation Statistics		PR 5078
6. AUTHOR(S)		
Linda S. Deliman		
7. PERFORMING ORGANIZATION NAME(S) AND ADDRESS(ES)		8. PERFORMING ORGANIZATION REPORT NUMBER
Applied Research Laboratory P.O. Box 30 State College, PA 16804-0030		TR-98-001
9. SPONSORING/MONITORING AGENCY NAME(S) AND ADDRESS(ES)		10. SPONSORING/MONITORING AGENCY REPORT NUMBER
Applied Research Laboratory P.O. Box 30 State College, PA 16804-0030		
11. SUPPLEMENTARY NOTES		
12a. DISTRIBUTION/AVAILABILITY STATEMENT		12b. DISTRIBUTION CODE
Unlimited distribution		
13. ABSTRACT (Maximum 200 words) An investigation into the underlying mechanisms that cause bottom reverberation fluctuation statistics to deviate from the typically assumed Rayleigh distribution reveals that sediment "patchiness" is a major contributor. The investigation involved processing both shallow water data and simulated data. The shallow water data, collected during two SACLANT Centre experiments, include low-frequency measurements made over chalk and clay sediments with varying degrees of roughness using different pulse types and pulse lengths. The processing produced both Rayleigh and non-Rayleigh statistics. The results indicate that sediment type, pulse type, and pulse length are not a factor <u>per se</u> in the deviations of the statistics from Rayleigh. However, sediment "patchiness" defined as an ensonified area containing patches which contribute largely different backscattering strengths within the area, does cause the statistics to deviate from Rayleigh. The simulated data reinforce these conclusions and provide insight into the spatial and temporal extent of the "patchiness" required to cause a deviation in the statistics.		
14. SUBJECT TERMS		15. NUMBER OF PAGES
sediment reverberation		Approx. 200
fluctuation statistics		16. PRICE CODE
17. SECURITY CLASSIFICATION OF REPORT	18. SECURITY CLASSIFICATION OF THIS PAGE	19. SECURITY CLASSIFICATION OF ABSTRACT
UNCLASSIFIED	UNCLASSIFIED	UNCLASSIFIED
20. LIMITATION OF ABSTRACT		
UNCLASSIFIED		

## ABSTRACT

An investigation into the underlying mechanisms that cause bottom reverberation fluctuation statistics to deviate from the typically assumed Rayleigh distribution reveals that sediment “patchiness” is a major contributor. The investigation involved processing both shallow water data and simulated data. The shallow water data, collected during two SACLANT Centre experiments, include low-frequency measurements made over chalk and clay sediments with varying degrees of roughness using different pulse types and pulse lengths. The processing produced both Rayleigh and non-Rayleigh statistics. The results indicate that sediment type, pulse type, and pulse length are not a factor *per se* in the deviations of the statistics from Rayleigh. However, sediment “patchiness” defined as an ensonified area containing patches which contribute largely different backscattering strengths within the area, does cause the statistics to deviate from Rayleigh. The simulated data reinforce these conclusions and provide insight into the spatial and temporal extent of the “patchiness” required to cause a deviation in the statistics.

## TABLE OF CONTENTS

<b>LIST OF FIGURES .....</b>	<b>vii</b>
<b>LIST OF TABLES .....</b>	<b>xiv</b>
<b>Chapter 1 INTRODUCTION .....</b>	<b>1</b>
1.1 Motivation .....	1
1.2 Research Objectives .....	3
1.3 Thesis Outline .....	4
<b>Chapter 2 SCATTERING THEORIES AND MODELS .....</b>	<b>7</b>
2.1 Fundamental Theories of Scattering .....	7
2.1.1 Reflected and transmitted intensity .....	8
2.1.2 Bottom scattering mechanisms .....	9
2.1.3 Scattering from interface roughness .....	10
2.1.3.1 Helmholtz-Kirchhoff integral .....	11
2.1.3.2 Kirchhoff approximation .....	13
2.1.3.3 Rayleigh-Rice approximation .....	13
2.1.3.4 Composite roughness theory .....	14
2.1.4 Scattering from volume inhomogeneities .....	15
2.1.4.1 Density and sound speed variations .....	15
2.1.4.2 Born approximation .....	16
2.1.4.3 Sediment granularity and Biot's theory .....	18
2.1.4.4 Shear Waves .....	18
2.1.5 Definition of Scattering Strength .....	19
2.2 Model for backscattering strengths .....	20
2.2.1 Interface roughness model .....	21
2.2.2 Volume scattering model .....	22
2.3 Summary .....	23
<b>Chapter 3 BOTTOM REVERBERATION FLUCTUATION STATISTICS .....</b>	<b>29</b>
3.1 Definition of Fluctuations .....	29
3.2 Statistics of Fluctuations .....	30
3.2.1 Statistics of pressure amplitudes .....	32
3.2.1.1 Rayleigh distribution .....	33
3.2.1.2 Rayleigh cumulative distribution .....	39
3.2.1.3 Rayleigh probability of false alarm .....	40
3.2.1.4 Rician distribution .....	41
3.2.2 Statistics of intensity .....	42

3.2.2.1 Exponential, chi-square, and gamma probability density function .....	43
3.2.2.2 Exponential cumulative distribution .....	44
3.2.2.3 Exponential probability of false alarm.....	45
3.2.3 Other applicable distributions.....	45
3.2.3.1 Weibull distribution.....	46
3.2.3.2 Lognormal distribution .....	47
3.2.3.3 Mixture and bimodal distributions .....	49
3.3 Statistical tests .....	50
3.3.1 Goodness-of-fit tests .....	50
3.3.1.1 Chi-square test .....	51
3.3.1.2 Kolmogorov-Smirnov test.....	52
3.3.1.3 Anderson-Darling test.....	53
3.3.1.4 Kuiper's test.....	54
3.3.2 Other statistical tests.....	54
3.3.2.1 Run's test.....	55
3.3.2.2 Autocorrelation .....	55
3.4 Summary .....	57
<b>Chapter 4 RELATED THEORETICAL AND EXPERIMENTAL APPROACHES .....</b>	<b>65</b>
4.1 Theoretical Approaches .....	65
4.1.1 Intensity fluctuations of propagating energy.....	66
4.1.2 Amplitude fluctuations of sediment scattered energy .....	69
4.1.3 Models of bimodal fluctuations in scattered sound .....	73
4.2 Experimental Approaches .....	78
4.2.1 Intensity fluctuations of propagating energy.....	79
4.2.2 Amplitude fluctuations of sediment scattered energy .....	79
4.2.3 Relationship of interface roughness to fluctuation statistics .....	84
4.3 Summary .....	85
<b>Chapter 5 IN-WATER REVERBERATION DATA .....</b>	<b>92</b>
5.1 Processing Technique .....	92
5.2 Celtic Duet Experiment .....	94
5.2.1 Site A 400 Hz CW.....	95
5.2.2 Site A 365-425 Hz HFM.....	99
5.2.3 Site C 400 Hz CW .....	100
5.2.4 Site A 1280 Hz CW .....	102
5.3 Ogopogo Experiment.....	103
5.4 Summary .....	105
<b>Chapter 6 SIMULATION STUDIES .....</b>	<b>141</b>
6.1 Development of the Simulation .....	141
6.1.1 Generating time series .....	142
6.1.2 Processing the time series .....	142
6.1.3 Verification of the simulation .....	142

<b>6.2 Simulation Studies .....</b>	<b>145</b>
6.2.1 Sediment parameter study .....	145
6.2.2 Sediment mixture study.....	149
6.2.3 Beampattern study .....	153
6.2.4 Sound velocity profile study .....	156
<b>6.3 Summary .....</b>	<b>157</b>
<b>Chapter 7 CONCLUSIONS.....</b>	<b>179</b>
7.1 Thesis Summary .....	179
7.2 Future Research .....	181
<b>REFERENCES .....</b>	<b>182</b>

## LIST OF FIGURES

<i>Figure 1-1:</i> Probability density functions for noise and for noise plus signal. ....	6
<i>Figure 2-1:</i> Reflection and transmission at a plane fluid boundary from an acoustic plane wave at oblique incidence. The acoustic impedance $Z$ is equal to $\rho c$ where $\rho$ is density and $c$ is sound speed. ....	25
<i>Figure 2-2:</i> Surface scattering centers contributing to interface scattering. The secondary sources expand spherically. ....	25
<i>Figure 2-3:</i> Changes in the scattered energy distribution as surface roughness increases ((a) smooth surface, (b) slightly rough surface, (c) very rough surface). As roughness increases, the plots show the reduction in the strong specular field and the appearance of a widely spread diffuse field. For very rough surfaces the field is totally diffuse [Ogilvy [3] pg 5]. ....	26
<i>Figure 2-4:</i> a) Kirchhoff approximation requires locally plane surface. b) Rayleigh-Rice approximation requires the height variations of the surface roughness to be small relative to the reference height $h_0$ . c) Composite roughness theory combines the two roughness scales. ....	27
<i>Figure 2-5:</i> Born Approximation applied to small perturbations of density and sound speed in the sediment. Secondary sources are excited by the transmitted energy and expand spherically. ....	28
<i>Figure 3-1:</i> Scattering geometry depicting the large number of scatterers located randomly on the volume ensonified by the source. The phase of the scatterers are uniformly distributed between 0 and 360 degrees. [Reference 13] ....	58
<i>Figure 3-2:</i> Complex Gaussian reverberation: (a), (b) the quadrature components $x$ and $y$ are Gaussian, (c) the envelope is Rayleigh, (d) and the phase is uniformly distributed. [Reference 53] ....	58
<i>Figure 3-3:</i> Rayleigh probability density function (dashed line) estimated by a histogram (bars). ....	59
<i>Figure 3-4:</i> Rayleigh cumulative distribution function. ....	59
<i>Figure 3-5:</i> Rayleigh Probability of False Alarm (PFA) ....	59
<i>Figure 3-6:</i> Rician density function where $\alpha = A / \sigma$ and $v = P / \sigma$ . [Reference 53] ....	60

<i>Figure 3-7: Weibull density functions for <math>c</math> equal to 0.8, 1.2, 2. For <math>c = 2</math>, the density function corresponds to a Rayleigh density. Note larger area under tails for <math>c</math> equal 0.8 and 1.2. [Reference 57]</i> .....	60
<i>Figure 3-8: Lognormal densities. [Reference 77]</i> .....	61
<i>Figure 3-9: Kolmogorov-Smirnov statistic <math>D</math>. A measured distribution of values in <math>x</math> (shown as <math>N</math> dots on the lower abscissa) is to be compared with a theoretical distribution whose cumulative distribution is plotted as <math>F(x)</math>. A step-function cumulative distribution <math>S_N(x)</math> is constructed, one that rises an equal amount at each measured point. <math>D</math> is the greatest distance between the two cumulative distributions. [Reference 57]</i> .....	62
<i>Figure 3-10: Runs test a) random, b) moderately correlated, c) highly correlated.</i> .....	63
<i>Figure 3-11: An autocorrelation function depicting the sampling interval calculation.</i> .....	64
<i>Figure 4-1: Plots of reflection coherence functions versus frequency from Stanton [67]. The data are from clay and silt sediments, where the major source of echo fluctuations is due to water/sediment interface microroughness.</i> .....	87
<i>Figure 4-2: PFA calculated from the Rician distribution using digitized reflection coherence functions published in Stanton's article [67]. The dashed line is the Rayleigh distribution.</i> .....	88
<i>Figure 4-3: Histogram of reverberation envelope fluctuations about the mean modeled by McCammon with the mixture distribution. The dashed lines is the Rayleigh pdf and the amplitude is normalized by the mean.</i> .....	88
<i>Figure 4-4: Jackson <i>et al.</i> PFAs digitized and plotted from data published in reference 86</i> .....	89
<i>Figure 4-5: Boehme and Chotiros' PFAs digitized and plotted from data published in reference 16.</i> .....	90
<i>Figure 4-6: Chotiros <i>et al.</i>'s PFAs digitized and plotted from data published in reference 8.</i> .....	90
<i>Figure 4-7: Stanic and Kennedy's PFAs digitized and plotted from data published in reference 13.</i> .....	91
<i>Figure 4-8: Stanic and Kennedy's PFAs digitized and plotted from data published in reference 14.</i> .....	91
<i>Figure 5-1: Representative reverberation 400 Hz CW from Site A of Celtic Duet, a chalk, limestone and sand bottom. Portions of the recordings used to compute statistics are shown. Time was sub-sampled, using every 20th point only.</i> .....	107

<i>Figure 5-2: Signal portion of the Site A 400 Hz CW reverberation time series in Figure 5-1</i> .....	107
<i>Figure 5-3: Representative reverberation temporal correlation on Beam 33, signal portion from 22 to 57 sec for Site A 400 Hz CW. Correlation lengths to 0.7 average 20 points (0.4 sec)</i> .....	108
<i>Figure 5-4: Overlay of all signal sections from all 13 beams, Site A 400 Hz CW</i> .....	108
<i>Figure 5-5: Coefficient of variation of 13 beams versus time in signal portion of Site A 400 Hz CW data set</i> .....	109
<i>Figure 5-6: Signal sequence Site A 400 Hz CW normalized to unity mean. Note that the spikes appear to be periodic. This appearance is caused by the long pulses which give long lasting peaks in Figure 5-4, so that even sampling every 20th point, these peaks remain for 3 to 4 samples and show up as rhythmic spikes in the appended sequence</i> .....	109
<i>Figure 5-7: a) Runs test over beam, Site A 400 Hz CW, plotting the nth point in the sequence in Figure 5-6 versus the n + 1th point for all points in the sequence. b) Runs test over time, Site A 400 Hz CW, plotting the nth point versus the n + 13th point. The structure shows a diagonal distribution rather than a random one, indicating that the sequence contains temporal correlation</i> .....	110
<i>Figure 5-8: Histogram of fluctuations in signal sequence in Figure 5-6 versus signal amplitude above the mean, Site A 400 Hz CW. Standard deviation is 0.618</i> .....	111
<i>Figure 5-9: Log probability of false alarm versus signal amplitude, Site A 400 Hz CW</i> .....	111
<i>Figure 5-10: a) Same as Figure 5-6 except the signal is sparsely sampled every 80th point. b) Same as Figure 5-7b except the signal is sparsely sampled every 80th point. c) Same as Figure 5-9 except the signal is sparsely sampled every 80th point</i> .....	112
<i>Figure 5-11: Log PFA for 2 pulses each from 5 legs from Site A 400 Hz CW</i> .....	113
<i>Figure 5-12: Expanded plot of noise section from Figure 5-1, Site A 400 Hz CW, Beam 33</i> .....	114
<i>Figure 5-13: Noise coefficient of variation versus time, Site A 400 Hz CW, averages taken across 13 beams</i> .....	114
<i>Figure 5-14: Noise sequence after normalizing to unity among all beams at each time point, Site A 400 Hz CW</i> .....	115
<i>Figure 5-15: Noise runs test for adjacent points n and n + 1, equivalent to beam-to-beam correlations, Site A 400 Hz CW</i> .....	115

<i>Figure 5-16: Noise runs test for every 13th point, equivalent to temporal correlation, Site A 400 Hz CW.....</i>	116
<i>Figure 5-17: Noise histogram of sequence in Figure 5-14, Site A 400 Hz CW.....</i>	116
<i>Figure 5-18: Noise log PFA from Figure 5-17, Site A 400 Hz CW.....</i>	117
<i>Figure 5-19: Noise log PFA for 10 pulses at Site A 400 Hz CW.....</i>	117
<i>Figure 5-20: Beam #33 intensity time series centered at 395 Hz for an hyperbolic FM pulse (HFM) from Site A. Signal and noise portions are marked.....</i>	118
<i>Figure 5-21: Signal portion of the Site A 395 Hz HFM time series in Figure 5-20.....</i>	118
<i>Figure 5-22: Coefficient of variation of 13 beams from Site A 395 Hz HFM time series sampled every 5th point (0.1 sec).....</i>	119
<i>Figure 5-23: Signal sequence for Site A 395 Hz HFM to compare to Figure 5-6.....</i>	119
<i>Figure 5-24: a) Runs test over beam for Site A 395 Hz HFM, to compare with Figure 5-7a. b) Runs test over time for Site A 395 Hz HFM to compare with Figure 5-7b.....</i>	120
<i>Figure 5-25: Signal fluctuation histogram, Site A 395 Hz HFM.....</i>	121
<i>Figure 5-26: Signal log PFA, Site A 395 Hz HFM, for two sampling intervals, 0.4 seconds/sample (solid line) and 0.1 seconds/sample (dashed-dot line).....</i>	121
<i>Figure 5-27: Signal log PFA for pulses from 5 legs at 0.1 seconds/sample, Site A 395 Hz HFM.....</i>	122
<i>Figure 5-28: Noise histogram of fluctuations, Site A 395 Hz HFM.....</i>	122
<i>Figure 5-29: Noise log PFA, Site A 395 Hz HFM (solid line = 0.4 seconds/sample, dashed line = 0.1 seconds/sample).....</i>	123
<i>Figure 5-30: Noise log PFA, Site A 395 Hz HFM, from 5 pulses sampled at 0.1 seconds/sample.....</i>	123
<i>Figure 5-31: Beam #33 intensity time series, Site C 400 Hz CW.....</i>	124
<i>Figure 5-32: Signal portion of the Site C 400 Hz CW time series in Figure 5-31.....</i>	124
<i>Figure 5-33: Signal sequence, Site C 400 Hz CW to compare to Figure 5-6.....</i>	125
<i>Figure 5-34: a) Runs test over beam, Site C 400 Hz CW. b) Runs test over time, Site C 400 Hz CW.....</i>	126
<i>Figure 5-35: Histogram of fluctuations, Site C 400 Hz CW.....</i>	127

<i>Figure 5-36: Signal log PFA, Site C 400 Hz CW.....</i>	127
<i>Figure 5-37: Signal log PFA for pulses from 4 legs, Site C 400 Hz CW.....</i>	128
<i>Figure 5-38: Ship log information. Wind speed shown in the center left graph for Site A.....</i>	129
<i>Figure 5-39: Ship log information. Wind speed shown in the center left graph for Site C.....</i>	130
<i>Figure 5-40: Noise log PFA from the noise portion of Figure 5-31, Site C 400 Hz CW.....</i>	131
<i>Figure 5-41: a) Leg 1 - Beam #65 intensity time series, Site A 1280 Hz CW. b) Leg 4 - Beam #65 intensity time series, Site A 1280 Hz CW.....</i>	132
<i>Figure 5-42: a) Leg 1 - Signal portion of the beam time series, Site A 1280 Hz CW. b) Leg 4 - Signal portion of the beam time series, Site A 1280 Hz CW.....</i>	133
<i>Figure 5-43: a) Leg 1 - Signal sequence (skipping beam 45 which was judged contaminated by local shipping noise), Site A 1280 Hz CW. b) Leg 4 - Signal sequence (skipping beam 45 which was judged contaminated by local shipping noise), Site A 1280 Hz CW. (Note a vertical scale change).....</i>	134
<i>Figure 5-44: a) Leg 1 - Runs test over beam and over time, Site A 1280 Hz CW. b) Leg 4 - Runs test over beam and over time, Site A 1280 Hz CW.....</i>	135
<i>Figure 5-45: a) Leg 1 - Signal histogram of fluctuations, Site A 1280 Hz CW. b) Leg 4 - Signal histogram of fluctuations, Site A 1280 Hz CW.....</i>	136
<i>Figure 5-46: a) Leg 1 - Signal log PFA, Site A 1280 Hz CW. b) Leg 4 - Signal log PFA, Site A 1280 Hz CW.....</i>	137
<i>Figure 5-47: Signal log PFA for pulses from 5 legs, Site A 1280 Hz CW.....</i>	138
<i>Figure 5-48: Noise log PFA for pulses from 5 legs, Site A 1280 Hz CW.....</i>	138
<i>Figure 5-49: A typical Ogopogo time series at 398 Hz from beam 33 of explosive shot 19....</i>	139
<i>Figure 5-50: Typical log of the PFA curves for signal and noise sections of the Ogopogo data set.....</i>	139
<i>Figure 5-51: Ogopogo explosive signal, 630 Hz and 398 Hz, showing the log PFA re-normalized to show the difference between the signal and noise portions relative to the theoretical Rayleigh curve.....</i>	140
<i>Figure 6-1: Example of simulation verification test where zero mean Gaussian distributions are used to generate the x and y components of the pressure amplitude. The top two plots are histograms of the x and the y components with the dashed line being the Gaussian distribution. The bottom two plots are the histogram and PFA of the simulated reverberation with the dashed line being the Rayleigh distribution.....</i>	158

<i>Figure 6-2: Skewed Gaussian distributions for the spectral strength parameter <math>w_2</math> and the sediment volume parameter <math>\sigma_2</math> input to the backscatter model. The mean, standard deviation, skewness, and kurtosis are given in units of <math>m^4</math> for the spectral strength and are dimensionless for the volume parameter.</i> .....	159
<i>Figure 6-3: Backscatter curves for 5 to 85 degree grazing angles and the corresponding normalized histogram when the spectral strength (labeled ss on plots) and volume parameter (labeled vp on plots) are varied simultaneously.</i> .....	160
<i>Figure 6-4: Standardized histograms of intensities, zero mean Gaussian <math>x</math> and <math>y</math> components, and amplitude time series generated by the simulation.</i> .....	161
<i>Figure 6-5: Normalized fluctuation sequence, its histogram, and the runs tests for the twelve amplitude reverberation time series shown in the lower right corner of Figure 6-4.</i> .....	162
<i>Figure 6-6: The cumulative distribution (cdf) of sand and the PFAs for all three bottoms (sand, gravel, and mud/clay) are presented with the test statistics printed on the plots. The test statistics indicate that the null hypothesis can not be rejected.</i> .....	163
<i>Figure 6-7: a) The top plot is the PFA for the all mud sediment. b) The bottom plot is the PFA for the all gravel sediment.</i> .....	164
<i>Figure 6-8: PFAs when 12 gravel amplitudes out of 24 are added to 1, 18, 36, and 54 time slices.</i> .....	165
<i>Figure 6-9: An overlay of PFAs from mixing 12 gravel amplitudes with 12 mud amplitudes for 1, 9, 18, 27, 36, 45, 54, 63, and 72 time slices and the three test statistics for each of the PFAs. The test statistics are plotted against the number of time slices containing the 12 gravel amplitudes.</i> .....	166
<i>Figure 6-10: The combined PFA plots when 15, 18, 21, and 24 gravel amplitudes are added, respectively, to 1, 9, 18, 27, 36, 45, 54, 63, and 72 time slices.</i> .....	167
<i>Figure 6-11: The corresponding Kuiper's test statistic for each of the plots shown in Figure 6-10.</i> .....	168
<i>Figure 6-12: The top two PFAs compare two different mixes of 50% mud and 50% gravel - one is Rayleigh and one is not. The bottom two PFAs compare two different mixes of 75% mud and 25% gravel- again, one is Rayleigh and one is not.</i> .....	169
<i>Figure 6-13: Comparison of PFAs processed with 33 beams between +30 and -30 degrees centered around the broadside beam for wide beams (400 Hz) and narrow beams (750 Hz).</i> .....	170

<i>Figure 6-14: Comparison of PFAs processed with every other beam between +30 and -30 degrees giving a total of 17 beams for wide beams (400 Hz) and narrow beams (750 Hz).</i> .....	171
<i>Figure 6-15: The beam to beam runs test for the 17 wide (400 Hz) and narrow (750 Hz) beams.</i> .....	172
<i>Figure 6-16: Comparison of PFAs processed with every second beam between +30 and -30 degrees giving a total of 11 beams for wide beams (400 Hz) and narrow beams (750 Hz).</i> .....	173
<i>Figure 6-17: Example results when the gravel patch was seen in the mainlobes of all 17 beams as the number of time slices containing gravel was varied. The PFAs were formed by processing every other beam between +30 and -30 degrees giving a total of 17 beams at 400 Hz. The Kuiper's test statistic versus the number of time slices with gravel is also shown. All acceptance levels were above 88%.</i> .....	174
<i>Figure 6-18: Example results when the gravel patch was seen only in the sidelobes of the 17 beams as the number of time slices containing gravel was varied and the corresponding Kuiper's test statistic versus the number of time slices containing gravel. All PFAs were identical and the acceptance levels were all 100%.</i> .....	175
<i>Figure 6-19: Example results when the gravel patch was seen by half of the 17 beams as the number of time slices containing gravel was varied and the corresponding Kuiper's test statistic versus the number of time slices containing gravel. The PFAs and acceptance levels get further away from Rayleigh as the number of time slices containing gravel increases.</i> .....	176
<i>Figure 6-20: Gaussian histogram of sound speeds and the resulting normalized distribution of the fluctuation in bottom grazing angle caused by varying the SVP.</i> .....	177
<i>Figure 6-21: The baseline PFA generated with the isovelocity SVP compared to the PFA generated by varying the SVP at each sample point in the ensemble. The acceptance level of the baseline is 100% and the acceptance level with the varied SVP is above 96%.</i> .....	178

**LIST OF TABLES**

<i>Table 2-1: Input parameters for Mourad and Jackson's low-frequency bottom backscatter model.....</i>	24
<i>Table 4-1: Journal Articles with High Frequency Fluctuation Statistics.....</i>	80
<i>Table 4-2: Research hypotheses investigated in the simulation studies of Chapter 6. ....</i>	86
<i>Table 5-1: Site A 400 Hz CW - Correlation length of signal section for each pulse number and beam. Lengths are defined as 0.7 correlation and are expressed as the number of samples. Time equivalent would be the product of the table entry and 0.02 sec/sample. Mean entry excluding obvious outliers is 20 ± 8. ....</i>	96

# Chapter 1

## INTRODUCTION

### 1.1 Motivation

The detection performance of an active sonar receiver is based on the ability of the design engineer to accurately calculate a detection threshold. If the threshold is too high, only strong signals will be detected. If the threshold is too low, too many false alarms will be detected. To set a detection threshold, the design engineer must have a knowledge of the desired levels for the probability of detection (defined as the probability that a signal, when present, will be detected) and of the probability of false alarm (defined as the probability that a threshold crossing is caused by noise) [1]. The probability of detection PD and the probability of false alarm PFA are determined by areas under the overlapping probability density functions of the noise and of the signal plus the noise as shown in *Figure 1-1*. The two probabilities change as the detection threshold, T, is varied.

When the probability of detection is plotted against the probability of false alarm for various detection thresholds, a family of curves is produced called receiver operating characteristics (ROC) curves. ROC curves have historically been calculated based on the assumption that the probability density function of the noise is caused by a narrowband Gaussian process. However, in shallow water, data published as well as those contained in this thesis will show that the scattering statistics of sediment reverberation is not always a Gaussian random

process. It can have higher level fluctuations than would be expected for a Gaussian process. And, with sediment reverberation being the limiting factor affecting the shape of the noise curve in *Figure 1-1* for littoral environments, this means the false alarm probability will be higher than expected, leading to inefficient detection performance of the active sonar in shallow water.

The use of the term ‘backscattering statistics’ refers to the statistical distribution of the fluctuations in the amplitude of a boundary scattered signal about its mean reverberation level. If the amplitude fluctuations are caused by a Gaussian random process, then the backscattering statistics follow the Rayleigh distribution [5]. It is the width or spread of this distribution that predicts how frequently the reverberation will exceed the mean value, and how loud it will be. When the distribution of fluctuations about the mean shows significantly more spread than is expected by the assumed Rayleigh distribution, it is an indication that occasional high-level bursts of reverberation occur more frequently than would be anticipated, leading to an unexpectedly high false alarm rate in the detection processing.

Several published authors have postulated theories as to the factors causing the backscattering statistics to have a wider spread than is expected for a Rayleigh distribution. Stanic and Kennedy [13, 14], after analyzing data from a sandy site and a coarse shell site, feel the statistics vary as a function of frequency, grazing angle, and beamwidth; however, the variations were not consistent between the two sites. Therefore, they postulate that the backscattering statistics are not only a function of the scatterers located on the sea floor but must be a function of scatterers from both the sediment surface and the volume of the sediment. Chotiros *et al.* [8] and Boehme and Chotiros [16] analyzed data from two different sandy sites and concluded that the measurements made with a wide beam receiver follow a Rayleigh distribution due to the wider field of averaging, while measurements made with a narrower beamwidth consistently departed from

Rayleigh. They felt any evidence of frequency dependence was inconclusive by virtue of the large variations in the reported results, even for similar bottom types. They suggested that knowledge of the sediment type is not sufficient to allow detailed comparisons of the high frequency measurements.

Theoretical approaches have also been taken to provide explanations as to the physical factors affecting the backscattering statistics. For example, McDaniel [17] developed a model that assumes the sediment elevation spectrum is separable into down-range and cross-range components, and that the fluctuations of both components are chi-square distributed with the degrees of freedom dependent upon the extent of the scattering patch size. She compared her model to the data published by Chotiros *et al.* [8] and obtained satisfactory results. Her results showed that a small scattering patch size, due to narrow beamwidths and/or short range, produced statistics with a wider spread than is expected for a Rayleigh distribution. However, Becker [10] applied McDaniel's model to Stanic and Kennedy's data [14] and concluded the comparison had enough discrepancies to deduce that backscattering statistics are dependent on other factors in addition to just beamwidth and range. Becker postulated that combining measurements with different mean scattering strengths due to anisotropic surfaces caused non-Rayleigh distributions.

## 1.2 Research Objectives

The overall objective of this research is to postulate the dominant physical causes of changes in the statistical distributions of ocean bottom reverberation fluctuations. The research will concentrate on shedding light through simulation on aspects of the production of non-Rayleigh statistics. This research includes a study of observed statistics for bottom backscattering

amplitude fluctuations that do not obey the Rayleigh distribution. However, measured data do not provide sufficient information to quantify what factors do influence these statistics and if they can be related to sediment type or bottom roughness or some other system parameter. Therefore, extensive simulations are included in the research to isolate and better study causes of statistical changes. The specific objectives of this research are to:

- 1) document measured statistical distributions for a variety of environments and frequencies;
- 2) determine through simulation the sensitivity of the fluctuation statistics to changes in the distributions of sediment parameters and to small scale variability in the sound speed profile;
- 3) determine the effect of beamwidth on spatially stationary and non-stationary realizations of the bottom; and,
- 4) postulate a theory as to when and why non-Rayleigh statistics occur.

### 1.3 Thesis Outline

To accomplish the research objectives, this thesis is organized as follows. Chapter 2 presents the fundamental theories on bottom backscatter. The currently available bottom backscatter models are presented with emphasis placed on describing the model chosen for the simulation portion of this thesis. Chapter 3 provides the definition of bottom reverberation fluctuations and details the statistics associated with fluctuations. Chapter 4 presents the background history of both theoretical and experimental approaches taken by others to provide a better understanding of fluctuations and to quantify the fluctuations. Chapter 5 presents non-

Rayleigh fluctuation statistics for low frequency, in-water data collected during two separate shallow water exercises conducted by the Strategic Allied Commander Atlantic Undersea Research Centre (SACLANTCEN), LaSpazia, Italy. The time series were processed as part of this thesis. Chapter 6 presents the simulation studies performed to provide the additional data needed to address the second and third research objectives listed in Section 1.2 above. The objectives are to determine the sensitivity of the fluctuation statistics to changes in the sediment parameters, the beamwidth, and the sound speed profile. And, Chapter 7 presents the conclusions of the research along with recommendations for further research.

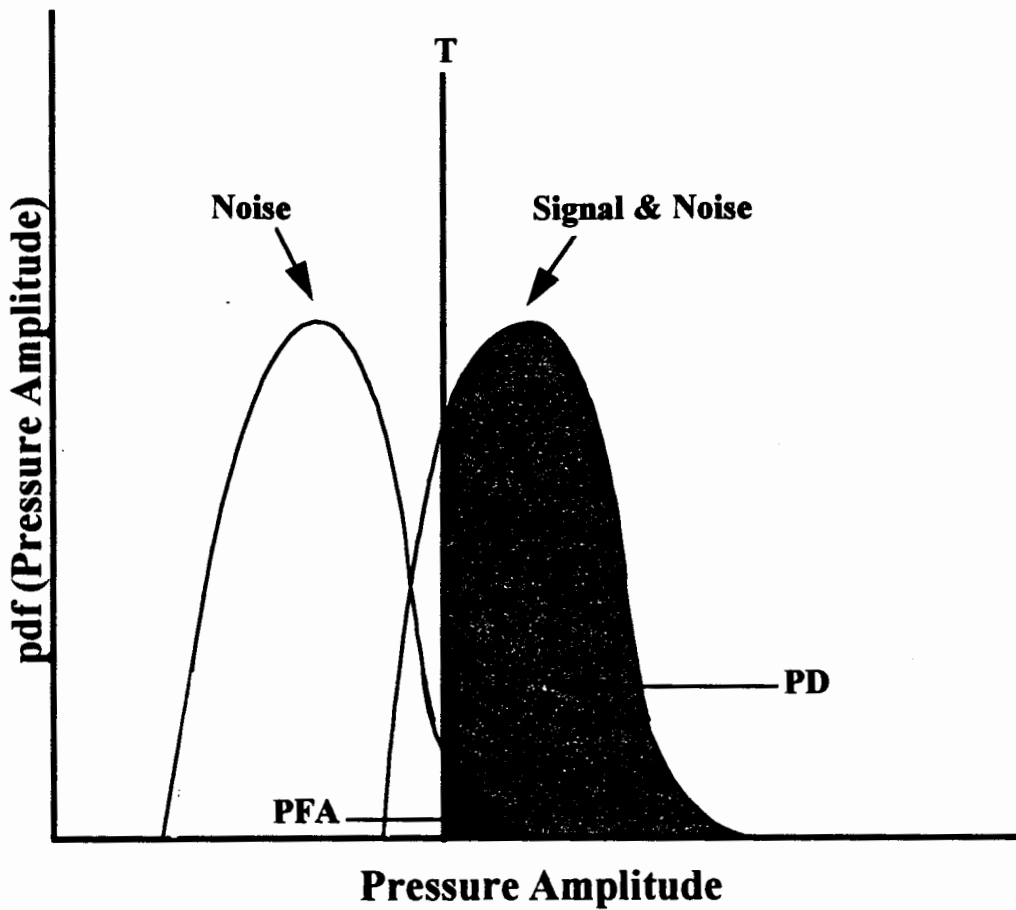


Figure 1-1: Probability density functions for noise and for noise plus signal.

## Chapter 2

### SCATTERING THEORIES AND MODELS

This chapter provides an overview of the fundamental theories of sediment scattering and highlights models currently available to predict the scattering strength of the sediment. The details of the scattering model chosen for the simulation studies performed in support of this thesis are also provided. Rigorous physical development of the scattering theories are not presented here because this thesis focuses on scattering statistics and not scattering theory. However, in order to understand the issues addressed in this thesis a basic understanding of scattering theory is required, which is the purpose of this chapter. References are provided for those interested in the detailed physical development of the scattering theories.

#### **2.1 Fundamental Theories of Scattering**

Bottom reverberation is caused by a combination of the reflected intensity being scattered from the roughness of the sediment surface and the transmitted intensity being scattered or reflected back into the water column by inhomogeneities within the sediment. The following section provides the theory for the reflection and transmission of intensity from an incident wave at oblique incidence to a smooth, lossless sediment.

### **2.1.1 Reflected and transmitted intensity**

When an acoustic plane wave hits a smooth bottom, some of the incident intensity is reflected at the surface of the sediment and some is transmitted into the sediment as shown in *Figure 2-1*. The amount of intensity that is reflected or transmitted depends on the acoustic impedance mismatch between the water and the sediment and on the grazing angle of the incident wave at the boundary [4].

The larger the acoustic impedance mismatch at the water/sediment interface, the greater the amount of energy reflected. The acoustic impedance is defined as the product of the density  $\rho$  and the compressional wave sound speed  $c$ . Referencing *Figure 2-1*, let subscript 1 designate water parameters at the interface of surface of the sediment and subscript 2 the sediment parameters. For fast, hard bottoms like sand, silt and gravel where  $\rho_1 c_1 < \rho_2 c_2$ , most of the incident intensity will be reflected; little energy penetrates the sediment. For slow, soft bottoms like mud, ooze and clay where  $\rho_1 c_1 \approx \rho_2 c_2$ , acoustic energy will be both reflected at the surface of the sediment and refracted into the sediment.

The grazing angle also plays a role in determining the amount of intensity reflected at the interface and the amount transmitted into the sediment. In ocean acoustics, since the important boundaries are horizontal, it is customary to measure angles relative to the horizontal and to call the angle of the incident wave with respect to the horizontal the *grazing angle* [4]. This is in contrast to the *incidence angle* which is defined as the angle of the incident wave measured with respect to the *normal* to the horizontal boundary. The role the grazing angle  $\theta_{graze}$  plays in the reflection of energy in a lossless medium can be explained using the reflection coefficient. The

*reflection coefficient* is the ratio of the reflected pressure amplitude  $P_r$  to the incident amplitude  $P_i$ ; it is the percentage of the incident wave that is reflected. The reflection coefficient [4] is

$$R = \frac{P_r}{P_i} = \frac{Z_2 \sin \theta_i - Z_1 \sin \theta_t}{Z_2 \sin \theta_i + Z_1 \sin \theta_t}$$

where  $Z_j$  is the acoustic impedance  $\rho_j c_j$ ,  $j = 1, 2$ ,  $\theta_i$  is the grazing angle of the incident wave, and  $\theta_t$  is the angle of the transmitted wave.

When  $R = 0$ , there is no reflected energy; all the energy is transmitted into the bottom.

This condition occurs for incident grazing angles that satisfy  $\sin \theta_i = \frac{Z_1}{Z_2} \sin \theta_t$ . Slow, soft

bottoms can have an angle  $\theta_i$  that satisfies this condition. The angle is then called the *angle of intromission*  $\theta_I$ . The angle of intromission is the grazing angle at which no reflection occurs; all energy is transmitted into the sediment. When  $R = -1$ , all the energy is reflected; no energy is transmitted into the bottom. Fast, hard bottoms have a *critical angle*  $\theta_c$  defined by

$\cos \theta_c = c_1 / c_2$ , resulting from Snell's law (which is  $\frac{\cos \theta_i}{c_1} = \frac{\cos \theta_t}{c_2}$ ). For grazing angles below

the critical angle, all the incident energy is reflected from the sediment interface; none of the energy penetrates the sediment volume.

### **2.1.2 Bottom scattering mechanisms**

Both the reflected and transmitted waves can be scattered. Scattering is defined as the reradiation of sound due to interference of the incident wave with a rough boundary or with inhomogeneities in the propagation path [1]. If we now add roughness to the above smooth

boundary, the reflected wave will be scattered by the roughness on the sediment surface. This type of scattering is called interface scattering. If we replace the simple lossless medium with a more complex, inhomogeneous sediment, the transmitted wave can be both refracted by variations in the sound speed and density gradients within the sediment and scattered by the inhomogeneous composition, gas bubbles, or discrete scattering layers of the sediment. This combination of refraction and scattering is called volume scattering. Bottom reverberation is the sum total of the scattering from all scattering mechanisms located on the surface of the sediment and within the sediment and therefore, includes both interface scattering and volume scattering.

### 2.1.3 Scattering from interface roughness

Interface scattering is caused by the roughness of the surface of the sediment. The roughness of a scattering surface depends on the properties of the wave being scattered. Both the frequency and grazing angle of the incident wave as well as the surface height variations determine how 'rough' any surface appears to be; i.e., its 'effective roughness'. A surface appears rougher for smaller incident wavelengths or for grazing angles closer to the surface normal. The *scale* of roughness, relative to the wavelength and grazing angle of the incident wave, is a major factor in determining how energy is scattered [3]. A commonly used criterion for specifying the roughness scale of a surface uses the Rayleigh roughness parameter. The Rayleigh roughness parameter is defined as  $2kh \cos \theta_{graze}$  where  $k$  is the acoustic wavenumber ( $k = \frac{\omega}{c_1} = \frac{2\pi}{\lambda}$ ),  $h$  is the height of the scatterer on the surface measured from some reference plane  $h_o$ , and  $\theta_{graze}$  is the grazing

angle. The Rayleigh criterion states that if  $2kh \cos \theta_{graze} < \frac{\pi}{2}$  then the surface is ‘smooth’; otherwise it is ‘rough’ [3].

Interface scattering can be visualized as scattering centers on the sediment surface as shown in *Figure 2-2*. The scattering centers are point sources reradiating the incident field impinging on the interface. This idea is called the Huygens’ principle: when a source ensonifies the surface, each incremental area on the surface becomes a source of a Huygens (or secondary) wavelet. The wavelets expand spherically. The sound pressure at a given location is the integral over all the wavelets [19].

The sound pressure at a given location depends on whether the wavelets constructively interfere to give a strong, specularly scattered field or whether they destructively interfere to give a more diffusely scattered field. The roughness scale of the surface determines how the wavelets will interfere with each other. *Figure 2-3* shows the effect of roughness on the scattered field. For a smooth surface, the wavelets constructively interfere leading to a strong coherent field in the specular direction. The specular wave is termed the *coherent field* because of its predictable and constant phase relative to that of the incident wave. As the roughness of the surface increases, destructive interference will occur in the specular direction, reducing the amplitude of the specular field. This scattered energy is termed the *diffuse* or *incoherent field* because of its wide angular spread and lack of phase relationship with the incident wave [3].

#### 2.1.3.1 Helmholtz-Kirchhoff integral

To model interface scattering, the secondary wavelets generated by the scattering centers are summed together using the Helmholtz-Kirchhoff integral (see Ogilvy [3] in Sec. 4.1.1 and

Clay & Medwin [19] in A10.1 and A10.2). The Helmholtz-Kirchhoff integral gives a mathematical description of the Huygens' principle and computes the pressure field  $p^{sc}(r)$  due to interface scattering at a position  $r$ . The computation involves subtracting the pressure field  $p^{inc}(r)$  due to the incident wave from the total pressure field  $p(r)$  at the location  $r$ . The scattered field as defined by the Helmholtz-Kirchhoff integral is :

$$p^{sc}(r) = p(r) - p^{inc}(r) \\ = \int_{S_0} \left[ p(r_0) \frac{\partial G(r, r_0)}{\partial n_0} - G(r, r_0) \frac{\partial p(r_0)}{\partial n_0} \right] dS_0$$

where  $S_0$  is the surface of the scatterer,  $n_0$  is the unit surface normal pointing towards the source and  $G(r, r_0)$  is the acoustic Green's function representing the effect at  $r_0$  of a point source at  $r$ . The free space Green's function is used:

$$G(r, r_0) = \frac{\exp(ik|r - r_0|)}{4\pi|r - r_0|}$$

where  $r_0$  is on the scattering surface and  $r$  is some distance from the scatterer.

In practice, the precise mathematical form of the pressure field for the Helmholtz-Kirchhoff integral is not known; therefore, approximations of the field are made. These approximations break the surface roughness into two different roughness scales by the very nature of the assumptions made on the pressure field and the boundary conditions satisfied. The two commonly used approximations are called the Kirchhoff approximation (or tangent plane method) and the Rayleigh-Rice approximation (or first-order perturbation theory).

### 2.1.3.2 Kirchhoff approximation

The Kirchhoff approximation or tangent plane method requires limitations on the rate of change of surface properties and is considered appropriate for ‘gently undulating’ surfaces. The theory behind this approximation assumes that the surface is flat in the location hit by the incident wave as shown in *Figure 2-4 a* and that the slope of (or tangent to) this locally flat surface has an orientation that is Gaussian distributed. The orientation of the slope determines the amount of energy backscattered to the receiver. This method provides a good approximation of surface scattering when the minimum radius of curvature  $R_{\min}$  of the surface is much greater than the acoustic wavelength ( $R_{\min} \gg \lambda$ ).

### 2.1.3.3 Rayleigh-Rice approximation

The Rayleigh-Rice approximation or first-order perturbation theory provides a good approximation for surfaces of small roughness where the scattered field is only slightly altered by the presence of roughness [3]. This method is only valid if surface height  $h$  is much less than the wavelength of the incident wave and, in addition, the surface slope is sufficiently small [25]. More formally, these conditions are stated as the surface height function  $h(x, y)$  satisfies the restrictions

$$\begin{aligned}|h(x, y)| &<< \lambda \\ |\nabla h(x, y)| &<< 1\end{aligned}$$

where  $\lambda$  is the acoustic wavelength and  $\nabla$  is the gradient operator. The small scale roughness is depicted in *Figure 2-4 b*.

The theory behind this approximation assumes that the backscattering is dominated by a resonant interaction between the incident acoustic field and the component of the surface roughness whose wavelength is half that of the acoustic wavelength (which is Bragg's Law for monostatic first-order backscattering). This implies there is only one roughness scale on the surface dominating the backscattering - it is the component of roughness whose wavelength is half that of the acoustic wavelength. (For details and limitations on both the Kirchhoff and the Rayleigh-Rice approximations and a complete list of references associated with the approximations, see Ogilvy [3]; Liszka [20]; McDaniel and Gorman [25, 26]; and Jackson *et al.* [15].)

#### 2.1.3.4 Composite roughness theory

The composite roughness theory combines both the Kirchhoff and the Rayleigh-Rice approximations into one model and is depicted in *Figure 2-4 c*. The composite roughness theory assumes the rough surface can be divided into large scale and small scale roughness [26]. This model assumes that backscattering is due to small scale roughness, with the local grazing angle dependent on the slope of the large scale surface roughness [15]. The Rayleigh-Rice approximation is applied to the small scale interface roughness. The Kirchhoff approximation is applied to incorporate the change of the local grazing angle of the incident wave due to the slope  $f_x$  of the large scale roughness. (For details and limitations on the composite roughness theory, see McDaniel and Gorman [25, 26]; and Jackson *et al.* [15].)

#### **2.1.4 Scattering from volume inhomogeneities**

Recently, experimental results have shown the importance of scattering by sediment volume inhomogeneities at both high and low frequencies [15, 31, 32]. The physical mechanisms causing the sediment volume scattering are not yet completely understood. However, much progress has been made over the past decade toward increasing our understanding of the major scattering mechanisms. The sediment volume scatterers are divided by Tang [23] based on their scattering strength into strong scatterers such as buried gas bubbles, rocks, shells, and hard rough bedrock, and weak scatterers such as variations in the acoustic properties of the sediment.

##### **2.1.4.1 Density and sound speed variations**

For weak scatterers, the variation in the acoustic properties are typically assumed [6, 23, 22, 24] to be variations of the sound speed and density within the sediment relative to their mean values of  $c_2$  and  $\rho_2$  depicted in *Figure 2-1*. The general assumption is that these small variations or fluctuations of the sound speed and density about their mean values cause the transmitted intensity to be reflected at impedance discontinuities back into the water column and therefore, increase the strength of the scattering return from the bottom.

Scattering due to small variations in density and sound speed within the sediment result from variations of porosity in very small pockets throughout the sediment. Yamamoto [37] determined through analyses of core samples and acoustic tomograms that density fluctuations are proportional to the velocity fluctuations. He also determined that the density fluctuations are the dominant scattering mechanism because they are usually much larger than velocity fluctuations with this tendency being more pronounced in softer sediments. He then developed a method to

obtain 3-D power spectra of density and velocity from core samples. This method was implemented in a sonar equation model for predicting backscatter. After comparing his model to both high frequency (10-100 kHz) [2] and low frequency (0.1-5 kHz) [6] backscattering strengths, he concluded that volume scattering is a dominant mechanism of acoustic backscattering from not only soft sediments but also dense sediments in the high and low frequency ranges.

#### 2.1.4.2 Born approximation

The small variations in density and sound speed within the sediment act to scatter spherical waves and Huygens' wavelets are used in the scattering theory. For volume scattering, it is not the incident wave exciting the secondary sources; it is the transmitted wave. Also, the roughness is not related to the height variations of the surface relief, but instead, it is related to the small perturbations of density and sound speed around their mean values [23]. The solution technique commonly applied to this problem is to find the far-field solution for the Born approximation of the wave equation based on the assumptions of weak and single scattering [37].

The Born approximation assumes that the wave scattered by a small volume within the sediment is independent of what has been scattered elsewhere [41]. Yamamoto [37] clearly defines each step in the technique. A brief overview will be provided here. The scattering takes place only within a small scattering volume  $V$  of the sediment in which the density and sound speed fluctuate as shown in *Figure 2-5*. Outside the scattering volume is a fluid sediment with constant density  $\rho_2$  and constant sound speed  $c_2$  with no variations and no attenuation. The Helmholtz equation for the acoustic pressure  $p$  and angular frequency  $\omega$  is given as

$$\rho \nabla \cdot \left( \frac{1}{\rho} \nabla p \right) + \frac{\omega^2}{c^2} p = 0$$

and is modified by setting  $c = c_2 + dc$  where  $c_2$  is the speed of sound of the sediment plus the slight fluctuation in the sediment sound speed  $dc$ , and  $\rho = \rho_2 + d\rho$  where  $\rho_2$  is the density of the sediment plus the slight fluctuation in the sediment density  $d\rho$ . The small fluctuations of the sediment sound speed  $dc$  and density  $d\rho$  are defined by

$$c = c_2 + dc = c_2(1 + \mu), \\ \rho = \rho_2 + d\rho = \rho_2(1 + \eta)$$

where  $c_2$  and  $\rho_2$  are the mean sediment values and the relative variations  $\mu$  and  $\eta$  are assumed to be small. The sediment wavenumber is  $k_2 = \omega/c_2$ . The Helmholtz equation then becomes

$$\nabla^2 p + k_2^2 p = 2k_2^2 \mu p + k_2^2 \eta p + \nabla \cdot (\eta \nabla p).$$

First-order perturbation theory and the Born approximation are then applied to this equation to remove multiple scattering terms and obtain an approximate solution for the scattered field. This method is for weak, *single* layer scatterers.

Tang [23] presents a theory for stacking weak scattering layers. His theory starts with the first-order perturbation theory and the Born approximation used for one layer of volume scattering and expands it to multiple layers with different statistical variances describing the sound speed and density variations for each layer. He feels the expanded model will more accurately address the natural sedimentation processes where layers of different scattering strengths are often present in stacks on the seafloor.

#### 2.1.4.3 Sediment granularity and Biot's theory

Boyle and Chotiros [38] and Yelton *et al.* [39] took a different approach. They modeled the sediment grains and gas bubbles structurally by extending Biot's theory, which is based on the propagation of sound through a fluid-filled porous solid medium. Yelton *et al.* [39] started with Biot's theory of acoustic propagation of elastic waves in a fluid-saturated porous solid. They felt the theory contained the basic mechanisms of acoustic interaction as far as forward propagation is concerned, but it did not have a mechanism to account for scattering and any associated losses due to granularity of the sediment. They have extended Biot's theory to include the effects of granularity using a brute force, numerical simulation approach to obtain results quickly. In their initial study, the agreement between model predictions and experimental measurements indicates that their approach is feasible.

#### 2.1.4.4 Shear Waves

Another complexity associated with volume scattering is the fact that sediments sustain both compressional sound waves and shear waves as discussed by Clay and Medwin [19]. Many sediments such as mud and clay are unconsolidated meaning that the particles are not fused together. However, even unconsolidated sediments have enough rigidity to transmit shear waves. The particle displacement for shear waves is normal to the direction of propagation. Fluids do not transmit shear waves.

The absorption coefficient and speed of a shear wave differ considerably from those for a compressional wave. In sediments, the shear speed varies typically from 250 to 600 meters per second (m/s). In rock such as basalt, the shear speed is 2500 m/s while compressional speed is

7000 m/s. In seawater, the compressional speed is about 1500 m/s, whereas in sediments it can vary from 1500 up to 1800 m/s or more [27]. Typically, attenuation of shear waves is 10 to 100 times greater than that of compressional waves.

In conclusion, volume scattering is a complex physical process to understand and to model. The general assumptions are that high frequency waves (above 10 kHz) will only penetrate the very top centimeters because absorption within the sediment is so high (and increases with frequency). Therefore, due to the smaller wavelength, interface roughness should be the dominant scattering mechanism. Low frequency intensity will penetrate more deeply and be reflected back into the water column from the multiple volume layers or even a hard rough bedrock, especially in soft sediments.

### **2.1.5 Definition of Scattering Strength**

The ratio upon which bottom reverberation is calculated is called the scattering strength  $S$  per unit area [1]. *Scattering strength* is a measure of the scattering ability of the bottom, expressed in decibels per yard squared, and defined as

$$S = 10 \log \left( \frac{I_s}{I_i} \right)$$

where  $I_i$  is the incident intensity and  $I_s$  is the scattered intensity corrected to a reference distance of 1 yard.

In a monostatic geometry, when a pulse of underwater sound strikes the bottom of a sea, bay or river, a portion of the intensity is returned or scattered back to the source in which case the

quantity  $S$  is more specifically termed backscattering strength  $S_B$ . This backscattering is the bottom reverberation that would be received back at the location of the source [29]. The coherent, specular reflection does not contribute to backscattering because it is not received back at the source location due to its forward reflection angle.

Another commonly used variation of the scattering strength is the scattering cross section of a unit area. It is the ratio of the scattered power, referenced to 1 yard, to the intensity incident on a unit area. Since it is assumed that the scattering is uniformly distributed over a hemisphere of the secondary wavelets (see *Figure 2-2*), the relationship between the scattering strength and the scattering cross section is:

$$S = 10 \log \frac{m_s}{2\pi}$$

where  $m_s$  is the scattering cross section of a unit area.

## 2.2 Model for backscattering strengths

The scattering mechanisms currently modeled for a bottom boundary are interface scattering from bottom roughness (Clay and Medwin [19]; Kuo[21]; and Ogilvy [11] ) and volume scattering from sediment inhomogeneities (Ivakin and Lysanov [22]; Hines [24]; and Tang [ 23]). Both mechanisms were combined by Crowther [7], Boyle and Chotiros [38], Mourad and Jackson [6], and Jackson *et al.* [15].

In reference 6, Mourad and Jackson present their low-frequency bottom backscatter model. This model was chosen to generate bottom backscatter strengths that were used as inputs to the simulation portion of the research described in support of this thesis. The criteria applied in

choosing a model included it having a feature to vary the input parameters for interface roughness scattering and sediment volume scattering independently.

Mourad and Jackson's model [6] includes independent input parameters for varying both the roughness interface and sediment volume scattering contributions. Their model assumes that the two scattering mechanisms are uncorrelated. It does not include volume scattering from layers, granularity, or a sediment/bedrock interface. However, the model does contain all the necessary features and robustness required to generate backscattering strengths utilized in forming bottom reverberation time series for analysis in support of this thesis.

### **2.2.1 Interface roughness model**

For rough interface scattering, Mourad and Jackson's model [6] employs the composite roughness theory for low and intermediate grazing angles (up to about  $75^\circ$ ) and the Kirchhoff theory for large grazing angles up to normal incidence. These two theories are spliced together using an interpolation rule to give a smooth curve.

The composite roughness and Kirchhoff theories calculate average contributions to backscatter based on a statistical description of the rough surface. The roughness of the surface is taken to be isotropic and described by a Gaussian random process. The roughness statistics are governed by a spectrum  $W(K)$  that is proportional to a power of the wavenumber  $K$ :

$$W(K) = \beta K^{-\gamma}$$

where  $\beta = w_2 / h_0$ ;  $w_2$  controls the strength of the interface roughness spectrum and  $\gamma$  controls the shape of the spectrum;  $h_0$  is the reference length equal to 1 meter. To provide control over roughness, Mourad and Jackson's model has  $w_2$  and  $\gamma$  as inputs.

The interface roughness model [6] also allows for differences in average sound speed  $c_i$  and density  $\rho_i$  between the sediment ( $i = 2$ ) and the overlying water ( $i = 1$ ). This information is represented in three of the eight geoacoustical input parameters to their model:

$$c_1,$$

$$\nu = \frac{c_2}{c_1}, \text{ and}$$

$$\rho = \frac{\rho_2}{\rho_1}$$

which are, respectively, the sound speed of water at the interface, the sound-speed ratio, and the density ratio, all defined at the water/sediment interface. This is important to note, because the sediment volume scattering model includes a gradient in sound speed, i.e.,  $c_2(z)$ . Therefore, they define the parameter  $\nu = c_2 / c_1$  to be  $c_2(0) / c_1$ , where  $c_2(0)$  is the average value of the sediment sound-speed profile taken over the top ten meters of the sediment.

### 2.2.2 Volume scattering model

For volume scattering, Mourad and Jackson use an approach that is very similar to the model published by Ivakin [42]. They assume that a distribution of omnidirectional point scatterers in the sediment causes the backscatter of sound that has been transmitted into the body of the sediment. First-order perturbation theory and the Born approximation are then applied to

neglect multiple scattering terms and obtain an approximate solution for a weakly scattered field. They represent the strength of the scatterers by a dimensionless model parameter  $\sigma_2$ , with

$$\sigma_2 = \sigma_v / \alpha,$$

where  $\sigma_v$  is the volume scattering cross section and  $\alpha$  is the attenuation coefficient of the sediment. The amount of volume scattering applied by the model is controlled by the input parameter  $\sigma_2$ . The volume scattering strength is directly proportional to  $\sigma_v$ . Therefore, if we double  $\sigma_2$  via a doubling of  $\sigma_v$ , there will be a three decibel rise in volume scattering strength.

The eight input parameters for Mourad and Jackson's model are listed in *Table 2-1*. Of the eight input parameters, the volume parameter  $\sigma_2$  controls the contribution of sediment volume scattering to the total scattering strength without affecting the contribution of interface scattering. The spectral strength  $w_2$  and the spectral exponent  $\gamma$  control the contribution of interface scattering to the total scattering without affecting the contribution of sediment volume scattering. The other parameters affect the contributions from both the sediment volume scattering and the interface scattering by changing the amount of energy reflected at the interface and transmitted into the sediment and will remain constant in the simulation studies.

### 2.3 Summary

In summary, Mourad and Jackson's model was chosen to generate backscattering strengths for the simulation portion of the research for this thesis since the model combines interface roughness and sediment volume scattering and allows each to be controlled independently. Interface roughness is modeled using the composite roughness theory for grazing angles less than

$75^\circ$  and the Kirchhoff approximation for angles greater than  $75^\circ$ . The volume scattering is modeled with the first-order perturbation theory and the Born approximation.

*Table 2-1:* Input parameters for Mourad and Jackson's low-frequency bottom backscatter model.

Symbol	Name	Definition
$f$	Frequency	Frequency of sound (1/sec)
$c_1$	Water sound speed	Sound speed in water at the water/sediment interface (m/s)
$\rho$	Density ratio	Ratio of sediment mass density to water mass density
$v$	Sound speed ratio	Ratio of sediment sound speed at water/sediment interface to water sound speed
$g$	Sound speed gradient	Slope of sediment sound speed profile at water/sediment interface (1/s)
$l$	Loss parameter	Ratio of imaginary wave number to real wave number for the sediment
$\sigma_2$	Volume parameter	Ratio of sediment volume scattering cross section to sediment attenuation coefficient
$\gamma$	Spectral exponent	Exponent of bottom surface spectrum
$w_2$	Spectral strength	Strength of bottom surface spectrum ( $m^4$ ) at the wavenumber of 1 rad/m

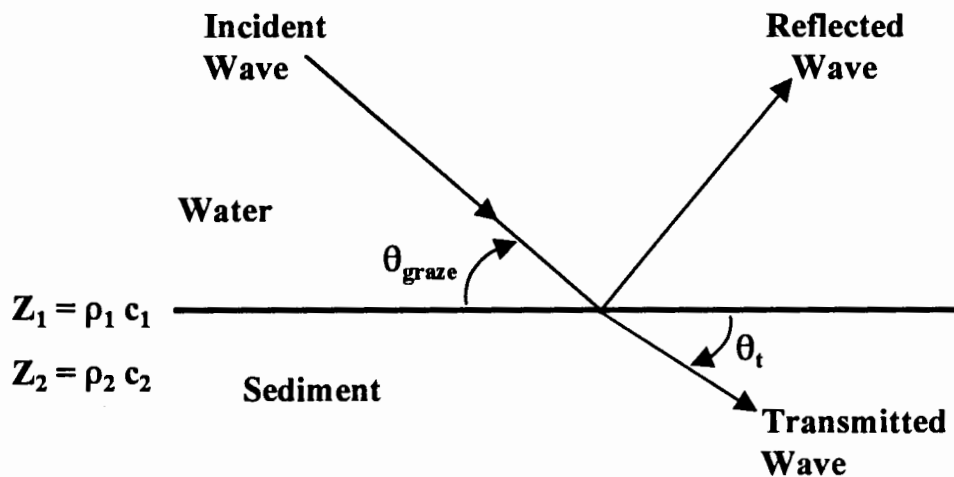


Figure 2-1: Reflection and transmission at a plane fluid boundary from an acoustic plane wave at oblique incidence. The acoustic impedance  $Z$  is equal to  $\rho c$  where  $\rho$  is density and  $c$  is sound speed.

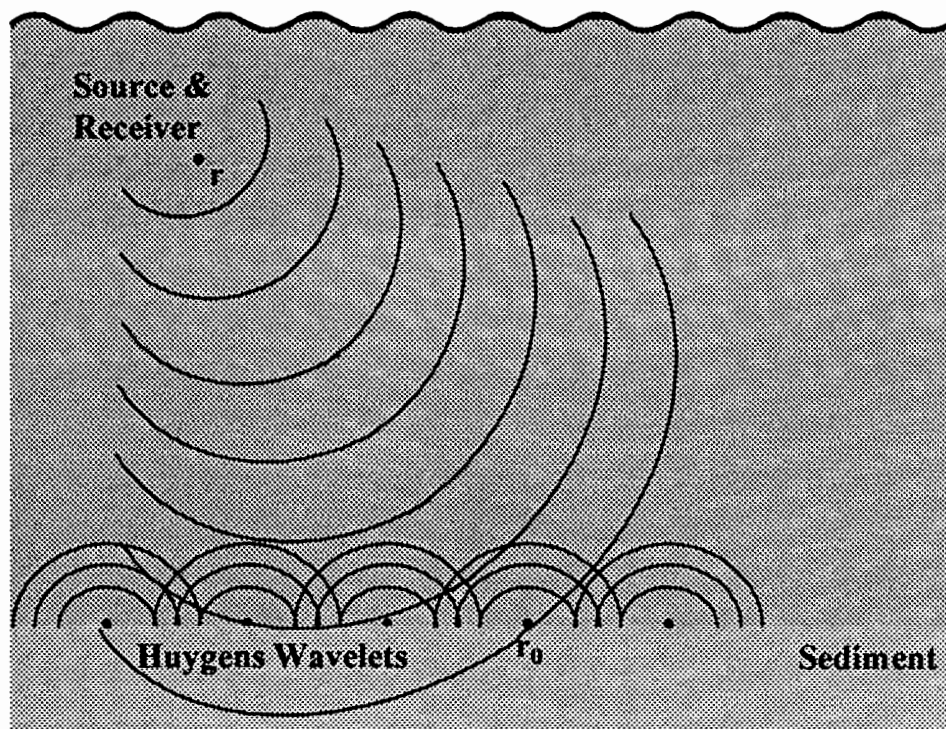


Figure 2-2: Surface scattering centers contributing to interface scattering. The secondary sources expand spherically.

**Incident Wave**      **Specular Direction**

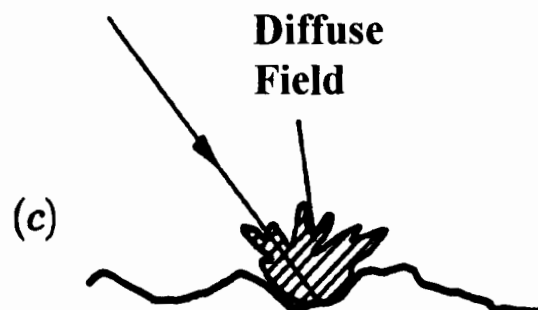
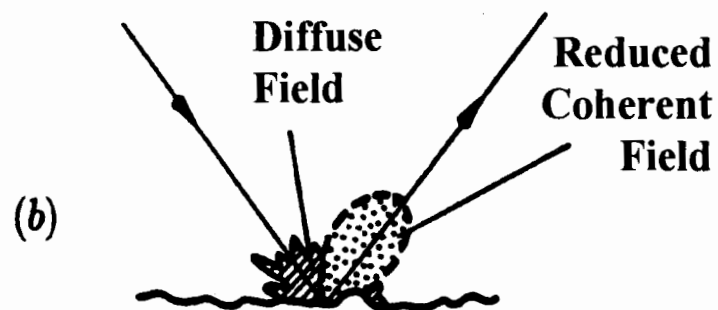
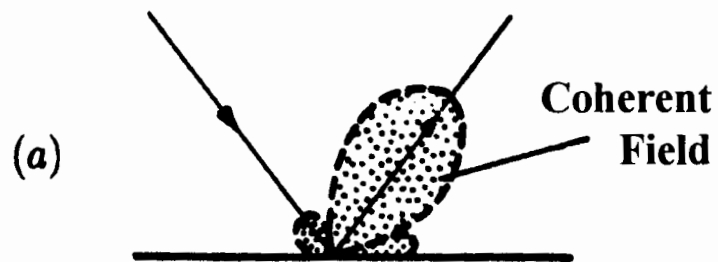


Figure 2-3: Changes in the scattered energy distribution as surface roughness increases ((a) smooth surface, (b) slightly rough surface, (c) very rough surface). As roughness increases, the plots show the reduction in the strong specular field and the appearance of a widely spread diffuse field. For very rough surfaces, the field is totally diffuse [Ogilvy [3] pg. 5]

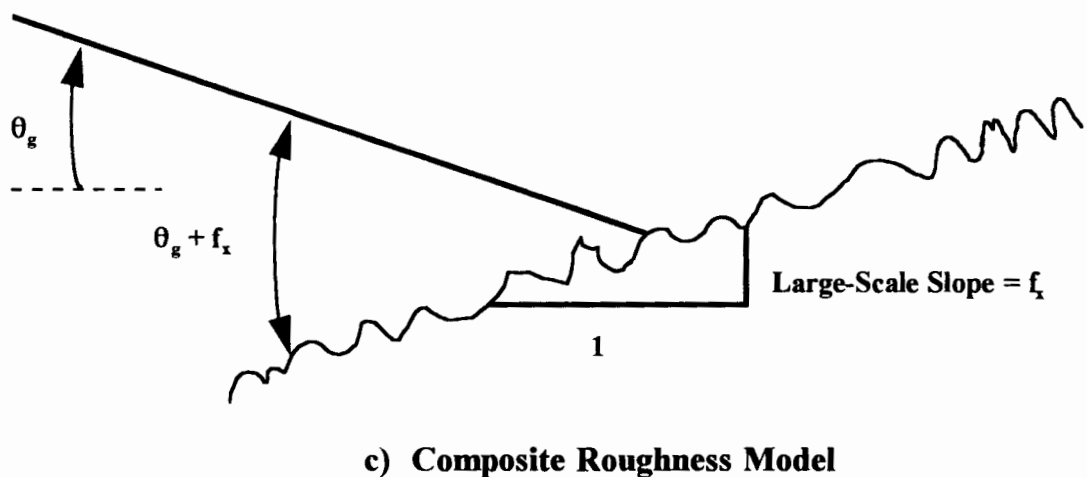
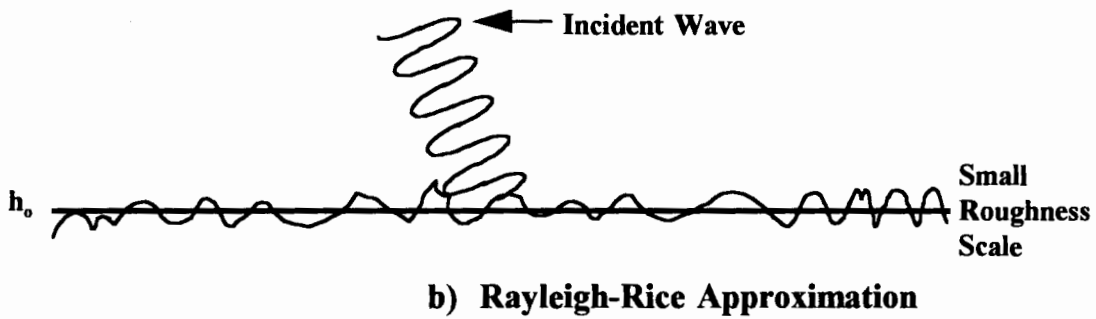
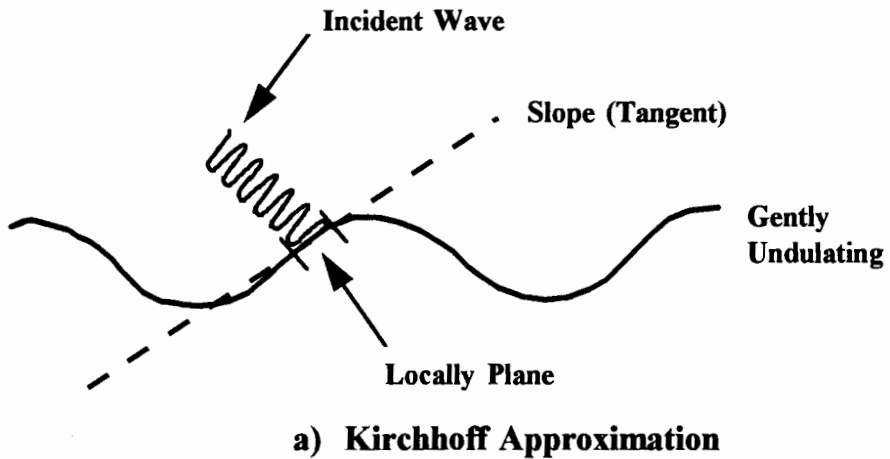


Figure 2-4: a) Kirchhoff approximation requires locally plane surface. b) Rayleigh-Rice approximation requires the height variations of the surface roughness to be small relative to the reference height  $h_0$ . c) Composite roughness theory combines the two roughness scales. [Reference 3,15]

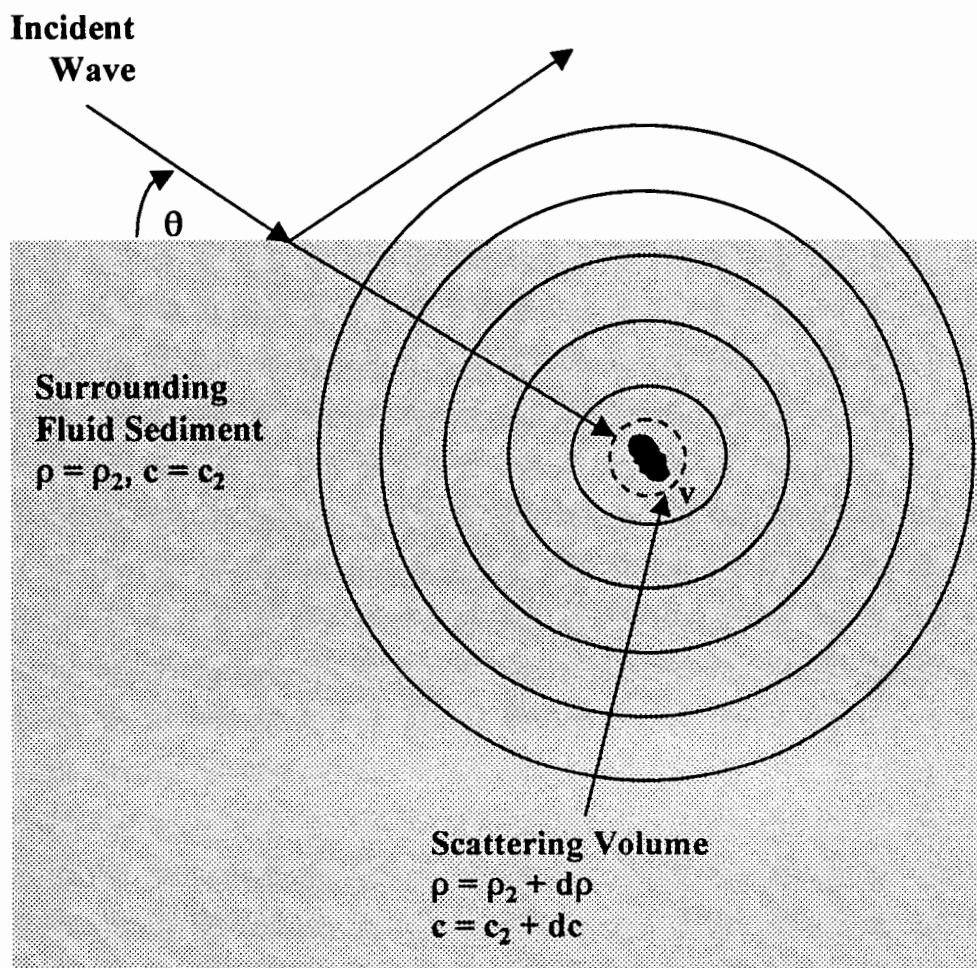


Figure 2-5: Born approximation applied to small perturbations of density and sound speed in the sediment. Secondary sources are excited by the transmitted energy and expand spherically.

## Chapter 3

### BOTTOM REVERBERATION FLUCTUATION STATISTICS

This chapter provides the definition and statistics for fluctuations of bottom reverberation. The main purpose of this chapter is to provide the fundamental statistical background required to understand the research and conclusions presented in the following chapters.

#### 3.1 Definition of Fluctuations

For the purpose of this thesis, a fluctuation means a change in the amplitude of the acoustic pressure observed to occur during seconds or fractions of a second; it is the short-term variability of a signal. If several acoustic transmissions are sent out under the exact same circumstances, the received pressure amplitude at time  $t$  should be constant [44]. However, no two transmissions will occur under precisely the same circumstances because of multipath interference, surface motion, internal waves, microstructure, and other propagation effects [52]. Therefore, the received pressure amplitude at time  $t$  deviates from the average pressure amplitude (or mean value) for time  $t$ . Each individual amplitude at time  $t$  fluctuates around the mean value of the set of amplitudes received at the same time  $t$  seconds into the signal.

These fluctuations are considered to be *random processes* that can be described by statistical distributions. To properly set active detection thresholds, sonar designers need to know what the probability is of finding, at the output of their signal processor, a reverberation amplitude

that exceeds the mean by a given number of decibels [52]. The technique used to capture this information is to represent the fluctuations in amplitude by a statistical distribution.

### 3.2 Statistics of Fluctuations

As stated in Physics of Sound in the Sea [44], when describing fluctuations quantitatively, we need an expression that characterizes the magnitude of the fluctuation. The magnitude of the fluctuation is the amount by which an individual signal deviates from the mean value. Three different quantities are commonly used to express the magnitude of a received signal: the pressure amplitude, the intensity, and the level. When we consider a sequence of  $N$  signals received under apparently identical conditions, we can characterize this sequence by three sets of quantities: amplitudes, intensities, and levels of all the individual members of the sample.

The three quantities are closely related and one can be converted into another by means of two equations

$$I = \frac{P^2}{2\rho c}, \quad 3.1$$

$$L = 10 \log \frac{I}{I_0} = 20 \log \frac{P}{P_0},$$

where  $P$  stands for pressure amplitude,  $I$  for intensity and  $L$  for the level in decibels.  $I_0$  and  $P_0$  are the referenced intensity and referenced pressure amplitude, respectively and  $\rho c$  is the acoustic impedance. To each of these three sets we may assign an average quantity called the arithmetic mean  $\mu$  where

$$\begin{aligned}\mu_P &= \frac{1}{N}(P_1 + P_2 + \dots + P_N), \\ \mu_I &= \frac{1}{N}(I_1 + I_2 + \dots + I_N), \\ \mu_L &= 10 * \log \frac{1}{N}(I_1 + I_2 + \dots + I_N),\end{aligned}\tag{3.2}$$

We refer to these quantities as the estimated mean amplitude, mean intensity, and mean level of the sample, respectively. The research presented in this thesis uses pressure amplitude to quantify the fluctuations and therefore, the quantities relative to describing amplitude fluctuations will be highlighted.

In fluctuating signals, individual amplitudes deviate from the mean amplitude. Some of the deviations will be above the mean value and some below. To express the spread of the amplitudes around the mean amplitude, a common procedure is to square the deviation of each individual amplitude from the mean amplitude and to average these squared deviations. This quantity is called the sample variance  $\sigma^2$  where

$$\sigma^2 = \frac{1}{N-1} \sum_{i=1}^N (P_i - \mu)^2, \quad \mu = \mu_P.\tag{3.3}$$

The square root of the mean of the squared deviations is called the root-mean-square (rms) deviation of the amplitude or, more briefly, the standard deviation,  $\sigma$ . If the standard deviation is divided by the mean amplitude, the resulting dimensionless quantity is called the *relative* standard deviation [44] or, more commonly, the coefficient of variation  $cv$  where

$$cv = \frac{\sigma}{\mu}.\tag{3.4}$$

The coefficient of variation  $cv$  is a measure of how much swing (or variation) about the mean amplitude exists in the data. It is used as an expression to compare variability between several sets of results to determine if they are similar in their degree of variability. Two other quantities mentioned in this thesis are the skewness and the kurtosis. The skewness characterizes the degree of asymmetry of a distribution around its mean [57]. Skewness is a nondimensional number that characterizes only the shape of the distribution. The kurtosis is also a nondimensional quantity that measures the relative peakedness or flatness of a distribution. The skewness and kurtosis are usually defined as

$$\text{Skewness} = \frac{1}{N} \sum_{i=1}^N \left[ \frac{P_i - \mu}{\sigma} \right]^3 \quad 3.5$$

$$\text{Kurtosis} = \frac{1}{N} \sum_{i=1}^N \left[ \frac{P_i - \mu}{\sigma} \right]^4$$

where  $\sigma$  is the distribution's standard deviation.

### 3.2.1 Statistics of pressure amplitudes

Reverberation has classically been assumed to be a Gaussian random process. This assumption is based on the *central limit theorem* which states that the sum of a large number of independent random samples will tend towards a Gaussian random process. Reverberation is treated as a random process constructed by a linear superposition of individual echoes (i.e., wavelets) emanating from a large number of point scatterers distributed independently over the ensonified volume [53]. *Figure 3-1* shows the scattering geometry. Each of the scatterers located on and within the ensonified volume will return a weak echo with a random amplitude and a

random phase between zero and  $2\pi$ . The resultant of all these individual echoes interfering with each other in a random manner will be Gaussian reverberation.

The amplitude fluctuations of Gaussian reverberation are described by the Rayleigh distribution. The Rayleigh distribution is of main interest for understanding the research described in the remaining chapters and is presented first. However, in order to discuss relevant work performed in other areas of fluctuation statistics, information will be provided on distributions commonly used to analyze and characterize fluctuations.

### 3.2.1.1 Rayleigh distribution

The Rayleigh probability density function (pdf) for the amplitude (also referred to as the envelope of the signal) of a Gaussian process is derived in several references [4, 5, 44, 46]. The derivations start by assuming the in-phase  $x$  and in-quadrature  $y$  components of the received *complex* reverberation signal  $n(t)$  at time  $t$  are Gaussian distributed where  $n(t) = x(t) + j y(t)$ . This assumption is based on the central limit theorem where the  $x$  and  $y$  components of the complex signal are the algebraic sum of the  $x_i$  and  $y_i$  components of each of the point scatterers located on and within the ensonified volume of *Figure 3-1*.

The central limit theorem asserts the Gaussian distribution (also called the *normal* distribution) will result quite naturally from the sum of a large number of independent random variables acting together [55]. To be a bit more specific, let  $x_1(t), x_2(t), \dots, x_N(t)$  be  $N$  mutually independent random variables whose individual distributions are not specified and may be

different. Let  $\mu_i$  and  $\sigma_i^2$  be the mean and variance of each random variable  $x_i(t)$ ,  $i = 1, 2, \dots, N$ . Consider the sum random variable

$$\begin{aligned} x(t) &= \sum_{i=1}^N a_i x_i(t), \\ \mu_x &= \sum_{i=1}^N a_i \mu_i, \\ \sigma_x^2 &= \sum_{i=1}^N a_i^2 \sigma_i^2 \end{aligned} \tag{3.6}$$

where  $a_i$  are arbitrary fixed constants. The central limit theorem states that under fairly common conditions, the sum random variable  $x(t)$  will be Gaussian distributed as  $N \rightarrow \infty$  with mean  $\mu_x$  and variance  $\sigma_x^2$ . Historically, the Gaussian distribution has been used to represent the  $x$  and  $y$  component of the received complex reverberation signal  $n(t)$ .

Due to the randomness of the phase, the  $x_i$  and  $y_i$  components from each of the point scatterers are just as likely to be negative as they are to be positive. Therefore, the Gaussian distributions defining the  $x$  and  $y$  components of the complex signal are centered about the zero point. In other words, the probability of the  $x$  component of the received complex reverberation signal at time  $t$  having a value between  $x$  and  $x+dx$  is given by a zero mean Gaussian probability density function. And, the probability of the  $y$  component having a value between  $y$  and  $y+dy$  is also given by a zero mean Gaussian density function. The zero mean Gaussian density functions for the  $x$  and  $y$  components are

$$\begin{aligned} f_{Gaus}(x) &= \frac{1}{\sigma_x \sqrt{2\pi}} e^{-x^2/2\sigma_x^2}, \\ f_{Gaus}(y) &= \frac{1}{\sigma_y \sqrt{2\pi}} e^{-y^2/2\sigma_y^2} \end{aligned} \tag{3.7}$$

where  $\sigma_x^2$  and  $\sigma_y^2$  are the variances of the  $x$  and  $y$  components, respectively.

The received complex reverberation signal  $n(t)$  is given by

$$n(t) = x(t) + j y(t) \quad 3.8$$

where  $x$  is the in-phase component and  $y$  is the in-quadrature component of  $n(t)$ . Since  $n(t)$  is a linear sum of two zero mean, Gaussian random variables,  $n(t)$  is also a Gaussian random variable with variance  $\delta^2 = \sigma_x^2 + \sigma_y^2$ . The pressure amplitude  $P$  and phase  $\theta$  of  $n(t)$  are given in polar coordinates as

$$P = \sqrt{x^2 + y^2}, \quad P \geq 0 \quad 3.9$$

$$\theta = \tan^{-1} \frac{y}{x}.$$

and the rectangular relationships for  $x$  and  $y$  are

$$\begin{aligned} x &= P \cos \theta, \\ y &= P \sin \theta. \end{aligned} \quad 3.10$$

The next step in the derivation is to find the combined probability of having the  $x$  component and  $y$  component of  $n(t)$  in a specified bin of infinitesimal width. This is called the joint density function of  $x$  and  $y$

$$df(x, y) = \frac{1}{2\pi\delta^2} e^{(-1/2\delta^2)(x^2+y^2)} dx dy. \quad 3.11$$

Substituting the polar coordinates for  $x$  and  $y$  and noting that  $dx dy = P dP d\theta$  yields

$$df(P, \theta) = \frac{P}{2\pi\delta^2} e^{-P^2/2\delta^2} dP d\theta. \quad 3.12$$

To obtain the Rayleigh density function for the pressure amplitude (or envelope of the signal), the final step is to integrate over  $\theta$  from zero to  $2\pi$  as follows

$$f_{Ray}(P) = \int_0^{2\pi} f(P, \theta) d\theta = \frac{P}{\delta^2} e^{-P^2/2\delta^2}, \quad P \geq 0. \quad 3.13$$

The mean and variance of the Rayleigh probability density function are

$$\mu_{Ray} = \frac{\delta\sqrt{\pi}}{\sqrt{2}}, \quad 3.14$$

and

$$\sigma_{Ray}^2 = \delta^2 \left(2 - \frac{\pi}{2}\right) \quad 3.15$$

where  $\delta^2$  is the variance of the underlying Gaussian distribution for  $n(t)$ .

By performing the integration  $f_{Ray}(\theta) = \int_0^{\infty} f(P, \theta) dP$  it may be shown that the phase is uniformly distributed, that is  $f_{Ray}(\theta) = \frac{1}{2\pi}$ ,  $0 \leq \theta \leq 2\pi$ . Figure 3-2 shows the probability density functions of the Gaussian quadrature components  $x$  and  $y$ , the Rayleigh amplitudes, and the uniform phase of complex Gaussian reverberation.

The envelope and phase samples at the same instant of time are statistically independent random variables since  $f(P, \theta) = f(P)f(\theta)$ . Statistical independence means that the  $x$  and  $y$  (or  $P$  and  $\theta$ ) components have no effect on one another. The probability of getting a specific  $x$  does not depend on  $y$  and  $y$  does not depend on  $x$ .

The Rayleigh probability density function has historically been used to describe the random nature of the fluctuations of the pressure amplitudes of reverberation. But what do we mean when we say the amplitude fluctuations are Rayleigh distributed? We mean that the

frequency of occurrence of an individual normalized amplitude is best described by a probability density function  $f\left(\frac{P(t)}{\mu_{P(t)}}\right)$  that is Rayleigh distributed where  $\frac{P(t)}{\mu_{P(t)}}$  is the quantity that defines the magnitude of the fluctuation.

The individual amplitudes  $P(t)$  are normalized by the mean amplitude  $\mu_{P(t)}$  where  $P_{Norm} = \frac{P(t)}{\mu_{P(t)}}$ . This normalization makes the mean of the distribution equal to unity. If the normalized amplitude is less than the mean, then  $P_{Norm}$  lies to the left of unity; if the normalized amplitude is greater than the mean, then  $P_{Norm}$  lies to the right of unity. The values greater than one make up the *tail* of the distribution and it is the tail of the distribution that is of most interest in this research.

With the mean of the normalized amplitudes equal to unity, we can use the relationship  $\mu_{Ray} = \frac{\delta\sqrt{\pi}}{\sqrt{2}} = 1$  from equation 3.14 which fixes the value of  $\delta^2$  to  $\frac{2}{\pi}$  and then, using equation 3.15, we can solve for  $\sigma_{Ray} = \sqrt{\delta^2(2 - \frac{\pi}{2})} = \sqrt{\frac{2}{\pi}(2 - \frac{\pi}{2})} = 0.5227$ . Therefore, if the normalized bottom reverberation amplitude fluctuations follow a Rayleigh distribution with mean equal one, the spread of the density function is defined by  $\sigma_{Ray} = 0.5227$ .

Figure 3-3 shows the Rayleigh density function. The density function provides the probability of occurrence of an individual normalized amplitude. The pdf is estimated by a technique called a histogram. The histogram displays the percentage of times a given value occurs in the data set. The histogram is a plot of the number of observed amplitudes  $P_{Norm}$  that fall within various specified amplitude bins, formally called interval classes.

The histogram is computed by dividing the full range of normalized amplitudes into an appropriate number of equal width bins, tabulating the number of amplitudes in each bin, and dividing by the product of the bin width and sample size,  $N$  [55]. The bins are centered around normalized amplitudes equally spaced from zero to plus infinity. The total area under the density function will be unity since all normalized amplitudes must fall between 0 and  $+\infty$ .

The histogram bins located to the far right of the mean in *Figure 3-3* are of the most interest when studying fluctuation statistics. These bins make up the tail of the distribution. If the height of the bins in the tail are higher than the assumed theoretical distribution indicated by the dashed line, then there are more large amplitude spikes received in the reverberation signal than predicted by the density function. This causes the false alarm rate to be higher than expected which, in turn, degrades detection performance.

The abscissa of the histogram in *Figure 3-3* is denoted the ‘Amplitude/Mean’. It is the value of the received reverberation amplitude normalized by the mean. Thus, a value of 4 corresponds to a reverberation excursion of four times the mean. To put these values within the context of a decibel (dB) loss, the value of 4 corresponds to an amplitude excursion of  $20 \log(4)$  or 12 dB above the mean. The ordinate of the histogram is the probability of occurrence of that amplitude. Under the Rayleigh distribution shown by the dashed line, the mean (Amplitude/Mean = 1) should occur about 71% of the time, while the value of 4 times the mean should occur 0.002% of the time.

It is difficult to discern the behavior in the tails from a visual examination of the pdf. The general technique used to more clearly compare the deviation of the tails of two distributions is to work with a plot of the probability of false alarm (PFA). The nature of the PFA curve is to

accentuate the tail of a distribution, that is, the behavior at large fluctuations. The PFA is obtained by subtracting the cumulative distribution from unity.

### 3.2.1.2 Rayleigh cumulative distribution

The cumulative distribution function (cdf) is the probability that an amplitude will be less than or equal to a specified amplitude. If  $f_{Ray}$  is the Rayleigh probability density function, the associated cumulative distribution  $F_{Ray}$  is

$$F_{Ray}(P) = \int_{-\infty}^P f_{Ray}(u) du = \int_0^P \frac{u}{\delta^2} e^{-u^2/2\delta^2} du \quad 3.16$$

which is the area under the graph of the density function to the left of a chosen value  $P$  and  $u$  is an integration variable. Continuing the integration, the theoretical cdf for the Rayleigh distributions is derived by making the following substitution into equation 3.16

$$\begin{aligned} x &= \frac{-u^2}{2\delta^2} & 3.17 \\ du &= -\frac{u}{\delta^2} dx \end{aligned}$$

Remembering that  $\delta^2 = \frac{2}{\pi}$ , the Rayleigh cdf is then given by

$$F_{Ray}(P) = \int_0^P \frac{u}{\delta^2} e^{-u^2/2\delta^2} du = \int_0^{-P^2/(4/\pi)} -e^x dx = 1 - e^{\frac{-P^2}{(4/\pi)}} \quad 3.18$$

A plot of  $F_{Ray}$  is shown in *Figure 3-4*.

When working with data, the cdf is estimated by summing the bins of the histogram to the left of a chosen normalized pressure amplitude  $P$  in *Figure 3-3*. This works because the cdf is just the area under the density function to the left of  $P$ . The cdf does not produce the visual ability to highlight the variations in the tail of distributions; however, it does provide a nice stepping stone for calculating the probability of false alarm, which does highlight the tail.

### 3.2.1.3 Rayleigh probability of false alarm

The probability of false alarm (PFA) is equal to one minus the cumulative distribution. The PFA provides information about the area under the tail of the density function to the right of  $P$  by taking the entire area under the density function and subtracting the area to the left of  $P$ . The Rayleigh PFA is given by

$$PFA_{Ray}(P) = 1 - cdf = 1 - (1 - e^{\frac{-P^2}{(4/\pi)}}) = e^{\frac{-P^2}{(4/\pi)}} \quad 3.19$$

and *Figure 3-5* is a plot of the PFA in logarithmic space where the abscissa is the normalized amplitude  $P$ .

The quantity  $\log(PFA)$  is useful when comparing statistical results because of its sensitivity to small changes in the upper tail of the density function. However, this sensitivity requires the sample size to be sufficiently large in order to accurately represent the *occasional* high-level bursts of bottom reverberation that are characterized by the tail.

### 3.2.1.4 Rician distribution

The Rician (also called the Generalized Rayleigh) distribution is used to represent echo fluctuations that contain both the steady-state component of the coherent field and the random component of the diffuse field. The phase of the scattered (diffuse) energy has no fixed phase with respect to the phase of the incident energy. This is in contrast to the reflected (coherent) energy that has a fixed phase relative to the phase of the incident energy.

For very smooth surfaces, the coherent energy dominates the received signal because the contributions to this component add in phase to give a large amplitude. This coherent component is a constant, steady-state component meaning there is little fluctuation in the received amplitudes at time  $t$ . For very rough surfaces, less energy is reflected in the specular direction; therefore, the diffuse field dominates the received signal and the signal is completely random.

Rice [54] showed that the probability density function of the envelope containing both the coherent and diffuse components would be

$$f_{Rice}(P) = \frac{P}{\delta^2} e^{-(P^2+A^2)/2\delta^2} I_0\left(\frac{PA}{\delta^2}\right) \quad 3.20$$

where  $I_0$  is the modified Bessel function,  $A$  is related to the signal-to-noise ratio and, if

$P = P_{Norm}$ , then  $\delta^2 = \frac{2}{\pi}$ . As the field becomes more diffuse, the amplitude  $A$  approaches zero

and the Rician distribution approaches the Rayleigh distribution. For a smooth surface, the amplitude  $A$  becomes large and the Rician distribution approaches the Gaussian distribution.

*Figure 3-6* shows the Rician distribution for several values of  $A$  where  $\alpha = A / \sigma$  and  $v = P / \sigma$ .

The significance of this distribution is that it shows what happens when the fluctuations are caused by a narrowband random process not being entirely zero mean. That is, there is a

mean, steady-state amplitude  $A$  inherent within the original complex data used to form the amplitudes. The coherent amplitude will bias the underlying distribution. The coherent component

$A$  can be related to the signal-to-noise ratio as shown in *Figure 3-6* by  $\frac{\alpha^2}{2} = \frac{\text{signal power}}{\text{noise power}}$ .

### 3.2.2 Statistics of intensity

The statistics of *intensity* are also commonly used to describe fluctuations [45, 47, 51] in reverberation and propagation signals. Recalling equation 3.1, the intensity is related to the

pressure amplitude by  $I = \frac{P^2}{2\rho c}$ ; the historical derivation of the statistical distribution that

describes the fluctuation in the intensity begins just like the derivation above for pressure amplitudes.

The derivation starts by assuming the  $x$  and  $y$  components of the received *complex* reverberation signal  $n(t)$  at time  $t$  are from a Gaussian distribution. This assumption is based on the central limit theorem where the  $x$  and  $y$  components of the complex signal are the algebraic sum of the  $x_i$  and  $y_i$  components of each of the point scatterers located on and within the volume of *Figure 3-1*. The  $x$  and  $y$  components are zero mean Gaussian distributions and the intensity

$I$  is defined by  $I = \frac{x^2 + y^2}{2\rho c}$  where  $I$  is the sum of the squares of two independent, zero mean

Gaussian variables.

### 3.2.2.1 Exponential, chi-square, and gamma probability density function

The probability density function of the sum of the squares of two independent Gaussian variables with zero mean and equal variance is given in [4] by the convolution of the density functions for  $x$  and  $y$

$$f_{\text{exp}}(I) = f_{\text{Gaus}}(x) \otimes f_{\text{Gaus}}(y) = \frac{1}{\sigma_x \sqrt{2\pi}} e^{-x^2/2\sigma_x^2} \otimes \frac{1}{\sigma_y \sqrt{2\pi}} e^{-y^2/2\sigma_y^2} \quad 3.21$$

$$= \frac{1}{2\sigma_x^2} e^{-I/2\sigma_x^2} = \frac{1}{\langle I \rangle} e^{-I/\langle I \rangle}$$

with

$$\mu_{\text{exp}} = 2\sigma_x^2 = \langle I \rangle \quad 3.22$$

$$\sigma_{\text{exp}}^2 = 4\sigma_x^4$$

where the variances of the underlying Gaussian distributions of  $x$  and  $y$  are equal ( $\sigma_x^2 = \sigma_y^2$ ) and the mean intensity  $\langle I \rangle$  equals twice the underlying Gaussian variance  $\sigma_x^2$ . This distribution is called an exponential distribution which is a special case of the chi-square distribution with two degrees of freedom. A chi-square distribution results from the sum of the squares of  $N$  independent Gaussian variables with zero mean and equal variance. If  $y = x_1^2 + x_2^2 + \dots + x_N^2$ , then the resulting density function  $f(y)$  is shown to be [4]

$$f_{\text{chi}^2}(y) = \frac{(y/\sigma_x^2)^{N/2-1}}{\sigma_x^2 2^{N/2} \Gamma(N/2)} e^{-y/2\sigma_x^2} \quad 3.23$$

with

$$\begin{aligned}\mu_{\text{Chi}^2} &= N\sigma_x^2 \\ \sigma_{\text{Chi}^2}^2 &= 2N\sigma_x^4\end{aligned}\quad 3.24$$

where  $\Gamma(\cdot)$  is the gamma function. In normalized form with  $\sigma_x^2 = 1$ , this is called the chi-square density function with  $N$  degrees of freedom.

The chi-square density function belongs to the gamma family of distributions. The gamma density function is defined as

$$f_{\text{Gamma}}(y) = \frac{1}{\beta^\alpha \Gamma(\alpha)} y^{\alpha-1} e^{-y/\beta} \quad 3.25$$

with

$$\begin{aligned}\mu_{\text{Gamma}} &= \alpha\beta \\ \sigma_{\text{Gamma}}^2 &= \alpha\beta^2\end{aligned}\quad 3.26$$

where the chi-square density function is the special case of  $\beta = 2\sigma_x^2$  and  $\alpha = N/2$ . The chi-square density function with  $N = 2$  degrees of freedom is called the exponential density function and the exponential density function has classically been used to define intensity fluctuations.

### 3.2.2.2 Exponential cumulative distribution

The cumulative distribution function is the probability that an intensity will be less than or equal to a specified intensity. If  $f_{\text{exp}}$  is the exponential probability density function, the associated cumulative distribution  $F_{\text{exp}}$  is

$$F_{\text{exp}}(I) = \int_{-\infty}^I f_{\text{exp}}(u) du = \int_0^I \frac{1}{2} e^{-u/2} du = 1 - e^{-I/2} \quad 3.27$$

which is the area under the graph of the density function to the left of  $I$  and  $u$  is an integration variable.

### 3.2.2.3 Exponential probability of false alarm

The probability of false alarm (PFA) is equal to one minus the cumulative distribution.

The exponential PFA is given by

$$PFA_{\text{exp}}(I) = 1 - cdf = 1 - (1 - e^{-I/2}) = e^{-I/2} \quad 3.28$$

In summary, the Rayleigh and the exponential distributions are the classical assumptions made in detection theory for describing the probability density function of noise in a reverberation limited environment. They both stem from the same assumption that reverberation noise is a Gaussian random variable. However, experimental data presented in the next two chapters show that reverberation is not always Gaussian, and therefore, the envelope and intensity statistics are not accurately described by the Rayleigh and exponential distributions.

### 3.2.3 Other applicable distributions

Other distributions used to describe fluctuation statistics are the Weibull, lognormal, and mixture models. These distributions provide some flexibility to adjust the theoretical density functions to match non-Gaussian fluctuation data. The Weibull and lognormal distributions have

parameters that permit the scale of the PFA and the shape of the tail to be varied. The mixture model has a parameter to control the percentage of contributions from different distributions making up the mixture. Changing this parameter manipulates the shape of the density function.

### 3.2.3.1 Weibull distribution

The Weibull distribution is a family of distributions developed by the Swedish physicist Waloddi Weibull [59]. A random variable  $X$  is said to have a Weibull distribution with free parameters  $x_u$ ,  $b$ , and  $c$  ( $b > 0, c > 0$ ) if the probability density function of  $X$  is

$$f_{Weib}(x - x_u; c, b) = \frac{c}{b^c} (x - x_u)^{c-1} e^{-(x-x_u)/b)^c} \quad x \geq 0 \quad 3.29$$

and

$$\begin{aligned} \mu_{Weib} &= b\Gamma(1 + \frac{1}{c}) & 3.30 \\ \sigma_{Weib}^2 &= b^2 \{ \Gamma(1 + \frac{2}{c}) - [\Gamma(1 + \frac{1}{c})]^2 \} \end{aligned}$$

where the parameter  $x_u$  shifts the abscissa of the pdf,  $b$  is a shape parameter ruling the tail decay and  $c$  is a scale parameter related to the common variance of the underlying quadrature components [58]. The computation of the mean and variance involves the gamma function  $\Gamma(\cdot)$ .

By varying the parameters, a number of different distributional shapes can be obtained including the exponential and the Rayleigh distributions. The exponential distribution is obtained when the parameters are set  $x_u = 0$ ,  $c = 1$ , and  $b = 2$ . The Rayleigh distribution is obtained

when the parameters are set  $x_u = 0$ ,  $c = 2$ , and  $b = 4/\pi$ . As shown in *Figure 3-7* for  $c < 2$ , the distribution contains more area under its tail than does the Rayleigh distribution [57].

The Weibull cumulative distribution function is

$$\begin{aligned} F_{Weib}(x - x_u; c, b) &= \int_{-\infty}^x f_{Weib}(u) du = \int_0^x \frac{c}{b^c} (u - x_u)^{c-1} e^{-(u-x_u)/b} du \\ &= 1 - e^{-(x-x_u)/b} \end{aligned} \quad 3.31$$

and the probability of false alarm is given by

$$\begin{aligned} PFA_{Weib}(x - x_u, c, b) &= 1 - cdf = 1 - (1 - e^{-(x-x_u)/b})^c \\ &= e^{-(x-x_u)/b} \end{aligned} \quad 3.32$$

The Weibull distribution is often used to match PFA data because the PFA data can be plotted as a straight line to determine its three free parameters  $x_u$ ,  $b$ , and  $c$ . Determining the free parameters from the PFA data defines the Weibull distribution that best fits the data. To obtain the three parameters, the logarithm of the negative logarithm of the PFA data is plotted

$$y = \log(\log(1/PFA_{Weib})) = c [\log(x - x_u) - \log b] = c(z - z_0) \quad 3.33$$

A plot of  $y$  versus  $z$  will be a straight line with slope  $c$  and intercept at  $x = x_u + 1$  of  $z_0 = c \log b$ .

### 3.2.3.2 Lognormal distribution

The lognormal distribution is often used in the open literature for comparison to measured probability of false alarm curves [47, 13, 16, 7], however, there is no physical justification for its use. The lognormal distribution, like the Weibull distribution, provides a family of distributions

obtained by varying the mean and variance of the associated Gaussian distribution. A random variable  $X$  is log-normally distributed if  $Y = \ln X$ , where  $\ln$  represents the natural logarithm and  $Y$  is Gaussian (normally) distributed with mean  $\mu$  and variance  $\sigma^2$ . The probability density function of a lognormal random variable is

$$f_{\log n}(x; \mu, \sigma) = \frac{1}{x \sqrt{2\pi} \sigma} e^{-\frac{1}{2\sigma^2}[\ln(x) - \mu]^2} \quad 3.34$$

and

$$\begin{aligned} \mu_{\log n} &= e^{\mu + \sigma^2/2} \\ \sigma_{\log n}^2 &= e^{2\mu + \sigma^2} (e^{\sigma^2} - 1) \end{aligned} \quad 3.35$$

where  $\mu$  and  $\sigma$  are the mean and standard deviation of  $\ln X$  and not  $X$ .

Because  $\ln X$  has a Gaussian distribution, the cumulative density function of  $X$  can be expressed in terms of the cumulative density function of a standard Gaussian random variable  $Z$  [57]. For  $x \geq 0$ ,

$$\begin{aligned} F_{\log n}(x; \mu, \sigma) &= \text{Prob}(X \leq x) = \text{Prob}[\ln(X) \leq \ln(x)] \\ &= P(Z \leq \frac{\ln(x) - \mu}{\sigma}) = \Phi\left(\frac{\ln(x) - \mu}{\sigma}\right) \end{aligned} \quad 3.36$$

where  $\Phi(z)$  is the cumulative distribution of a standard Gaussian random variable;

$$\Phi(z) = \int_0^z f_{Gauss}(u; \mu, \sigma) du = \int_0^z \frac{1}{\sqrt{2\pi}} e^{-u^2/2} du \quad 3.37$$

$$\text{with } z = \frac{\ln(x) - \mu}{\sigma}$$

The tails of the lognormal distribution are adjusted by varying the two free parameters  $\mu$  and  $\sigma$  as shown in *Figure 3-8*. In general, the lognormal distribution has a higher tail than the Rayleigh distribution meaning that higher amplitude spikes can be expected in the fluctuation time series when the data is log-normally distributed versus when the data is Rayleigh distributed.

### 3.2.3.3 Mixture and bimodal distributions

Another technique for characterizing fluctuation statistics utilizes mixture models [60]. By varying the parameters of a mixture model, the resulting probability density function can be forced to assume a variety of different shapes, some of which are bimodal; that is, the density has two distinct local maximums [61].

A mixture model consists of a mixture or weighted sum of distributions. A mixture of Gaussian densities is often referred to as a *contaminated* normal distribution. The density function for the Gaussian-Gaussian mixture is defined as the class of density functions given by the sum of two individual Gaussian densities

$$f_{\text{mix}}(x) = (1 - \varepsilon)f_{\text{Gaus1}}(x) + \varepsilon f_{\text{Gaus2}}(x) \quad 3.38$$

where  $f_{\text{Gaus1}}$  represents the nominal Gaussian density,  $f_{\text{Gaus2}}$  the Gaussian contamination density, and the mixing parameter  $\varepsilon$  controls the degree to which  $f_{\text{Gaus2}}$  contaminates  $f_{\text{Gaus1}}$ .

The *mode* of a distribution is the value that occurs the most. Fluctuations with a bimodal density function have more than one central tendency or typical value around which to fluctuate. Experimenters [10] postulate that non-Rayleigh amplitude fluctuations are caused by two equally

strong scattering events, violating the central limit theorem. The fluctuations are caused by a main scattering event being contaminated with another random scattering event. The strong contamination causes the density function to be bimodal and warrants the use of mixture models to fit the data.

### **3.3 Statistical tests**

Statistical tests have been developed [59, 60, 61, 62] that indicate when the observed data is not consistent with a theoretical distribution such as a Rayleigh distribution. This type of test is called a *goodness-of-fit* test since it tests how well the theoretical distribution “fits” the observed data [56]. Four tests of this type were calculated for this thesis. One of the tests called the Chi-square test was applied to the histogram. The other three were applied to the cumulative distribution and they are the Kolmogorov-Smirnov, Anderson-Darling, and Kuiper’s tests. Two other plots called the runs test and the autocorrelation are used to graphically evaluate the randomness of the samples (runs test) and relationships between samples (autocorrelation) of the in-water data and the simulated normalized amplitudes.

#### **3.3.1 Goodness-of-fit tests**

Given two sets of data, we can ask the question: Are the two sets drawn from the same distribution function, or from different distribution functions [57]? Equivalently, in proper statistical language, “Can we disprove, to a certain required *level of significance*, the null hypothesis that the two data sets are drawn from the same distribution function?” Disproving the null hypothesis in effect proves that the data sets are from different distributions. Failing to

disprove the null hypothesis, on the other hand, only shows that the data sets can be consistent with a distribution function. The tests do not *prove* that two data sets come from the same distribution. Accepting the null hypothesis only means that the data sets are *possibly* from the same distributions and does not prove the null hypothesis because the data may be giving incomplete information about the observed distribution.

The level of significance is related to the degree of certainty you require in order to reject the null hypothesis. The significance level indicates the probability of incorrectly rejecting the null hypothesis when it is actually true. When we obtain a “significant” value of a test statistic and reject the null hypothesis, we say that we have sufficient evidence to declare that the hypothesis is false because there would be only a small probability of obtaining such a significant value if the null hypothesis were true [64].

Goodness-of-fit hypothesis tests should be regarded as a way of trying to systematically detect fairly gross disagreement between the data and the theoretical distribution. Furthermore, many of these kinds of tests are not very powerful, i.e., they are not very sensitive to subtle disagreements between the data and the theoretical distribution. This is generally true of the chi-square and Kolmogorov-Smirnov tests, presented below [56].

### 3.3.1.1 Chi-square test

Suppose that  $N_i$  is the number of normalized amplitudes in the  $i$ th bin of the histogram, and that  $n_i$  is the number expected according to a known distribution [57]. Note that the  $N_i$ ’s are integers, while the  $n_i$ ’s may not be. Then the chi-square test statistic is

$$\chi^2 = \sum_i \frac{(N_i - n_i)^2}{n_i} \quad 3.39$$

where the sum is over all the bins of the histogram. A large value of  $\chi^2$  indicates that the null hypothesis (that the  $N_i$ 's are drawn from the theoretical distribution represented by the  $n_i$ 's) is rather unlikely.

The chi-square test is very dependent on the choice of bin size or class intervals. Choosing the optimal number of bins is dependent on the form of the theoretical distribution. This is a major drawback of the chi-square test [56]. In some situations, entirely different conclusions can be reached from the *same* data set depending on how the bins are specified. The chi-square test performs well against the very highly skewed distributions but in general does not have good sensitivity overall [62]. Because of this insensitivity and inconsistent behavior, the chi-square test was eventually dropped from the analysis in favor of the following three test statistics which are performed on the cumulative distribution function.

### 3.3.1.2 Kolmogorov-Smirnov test

The Kolmogorov-Smirnov (K-S) test compares the observed cumulative distribution  $S_N(x)$  with a known theoretical cumulative distribution  $F(x)$  as shown in *Figure 3-9* [57]. All cumulative distributions agree at the smallest allowable value of  $x$  (where they are zero), and at the largest allowable value of  $x$  (where they are unity). It is the behavior between the largest and smallest values that distinguishes distributions. The K-S test is a particularly simple measure. It is defined as the *maximum value D* of the absolute difference between two cumulative distributions

(see *Figure 3-9*). Thus, for comparing one data set's  $S_N(x)$  to a known cumulative distribution function  $F(x)$ , the K-S test statistic is

$$D = \max_{-\infty < x < \infty} |S_N(x) - F(x)| \quad 3.40$$

The K-S test is good at finding shifts in a probability distribution [57], especially changes in the median value, where  $F(x) = 0.5$ . (The median value is the middle or center value of the data when the data are listed in order of magnitude). The K-S test is less sensitive at the extreme ends of the distribution where  $F(x)$  is near 0 or 1. The reason is that the difference  $|S_N(x) - F(x)|$  does not have a probability distribution that is independent of  $x$ . Rather, its variance is proportional to  $F(x)[1 - F(x)]$ , which is largest at  $F = 0.5$ . Since the K-S statistic is the maximum difference over all  $x$  of the two cumulative distributions, a deviation that might be statistically significant at its own value of  $x$  gets compared to the expected chance deviation at  $F = 0.5$ , and is thus discounted. A result is that, while the K-S test is good at finding *shifts* in a distribution, it is not always good at finding *spreads* which affect the tails of the probability distribution.

### 3.3.1.3 Anderson-Darling test

One way of increasing the power of the K-S statistic out in the tails is to use a stabilized or weighted statistic like the Anderson-Darling test statistic [60]

$$D^{**} = \int_{F=0}^1 \frac{|S_N(x) - F(x)|}{\sqrt{F(x)[1 - F(x)]}} dF(x) \quad 3.41$$

where the weighting function  $\frac{1}{\sqrt{F(x)[1-F(x)]}}$  corrects the sensitivity of the K-S test to the median value.

#### 3.3.1.4 Kuiper's test

Another approach, which is simpler and more direct is due to Kuiper [57]. The approach, which guarantees equal sensitivities at all values of  $x$ , is to wrap the  $x$  axis around into a circle, and to look for a statistic that is now invariant under all shifts and parameterization on the circle.

The Kuiper's test statistic, defined as

$$V = D_+ + D_- = \max_{-\infty < x < \infty} [S_N(x) - F(x)] + \max_{-\infty < x < \infty} [F(x) - S_N(x)], \quad 3.42$$

is the sum of the maximum distance of  $S_N(x)$  above  $F(x)$  and the maximum distance of  $S_N(x)$  below  $F(x)$ .

The Anderson-Darling and Kuiper's statistics were the most robust tests and gave similar results. All three tests, the Kolmogorov-Smirnov, Anderson-Darling, and Kuiper's tests will be applied to the cumulative distributions of the simulated bottom reverberation amplitude fluctuations presented in Chapter 6. Their level of significance will provide the basis for determining when the observed data is non-Rayleigh.

#### 3.3.2 Other statistical tests

In statistical data analysis, it is desirable to establish if a sequence of observations are statistically independent or if they include an underlying trend [55]. The two tests used extensively

in the following chapters to evaluate randomness and independence of the samples forming the statistical ensemble are the runs test and the autocorrelation. The autocorrelation sequence, while not strictly speaking a test, is a measure of the dependence between values of the random processes at different times [65]. The temporal autocorrelation function was used to determine the minimum time sampling interval of the reverberation time series to ensure independent samples. The runs test was used to visually determine if the ensemble of amplitude fluctuations was random or if there was an underlying relationship between the samples making up the fluctuation ensemble.

### 3.3.2.1 Run's test

A runs test is useful for testing whether certain patterns of experimental outcomes are random [63]. This test is referred to as a nonparametric, or distribution-free test since information about the underlying distribution is not required to perform the test. The runs test is a scatter plot or lag plot which plots  $x_k$  against  $x_{k+n}$  where  $x$  is a sample of the amplitude fluctuation ensemble. Example results of a runs test are shown in *Figure 3-10*. The dots on the plot should be scattered randomly if the samples are uncorrelated and fluctuate independently of each other. If a pattern such as a line becomes visible in the dots, it indicates that the samples move in relationship to each other - there is a trend in the data.

### 3.3.2.2 Autocorrelation

The autocorrelation sequence is a statistical average that provides a measure of the dependence between samples of the amplitude fluctuation ensemble at different times. In this

sense, it partially describes the time variation of a random signal [65]. The autocorrelation function  $R_{xx}(\tau)$  for a stationary ensemble is a measure of time-related properties in the data that are separated by fixed time delays [55].  $R_{xx}(\tau)$  equals

$$R_{xx}(t_1, t_1 + \tau) = \lim_{N \rightarrow \infty} \frac{1}{N} \sum_{k=1}^N s_k(t_1) s_k(t_1 + \tau) \quad 3.43$$

where  $s_k(t)$  is the reverberation amplitude time series from the  $k$ th realization. The autocorrelation can be estimated by delaying the record relative to itself by some fixed time delay  $\tau$  then multiplying the original record with the delayed record, and summing the resulting product values over the available record length or over some desired portion of this record length. The procedure is repeated for all time delays of interest.

*Figure 3-11* shows an autocorrelation function for random noise and how the autocorrelation was used in this thesis to choose the sampling interval of the reverberation time series. The abscissa is the sample number which is related to the time delay. The time delay is equal to the product of the sample number and sampling rate of the in-water amplitude time series. The dashed line drawn from 0.7 correlation to the abscissa indicates the number of samples that should be skipped to ensure that the correlation between samples is less than 0.7. The number of samples to skip multiplied by the sampling rate of the amplitude time series equals the sampling interval of the ensemble. The 0.7 correlation criteria is based on the 3 dB down points of the mainlobe of  $R_{xx}(\tau)$  since  $20 * \log_{10}(0.707) = 3 \text{ dB}$ .

### **3.4 Summary**

In summary, if the fluctuations are caused by a Gaussian random process, then the envelope or *amplitude* statistics follow the Rayleigh distribution and the *intensity* statistics follow an exponential distribution. When the distribution of fluctuations about the mean shows significantly higher tails than is expected by the assumed distribution, occasional high-level bursts of reverberation occur more frequently than would be anticipated, leading to an unexpectedly high false alarm rate in the detection processing. Models presented in this chapter that are commonly used to characterize these non-Gaussian fluctuations are the gamma, Weibull, lognormal, and mixture distributions. Statistical tests can be used to disprove that the data are from a theoretical distribution and to determine if data are random and uncorrelated. Test covered in this chapter include the Chi-square, Kolmogorov-Smirnov, Anderson-Darling, Kuiper's test statistics, the run's test, and the autocorrelation.

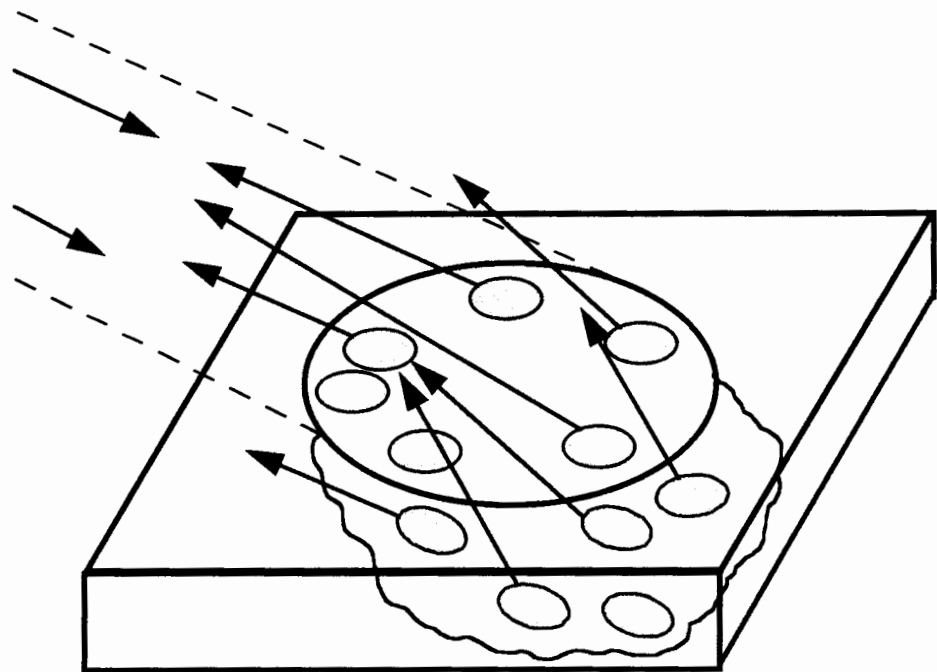


Figure 3-1: Scattering geometry depicting the large number of scatterers located randomly on the volume ensonified by the source. The phase of the scatterers are uniformly distributed between 0 and 360 degrees. [Reference 13]

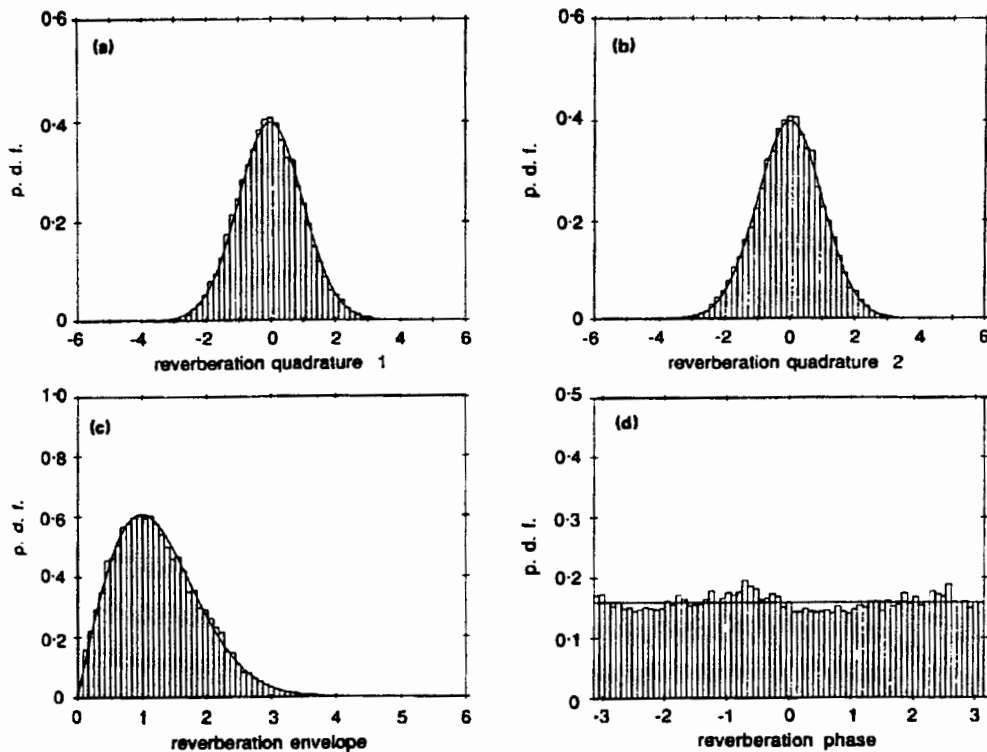


Figure 3-2: Complex Gaussian reverberation: (a), (b) the quadrature components  $x$  and  $y$  are Gaussian, (c) the envelope is Rayleigh, (d) and the phase is uniformly distributed. [Reference 53]

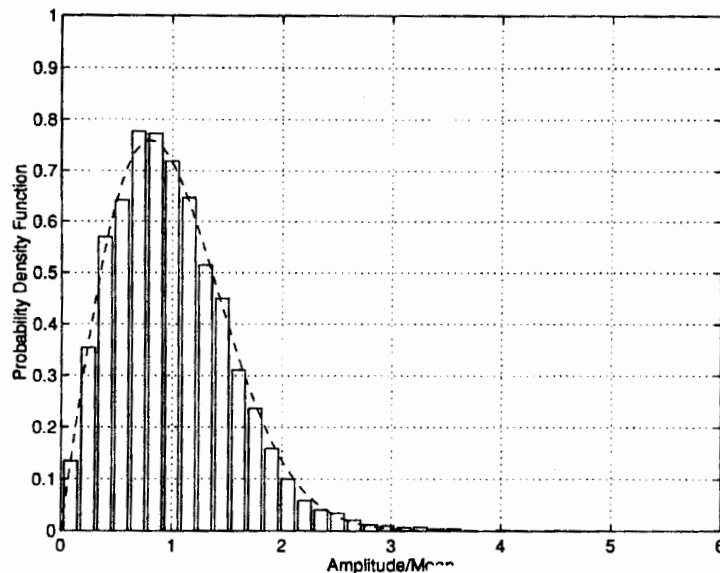


Figure 3-3: Rayleigh probability density function (dashed line) estimated by a histogram (bars).

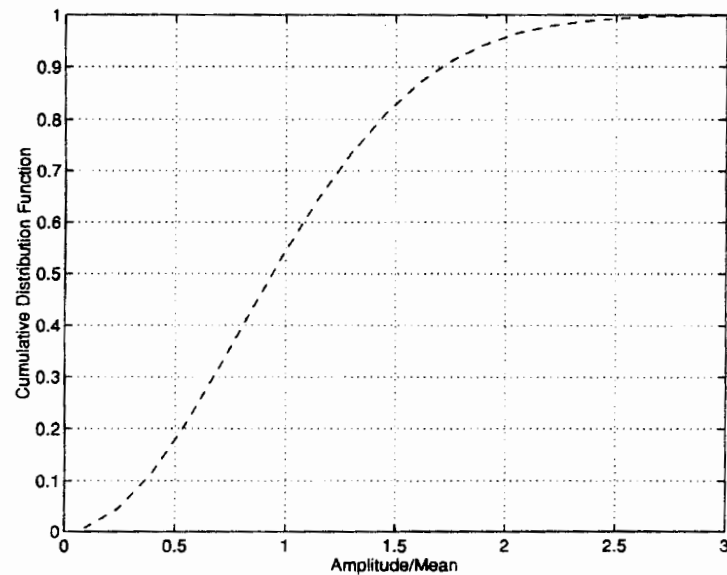


Figure 3-4: Rayleigh cumulative distribution function.

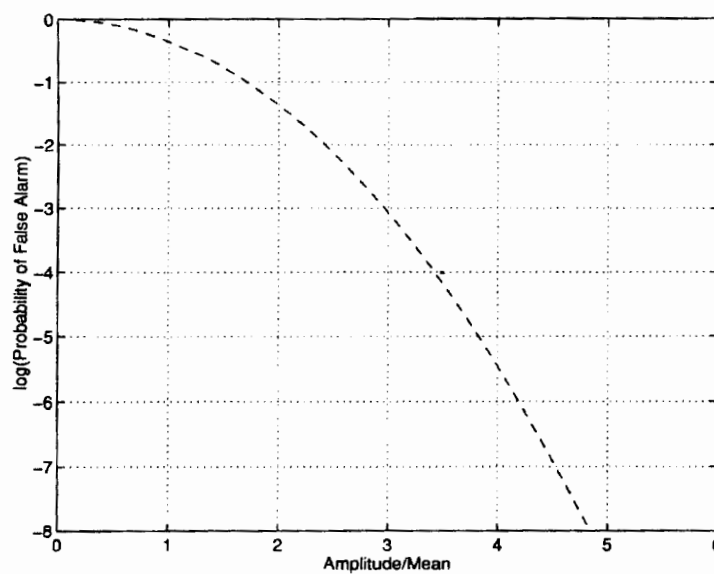


Figure 3-5: Rayleigh probability of false alarm (PFA).

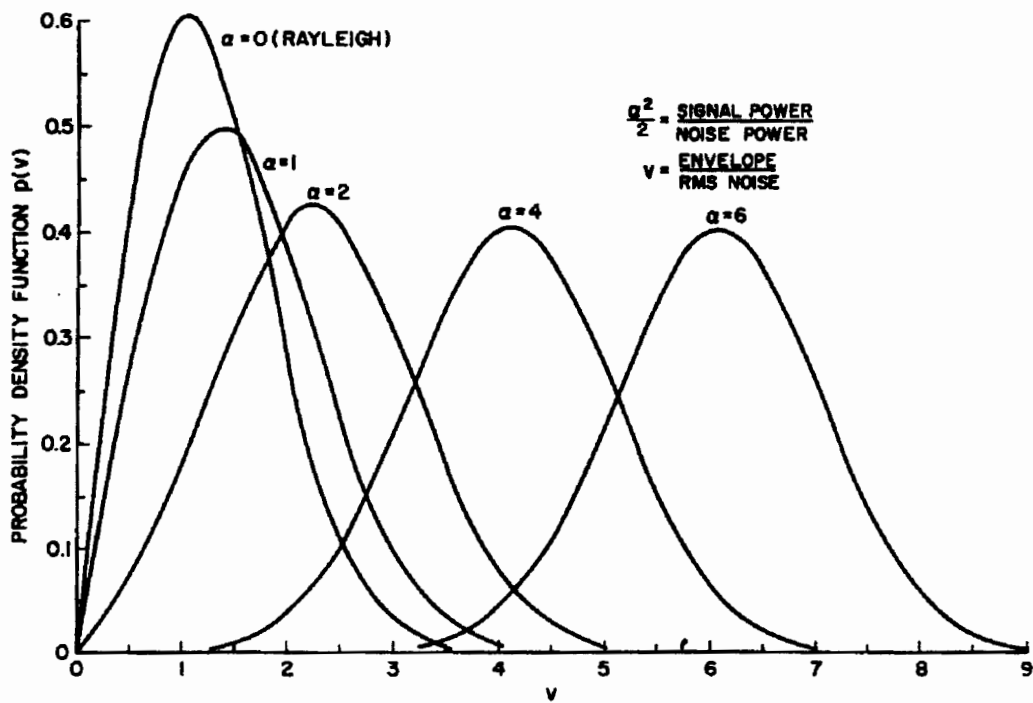


Figure 3-6: Rician density function where  $\alpha = \frac{A}{\sigma}$  and  $v = \frac{P}{\sigma}$  [Reference 53]

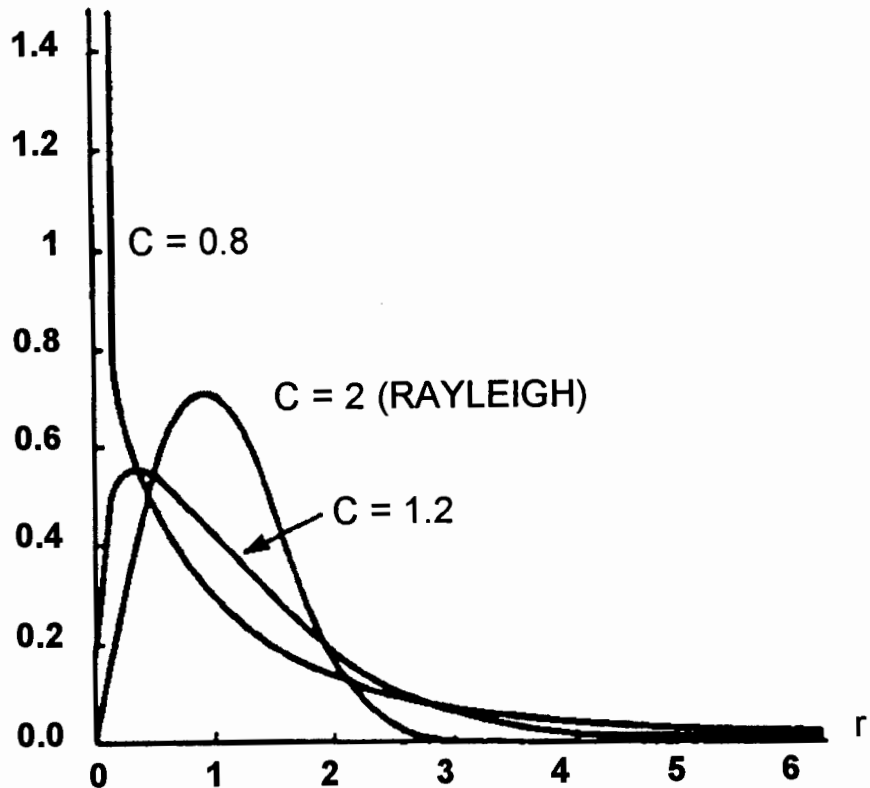


Figure 3-7: Weibull density functions for  $c$  equal to 0.8, 1.2, 2. For  $c = 2$ , the density function corresponds to a Rayleigh density. Note larger area under tails for  $c$  equal 0.8 and 1.2. [Reference 57]

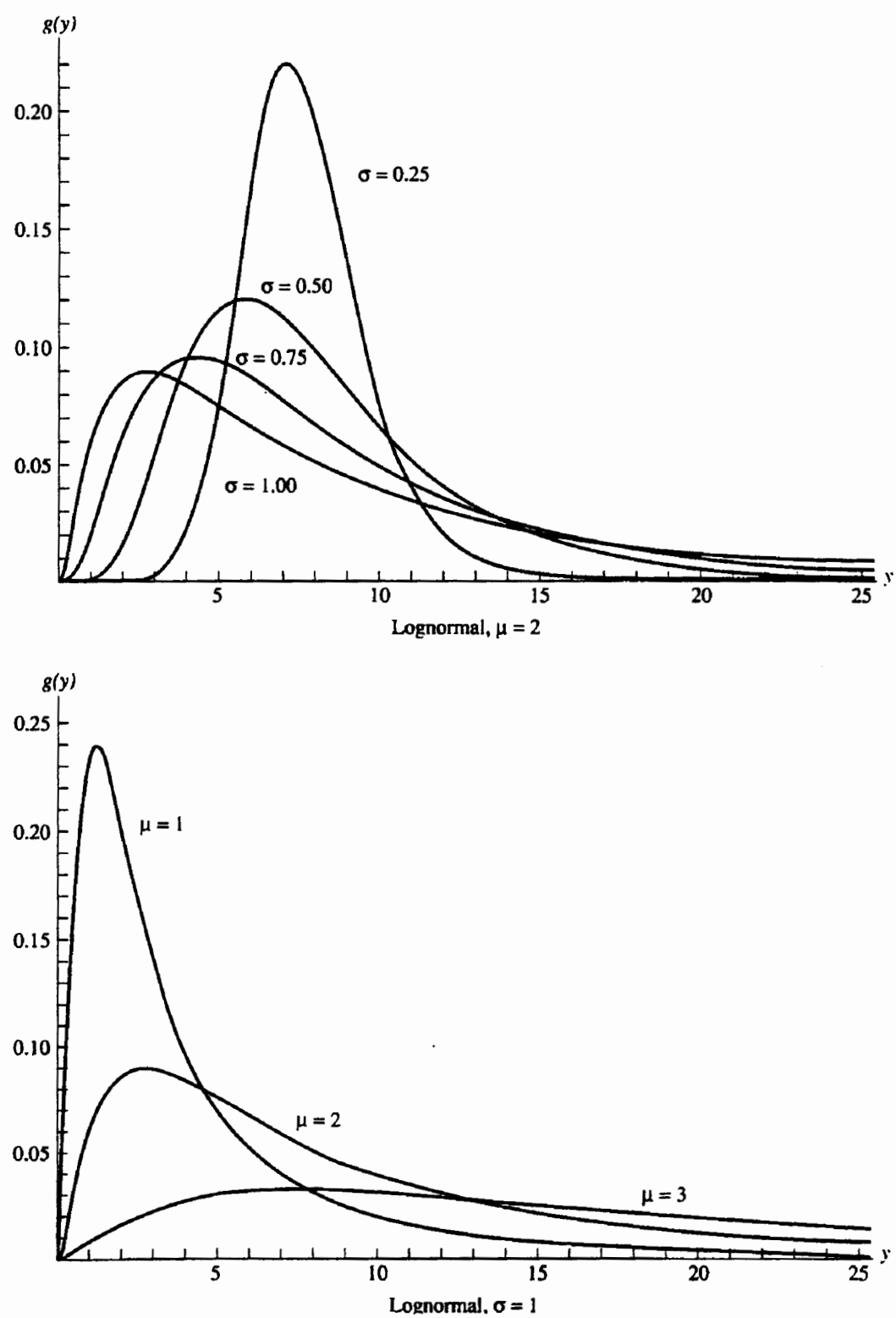


Figure 3-8: Lognormal densities. [Reference 77]

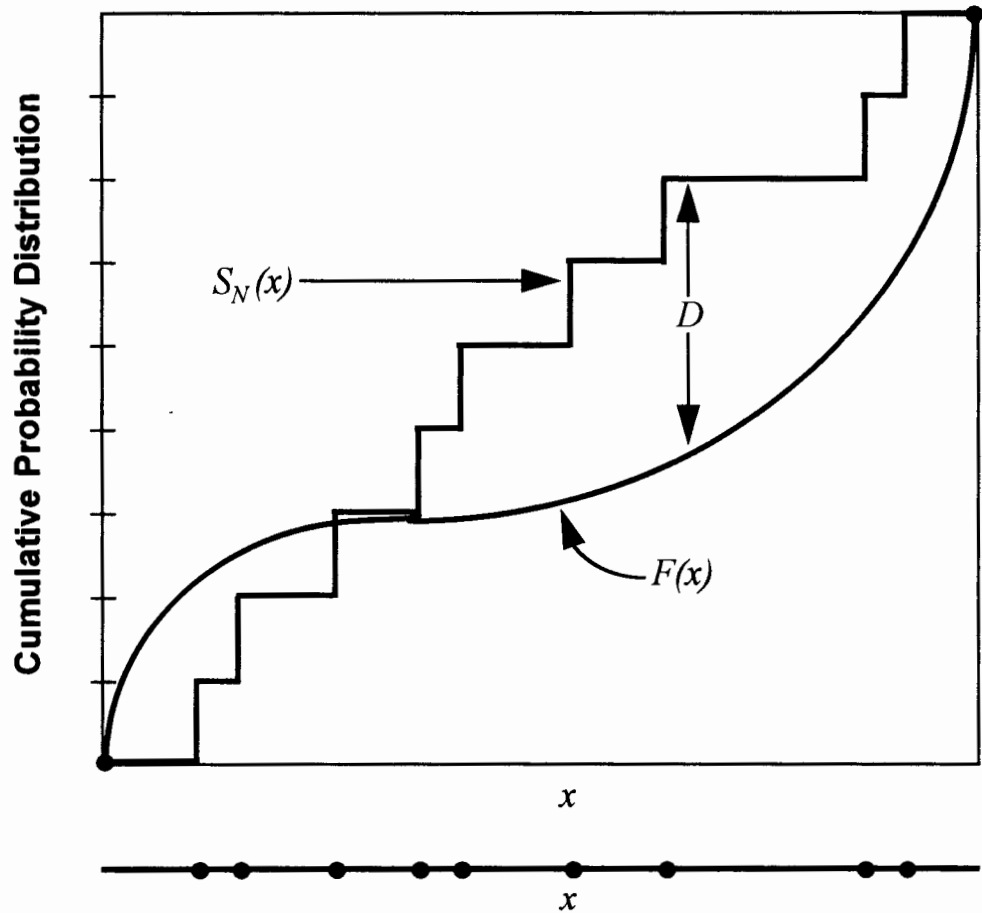


Figure 3-9: Kolmogorov-Smirnov statistic  $D$ . A measured distribution of values in  $x$  (shown as  $N$  dots on the lower abscissa) is to be compared with a theoretical distribution whose cumulative distribution is plotted as  $F(x)$ . A step-function cumulative distribution  $S_N(x)$  is constructed, one that rises an equal amount at each measured point.  $D$  is the greatest distance between the two cumulative distributions. [Reference 57]

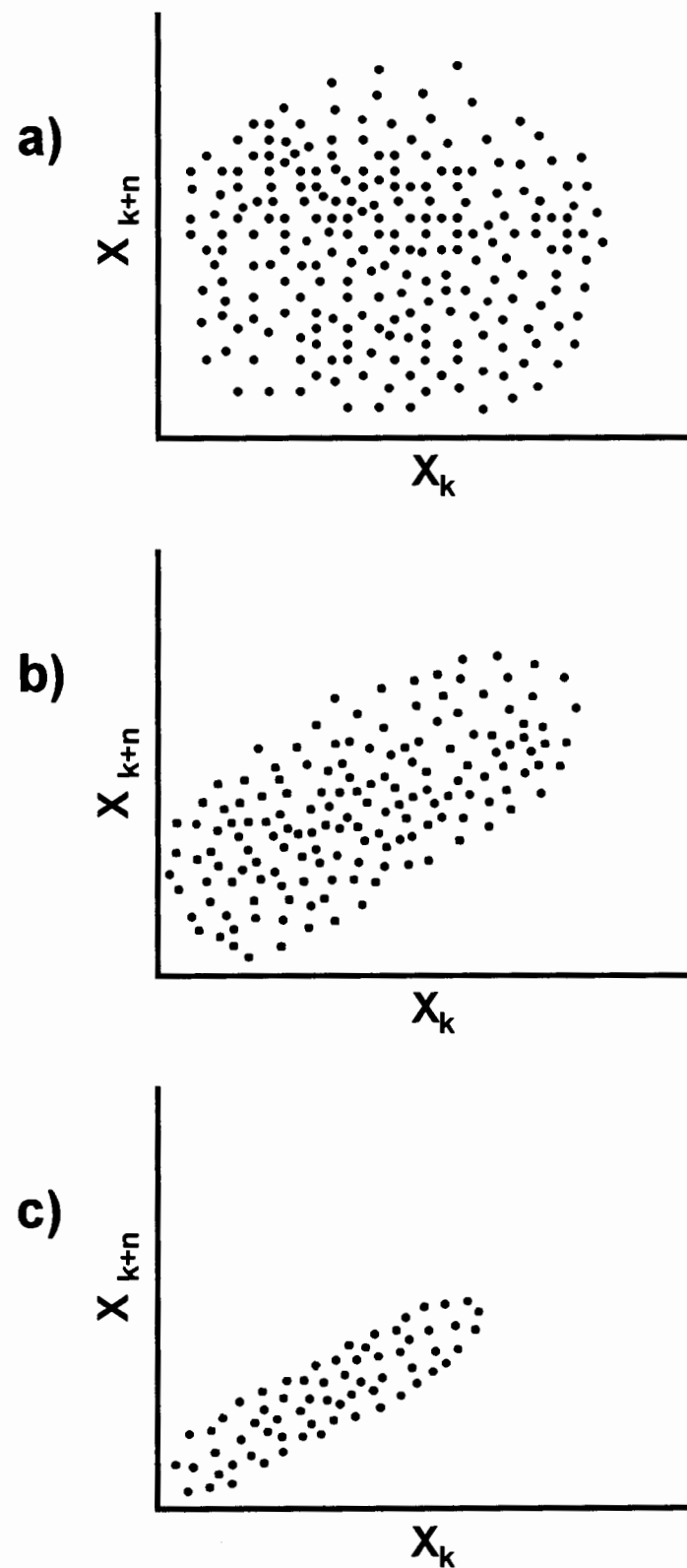


Figure 3-10: Runs test a) random, b) moderately correlated, c) highly correlated.

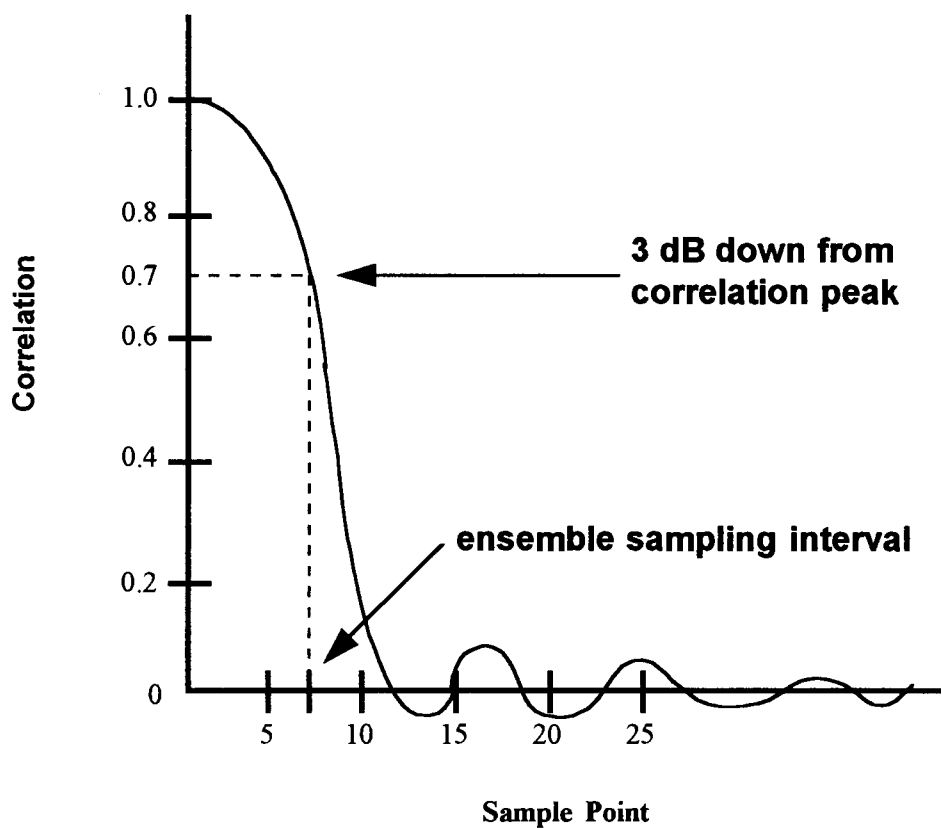


Figure 3-11: An autocorrelation function depicting the sampling interval calculation.

## Chapter 4

### RELATED THEORETICAL AND EXPERIMENTAL APPROACHES

The purpose of this chapter is to provide the foundation upon which the new contributions made by this thesis are built. The chapter includes both theoretical and experimental approaches taken by others to gain a better understanding of fluctuation statistics. The experimental approaches focus more heavily on the fluctuation statistics of measured time series while the theoretical approaches focus on modeling the fluctuations and understanding the physical causes of the fluctuations. The development of fluctuation statistics for bottom reverberation evolved from fluctuation statistics related to both propagation and to scattering.

#### 4.1 Theoretical Approaches

The theoretical approaches deal mainly with modeling the fluctuation statistics. Most of the models are compared to experimental (in-water) data but the main purpose of the research was to postulate a model for fluctuation statistics. Some of the models are parameterized by values linked to physical events in the fluctuating environment. One model is parameterized by the attenuation in multiple ray paths, another by changes in the sediment properties, and another by changes in system parameters like beamwidth and pulse length.

#### 4.1.1 Intensity fluctuations of propagating energy

When the noise from a distant sound in the sea is received, one of its most obvious characteristics is that it fluctuates, or changes with time [1]. Rapid and often violent changes of amplitude and phase are observed, especially with sinusoidal or narrowband signals. Stochastic fluctuations can be predicted only statistically. The fluctuations caused by multipath propagation at high frequencies fall in to this category.

Standard theories of long-range ocean acoustic propagation (e.g., ray trace or normal modes) show that the acoustic field can be represented as a superposition of vectors, each one arising due to propagation over a specific path through the ocean from source to receiver [47]. In 1970, Dyer [45] pointed out that multipath propagation can be modeled as a superposition of random vectors, where the acoustic amplitude and phase in each path are statistically independent random variables, and the acoustic energy is equipartitioned among the multipaths at the receiver. Then, if the acoustic phase in each path is uniformly distributed from  $0$  to  $2\pi$  and the number of paths  $N$  is sufficiently large, the quadrature components of the total received signal will be independent Gaussian random variables, and the intensity will satisfy an exponential density function.

In his article, Dyer also points out that taking the logarithm to the base 10 of the intensity to obtain a level  $L$  in decibels (dB) does not produce a lognormal distribution as commonly supposed. If the dB level  $L$  of the intensity (which Dyer calls the transmission loss) is defined as

$$L = -10 \log I$$

where the intensity  $I$  is exponentially distributed, then the distribution  $f(L)$  is a logarithmic transformation of a exponential distribution, not a lognormal distribution. (Section 3.2.3.2 states a

random variable  $I$  is log-normally distributed if the random variable  $z = \ln(I)$  has a normal distribution). To follow a lognormal distribution, the intensity  $I$  would have to be log-normally distributed rather than the assumed exponential distribution.

Dyer provides the distribution for the natural logarithm of an exponential distribution using the transformation  $z = \ln(I)$  and then using a conversion from the natural logarithm (to the base  $e$  where  $e = 2.718$ ) to the logarithm to the base 10. Dyer gives the density function of  $z$  (the natural logarithm of an exponential function defining the intensity) as

$$f(z) = \frac{1}{2\sigma_x^2} e^{(y-\exp y/2\sigma_x^2)}$$

$$\mu_z = \ln 2\sigma_x^2 - \gamma$$

$$\sigma_z^2 = \pi^2 / 6$$

where  $\sigma_x$  is the standard deviation of the underlying Gaussian distribution of the  $x$  and  $y$  quadrature components of the intensity  $I$  (see Section 3.2.2.1) and  $\gamma$  is Euler's constant ( $\gamma = 0.577$ ). Dyer then uses the fact that the natural logarithm is related to the logarithm to the base 10 and obtains the statistics of the level  $L$  from those of  $z$  where:

$$L = -10 * \log I$$

$$I = 10^{-L/10}$$

$$\ln I = \frac{-L}{10} \ln 10$$

$$L = -\frac{10 \ln I}{\ln 10} = -4.34z$$

Therefore, the standard deviation of Dyer's transmission loss  $f(L)$  is

$$\sigma_L = 4.34\sigma_z = 4.34\pi / \sqrt{6} = 5.57 \text{ dB}$$

Even though the distribution of the dB level  $L$  of the intensity is not lognormal, the lognormal distribution is still widely used for analyzing (approximately) the behavior of fluctuations because the tail of the lognormal distribution is, in general, higher than the Rayleigh distribution (see *Figure 3-8* in Section 3.2.3.2). A lognormal distribution with a standard deviation of 5.57 decibels is also commonly used in the open literature [8, 13, 47] to analyze fluctuation behavior without a physical justification for its use.

In 1996, Tappert and Tang [66], however, suggested a physical situation that does justify the use of the lognormal distribution. They postulated that the intensity fluctuations of acoustic signals propagating in a waveguide having lossy boundaries approach a lognormal distribution at long ranges. They performed Monte Carlo numerical propagation studies of intensity fluctuations in a realistic shallow water environment that simulates the Straits of Florida, including internal wave fluctuations and bottom roughness. Statistical analyses showed that the distribution of intensity of the random wave field saturates to the expected exponential distribution at short range (about 5 km) due to multipath effects; however, it approaches a lognormal distribution to an excellent approximation at long ranges.

They postulate a physically intuitive picture where the environmental fluctuations are rapidly transferring acoustic intensity back and forth between a large number of ray paths or normal modes that have different attenuation coefficients  $\alpha$ . Thus the acoustic intensity in an “average” ray path or normal mode suffers an attenuation that may be described as a random function of the attenuation in different ray paths or modes. This picture implies lognormal statistics by supposing that the acoustic intensity satisfies

$$dI / dr = \alpha(r)I$$

where the attenuation  $\alpha(r)$  is a random function of range  $r$ . The solution of this equation is

$$\ln I(r) = \text{const} - \int_0^r \alpha(u) du$$

where the central limit theorem implies that the random function defined by this integral becomes normally distributed as  $r \rightarrow \infty$  provided the correlation distance of  $\alpha(r)$  is small. It follows that  $\ln I(r)$  is normally distributed for large  $r$ , and hence  $I(r)$  approaches a lognormal distribution.

In summary, Dyer sets forth the statistics of a complex Gaussian process which for intensity is exponential. Dyer also points out that the logarithm of the intensity does not produce the lognormal distribution. However, the lognormal distribution, because of its higher tail, is commonly used in research related to fluctuation statistics. For example, in their research Tappert *et al.* postulate that the lognormal distribution is a good approximation of intensity fluctuations at long ranges. A theoretical lognormal distribution with a standard deviation of 5.57 decibels is commonly used for comparison to in-water experimental fluctuation data and examples from the open literature [8, 13, 47] are included in the following discussions.

#### 4.1.2 Amplitude fluctuations of sediment scattered energy

In 1985, Stanton [67] postulated that the shape of the probability density function (pdf) characterizing reverberation amplitude fluctuations could be predicted by the relative levels of coherent and incoherent scattering in the received signal. The echo from the rough seafloor is composed of two components: a coherent or reflected component, and an incoherent or scattered component. For perfectly smooth surfaces, only the reflected component is present. For very

rough surfaces, the scattered component dominates. For intermediate roughness, with the surface mean-squared roughness on the order of one-quarter acoustic wavelength, the two components will be equal.

Stanton postulates that when the seafloor is smooth, the echo is consistent from location to location. However, when it is rough, the echo will fluctuate. Using an electrical analogy, the scattered component of the echo acts like “noise” in the echo where the reflected component acts like a pure tone. In electrical signal theory, the fluctuations of a signal plus noise are described by the Rician probability density function (pdf).

Stanton’s model uses the coherence function as the signal-to-noise parameter of the Rician distribution (equation 3.20 in Section 3.2.1.4 of Chapter 3) to describe the echo amplitude fluctuations for all ranges of roughness. His coherence parameterized Rician pdf is given as

$$f_{CohRice}(P) = \frac{2(1+\gamma)P}{\langle P^2 \rangle} e^{-\frac{(1+\gamma)P^2 + \gamma \langle P^2 \rangle}{\langle P^2 \rangle}} I_0(q)$$

where

$$\gamma = \frac{\text{coherently reflected echo energy}}{\text{incoherently scattered echo energy}}, \quad \gamma \geq 0$$

$$q = \frac{2P[\gamma(1+\gamma)]^{\frac{1}{2}}}{\langle P^2 \rangle^{\frac{1}{2}}}$$

$I_0$  is the modified Bessel function,  $P$  is normalized by the mean-square amplitude  $\langle P^2 \rangle$  and  $\gamma$  is the effective signal-to-noise ratio in the original Rician formulation. His modified Rician pdf

becomes a Rayleigh distribution when  $\gamma = 0$  which implies a very rough surface scattering the sound instead of reflecting it coherently. For a smooth seafloor, the coherent energy dominates the scattering and the modified Rician approaches the Gaussian distribution.

In the article, Stanton uses the coherence data shown in *Figure 4-1* as inputs to the Rician distribution to predict the pdf of the acoustic scattering from the seafloor. He postulates that the major source of echo fluctuations in the data is due to water/sediment interface microroughness. The article contains plots of the reflection coherence function  $CF_R$  versus frequency of measurements from the Grand Banks of Newfoundland. The measurements were made over six 30 km<sup>2</sup> areas each of consistent sediment type. Stanton uses the measured coherence function to solve for  $\gamma$  where  $CF_R(f) = 1 / (1 + \gamma^{-1})$ . The plots published in the article are for silt and clay bottoms.

As part of the research for this thesis, the coherence function plots published in the article (*Figure 4-1*) were digitized and used as inputs to the Rician distribution in order to calculate the pdf and, ultimately, the probability of false alarm PFA. *Figure 4-2* is a plot of the PFAs calculated from the digitized coherence functions of three samples each from both silt and clay at 7.5, 10, and 12.5 kilo Hertz (kHz). Note that the PFA of the distribution always has a tail less than or equal to the Rayleigh distribution which is indicated by the dashed line. Stanton's distribution can not model fluctuations that have tails higher than Rayleigh because  $\gamma$  is always a fractional quantity less than unity and the distributions highest possible tail occurs at  $\gamma = 0$  implying total incoherent scattering of the energy.

In 1995, LeBlanc *et al.* [68] developed a model of the scattering of sound from the volume of the seafloor sediment. They evaluated the use of their volume reverberation model for remote

sediment classification. Data from several sediment types taken by a broadband digital sub-bottom profiler was used to develop their scattering model. In their article, LeBlanc *et al.* stated that both coherent and incoherent scattering sources exist within the sediment scattering environment. Coherent scattering is most prominent at the water/sediment boundary. They postulated that the roughness scale of the water/sediment boundary has a facet that is geometrically sized to be one-half the acoustic wavelength and arranged to scatter energy coherently, which is Bragg's Law for first-order scattering (see Section 2.1.3.3). They felt coherent reflection may also be observed within the sediment volume due to any object or group of objects with sufficient spatial extent and arranged geometrically to coherently reflect energy. However, most commonly, within the sediment volume, a significant number of incoherent scatterers are observed. The incoherent scatterers would produce a lesser amplitude when compared to coherent scattering events, though incoherent events conceivably comprise the majority of scatterers observed within a given sub-bottom return. This philosophy is the basis for their statistical model which they compared to sonar data.

The sonar they used to collect the data generates calibrated high-resolution acoustic returns with an 8 centimeter vertical resolution. Therefore, it was possible to separate surface scattering events from volume scattering events by time gating the signal returned from the sub-bottom. In applying their scattering model to sonar data collected from a 20 millisecond, 2 to 10 kiloHertz frequency modulated (FM) pulse taken in St. John's Harbor, New Brunswick, over a 0 to 2 meter depth interval, the results suggested the influence of two separate scattering mechanisms within the histograms. The lower amplitudes conform to the expected Rayleigh pdf for amplitude scattering. However, a high amplitude concentration of scattering events in the tail was attributed to coherent scattering events that were included in the top 2 meter observation window. Analysis

of many data sets indicated that the high amplitude coherent distribution occurs exclusively within the first half-meter of sediment depth, indicating that the water/sediment boundary was the cause of the high amplitude components.

In summary, two models of amplitude fluctuations were presented. Stanton's statistical model implies that sediment interface roughness controls the coherence of the scattered energy. His model uses the ratio of the coherent energy to the incoherent energy from the interface scattered sound in the Rician distribution to determine the shape of the amplitude reverberation fluctuations. The drawback of this technique is that the amplitude statistics can never be greater than Rayleigh. LeBlanc *et al.* postulate that the bulk of the received energy was coming from the sediment volume, filling in the mean values of the pdf, but that the higher amplitude fluctuations in the tail were caused by scattering of energy from the sediment interface roughness caused by Bragg's Law of first-order scattering. Their empirical model produced amplitude statistics greater than Rayleigh. A simulation study presented in Chapter 6 was designed to investigate the effects of varying the scattering contributions from the interface roughness and the sediment volume on the fluctuation statistics.

#### 4.1.3 Models of bimodal fluctuations in scattered sound

Drumheller [69] derived general expressions for the density and cumulative probability functions of the amplitude of a linear matched-filter output given a nonfluctuating target in a clutter-limited environment. (Clutter, a term commonly used by the radar community, is equivalent to the term reverberation used by the sonar community). The clutter amplitude distribution for the matched filter output was modeled as a Weibull distribution, i.e.,

$$f_{Weib}(r) = \frac{c}{b^c} r^{c-1} e^{-(r/b)^c}$$

where  $b$  is the scale parameter, and  $c > 0$  is the shape parameter that relates to the skewness of the distribution. Without loss of generality, the shape parameter was chosen to be

$$b = (\ln(2))^{-1/c}$$

giving  $f_{Weib}(r)$  a median value of unity. The Weibull distribution has found favor in detection theory since it provides a good model for the distribution of the amplitude response to non-Gaussian clutter.

Drumheller and Glasser [70] applied their method to experimental sonar data. The sonar data was acquired from a Critical Sea Test for sea surface scattering measurements conducted in Tufts Abyssal Plain near Alaska in March 1992. They processed 13467 returns originating from a 0.6 second linear frequency modulated (FM) sweep from 850 to 1090 Hertz. Although some noise was present, the environment was dominated by clutter.

The clutter amplitudes were non-Rayleigh. It appears that two distinct scattering events were contributing to the clutter amplitudes. The histogram formed by the data was similar to a Rayleigh density at the peak but its tail follows an exponential density function. To model the statistical behavior of the clutter amplitude, Drumheller and Glasser spliced Weibull densities together with parameter  $c = 2$  used to fit the Rayleigh portion near the peak and  $c = 1$  used to fit the exponential tail. It is thought that the shape of the tail is due to occasional large bubble plumes that exist near the surface since the experiment was conducted when wind speed was approximately 15 meters per second and breaking waves were present. It is likely that only one or two bubble plumes were present in any data point due to the beamforming and pulse compression.

It is postulated that the central limit theorem was violated when the dominate scattering contributions were caused by only one or two scattering events, and therefore, the results are non-Rayleigh.

McCammon [74] has conducted research on modeling the probability density function of low frequency (300-650 Hertz) bottom reverberation fluctuations. The fluctuations in the envelope of bottom reverberation time series measured in the Mediterranean were analyzed and found to follow non-Rayleigh statistical distributions. McCammon modeled the data with a mixture distribution because the data histograms suggested two distinct distributions. The data histograms were slightly less than Rayleigh around the peak but were much greater than Rayleigh in the tail as shown in *Figure 4-3*.

The major assumption of her approach was to postulate that the scattering is caused by two different and uncorrelated processes: one being the sediment reflection from roughness at the water/sediment interface and the other being scattering within the sediment volume due to inhomogeneities and layering. Thus, the assumptions are that the fluctuations are caused by changes in sediment properties, and that the variations in the interface reflected path are independent of the variations in the transmitted volume scattered path.

McCammon derived a mixture distribution for the statistics of two independent random Gaussian processes. This distribution was a combination of two Rayleigh terms and a mixture term. The free parameters were the standard deviations of the two scattering processes,  $\sigma_1$  and  $\sigma_2$ , and their strength ratio  $\varepsilon$ . The probability of false alarm was defined as

$$PFA_{mixture} = (1 - \varepsilon)^2 e^{-x^2/2\sigma_1^2} + \varepsilon^2 e^{-x^2/2\sigma_2^2} + 2\varepsilon(1 - \varepsilon)e^{-x^2/A_1} I_0(x^2 A_2)$$

where

$$A_1 = \frac{\sigma_1^2 + \sigma_2^2}{4\sigma_1^2\sigma_2^2}$$

$$A_2 = \frac{|\sigma_2^2 - \sigma_1^2|}{4\sigma_1^2\sigma_2^2}$$

The third term, the mixture term, has the form of the Rayleigh distribution multiplied by a Modified Bessel function with a quadratic argument and a scale parameter  $A_2$ . A criticism of this model is that its derivation also produces a non-uniform phase distribution.

McDaniel [17] assumes a mixture model based on two different scattering processes that are created solely by the statistical independence between the azimuthal extent of the beam and the range extent of the beam over a small patch of sediment with a two dimensional wave number roughness spectrum.

McDaniel [17] began her theoretical examination of the fluctuation distribution with the widely held theory of backscattering from rough surfaces, called the Rayleigh-Rice approximation (Section 2.1.3.3 of Chapter 2). The basic tenet of this theory is that the scattering is a resonant phenomena with facets of the surface roughness having surface wavelengths equal to one half the acoustic wavelength. The scattering strength predicted by this theory is directly proportional to the level of the surface roughness spectrum at the wave number corresponding to Bragg scattering.

McDaniel made the assumption that the surface roughness spectrum  $W$  is separable into down-range and cross-range components, and that the fluctuations of both components are chi-square distributed with degrees of freedom dependent upon the extent of the scattering patch size. The roughness spectrum is

$$W = XY$$

where  $X$  and  $Y$  are independent spectra measured along the orthogonal axes.  $X$  and  $Y$  are chi-square distributed with degrees of freedom

$$N_x = 2\tau\Delta f \quad (\text{down - range})$$

$$N_y = 2\phi^2 R k / 2\pi \quad (\text{cross - range})$$

where  $\tau$  is the pulse length,  $\Delta f$  is the bandwidth of the transmitted pulse, making  $\tau\Delta f$  the time bandwidth product;  $k$  is the acoustic wave number,  $\phi$  is the half-power beamwidth, and  $R$  is a modified reflection coefficient dependent on physical properties of the seafloor. The model implies that sediment interface roughness alone is responsible for the measured reverberation (this is a high frequency assumption).

The data McDaniel used to test her theories were the high frequency (30 kiloHertz) measurements of Chotiros *et al.* [8] and Boehme and Chotiros [16] in which they noted that the fluctuation statistics were dependent on the beamwidth of the transducer. They found that, for a wide beam receiver, the amplitude fluctuations followed Rayleigh, but, for narrower beamwidths, the fluctuations were better described by a lognormal distribution with a 5.57 dB standard deviation. (Chotiros *et al.* [8] and Boehme and Chotiros' [16] data sets will be discussed in more detail under the experimental approaches.) McDaniel was able to derive a theoretical beamwidth dependence that fit the data trends, although the frequency behavior was not modeled. Her theory predicted that wide beams should follow Rayleigh statistics because of the wider field of averaging.

In summary, all three models presented in this section are based on the postulation that the central limit theorem is violated causing non-Rayleigh amplitude fluctuation statistics. Drumheller and Glasser [70] model the fluctuations by splicing together two Weibull distributions. They

postulate that occasional large bubble plumes at the surface caused the non-Rayleigh statistics. McCammon postulated that the non-Rayleigh statistics were caused by a combination of two scattering mechanisms: scattering from the sediment interface roughness and scattering from the sediment volume. She used mixture models parameterized by the variances of the two underlying scattering mechanisms and a mixing term to model the statistics. McDaniel [17] assumes the two competing scattering processes are created solely by the statistical independence of the two dimensional roughness spectra between the azimuthal extent of the beam and the range extent of the beam.

The simulation studies presented in Chapter 6 investigate how a combination of scattering mechanisms affect the fluctuation statistics of bottom reverberation. One study investigates the statistical effect of varying the scattering contributions from the interface roughness and from the sediment volume portions of the total scattering. Another study investigates the statistical effect on the amplitude fluctuations of adding patches of gravel to a muddy bottom. And one study investigates the postulate that wider beams produce Rayleigh fluctuation statistics because of the wider field of averaging.

#### 4.2 Experimental Approaches

The experimental approaches deal mainly with the collection and statistical analyses of in-water data. The data sets provide additional information on fluctuation statistics relative to bottom types, frequencies, grazing angles, pulse types, pulse lengths, and beamwidths.

#### **4.2.1 Intensity fluctuations of propagating energy**

In 1978, Frisk [47] studied the intensity statistics of signals received from three sources (9.8, 110, and 262 Hertz) towed at long ranges (100-3000 kilometers). He tested the experimental probability density functions for the intensity against the following theoretical densities using the Kolmogorov-Smirnov (K-S) test: exponential, Gamma, lognormal with a standard deviation equal to the standard deviation of the measured average transmission loss, and lognormal with a standard deviation of 5.57 decibels.

Frisk found that no single function adequately represented the experimental density functions at all three frequencies, and none of the functions seemed suitable at 262 Hertz. At 110 Hertz, the lognormal distribution with standard deviation 5.57 decibels gave good results ( $\geq 90\%$  acceptance) and the lognormal distribution with the standard deviation of the measured average transmission loss yielded fair results ( $\geq 85\%$  acceptance). At 9.8 Hertz, three functions (Gamma, lognormal, and lognormal with 5.57 decibel standard deviation) gave excellent results ( $\geq 95\%$  acceptance), while one (exponential) yielded fair results.

Frisk concluded that no single density function adequately represented the experimental density functions at all three frequencies. And, the ability of all the functions to describe the experimental results decreased with increasing frequency.

#### **4.2.2 Amplitude fluctuations of sediment scattered energy**

Five articles published the statistics of measured amplitude fluctuations in shallow water for sediment reverberation at high frequencies (20 to 180 kiloHertz). *Table 4-1* list the titles and reference of the articles, frequencies, bottom types, and grazing angles (if available) for the

Table 4-1: Journal Articles with High Frequency Fluctuation Statistics

Article	Frequency (kHz)	Bottom Type	Grazing Angle (deg)
<b>Jackson's Various Sites</b> "Second Report on TTCP Bottom Scattering Measurements: Data Summary" (Reference [75])	35 80	Puget Sound 1980 Site 1: Silt, Fine Sand, Shell Puget Sound 1980 Site 2: Fine Sand, Live Shell Puget Sound 1979 Site 1: Silt, Fine Sand, shell Falmouth Site 1: Sand, Shell, Hard Clay Puget Sound 1980 Site 1: Silt, Fine Sand, Shell Puget Sound 1980 Site 2: Fine Sand, Live Shell	24, 30 24, 30 30 25, 30 24 24
<b>Chotiros' Charleston</b> "Acoustic backscatter at low grazing angles from the ocean bottom" (Reference [16])	30 (NB) 30 (WB)	Charleston, South Carolina: Medium sand	
<b>Chotiros' San Diego</b> "Acoustic backscatter at low grazing angles from the ocean bottom, Part II. Statistical characteristics of bottom backscatter at a shallow water site" (Reference [8])	30 (NB) 30 (WB)	San Diego, California: Patches of coarse and fine sand	
<b>Stanic's Panama City</b> "Reverberation Fluctuations from a Smooth Seafloor" (Reference [13])	20 40 60 90 (NB) 90 (WB) 110 150 180	Panama City, Florida: Smooth, sandy, featureless	9.5, 20, 30 9.5, 20, 30
<b>Stanic's Jacksonville</b> "Fluctuations of high-frequency shallow-water seafloor reverberation" (Reference [14])	20 (NB) 20 (WB) 40 60 90 (NB) 90 (WB1) 90 (WB2) 110 130 150 180	Jacksonville, Florida: Dense layer of coarse shells and shell fragments	18, 28 18, 28 8.8, 18, 28 8.8, 18, 28 8.8, 18, 28 8.8, 18, 28 8.8, 18, 28 10, 18, 28 10, 18, 28 10, 18, 28 10, 18, 28

statistics. The fluctuation statistics were displayed in the articles in the form of probability of false alarm (PFA) plots. The PFAs range from below Rayleigh to Rayleigh to above Rayleigh.

The statistics were calculated from bottom reverberation time series collected during in-water experiments conducted at various shallow water sites and with various measurement techniques. All of the articles included or referenced an auxiliary article that includes environmental measurements of the site location such as core samples and/or photographs of the sea floor.

The data from the articles cover a wide variety of bottom types, frequencies, grazing angles, pulse types, pulse lengths, and beamwidths but they provide enough similarity to determine if trends exist relative to these parameters. The data also include a variation of other factors of interest such as the ensonified patch size and pure tone continuous wave (CW) pulses versus linear frequency modulated (FM) pulses.

To permit a visual comparison of the data, the plots were electronically digitized providing  $x$  and  $y$  coordinate positions for selected points on the plots. All five authors plotted the PFAs with the logarithm of the PFA as the dependent variable; however, the form of the independent variable varied from author to author. Some authors used the square of the normalized amplitude, others used the logarithm of the normalized amplitude. Once the plots were digitized, the independent variable for all plots were converted to the normalized amplitude by taking the inverse logarithm, square root, or both. Then, for each article, the PFAs published in that article were overlaid onto one plot as shown in *Figures 4-4 through 4-8*. To permit a visual comparison of data, the scale of the axes is consistent from plot to plot and the theoretical Rayleigh PFA is plotted with a dashed line on each plot.

Jackson *et al.* [86] wrote an article containing statistics on data taken at three sites each with a different sediment type using a towed acoustic measurement system. Data was recorded at two different frequencies of 35 and 80 kHz and two different grazing angles of 24 and 30 degrees. Four CW pulse lengths ranging from 0.3 to 10 milliseconds were used along with different tow heights from the sea floor in order to vary the ensonified area or patch size. Each plot displayed PFAs for four different patch sizes. The PFA statistics for the Puget Sound sites exhibit Rayleigh-like behavior as can be seen by the majority of the curves in *Figure 4-4*. However, the Falmouth site exhibited a higher than Rayleigh PFA which they felt coincides with the physical characterization measurements of the site. These measurements indicated spatial inhomogeneity both in underlying sediment and in patchiness observed in the sand waves. Jackson *et al.* did not observe a significant frequency or grazing angle dependence at any site.

Boehme and Chotiros [16] and Chotiros *et al.* [8] published articles containing statistics on complementary data sets taken from two sites with similar bottom types using a stationary acoustic measurement system. The data sets were visually compared to a Rayleigh density and a lognormal density with a 5.57 dB standard deviation. Their objective was to identify dependence on beamwidth, range, and azimuth. The Charleston measurements were taken from a bottom with patches of fine and coarse sand using a 0.25 millisecond pulse and the San Diego measurements were taken from a medium sand bottom using a 1 millisecond, 4 kHz bandwidth linear FM pulse. The data sets were recorded at 30 kHz. Data from two beamwidths of 2.8 and 21 degrees were recorded. The PFAs range from Rayleigh to above Rayleigh as shown in *Figure 4-5* and *Figure 4-6*. Each figure displays all the data provided in each article for both beamwidths plotted onto one consistent set of axes; no averaging or combining of the data has been performed. The authors felt neither the Rayleigh nor the lognormal theoretical distributions accurately modeled the

fluctuations. Boehme and Chotiros and Chotiros *et al.* postulated that the measurements made with a widebeam array follow a Rayleigh distribution, while measurements made with a narrowbeam array consistently depart from Rayleigh. They reported very little difference between the density functions calculated for different azimuthal angle or ranges. The exception occurred for nonhomogeneous bottoms, where the distribution function showed a dependence on aspect angle. The authors concluded that this was caused by variations in the mean scattering level measured at different aspect angles due to highly directional scattering mechanisms on the ocean bottom [10].

Stanic and Kennedy [13, 14] published articles containing statistics on data taken from two sites with very different bottom types using a stationary acoustic measurement system. The Panama City measurements were taken from a smooth, sandy, featureless floor while the Jacksonville measurements were taken from a sea floor that was covered with a thick layer of coarse shells. Both data sets were recorded at frequencies of 20, 40, 60, 90, 110, 150, and 180 kHz and at grazing angles of approximately 10, 20, and 30 degrees. The Jacksonville data included measurements at 130 kHz and narrow beamwidth and wide beamwidth signals for 20 kHz. Areas ensonified by the narrow beamwidth signals were always located inside the areas ensonified by the widest beamwidth signals. The transmitted pulse was a 5 millisecond CW pulse. The PFAs from both sites range from below Rayleigh to Rayleigh to higher than Rayleigh as can be seen in *Figure 4-7* and *Figure 4-8*. Each figure displays all the data provided in each article for all frequencies, beamwidths and grazing angles plotted onto one consistent set of axes; no averaging or combining of the data has been preformed. Stanic and Kennedy compared these results to theoretical Rayleigh, lognormal with a 5.57 dB standard deviation, and standard Gaussian distributions. No theoretical distribution consistently modeled the fluctuations. They felt

the statistics vary as a function of frequency, grazing angle, and beamwidth; however, the variations were not consistent between the sandy site and the coarse shell site. Therefore, they felt the reverberation statistics are not only a function of scatterers located on the sea floor but must be a function of scatterers from both the surface interface and the volume of the sediment.

McDaniel [17], Boehme and Chotiros [16], Chotiros *et al.* [8], and Stanic and Kennedy [13, 14] postulate that the random component of the reverberation envelope increases with increased patch size. The patch size can be increased by increasing the range from the receiver (down range) or increasing the beamwidth (cross range). This concept was tested with the simulation and the results are presented in Chapter 6.

#### **4.2.3 Relationship of interface roughness to fluctuation statistics**

In 1990, the Office of Naval Research, under their Fundamental Research Initiative Program, sponsored a series of surface scattering measurements using the anechoic water tank at the Applied Research Laboratory of The Pennsylvania State University. The overall objective was to determine how spectral and statistical characteristics of a surface are related to the statistics of fluctuations [10]. Acoustic backscattering was measured for high frequencies (200 kHz) from both rough (gravel) and smooth (sand) random surfaces along with several monochromatic, or corrugated, surfaces. McCammon *et al.* [76] have found that the fluctuation statistics change when there are a multiplicity of differing mean levels in the scattering strength caused by the summing of returns from differing aspect angles of the corrugated surface. They called this type of surface a “patchy” surface. They hypothesized that this new criteria of patchiness must be

satisfied in some way before beamwidth or ensonified area alone can account for variations in the statistics [10].

Becker [10] continued the investigation of their hypothesis by performing statistical analysis of data generated at different aspects of a randomly rough surface. Becker modeled randomly rough surfaces as a statistical representation of varying heights and correlation lengths. An isotropic surface implies that the surface has the same statistical characteristics along any direction. He modeled anisotropy by introducing different surface height spectrum and/or correlation lengths in two perpendicular directions. Backscattering measurements were made from three surfaces: one was isotropic with a lognormal distribution of heights in  $x$  and  $y$ ; one had the same height distributions but different correlation lengths in  $x$  and  $y$ ; and, one had different height distributions but the same correlation lengths. Becker used a computer controlled machining tool to cut the exact surfaces desired for the measurements. He concludes that at 200 kHz, the statistics do not depend on the shape of the surface height distribution alone. The PFAs determined for each independent aspect of the three surfaces had the same shape. However, statistics from combined measurements with different mean scattering strengths yielded non-Rayleigh results. Becker postulated that the “patchy” surface can be caused by anisotropy in either surface height distribution or correlation lengths of the surface.

#### 4.3 Summary

The simulation studies presented in Chapter 6 were designed to investigate many of the research findings presented in the above discussions. Table 4-2 shows the relationship between

research issues and hypotheses of this chapter and the section in Chapter 6 that discusses the results of the simulation study designed to investigate the issue.

*Table 4-2: Research hypotheses investigated in the simulation studies of Chapter 6.*

Research Hypotheses	Reference	Thesis Chapter 6 Section
High amplitude fluctuations are caused by scattering from interface roughness.	LeBlanc et al. [68]	6.2.1 Vary surface roughness parameter $W(K)$
Non-Rayleigh statistics are caused by a non-random combination of interface scattering with sediment volume scattering.	McCammon [74]; and Jackson et al. [75]	6.2.1 Vary combination of surface roughness parameter $W(K)$ and volume parameter $\sigma_2$
Higher than Rayleigh statistics are caused by spatial inhomogeneity or patchiness of the surface interface.	Drumheller and Glasser [70]; Jackson et al. [75]; and Becker [10]	6.2.2 Mixture study - mix patches of gravel with mud
Widebeam measurements follow Rayleigh statistics while narrowbeam measurements are higher than Rayleigh.	Chotiros et al. [8]; Boehme and Chotiros [16]; and McDaniel [17]	6.2.3 Beampattern study
SVP variability coupled with sediment variations cause non-Rayleigh results	Stanic and Kennedy [13, 14]	6.2.4 SVP study

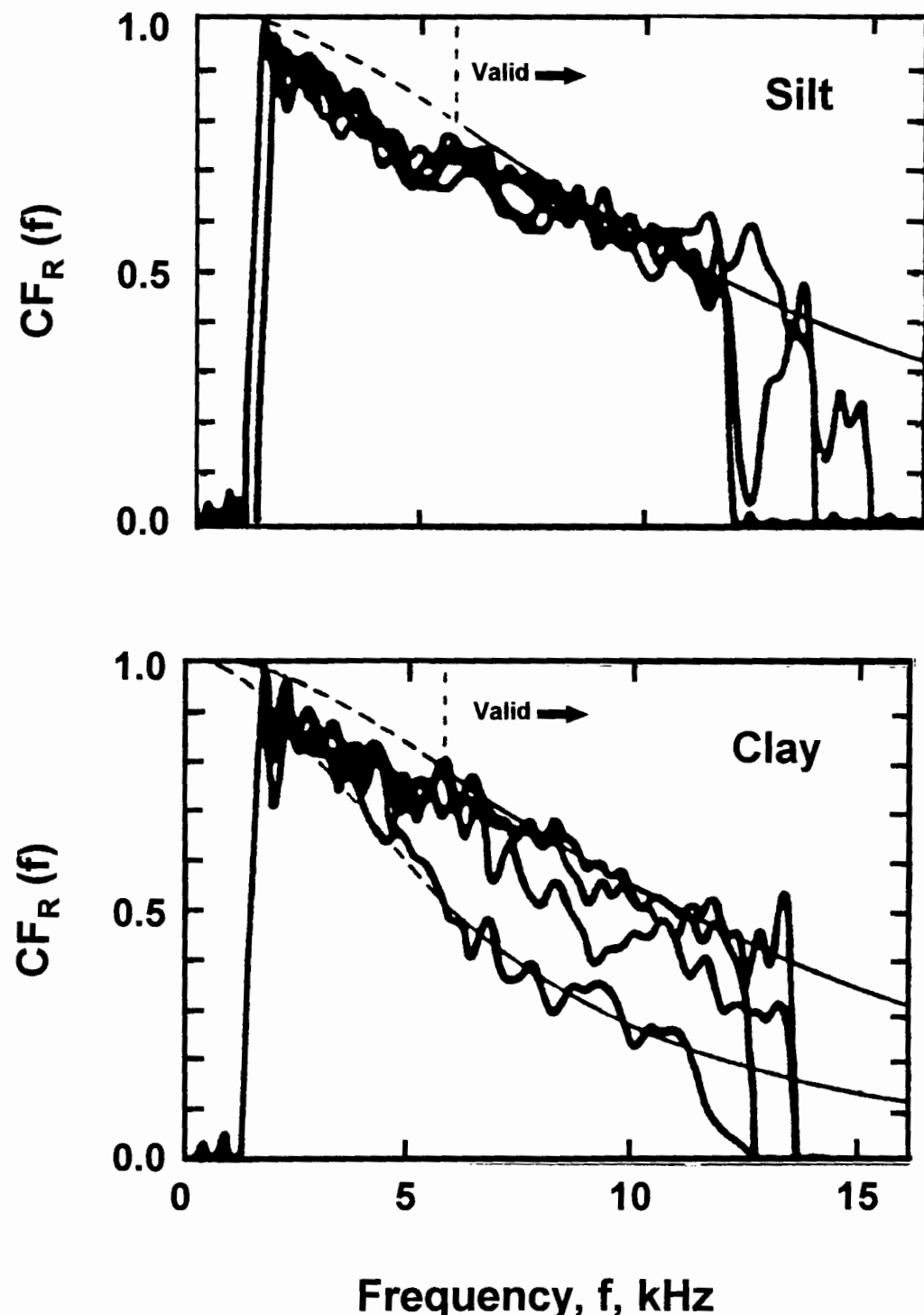


Figure 4-1: Plots of reflection coherence functions versus frequency from Stanton [67]. The data are from clay and silt sediments, where the major source of echo fluctuation is due to water/sediment interface microroughness.

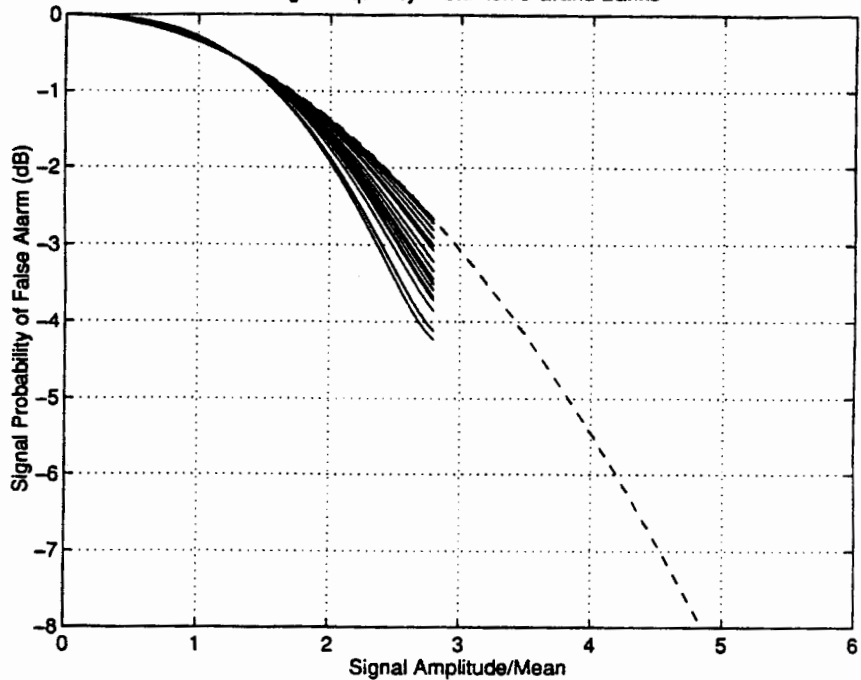


Figure 4-2: PFA calculated from the Rician distribution using digitized reflection coherence functions published in Stanton's article [67]. The dashed line is the Rayleigh distribution.

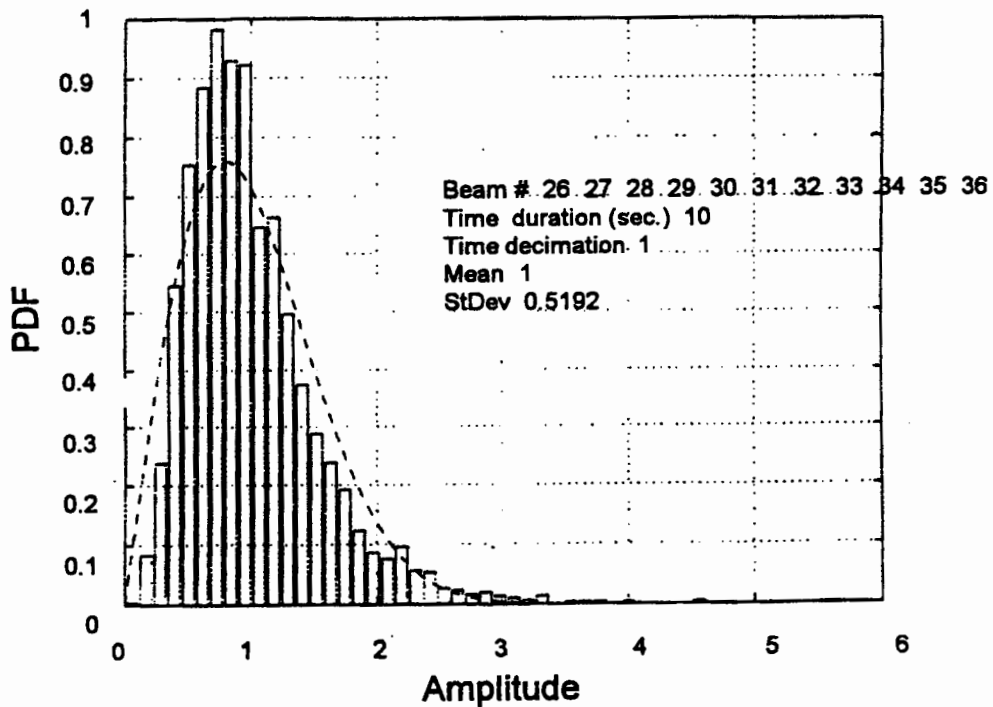


Figure 4-3: Histogram of reverberation envelope fluctuations about the mean modeled by McCammon with the mixture distribution. The dashed line is the Rayleigh pdf and the amplitude is normalized by the mean.

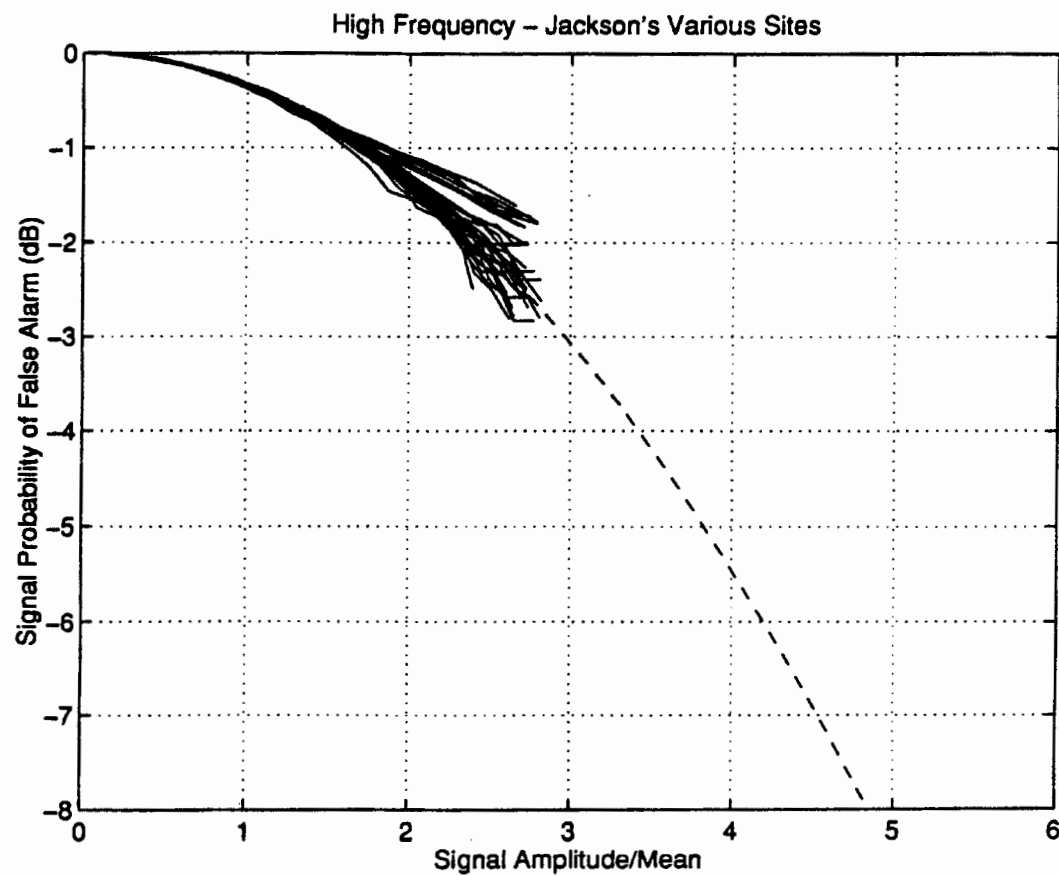


Figure 4-4: Jackson *et al.* PFAs digitized and plotted from data published in Reference 75.

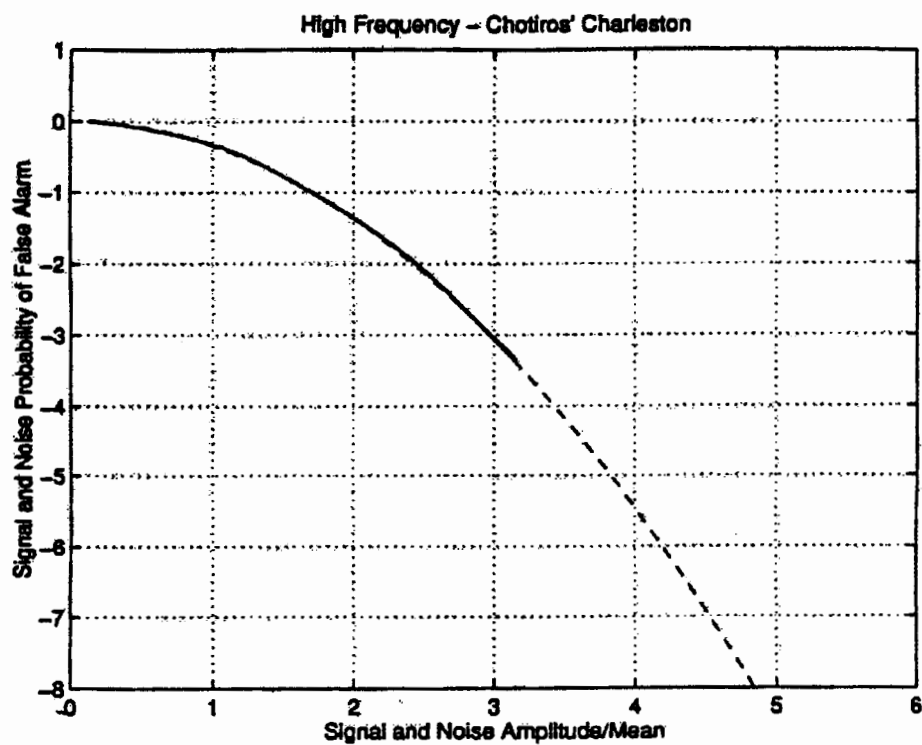


Figure 4-5: Boehme and Chotiros PFAs digitized and plotted from data published in Reference 16.

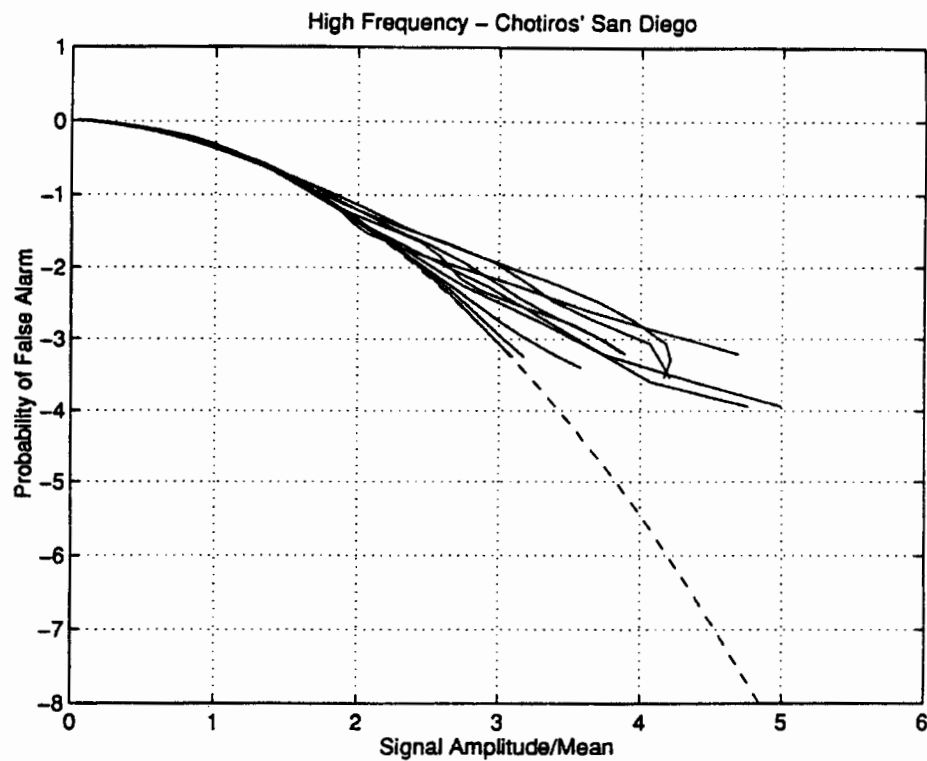


Figure 4-6: Chotiros *et al.*'s PFAs digitized and plotted from data published in Reference 8.

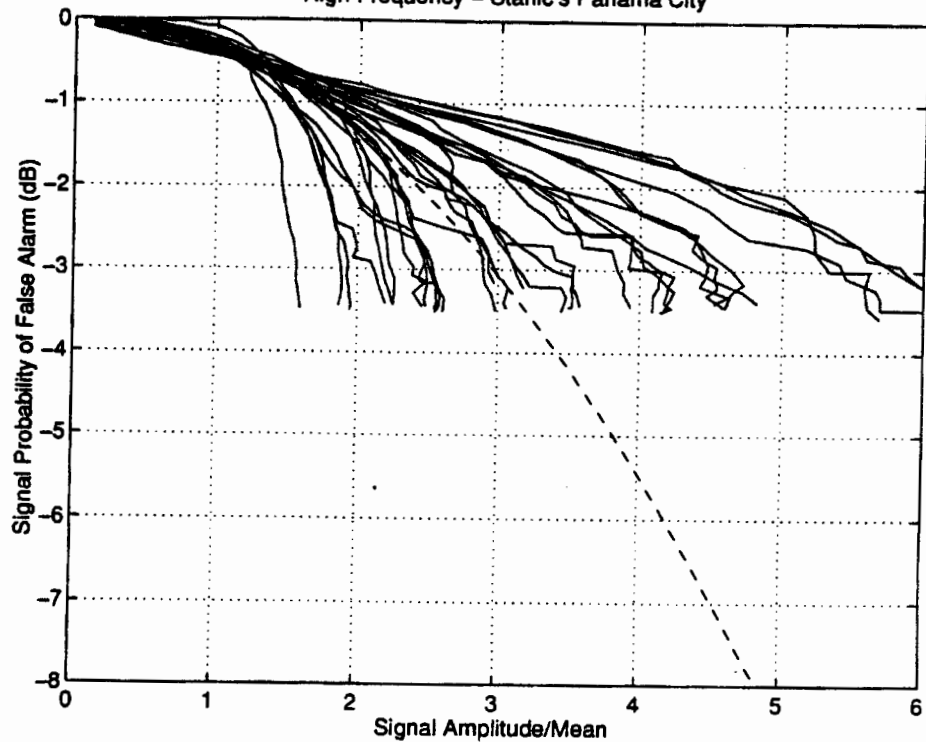


Figure 4-7: Stanic and Kennedy's PFAs digitized and plotted from data published in Reference 13.

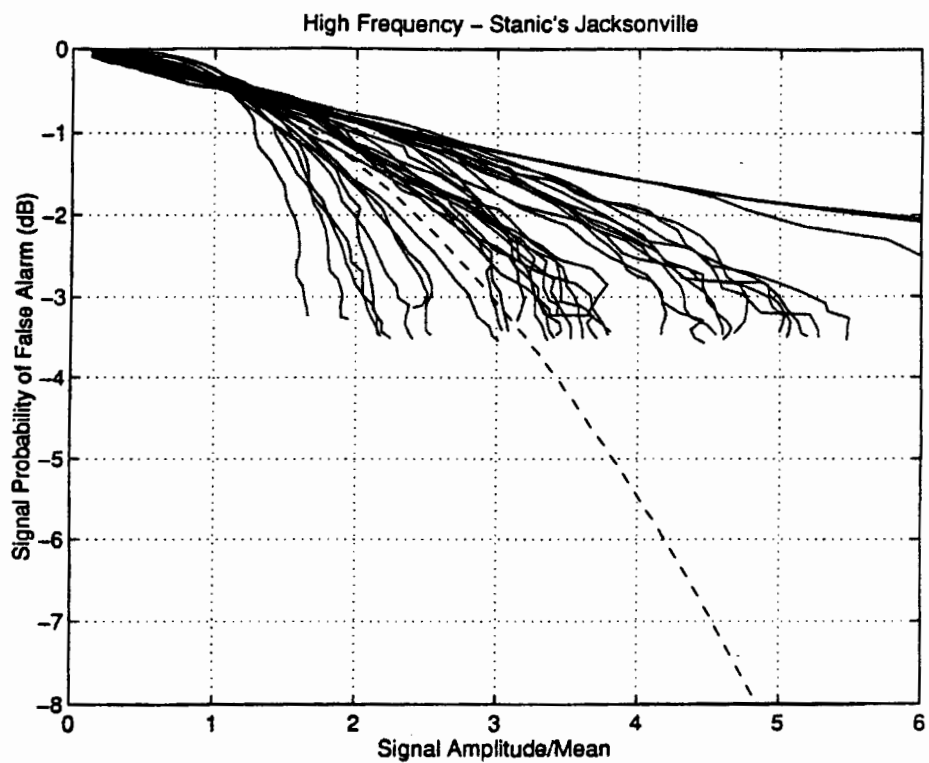


Figure 4-8: Stanic and Kennedy's PFAs digitized and plotted from data published in Reference 14.

## Chapter 5

### IN-WATER REVERBERATION DATA

As part of this thesis, low-frequency in-water reverberation time series were processed from two different shallow water experiments conducted by the SACLANT Centre, La Spazia, Italy. The purpose of this chapter is to describe the processing performed on the data, provide the details of each experiment such as the towed array receiver and site characteristics, and, most importantly, provide the results of the statistical analysis.

#### **5.1 Processing Technique**

The technique used to process the data is as follows: Reverberation intensity level time series were obtained for each beam from a towed horizontal line array. In most cases, only every other beam was chosen to minimize overlap between beams, and only the beams grouped around the broadside beam (the broadside beam is steered zero degrees and located perpendicular to the center of the array) were chosen to avoid the bias of increased beam level at end fire (the end fire beams are steered plus and minus ninety degrees from broadside). The angle window was roughly 40 to 140 degrees about the broadside beam. Next, the time series from each beam were lined up in time. This was accomplished by eye for the explosive charges (also called SUS charges) and by recorded timing information for the pulse data. The portion that will be referred to as the “signal” is a section of time of sediment reverberation that was chosen by visual inspection as being sufficiently above the noise to be clearly identified as a sediment return and, at the same time,

independent of azimuthal angle. That is, the chosen regions were relatively stationary among the beams, showing no large reflectors or other features at the same time in several beams. In addition, a section of the return that was clearly in the ambient noise was chosen to determine the behavior of the noise, and it will be referred to as the “noise.” *Figure 5-1* shows a representative time series with the signal and noise sections marked on the plot. Beams that were obviously contaminated by shipping noise were dropped from the analysis. The data in each section were reduced from intensity levels to pressure amplitudes by the relation  $10 \log I(t) = 20 \log P(t)$ .

Temporal autocorrelation functions were plotted for each beam. For the correlation computations, the signal and noise sections were each normalized to have zero mean. The length of time for which the autocorrelation was less than 0.7 (see Section 3.3.2.2 for details) was determined on the average over all beams, and this was designated to be the minimum time sampling interval. The signal portions were more correlated than the noise portions; therefore, the longer time interval between samples dictated by the signal’s correlation time was chosen for both portions to maintain consistency in plot comparisons. Then the signal and noise data were subsampled at this time interval. Next, the mean and standard deviation were found for each beam as a function of time and the coefficient of variation *cv* was plotted versus time.

For histograms, cumulative distributions and false alarm rates, these signal and noise data were each normalized to have unity mean by dividing by the mean amplitude of the chosen subset of beams at each time step (or bin). In this way, the effects of grazing angle dependence and pulse length and shape were removed without having to deconvolve the data and pulse. The values in each beam were then appended from each time bin to create a single sequence of fluctuations about unity. The sequences were plotted for visual inspection to check for correlated segments that might indicate deterministic features that would bias the distribution of the fluctuations. Runs tests were

performed to check the randomness of the sequences of fluctuations. The histogram, cumulative distribution function and the logarithm of the false alarm rate were computed and plotted. Statistical theory states the amplitude fluctuations from a Gaussian random process will follow a Rayleigh distribution. Therefore, on each of these plots, the Rayleigh predicted result has been displayed for comparison.

## 5.2 Celtic Duet Experiment

In June 1992, the SACLANT Centre conducted an experiment referred to as Celtic Duet [80] at three sites (A, B, and C) in the shallow water off the south west approaches to the United Kingdom. Reverberation time series from Sites A and C were processed as part of this thesis. The sound speed profiles were typical of the area for the summer. A fairly shallow warm layer was present at the surface of the ocean, overlaying a steep thermocline. The depth of the minimum sound speed was around 20 to 30 meters at Site A and 30 to 40 meters at Site C. The horizontal line array, located at a depth of 55 meters, was configured to form 65 beams for the low frequencies (365 to 425 Hertz) and 128 beams for the high frequency (1280 Hertz). The sources employed at 50 meters depth were 8 second continuous wave (CW) signals at various frequencies and a 2.4 second hyperbolic frequency modulated (HFM) signal with a 365 to 425 Hertz (Hz) bandwidth. In this thesis, the following data is presented:

1. Site A 400 Hz CW - 10 pulses
2. Site A 365-425 Hz HFM - 5 pulses
3. Site C 400 Hz CW - 5 pulses

#### 4. Site A 1280 Hz CW - 5 pulses

The CW and FM signals were transmitted sequentially during each leg of a pentagon shaped experimental track; therefore, the CW signals (400 and 1280 Hz) and the FM signal at Site A are looking at essentially the same sediment on each leg of the pentagon track. Site A was characterized as extremely flat and featureless with the sediment to the north composed of chalk and the sediment to the south composed of layers of chalk, limestone, and sand. During the experiment, the winds were calm, with only a slight swell. Site C was virtually flat. The sediment was chalk, with a thin patchy sediment cover and some upstanding chalk features. During the experiment at Site C, there were high winds of from 25 to 30 knots.

##### 5.2.1 Site A 400 Hz CW

At Site A, ten pulses were analyzed from an 8 second long CW at 400 Hz, sampled in time at 50 Hz giving 0.02 seconds per sample. For each pulse, thirteen beams (numbered 21, 23, 25, 27, 29, 31, 33, 35, 37, 39, 41, 43, and 45) were chosen for processing. Example figures for the data will be shown for the broadside beam number 33 for the second pulse recorded on the fourth leg of the pentagon shaped experimental track. An example of the beam intensity time series was shown in *Figure 5-1*. The sections chosen for signal and noise are designated on the plot. Note that the long pulse causes large coherent-looking returns in the signal portion. An expanded plot of just the signal portion in one beam is shown in *Figure 5-2*. Temporal correlation lengths to the 0.7 correlation level are listed in *Table 5-1* and an example plot is shown in *Figure 5-3*. Based on the values in *Table 5-1*, the average measured correlation length of 20 samples was calculated for the

data after eliminating outliers, the sampling interval was chosen to be 20 samples \* 0.02 sec/sample = 0.4 sec.

*Table 5-1: Site A 400 Hz CW - Correlation length of signal section for each pulse number and beam. Lengths are defined as 0.7 correlation and are expressed as the number of samples. Time equivalent would be the product of the table entry and 0.02 sec/sample. Mean entry excluding obvious outliers is  $20 \pm 8$ .*

Beam Number	Pulse Number									
	1	2	3	4	5	6	7	8	9	10
21	12	13	15	14	17	37	25	20	17	22
23	23	19	28	29	62	45	22	15.5	41	14
25	19.5	16.5	14.9	19	58	50	10	22	18	27
27	33	10	20	15	10	73	16.5	13	18	30
29	41	*	55	11	17	42	18	12.5	17	30
31	15	13	45	15	13	18	85	9	15	39
33	16.5	22	11	11.5	7	13.5	86	17	13.5	28
35	24	14.5	22	13	14	20	33	16	23	37
37	60	37	51	15	14	16.5	17	86	17	17
39	52	25	21.5	30	23	54	19	25	32	30.5
41	55	43	12.5	15	17	36	16	15	16	20
43	37	68	10.5	14	11	25	18	24	41	38
45	14	17	10	20	18	15	22	12	18	75

The signal sections from all the beams are overlayed in *Figure 5-4*. This overlay shows large peaks occurring randomly in time. If the large peaks had all been from the same beam, it would have indicated some deterministic feature along a bearing that would bias the fluctuations. However, a study of each beam in the overlay reveals that the peaks are randomly distributed among all the beams, with none dominating longer than a single isolated peak. Thus, the peaks

must come from a rather uniform distribution of features in azimuthal angle. Also, this plot visually demonstrates that features in one beam are not correlated with features in the other beams.

The coefficient of variation  $cv$  is the ratio of the mean and standard deviation at each time point (obtained by averaging over the 13 beams) and is plotted versus time in *Figure 5-5*. A good random sequence should have a random looking  $cv$ , as this one does, and if the distribution were Rayleigh, the  $cv$  would have the average value 0.5227. These data have an average  $cv$  of 0.618. After the data from all beams have been normalized to unity mean, they are appended to form a single sequence as shown in *Figure 5-6*. Note that the sequence in *Figure 5-6* looks somewhat periodic. This happened because the highest fluctuations persisted over 3 or 4 samples in the same beam, showing up in the same relative sequence positions. When another beam records a high peak, the periodicity shifts by a few positions. The runs tests in *Figure 5-7* confirm this diagnosis. The first plot, *Figure 5-7a*, shows the run tests comparing each point to the adjacent one,  $n$  to  $n + 1$ ; this is equivalent to comparing each beam to the next at the same time in the construction of the sequence. In this test, the points appear to be random, confirming that the beam-to-beam correlation is small. In the second plot, *Figure 5-7b*, the runs test is comparing point  $n$  with  $n + 13$ , skipping the points in between. This is a comparison of each adjacent point in time from the same beam. Because the peaks in all the beams persist over several sample points, this runs test shows a high degree of structure. It indicates that the beam time series retain a noticeable degree of correlation, even when sampling every 20th point. The question of temporal correlation and sampling interval was investigated by reprocessing the data at longer sampling intervals. The results are demonstrated in the next paragraph.

The histogram of the sequence in *Figure 5-6* is shown in *Figure 5-8*. The Rayleigh density function is shown by the dashed line for comparison. If the sequence had been created from a

Gaussian random process, then the amplitude distribution should have been Rayleigh. This histogram shows higher than expected values below the mean, and higher than expected values at amplitudes 3 to 4 times the mean. The logarithm of the probability of false alarm PFA is displayed in *Figure 5-9*. Recalling that the nature of the PFA is to highlight the tail of a distribution, in *Figure 5-9*, the tail of the PFA lies far above the expected Rayleigh distribution. To determine if the temporal correlation found in the sequence when sampled every 20th point is affecting the result, data sampled every 80th point was processed for comparison. *Figure 5-10* contains a sequence, run test, and PFA for the very sparsely sampled data, to be compared with *Figures 5-6*, *5-7b*, and *5-9*. The data is more random in the sparsely sampled case; the sequence does not look so periodic and the runs test over time does not have a diagonal structure. However, the PFA still shows a high tail; the decrease in points just decreases the range of the figure. Based on this test, a decision was made to retain some temporal correlation in the data in order to increase the number of points and PFA range. The remaining pulses at this site and frequency were processed and *Figure 5-11* displays the resulting non-Rayleigh PFA curves.

The noise section of the beam time series was also processed in the same manner as the signal section. *Figure 5-12* contains the expanded portion of the noise designated in *Figure 5-1*. *Figure 5-13* shows the noise coefficient of variation, which has an average value of 0.52, very close to the Rayleigh expected result. *Figure 5-14* shows the noise sequence, with no obvious periodicity. *Figure 5-15* and *Figure 5-16* contain the runs tests over beam and time, and are satisfactorily random looking. *Figure 5-17* displays the noise histogram and *Figure 5-18* shows the PFA. The noise PFA is a good match to the Rayleigh distribution. *Figure 5-19* shows the PFAs computed for the noise sections of all 10 of the pulses from Site A at 400 Hz. They are all evidently Rayleigh, in contrast to the signal sections in *Figure 5-11*.

### **5.2.2 Site A 365-425 Hz HFM**

For this set, five pulses from a 2.4 second long hyperbolic FM with a bandwidth of 60 Hz from 365 to 425 Hz, sampled in time at 75 Hz giving 0.013 seconds per sample were analyzed. For each pulse, thirteen beams (numbered 21, 23, 25, 27, 29, 31, 33, 35, 37, 39, 41, 43, and 45) were chosen for processing. Example figures for this data set will be shown for the broadside beam number 33 from the first pulse recorded on the second leg of the pentagon shaped experimental track. An example of the beam intensity time series is shown in *Figure 5-20*. The sections chosen for signal and noise are designated on the plot. An expanded image of just the signal portion is shown in *Figure 5-21*. Contrast this with the expanded portion of the CW signal in *Figure 5-2*. While the HFM is much more random appearing, with peaks and nulls spaced much closer together than in *Figure 5-2*, the presence of some large features can still be seen lasting 3 to 4 seconds that modulate the signal in a manner similar to that in *Figure 5-2*. Temporal correlation lengths (0.7 correlation) averaged under 0.04 seconds, roughly one tenth that of the 400 Hz CW case shown above. The data was processed at sampling rates of every 5th point (0.06 sec/sample) and every 20th point (0.26 sec/sample) for comparison.

Using the 0.26 sec/sample analysis for comparison with the CW case above, the coefficient of variation, *cv*, is plotted versus time in *Figure 5-22*. The average *cv* is 0.6097. The data sequence is shown in *Figure 5-23*. Contrasting this with *Figure 5-6*, note that the periodicity of the spikes in *Figure 5-6* is not found in these data. This is because these data have a much shorter correlation in time. Runs tests for the data are shown in *Figure 5-24 a and b* over beam and over time. In contrast with *Figure 5-7*, these tests remain random looking even over time because of the short correlation times. The histogram of the signal fluctuations is shown in *Figure 5-25*, and the probability of false alarm is shown in *Figure 5-26* where the difference in sampling intervals is

noted. These data are found to be as non-Rayleigh as were the 400 Hz CW shown in *Figure 5-9*, even though the time series, sequences and runs tests appeared more uniformly random than the CW case. The PFAs of all five pulses are shown in *Figure 5-27* for the sampling interval of 0.06 sec/sample. The 0.26 sec/sample data were similar.

The noise section of the beam time series was processed. *Figure 5-28* displays the noise histogram and *Figure 5-29* displays the noise probability of false alarm with the differences in sampling interval noted. *Figure 5-30* shows the noise PFAs for all five pulses. The data appear to be Rayleigh, as was found in the 400 Hz CW case shown in *Figure 5-19*.

### **5.2.3 Site C 400 Hz CW**

At site C, five pulses from an 8 second long CW, sampled in time at 50 Hz giving 0.02 seconds per sample were analyzed. For each, thirteen beams (numbered 21, 23, 25, 27, 29, 31, 33, 35, 37, 39, 41, 43, and 45) were chosen for processing. Example figures for the data will be shown for the broadside beam number 33 from the first pulse recorded on the second leg of the pentagon shaped experimental track. An example of the beam intensity time series is shown in *Figure 5-31*, where a rather intense feature is found at about 30 seconds. The sections chosen for signal and noise are designated on the plot. An expanded image of just the signal portion of this pulse is shown in *Figure 5-32*. Notice that the signal changes its character to a more noise-like signal after encountering the feature at 30 seconds, no doubt this is caused by sea floor shadowing. Contrast this with the expanded portion of the CW signal in *Figure 5-2*. Keeping in mind the scale change, note that the long time features in *Figure 5-2* are also found in parts of these data. Temporal correlation lengths (0.7 correlation) averaged under 0.14 seconds, roughly one third that

of the Site A 400 Hz CW case shown above. The data was processed at sampling rates of every 20th point (0.4 sec/sample) for comparison with Site A.

On processing, the average coefficient of variation was found to be 0.545. The data sequence is shown in *Figure 5-33*. Contrasting this with *Figure 5-6*, note that the periodicity of the spikes in *Figure 5-6* is also found in these data. Runs tests for the data are shown in *Figure 5-34 a and b* over beam and over time. In comparison with *Figure 5-7*, the same somewhat correlated behavior in time can be seen. The histogram of the signal fluctuation is shown in *Figure 5-35*, and the probability of false alarm is shown in *Figure 5-36*. In contrast to *Figure 5-9*, these data are found to be surprisingly Rayleigh, even though the time series, sequences, and runs tests appeared to exhibit the same behavior as the Site A 400 Hz CW data. The PFA of all four pulses are shown on *Figure 5-37*. To understand the surprisingly Rayleigh result of these data, the environment at Site C was examined. One important difference between the sites was the wind speed. Site A was visited during winds of 4 to 6 knots on average, while at Site C the winds were much higher, averaging about 26 knots during the experiment (see *Figure 5-38* and *Figure 5-39*). High winds would inject an additional randomness into the reverberation that might, by the central limit theorem, bring the statistics back to Rayleigh. This explanation is tentative, and further research is required to confirm it.

The noise sections of the beam time series were processed. *Figure 5-40* shows the noise PFAs for all four pulses. The data appear to be Rayleigh, as was found in the noise portions of all the previous cases.

#### **5.2.4 Site A 1280 Hz CW**

For this set, five pulses from an 8 second long CW, sampled in time at 50 Hz giving 0.02 seconds per sample were analyzed. For each, thirteen beams (numbered 41, 45, 49, 53, 57, 61, 65, 69, 73, 77, 81, 85, and 89 from the high frequency configuration of the array) were chosen for processing. Example figures for the data will be chosen from the broadside beam number 65 from the first pulse recorded on the first and fourth legs of the pentagon shaped experimental track. These data examples will contrast both Rayleigh and non-Rayleigh behavior in the same site. Examples of the beam intensity time series for these two legs are shown in *Figure 5-41*. The sections chosen for signal and noise are designated. Expanded images of just the signal portion are shown in *Figure 5-42*. Temporal correlation lengths (0.7 correlation) averaged under 0.10 sec. The data was processed at a sampling rate of every 10th point (0.30 sec/sample).

On processing, the average coefficient of variation was found to be 0.535, which is close to Rayleigh. The data sequences are shown in *Figure 5-43*. Note the vertical scale change, with leg four having smaller spikes. Runs tests for the data are shown in *Figure 5-44 a and b* over beam and time. Some temporal correlation is seen in the runs test over time at leg 1, which is not found in leg 4. The histograms of the signal fluctuations are shown in *Figure 5-45* and the probability of false alarm curves for the two legs are shown in *Figure 5-46*. The PFAs of all five legs are shown on *Figure 5-47*. These comparisons show two types of behavior at the same site and frequency. By contrast, the data in *Figure 5-9* were taken over the same sediment at 400 Hz, and all pulses had the same non-Rayleigh behavior. A tentative explanation for this finding is based on the Rayleigh-Rice theory of backscattering. This theory states that backscattering will be dominated by the resonant interaction between the incident acoustic field and the component of the surface roughness whose wavelength is half that of the acoustic wavelength (Bragg's Law of

monostotic first-order backscattering). Thus, one explanation might be that the sea floor and/or subsurface layers were composed of scattering patches that were sized at approximately 2 meters or larger, (roughly half the acoustic wavelength at 400 Hz), so as to resonate better with the 400 Hz signal than they did with the 1280 Hz signal. Additional research done by John Preston, Applied Research Laboratory, The Pennsylvania State University, found that a low scattering strength and a low bottom loss were required to match reverberation levels and slopes of the 400 Hz data. The values indicate a smooth, hard sediment, lending support to the idea of large scattering patches of chalky sediment layers. At higher frequencies, the sound would not penetrate as deeply into the sediment, and differences in sea floor roughness between the northern chalky sediment and the layered sediment of chalk, limestone, and sand to the south could cause the region to be anisotropic. This could explain why some legs of these 1280 Hz data were Rayleigh while others were not.

The noise section of the beam time series were processed. *Figure 5-48* shows the noise PFAs for all five pulses. The data appear to be Rayleigh, as was found in all previous cases.

### **5.3 Opopogo Experiment**

In June 1991, the SACLANT Centre conducted a reverberation experiment, referred to as Opopogo, in the shallow water off the Italian coast north of the island of Elba. The sources were 1-kg explosives detonated at a depth of 60 meters (m). The receiver was a 64 hydrophone array, towed at a nominal depth of 60 m behind the Centre's research vessel ALLIANCE. For the analysis presented here, four shots at relatively close source-receiver separations (5.5 to 10.5 km) were selected. The bottom was gently sloping to the west of depth approximately 100-150 m.

There were no major scattering features in this region. There was a trench to the west, but no scattering from the up-slope is contained in the data. A number of cores were available from previous experiments, which indicated that the bottom is primarily clay, mixed with some sand and silt. The sound speed profile was a typical shallow water summer profile, downward refracting with a strong thermocline between 40 and 50 m on the day of the experiment. On both days of the experiment, the surface reverberation is considered to be negligible due to the relatively calm sea surface, the downward-refracting sound speed profile and the source and receiver being below the thermocline. The importance of volume reverberation from biologics is not known. The ambient noise is high because this was a busy shipping area, and at long times after the direct blast arrival, several of the beams were contaminated by the noise from nearby ships and boats. These beams were not included in the analysis. Time series from explosive shots 5, 8, 10, and 19 were selected for analysis. The data were taken from the near-broadside beams in the 10 seconds immediately following the direct blast arrival. The total two-way propagation paths therefore range from 6.5 kilometer to 18 kilometer.

The data that were obtained had already received some processing from the Centre, and represented a one third octave band average of the raw reverberation levels. Time series were obtained for three center frequencies in Hertz: 316, 398, and 630. Because this averaging effectively smoothes the data, the fluctuations observed in both signal and noise portions of the time series were considerably less than Rayleigh. However, the signal portion of the return was always more variable than the noise portion. In order to compare these results to those obtained from the Celtic Duet experiment, the data was processed as before. *Figure 5-49* displays a typical time series. For the signal portion, 10 seconds of data was chosen from near the beginning of the return just after the direct blast to avoid the large deterministic features coming from the

surrounding islands and basin walls. Because the sediment reverberation lasted so long, unambiguous noise samples could only be obtained by using the section of the beam time series recorded before the shot was fired. PFA curves were obtained for both signal and noise and examples are as shown in *Figure 5-50*. Then, to mitigate the effect of the smoothing from band averaging, the data was re-mapped or re-normalized by taking the difference between the measured signal and the measured noise PFA and adding that to a theoretical Rayleigh PFA curve. The assumption is that the noise would have been Rayleigh before it was smoothed, and that the difference between signal and noise would scale to the same relative difference in the unsmoothed data (this assumption was verified by applying a box car average to the Celtic Duet data). This translation and re-normalization produced curves that were very similar to those from the Celtic Duet data. The resulting re-normalized PFAs are shown in *Figure 5-51* for 630 Hz and 398 Hz.

#### 5.4 Summary

Time series were analyzed from the Celtic Duet experiment and a comparison of the results were made for 8 second CW pulses and 2.4 second HFM pulses at Site A; 8 second CW pulses at both Site A and Site C; and 8 second CW pulses transmitted at both 400 Hz and 1280 Hz at Site A. The comparison of the CW pulses and HFM pulses at Site A showed that the CW fluctuation sequence was very periodic in contrast to the more random sequence of the HFM; however, both pulse types produced the same non-Rayleigh PFAs. Therefore, pulse type is not a factor that affects the fluctuation statistics. The comparison of the CW pulses at both Site A and Site C showed that the CW fluctuation sequences in both cases were similarly periodic; however, Site A produced non-Rayleigh PFAs while Site C produced Rayleigh PFAs. It is postulated that

the high wind speed at Site C added enough randomness to produce Rayleigh statistics. The comparison of the CW pulses transmitted at both 400 Hz and 1280 Hz at Site A showed that at 400 Hz the PFAs were all non-Rayleigh while at 1280 Hz some pulses were Rayleigh and others were non-Rayleigh. One explanation was that the sea floor was composed of scattering patches sized at approximately 2 meters so as to resonate better with the 400 Hz signal than with the 1280 Hz signal and therefore, cause a few scatterers to dominate the reverberation time series. Another explanation was that at higher frequencies, the sound did not penetrate as deeply into the sediment, and differences in sea floor roughness between the northern chalky sediment and the layered sediment to the south caused the region to be anisotropic possibly explaining why some legs of these 1280 Hz data were Rayleigh while others were not Rayleigh.

Time series were analyzed from the Ogopogo experiment; however, the data had been previously averaged into one third octave bands. An assumption was made that the noise would have been Rayleigh before it was smoothed. The data was re-mapped by taking the difference between the measured signal and the measured noise PFA and adding that to a theoretical Rayleigh PFA curve. This translation produced non-Rayleigh results for the soft clay sediments very similar to those from the Celtic Duet chalky sediments. Therefore, sediment type alone is not enough to cause non-Rayleigh fluctuation statistics.

One final point to be made from the processing of the data is that time correlation among sample points in the fluctuation sequence does not affect the statistics. Sparsely sampling the data to remove any temporal correlation in the sequence does not change the resulting statistics.

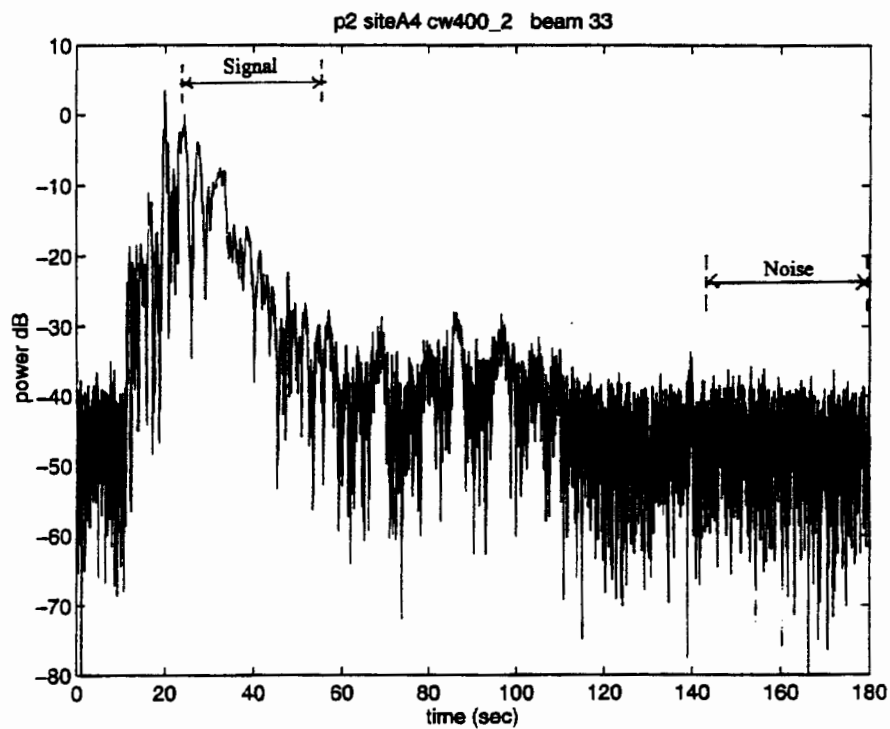


Figure 5-1: Representative reverberation 400 Hz CW from Site A of Celtic Duet, a chalk, limestone, and sand bottom. Portions of the recordings used to compute statistics are shown. Time was subsampled, using every 20th point only.

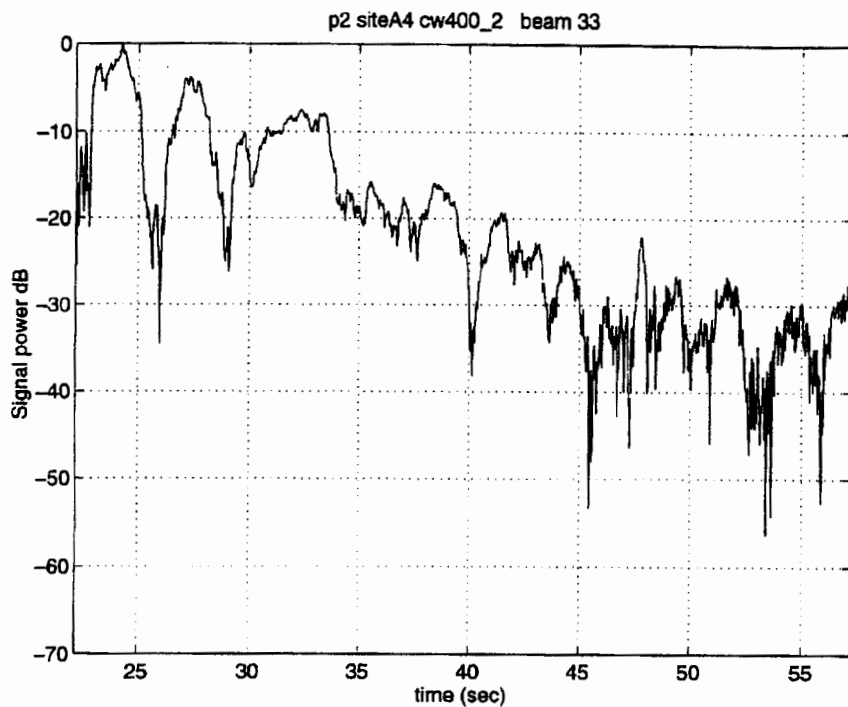


Figure 5-2: Signal portion of the Site A 400 Hz CW reverberation time series in Figure 5-1.

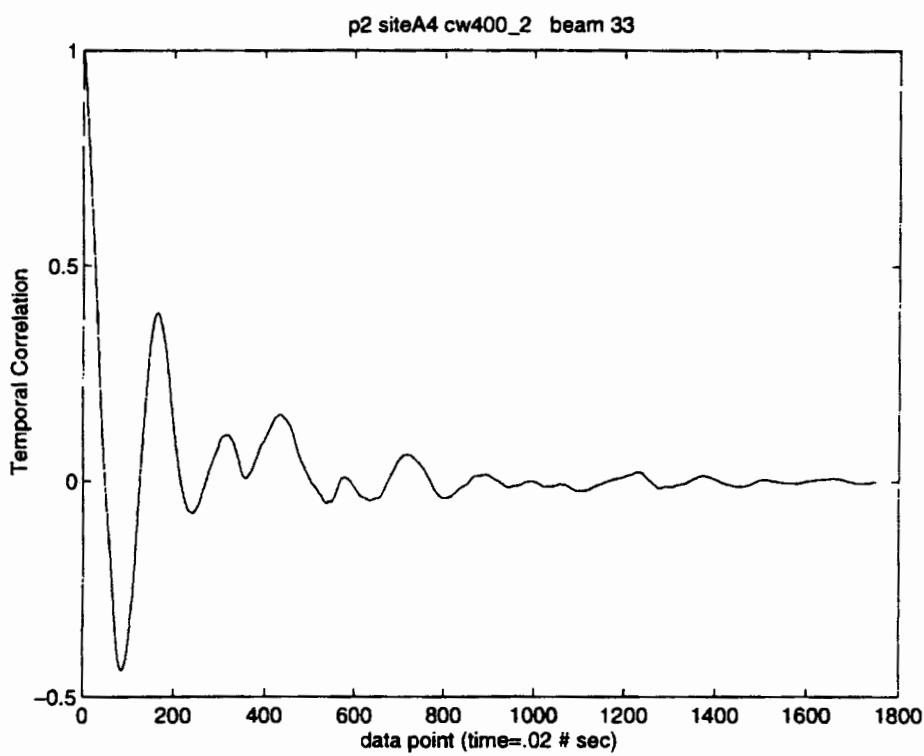


Figure 5-3: Representative reverberation temporal correlation on Beam 33, signal portion from 22 to 57 sec for Site A 400 Hz CW. Correlation lengths to 0.7 average 20 points (0.4 sec.)

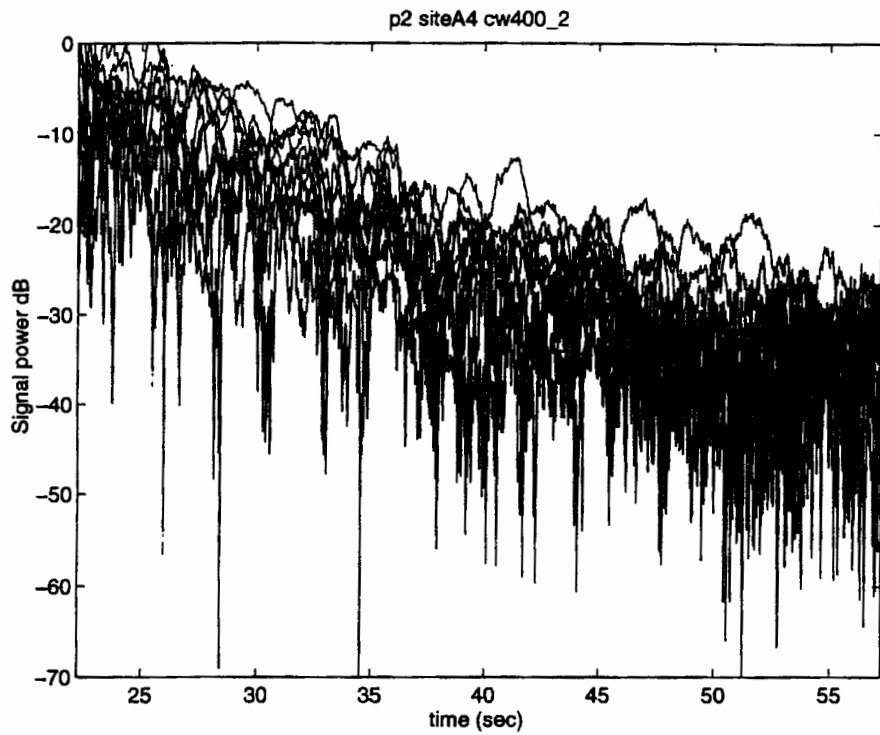


Figure 5-4: Overlay of all signal sections from all 13 beams, Site A 400 Hz CW.

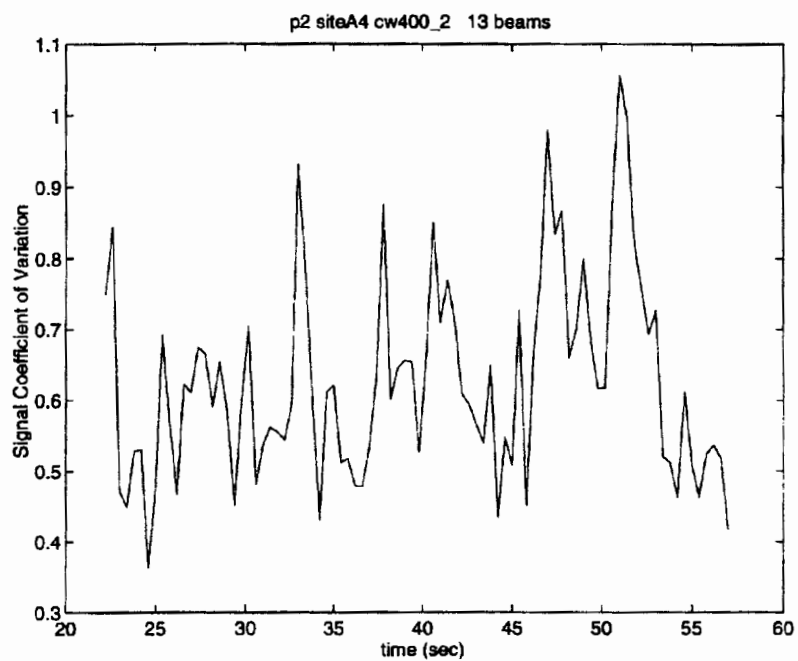


Figure 5-5: Coefficient of variation of 13 beams versus time in signal portion of Site A 400 Hz CW data set.

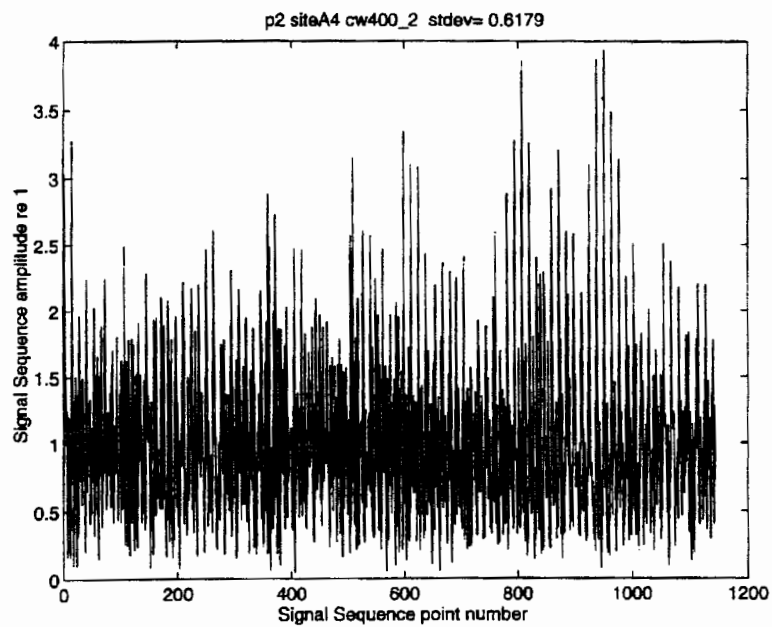


Figure 5-6: Signal sequence Site A 400 Hz CW normalized to unity mean. Note that the spikes appear to be periodic. This appearance is caused by the long pulses which give long lasting peaks in Figure 5-4, so that even sampling every 20th point, these peaks remain for 3 to 4 samples and show up as rhythmic spikes in the appended sequence.

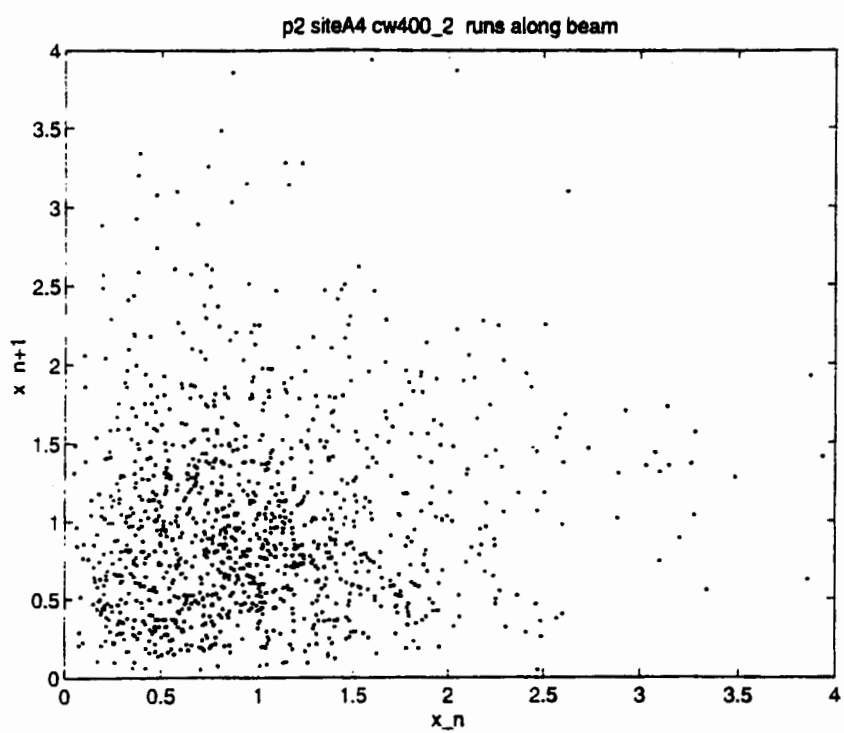


Figure 5-7a: Runs test over beam, Site A 400 Hz CW, plotting the  $n$ th point in the sequence in Figure 5-6 versus the  $n + 1$ th point for all points in the sequence.

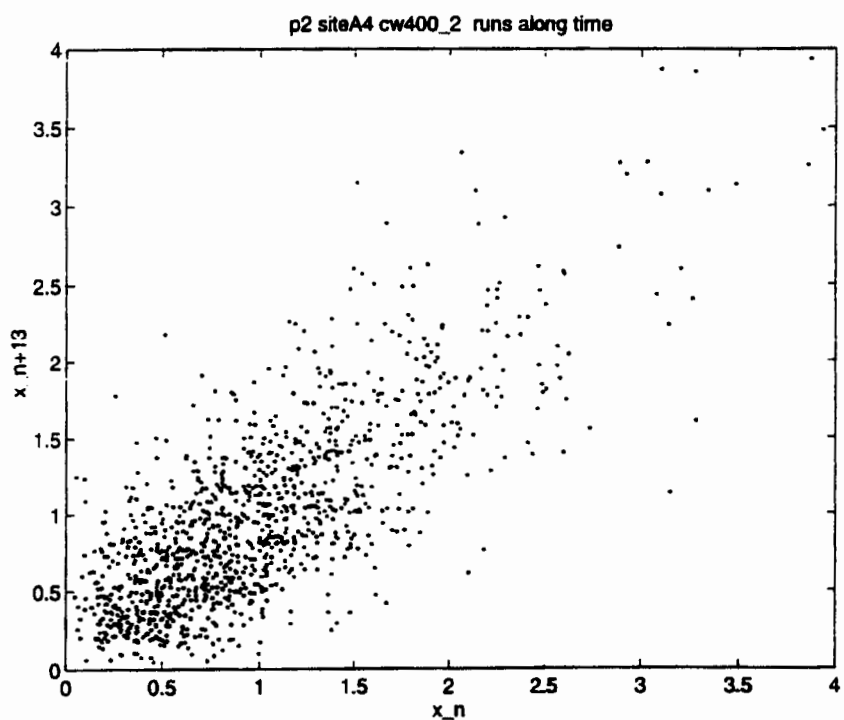


Figure 5-7b: Runs test over time, Site A 400 Hz CW, plotting the  $n$ th point versus the  $n + 13$ th point. The structure shows a diagonal distribution rather than a random one, indicating that the sequence contains temporal correlation.

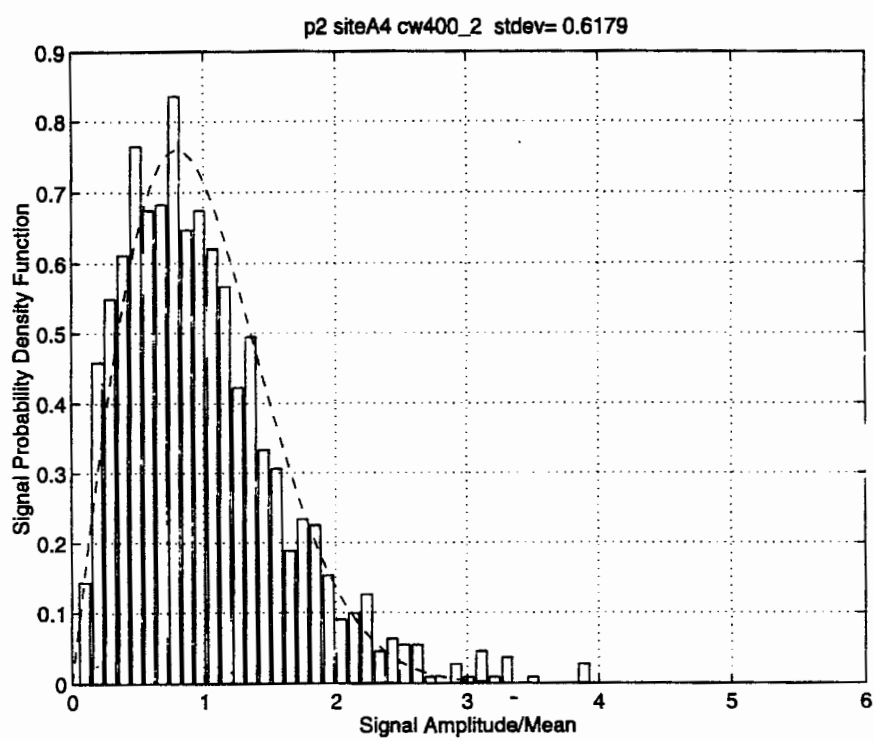


Figure 5-8: Histogram of fluctuations in signal sequence in Figure 5-6 versus signal amplitude above the mean, Site A 400 Hz CW. Standard deviation is 0.618.

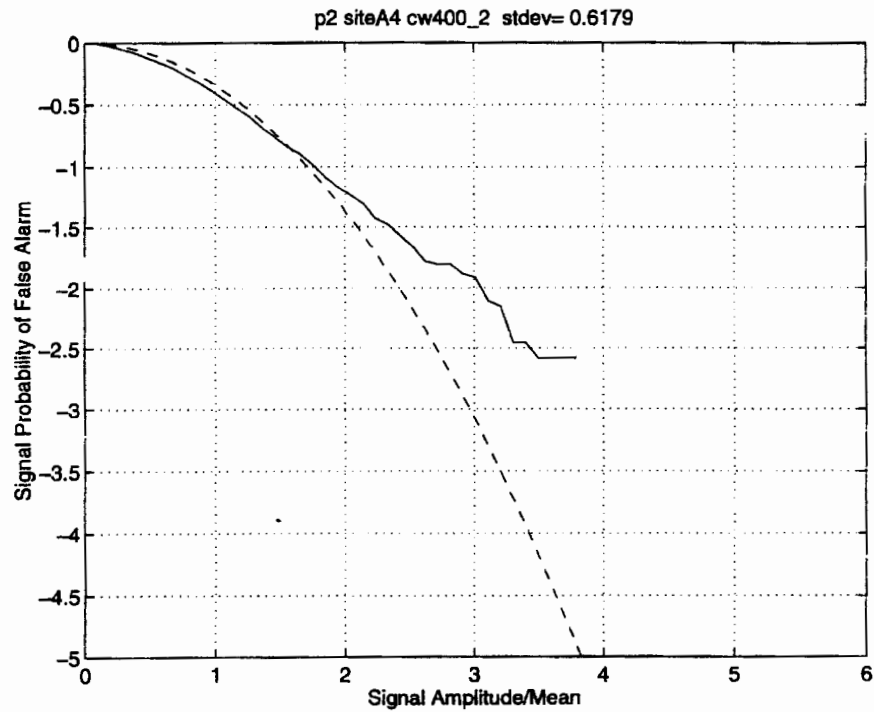


Figure 5-9: Log probability of false alarm versus signal amplitude, Site A 400 Hz CW.

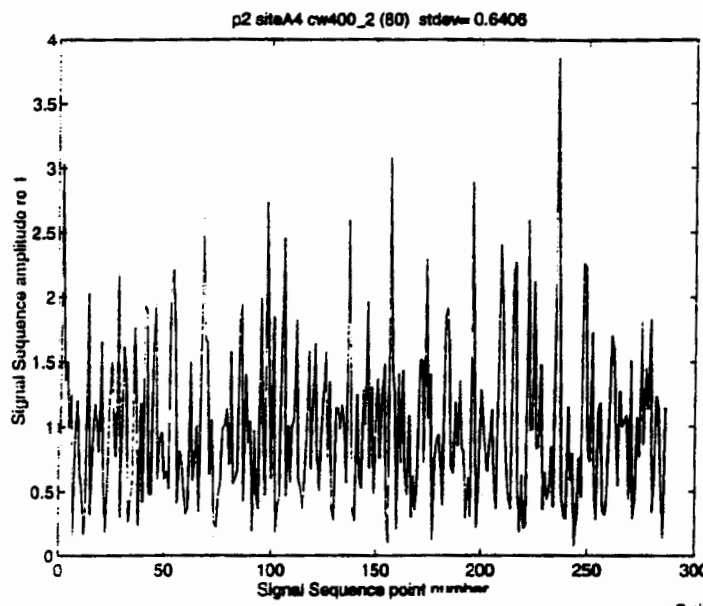


Figure 5-10a: Same as Figure 5-6 except the signal is sparsely sampled every 80th point.

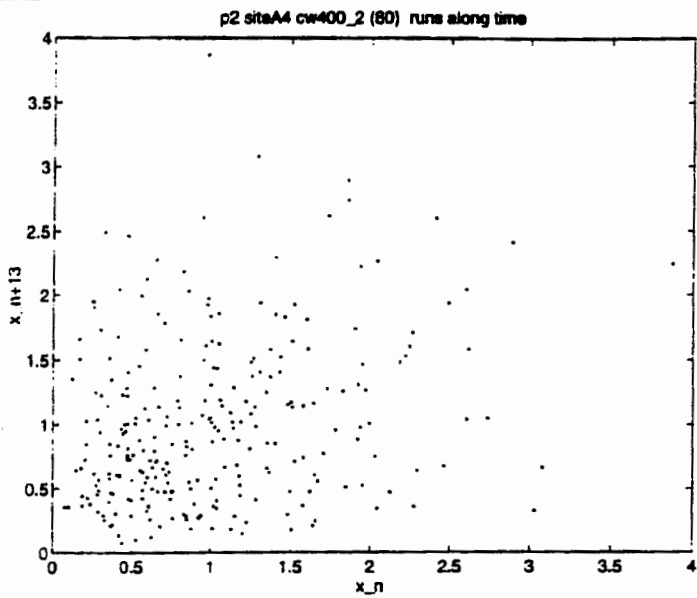


Figure 5-10b: Same as Figure 5-7b except the signal is sparsely sampled every 80th point.

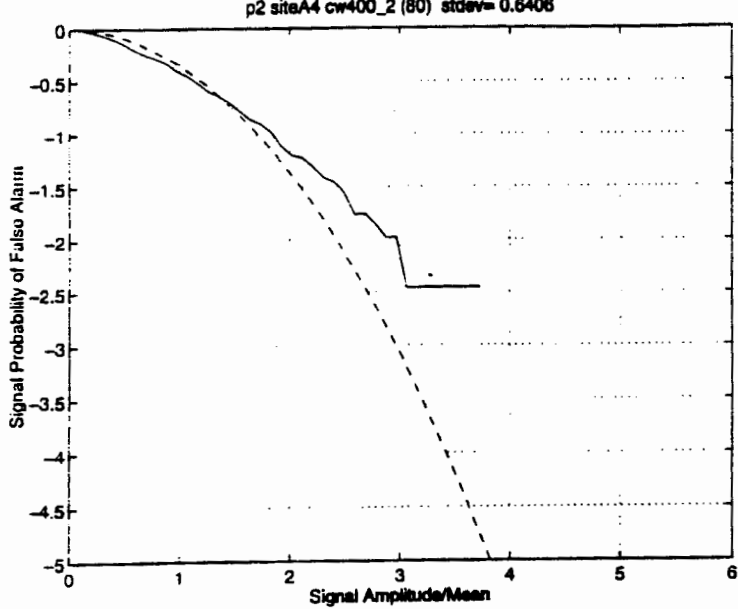


Figure 5-10c: Same as Figure 5-9 except the signal is sparsely sampled every 80th point.

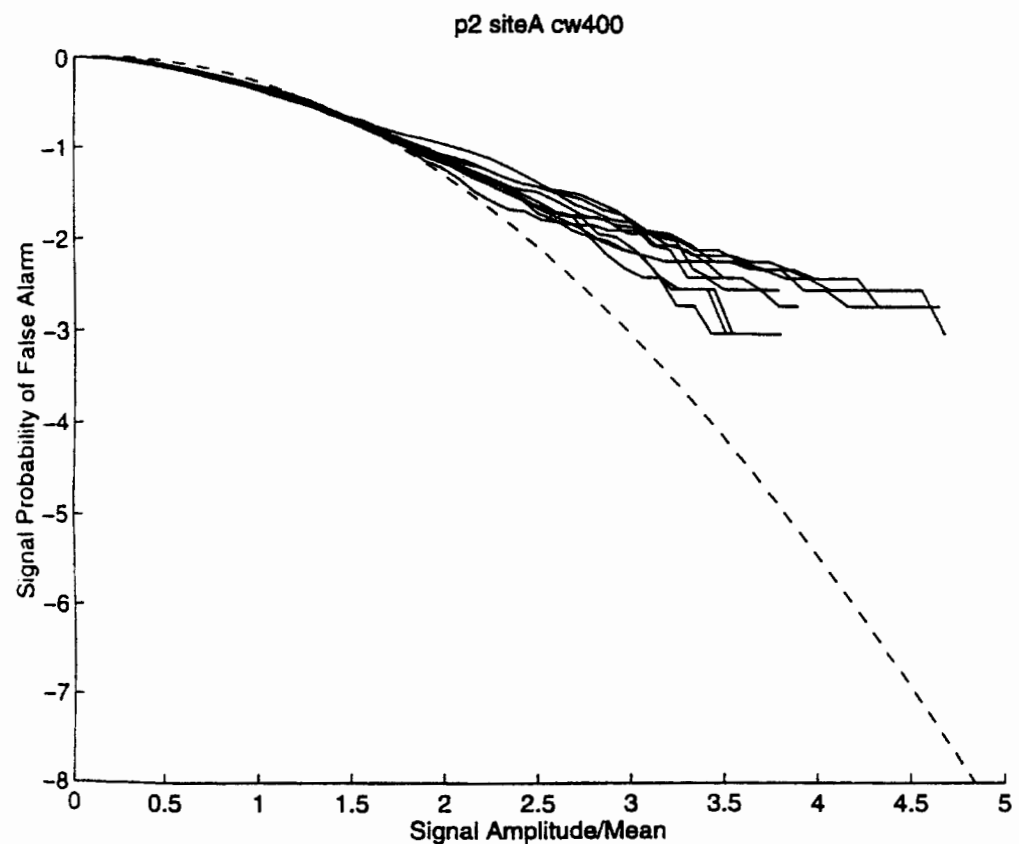


Figure 5-11: Log PFA for 2 pulses each from 5 legs from Site A 400 Hz CW.

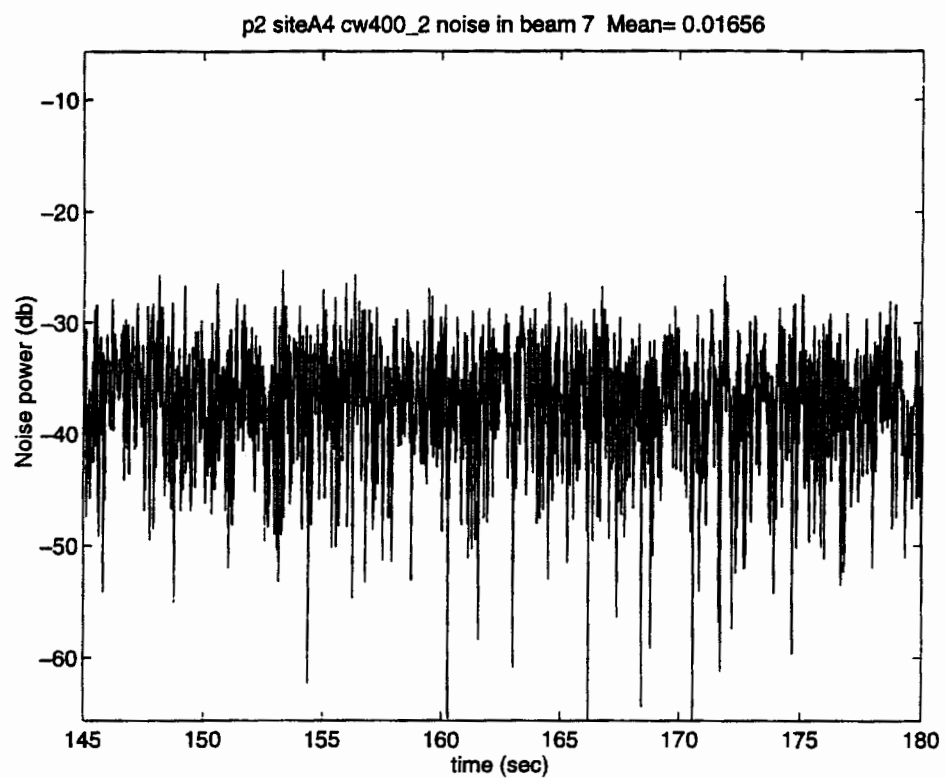


Figure 5-12: Expanded plot of noise section from Figure 5-1, Site A 400 Hz CW, Beam 33.

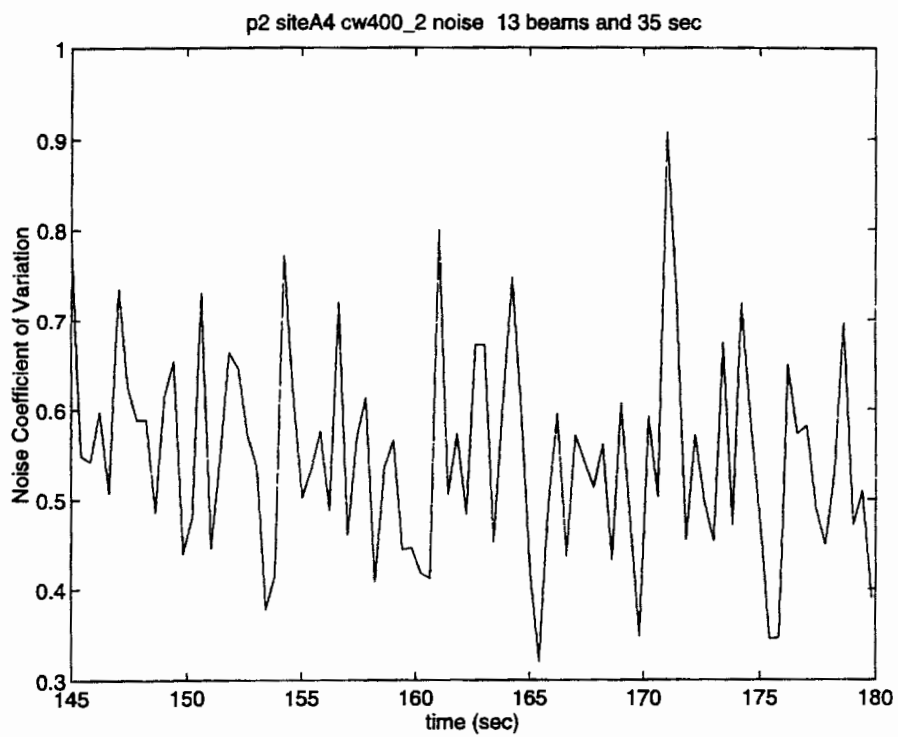


Figure 5-13: Noise coefficient of variation versus time, Site A 400 Hz CW, averages taken across 13 beams.

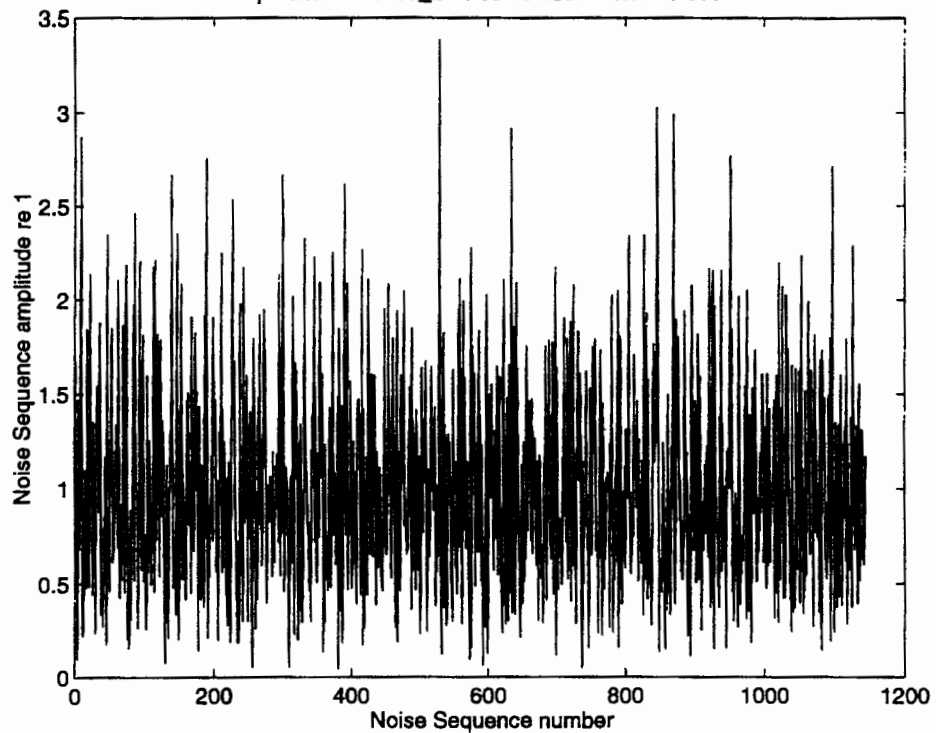


Figure 5-14: Noise sequence after normalizing to unity among all beams at each time point, Site A 400 Hz CW.

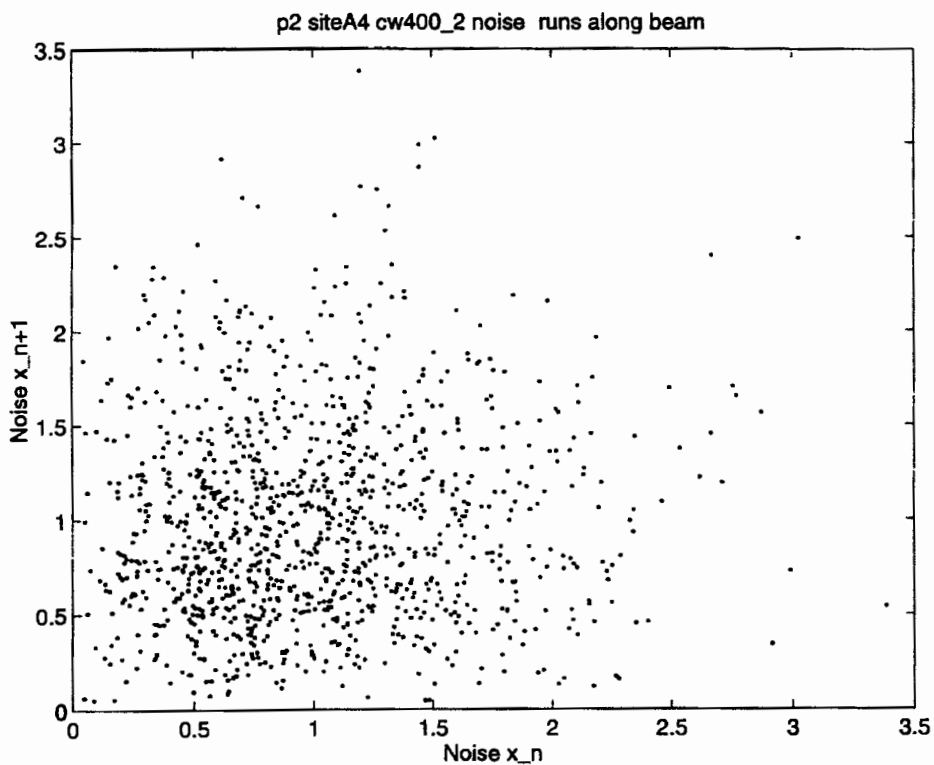


Figure 5-15: Noise runs tests for adjacent points  $n$  and  $n + 1$ , equivalent to beam-to-beam correlations, Site A 400 Hz CW.

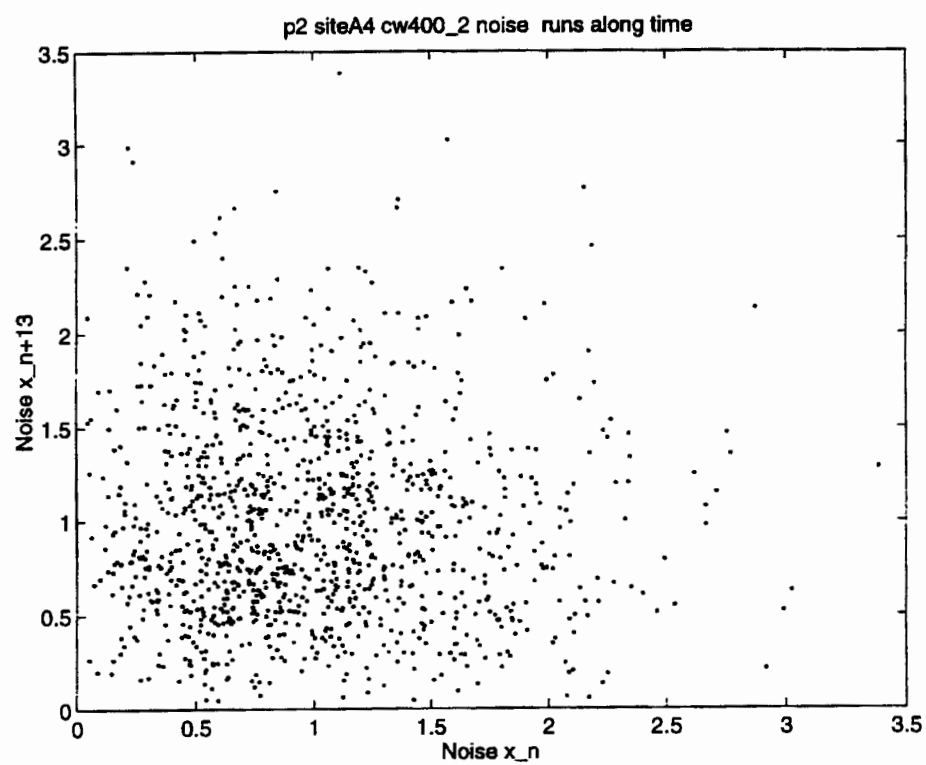


Figure 5-16: Noise runs test for every 13th point, equivalent to temporal correlation, Site A 400 Hz CW.

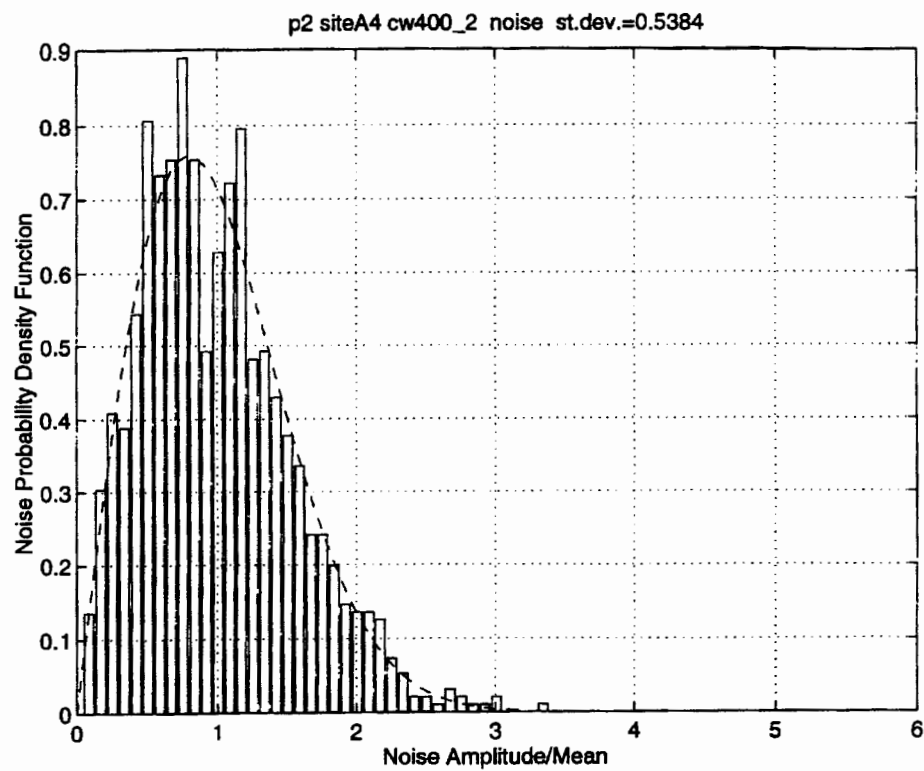


Figure 5-17: Noise histogram of sequence in Figure 5-14, Site A 400 Hz CW.

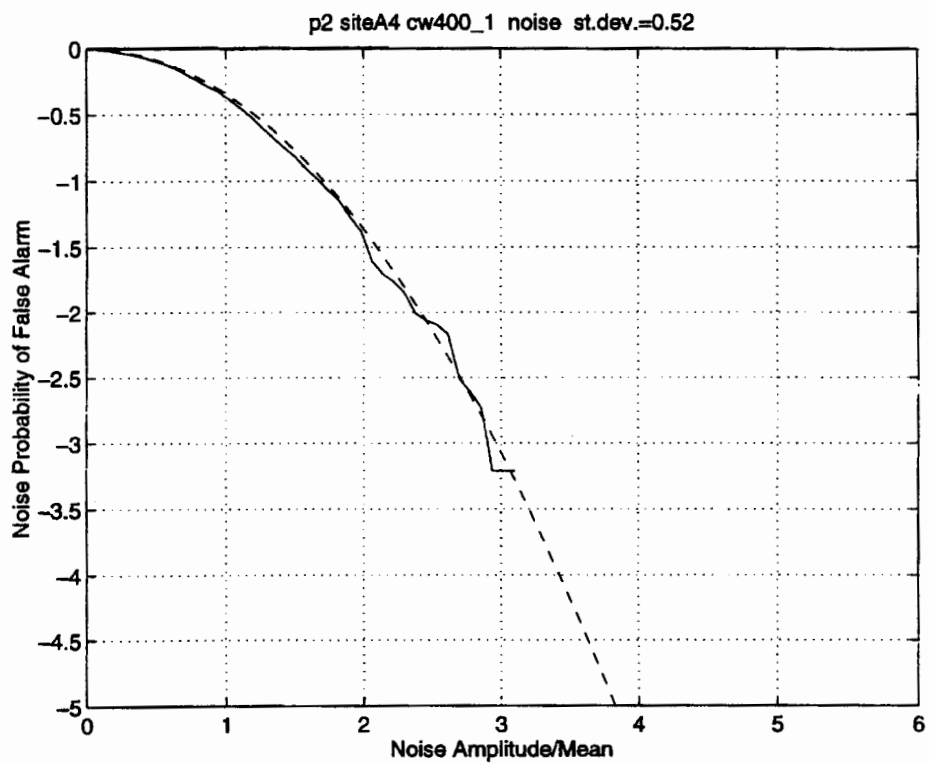


Figure 5-18: Noise log PFA from Figure 5-17, Site A 400 Hz CW.

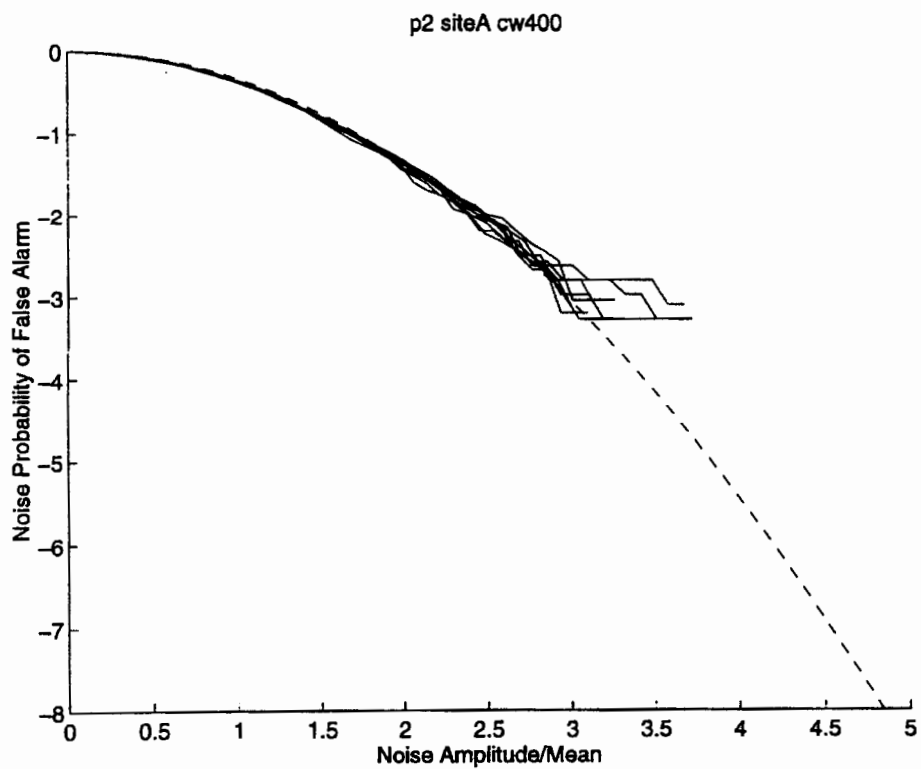


Figure 5-19: Noise log for 10 pulses at Site A 400 Hz CW.

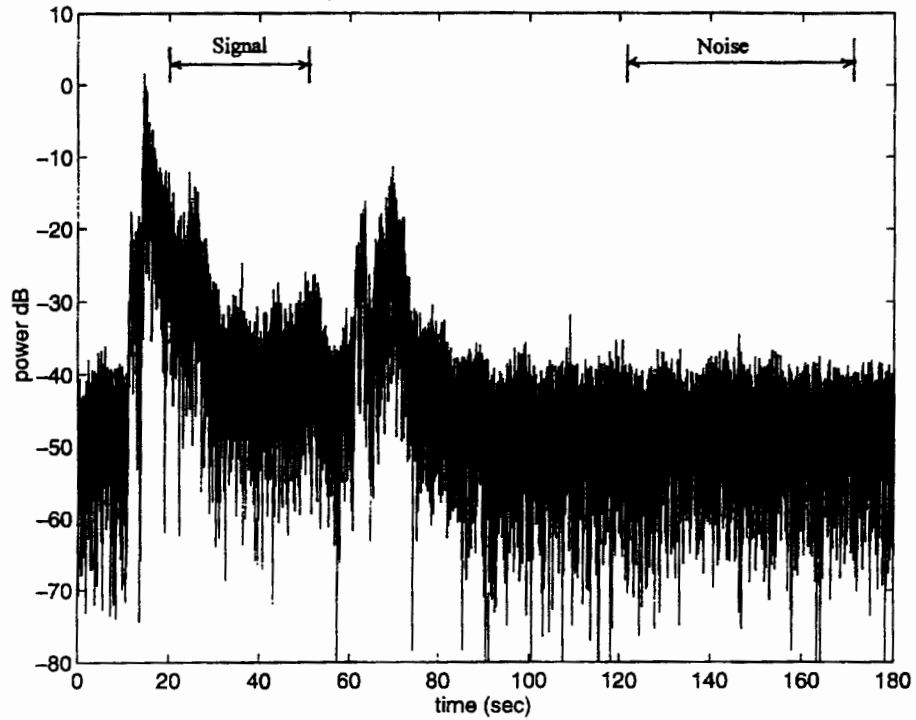


Figure 5-20: Beam #33 intensity time series centered at 395 Hz for an hyperbolic FM pulse (HFM) from Site A. Signal and noise portions are marked.

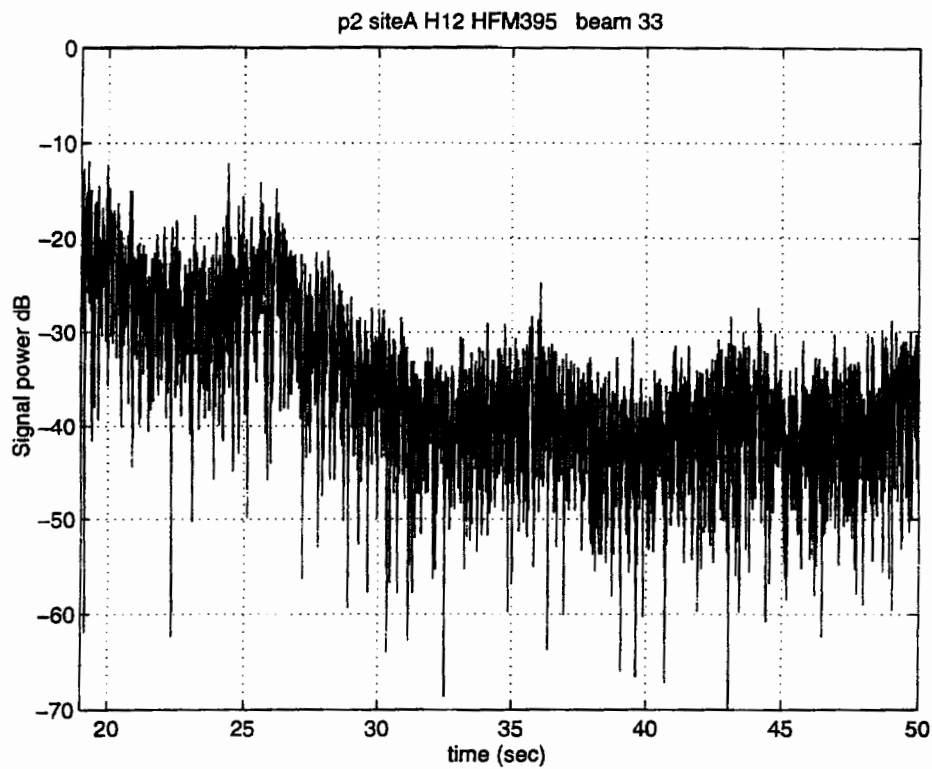


Figure 5-21: Signal portion of the Site A 395 Hz HFM time series in Figure 5-20.

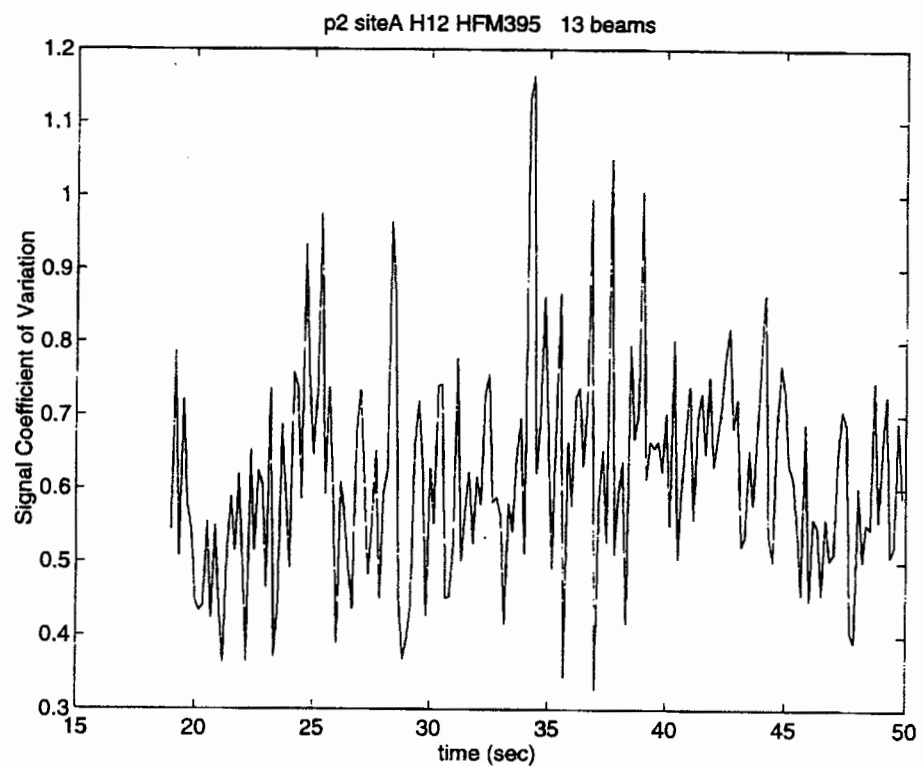


Figure 5-22: Coefficient of variation of 13 beams from Site A 395 Hz HFM time series sampled every 5th point (0.1 sec).

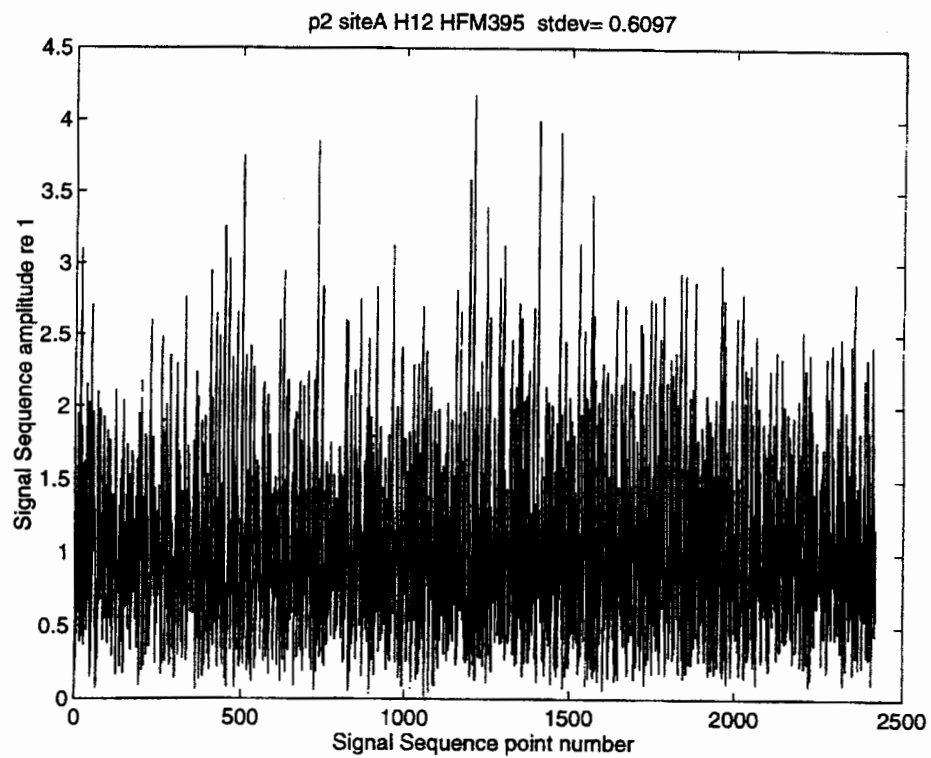


Figure 5-23: Signal sequence for Site A 395 Hz HFM to compare with Figure 5-6.

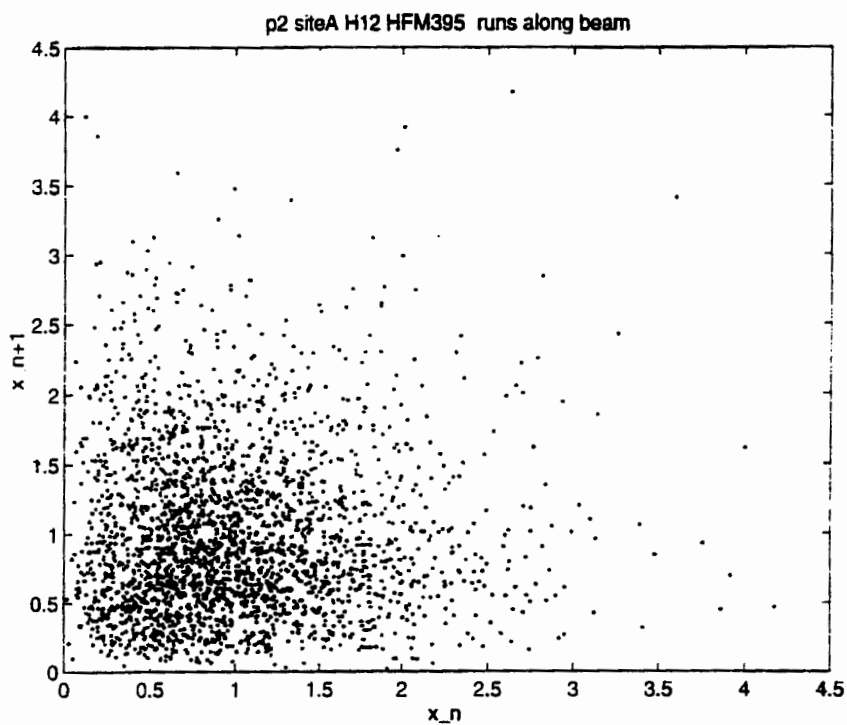


Figure 5-24a: Runs test over beam for Site A 395 Hz HFM, to compare with Figure 5-7a.

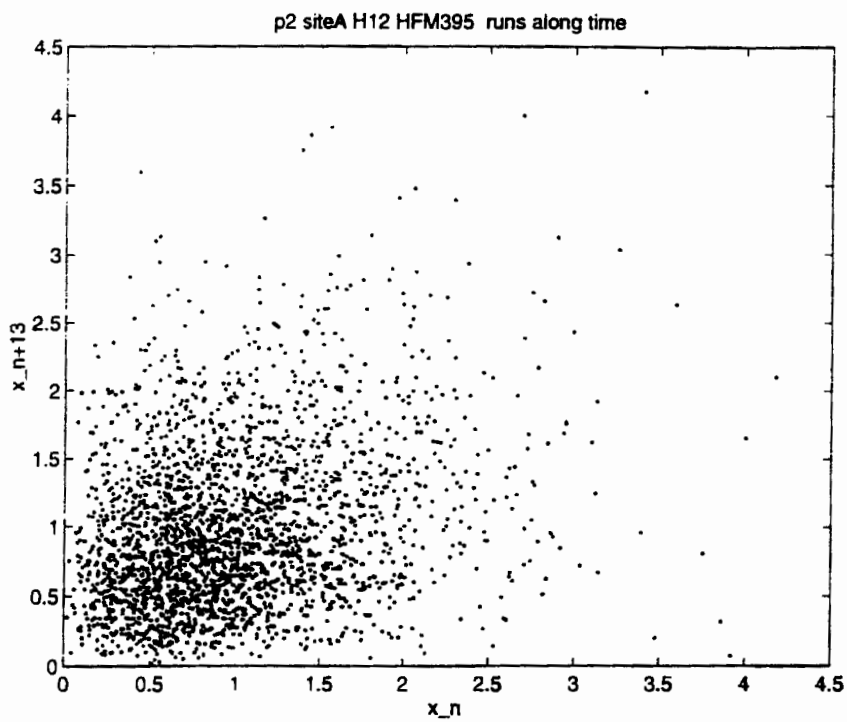


Figure 5-24b: Runs test over time for Site A 395 Hz HFM to compare with Figure 5-7b.

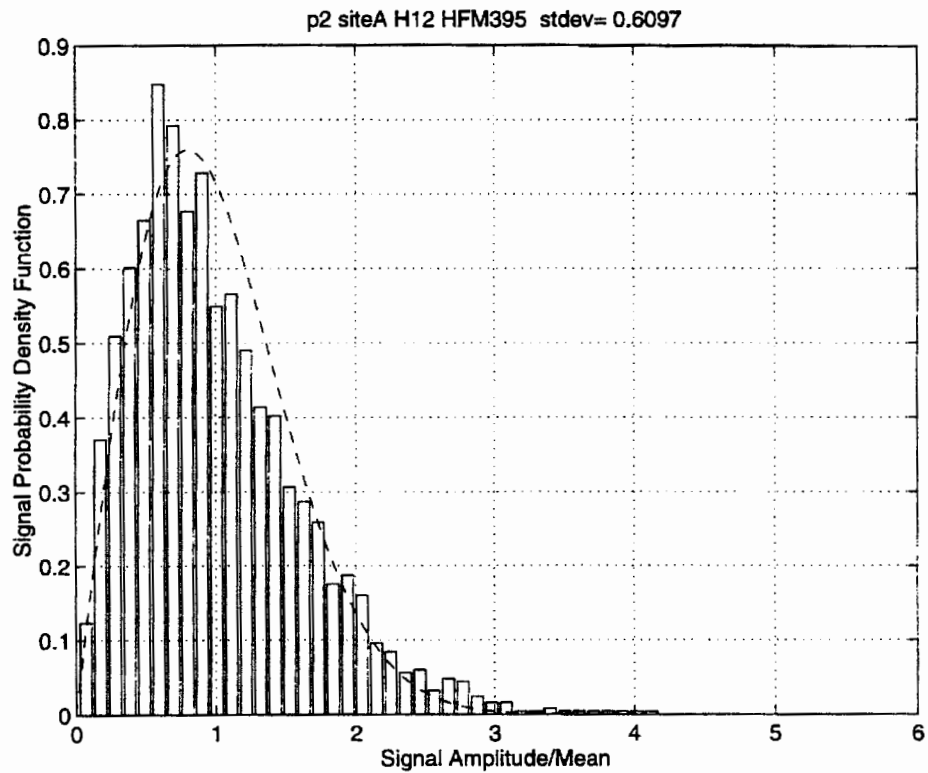


Figure 5-25: Signal fluctuation histogram, Site A 395 Hz HFM.

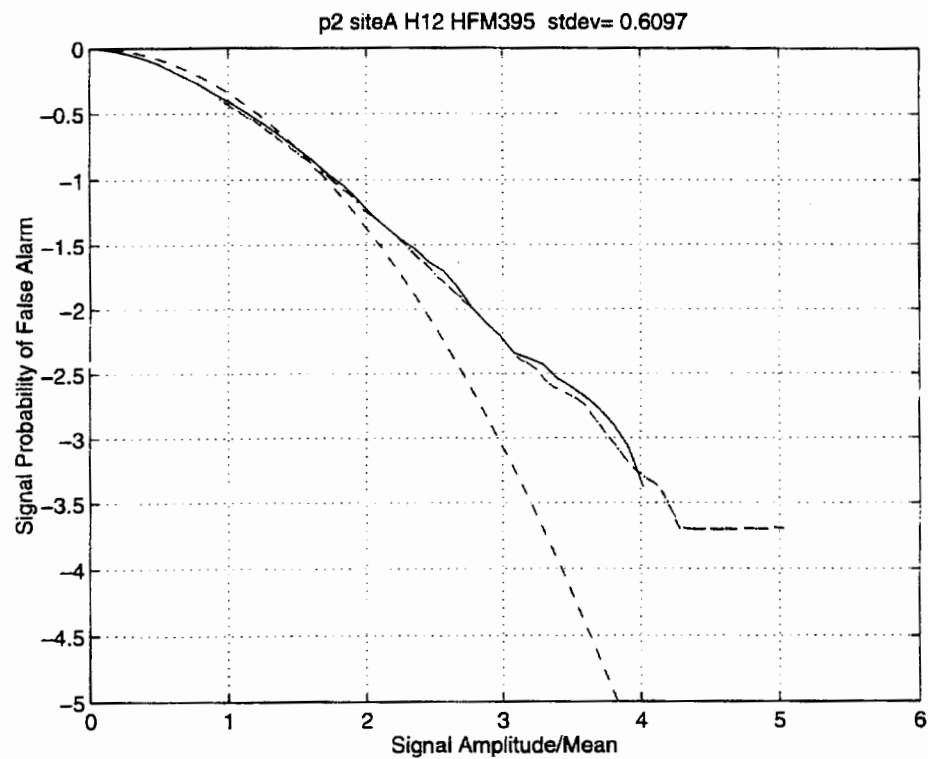


Figure 5-26: Signal log PFA, Site A 395 Hz HFM, for two sampling intervals, 0.4 seconds/sample (solid line) and 0.1 seconds/sample (dashed-dot line).

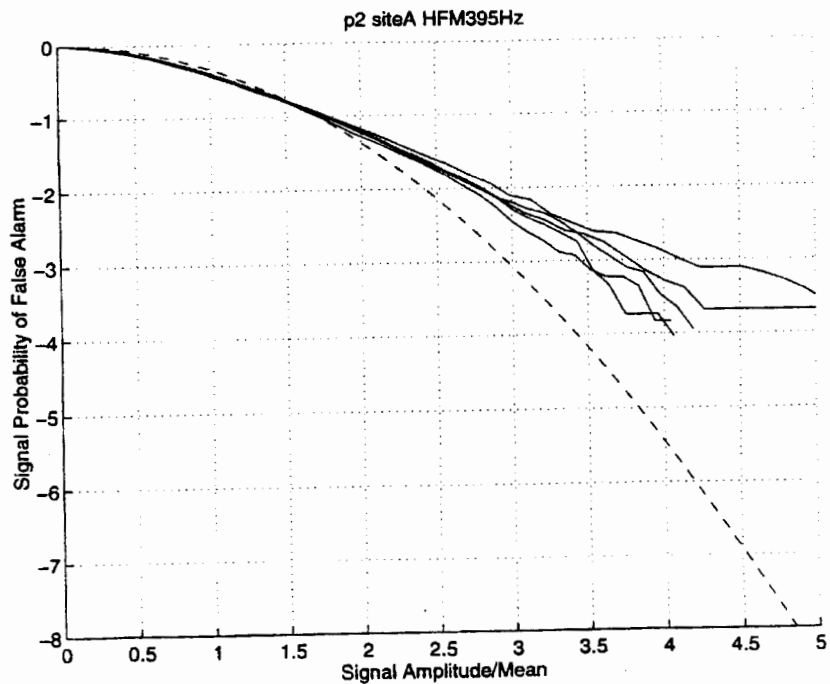


Figure 5-27: Signal log PFA for pulses from 5 legs at 0.1 seconds/sample, Site A 395 Hz HFM.

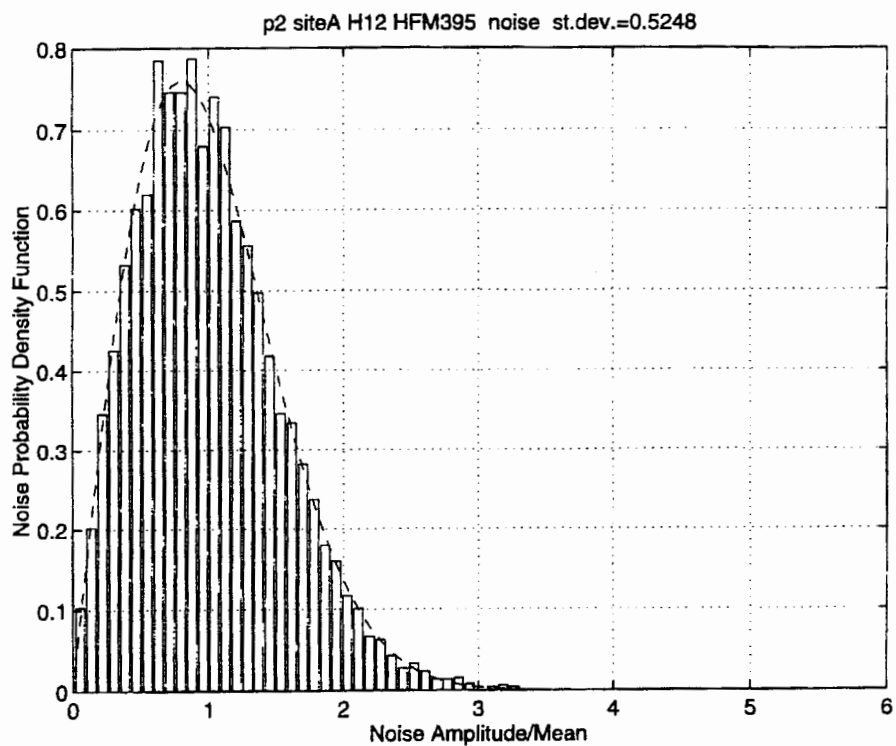


Figure 5-28: Noise histogram of fluctuations, Site A 395 Hz HFM.

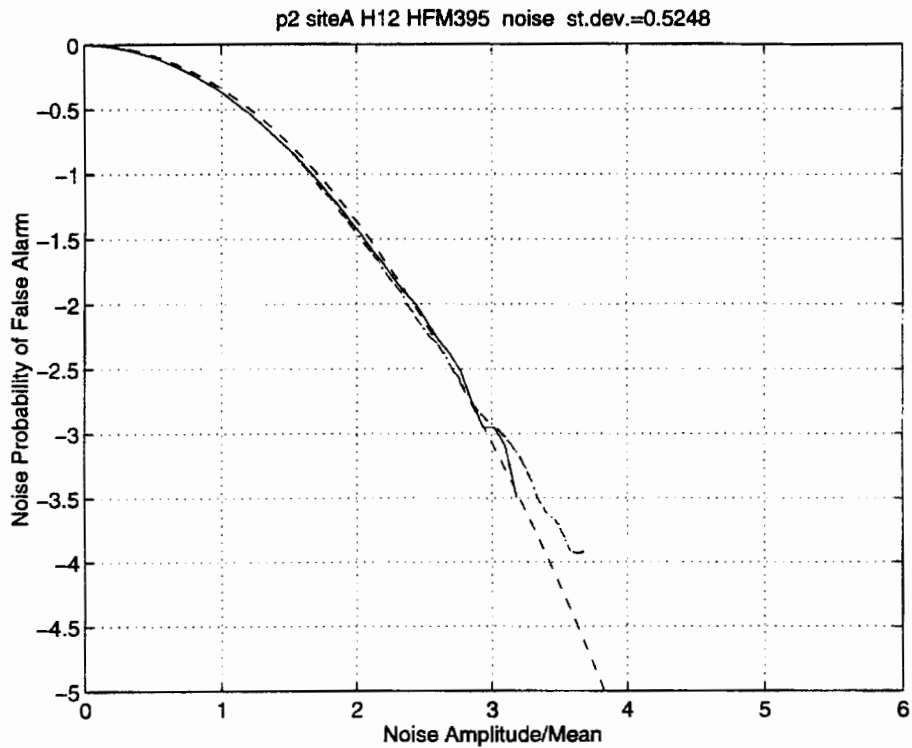


Figure 5-29: Noise log PFA, Site A 395 Hz HFM (solid line = 0.4 seconds/sample, dashed line = 0.1 seconds/sample).

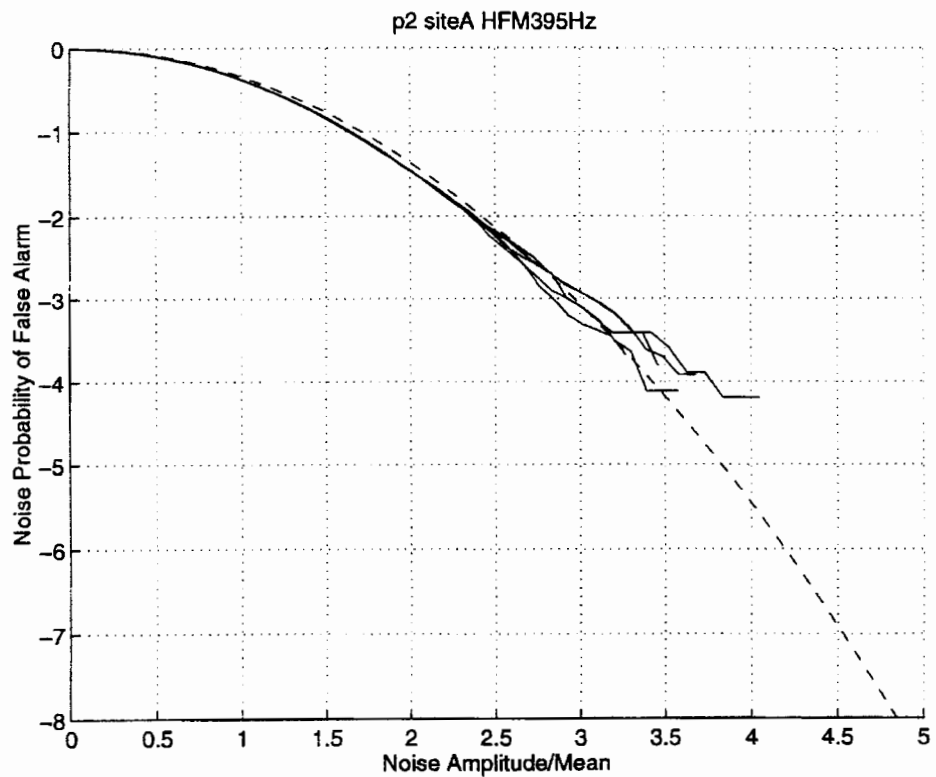


Figure 5-30: Noise log PFA, Site A 395 Hz HFM, from 5 pulses sampled at 0.1 seconds/sample.

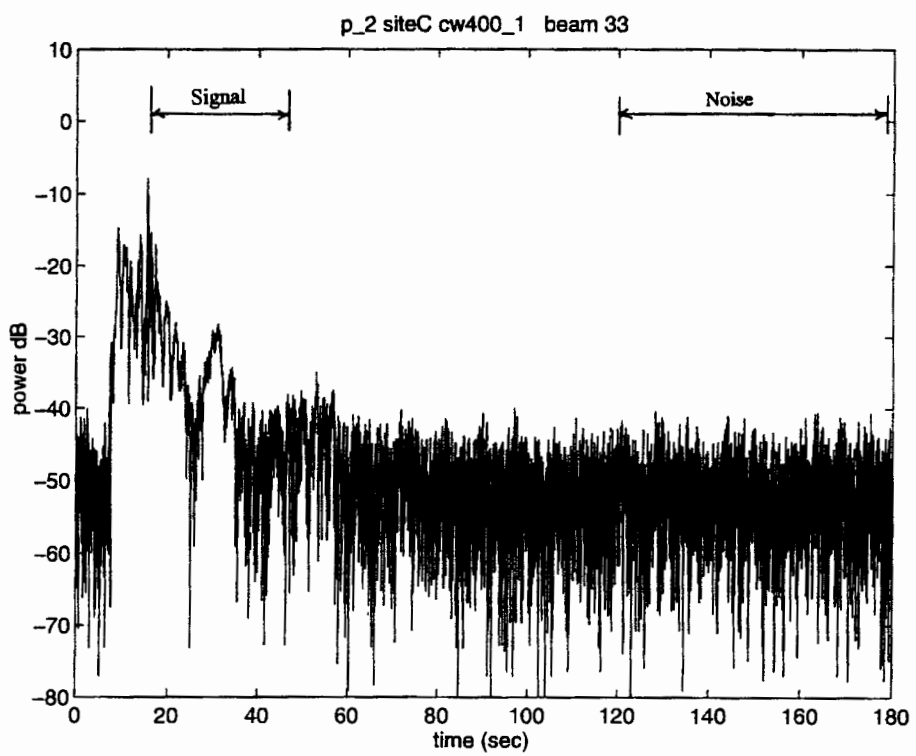


Figure 5-31: Beam #33 intensity time series, Site C 400 Hz CW

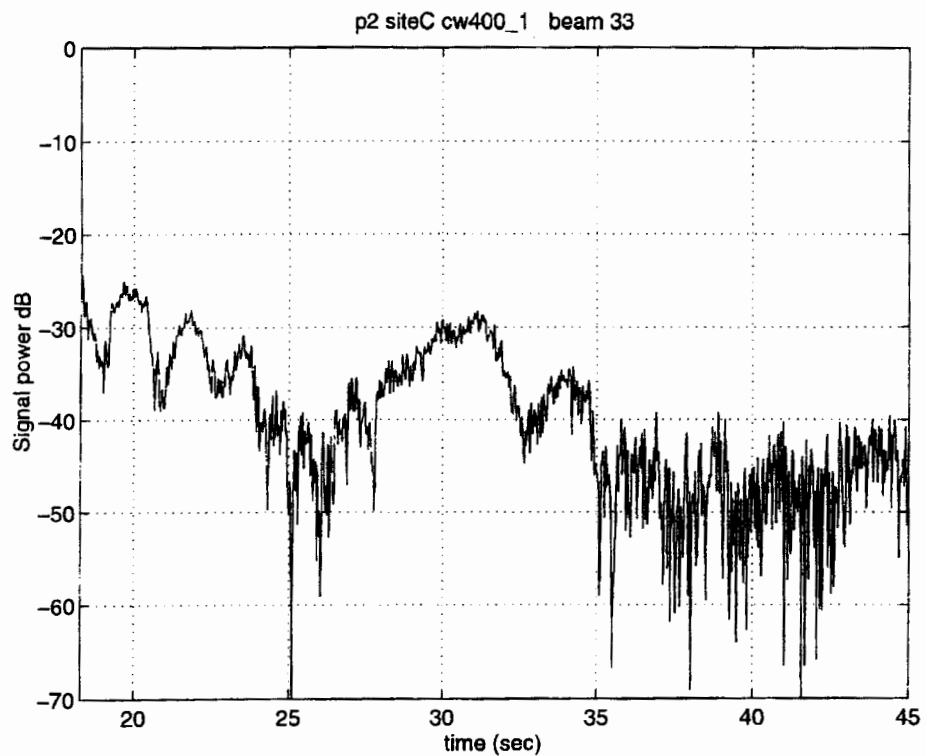


Figure 5-32: Signal portion of the Site C 400 CW time series in Figure 5-31.

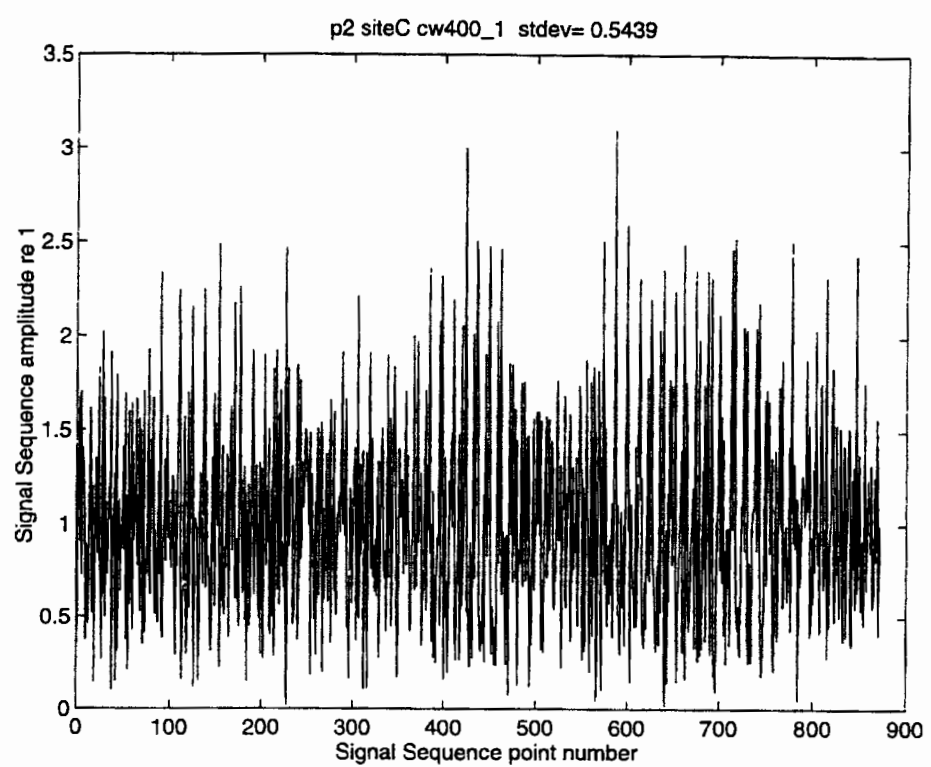


Figure 5-33: Signal sequence, Site C 400 Hz CW to compare with Figure 5-6.

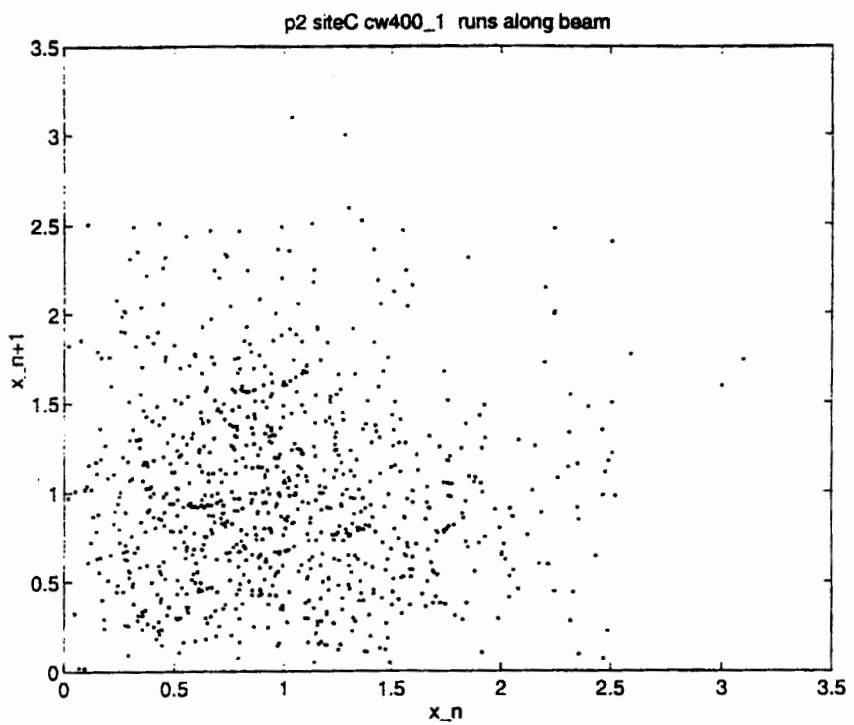


Figure 5-34a: Runs test over beam, Site C 400 Hz CW.

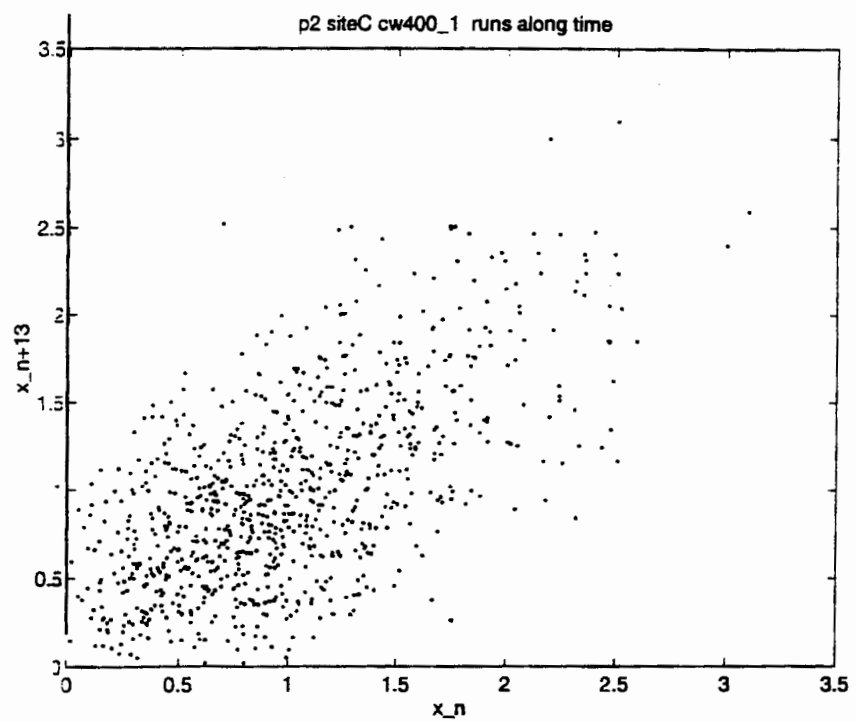


Figure 5-34b: Runs test over time, Site C 400 Hz CW.

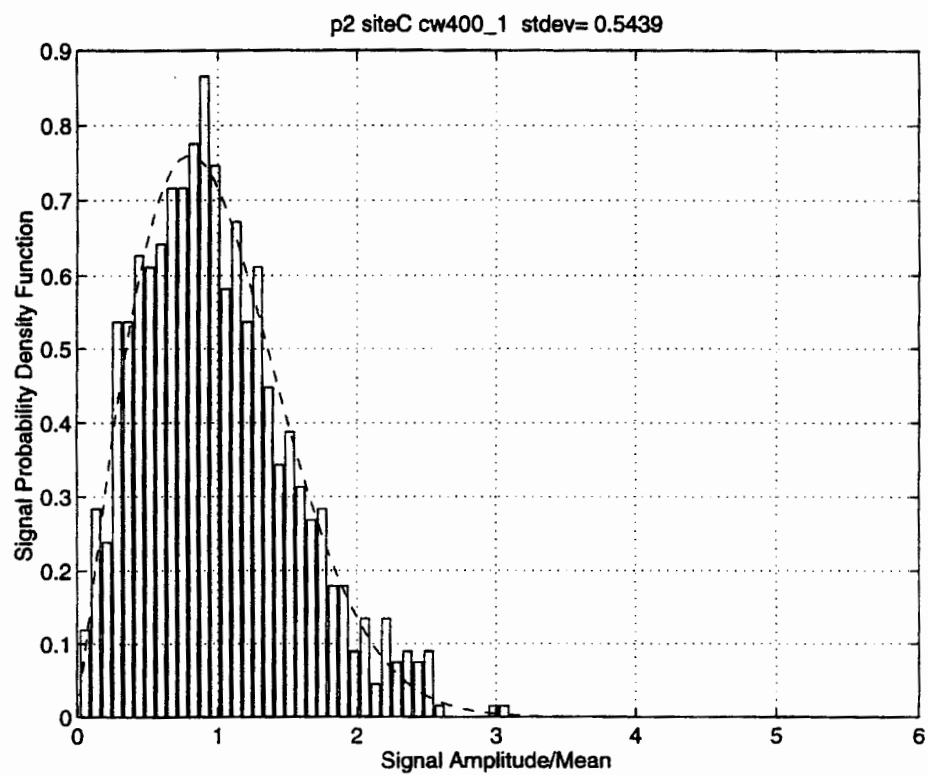


Figure 5-35: Histogram of fluctuations, Site C 400 Hz CW.

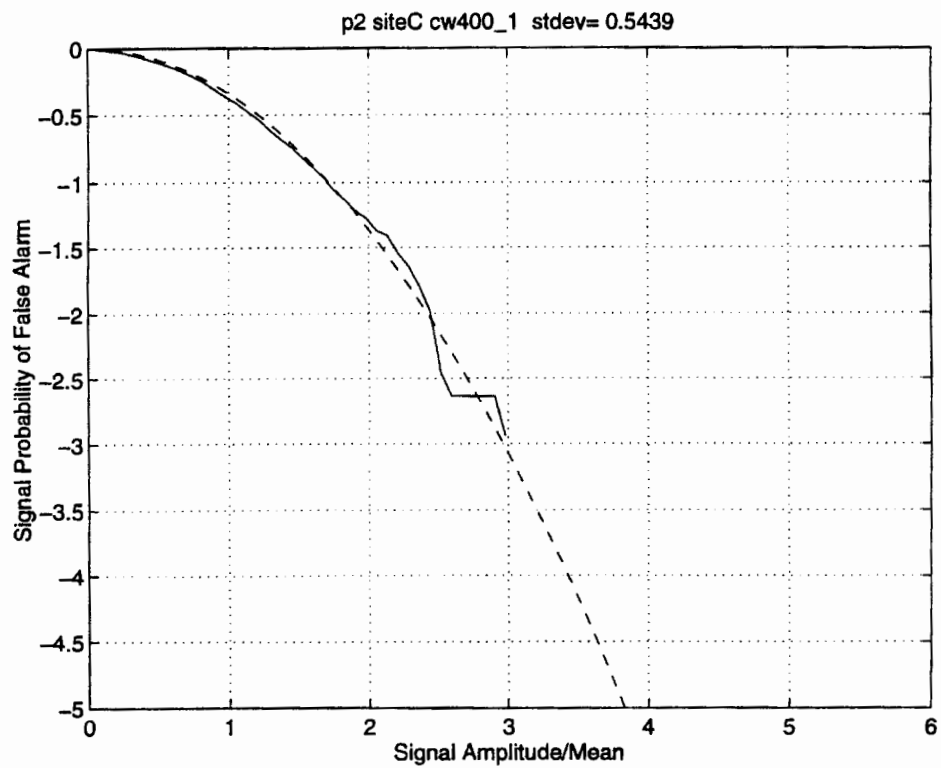


Figure 5-36: Signal log PFA, Site C 400 Hz CW.

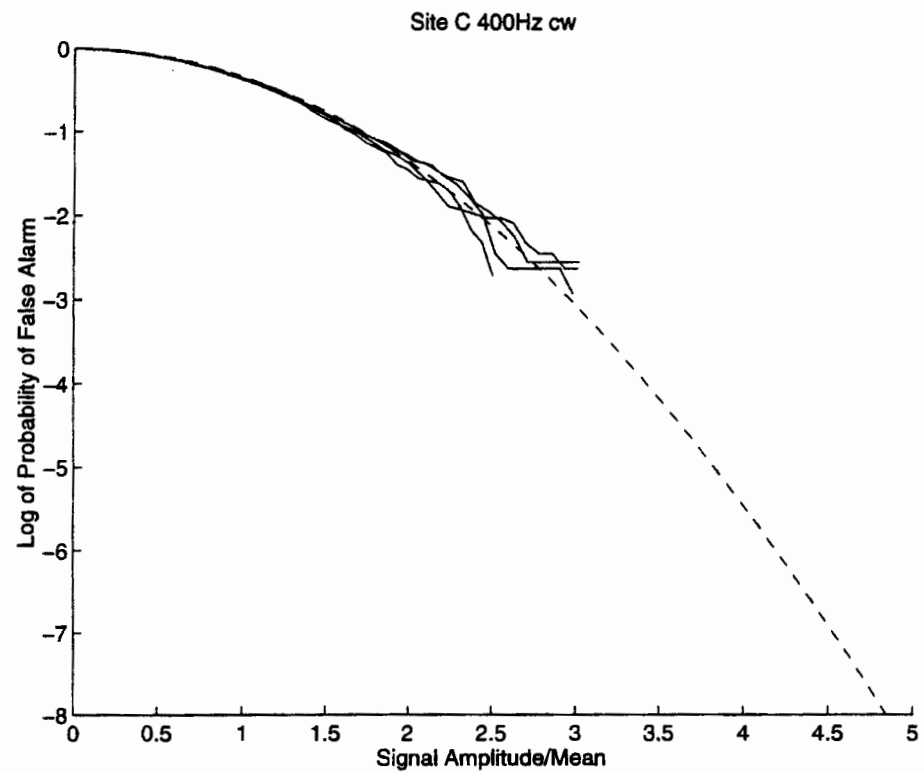


Figure 5-37: Signal log PFA for pulses from 4 legs, Site C 400 Hz CW.

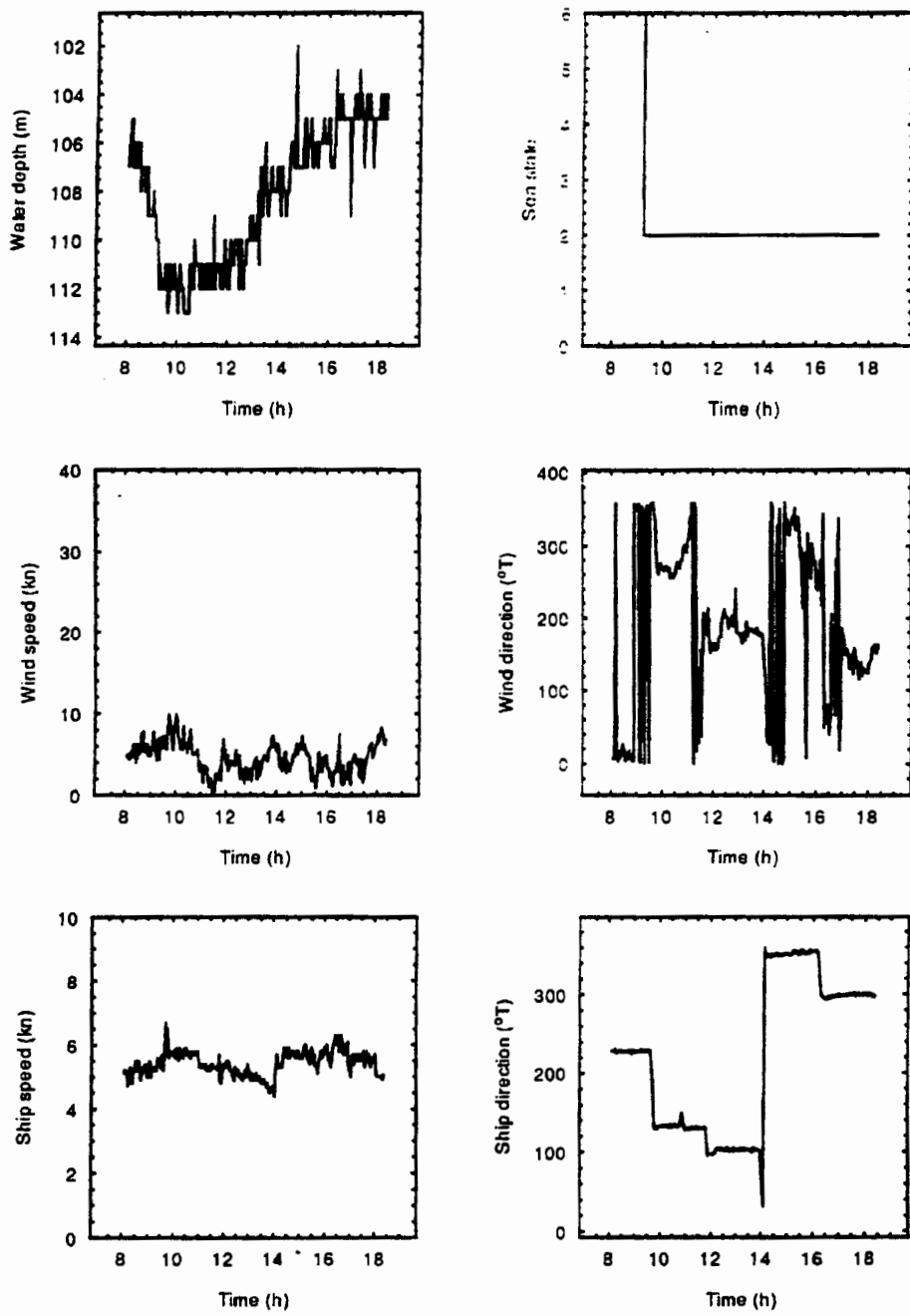


Figure 5-38: Ship log information. Wind speed shown in center left graph for Site A.

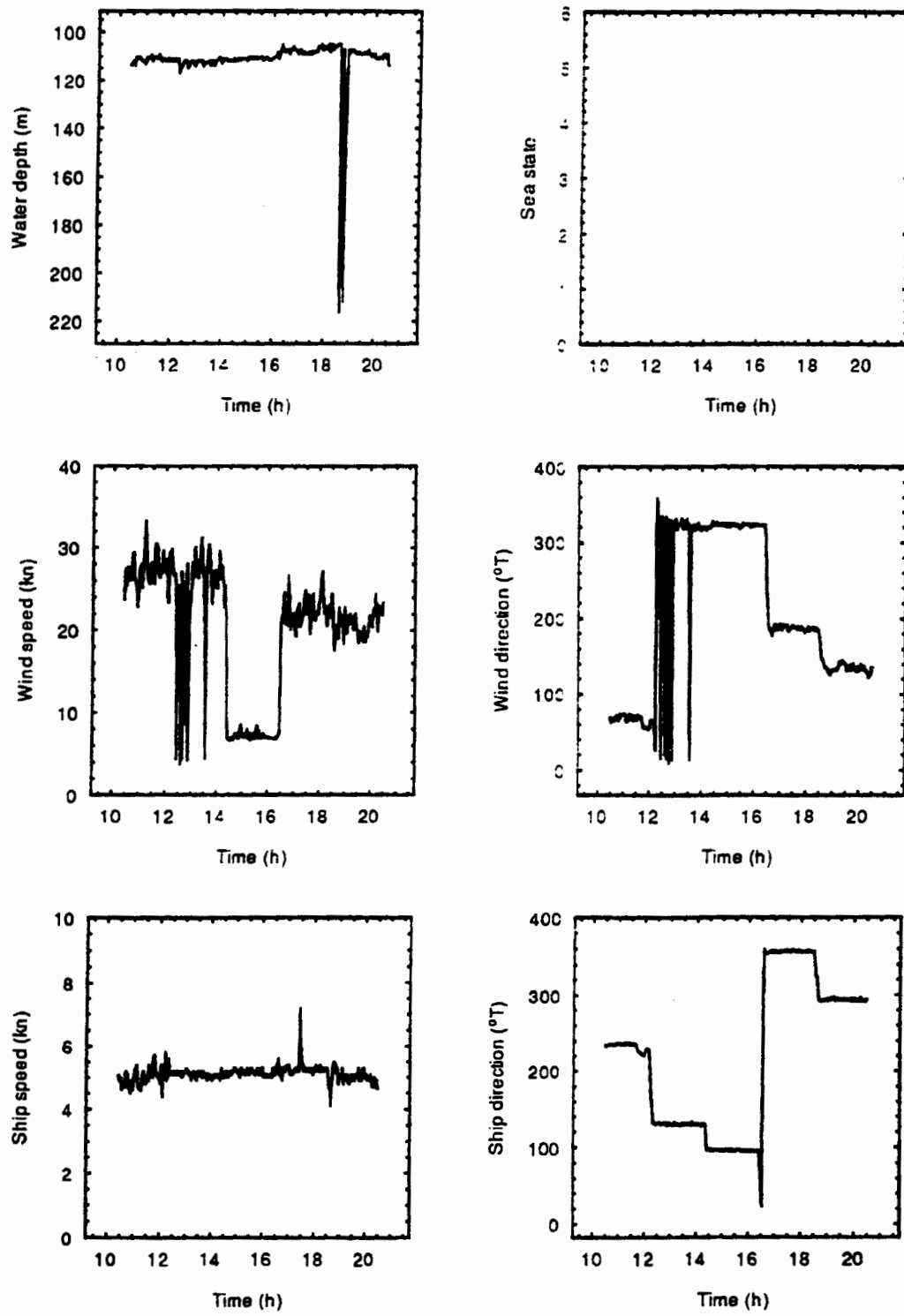


Figure 5-39: Ship log information. Wind speed shown in the center left graph for Site C.

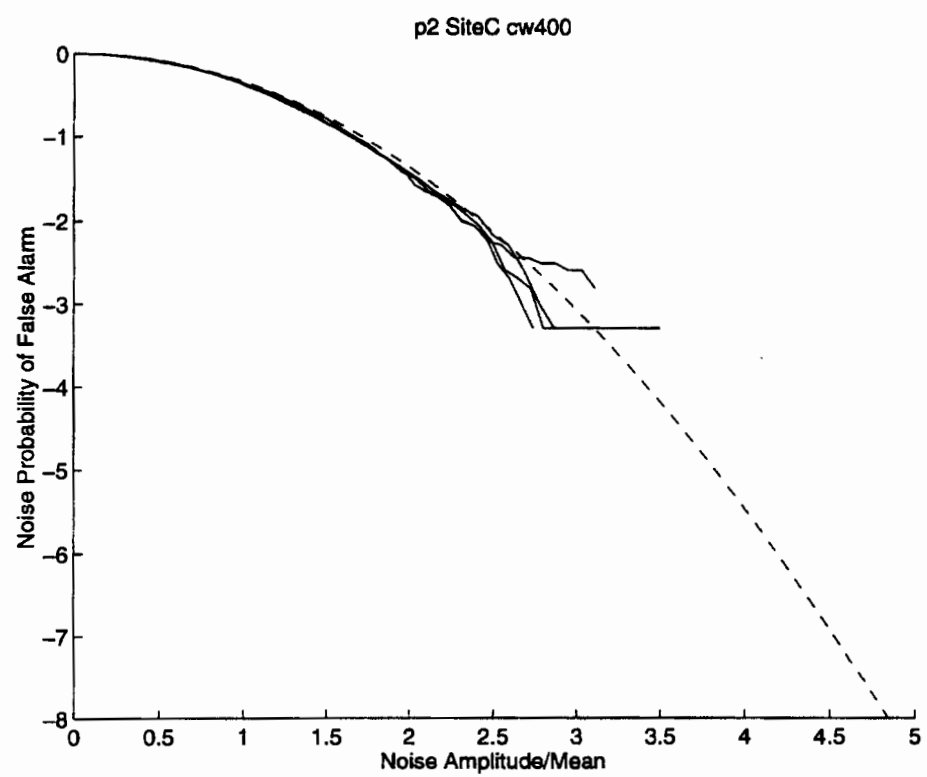


Figure 5-40: Noise log PFA from the noise portion of Figure 5-31, Site C 400 Hz CW.

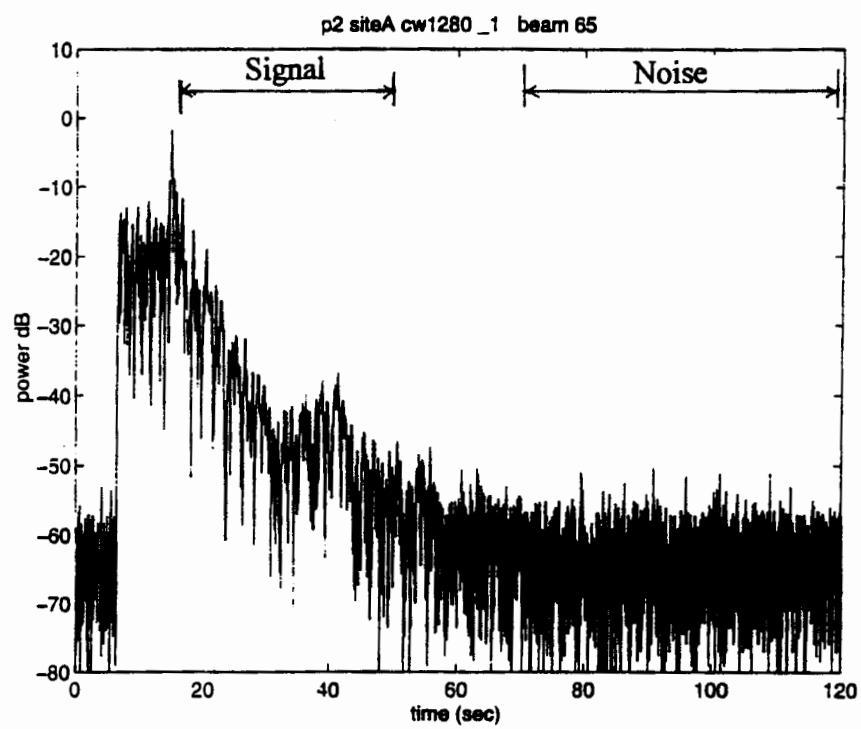


Figure 5-41a: Leg 1 -- Beam #65 intensity time series, Site A 1280 Hz CW.

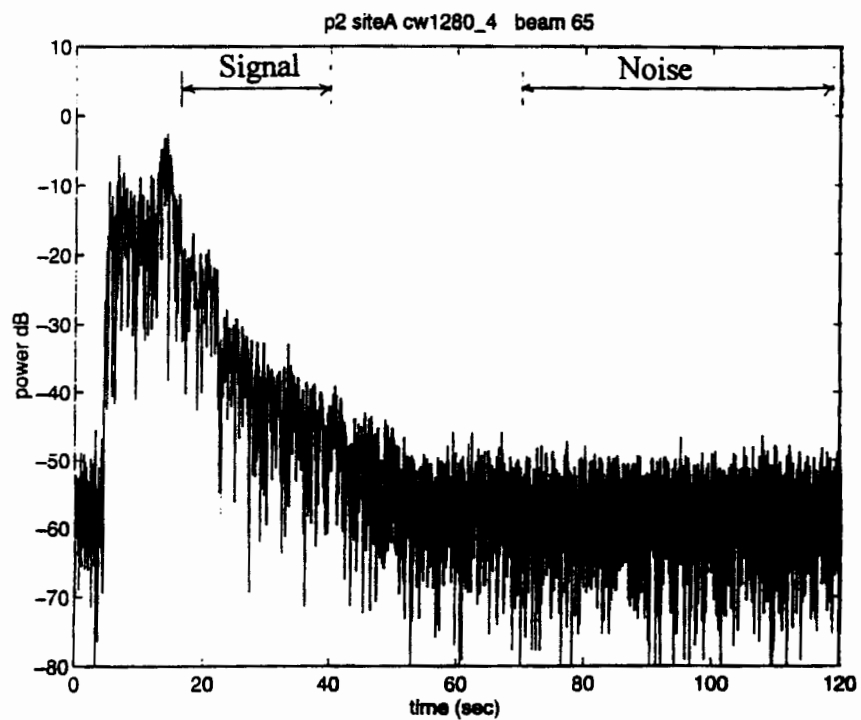


Figure 5-41b: Leg 4 -- Beam #65 intensity time series, Site A 1280 Hz CW

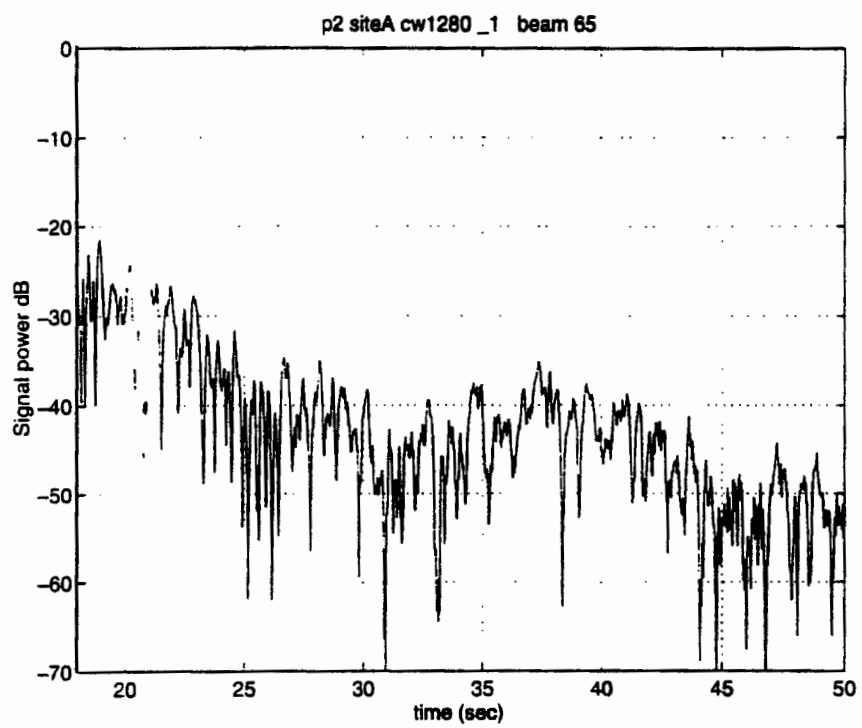


Figure 5-42a: Leg 1 -- Signal portion of the beam time series, Site A 1280 Hz CW.

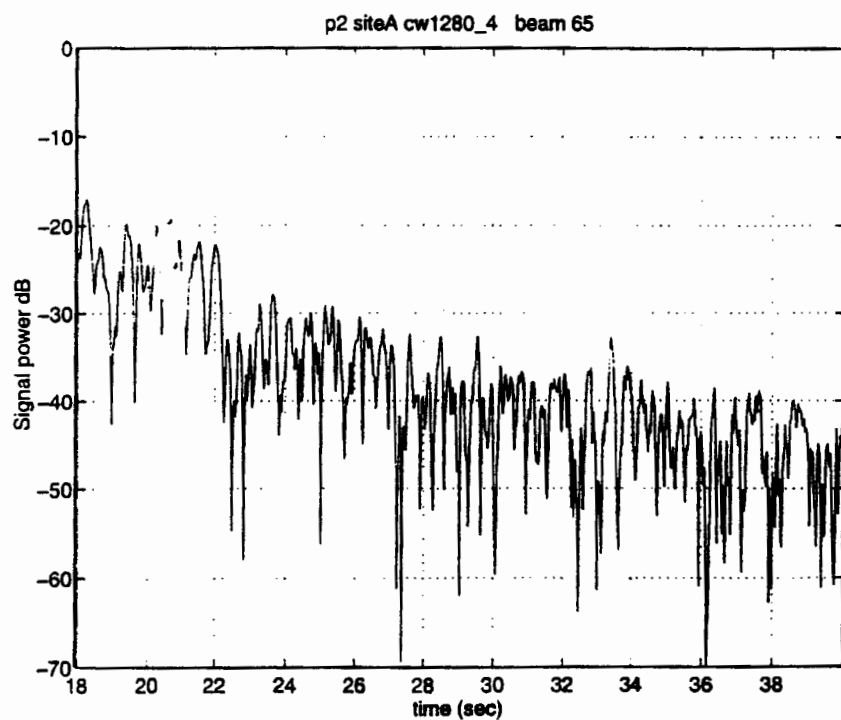


Figure 5-42b: Leg 4 -- Signal portion of the beam time series, Site A 1280 Hz CW.

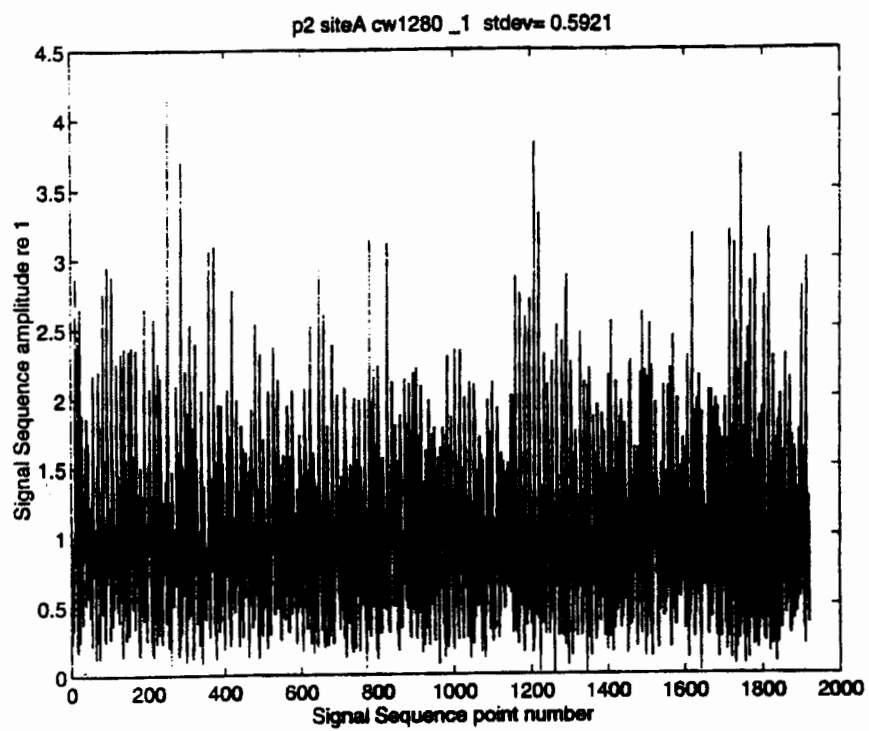


Figure 5-43a: Leg 1 -- Signal sequence (skipping beam 45 which was judged contaminated by local shipping noise), Site A 1280 Hz CW.

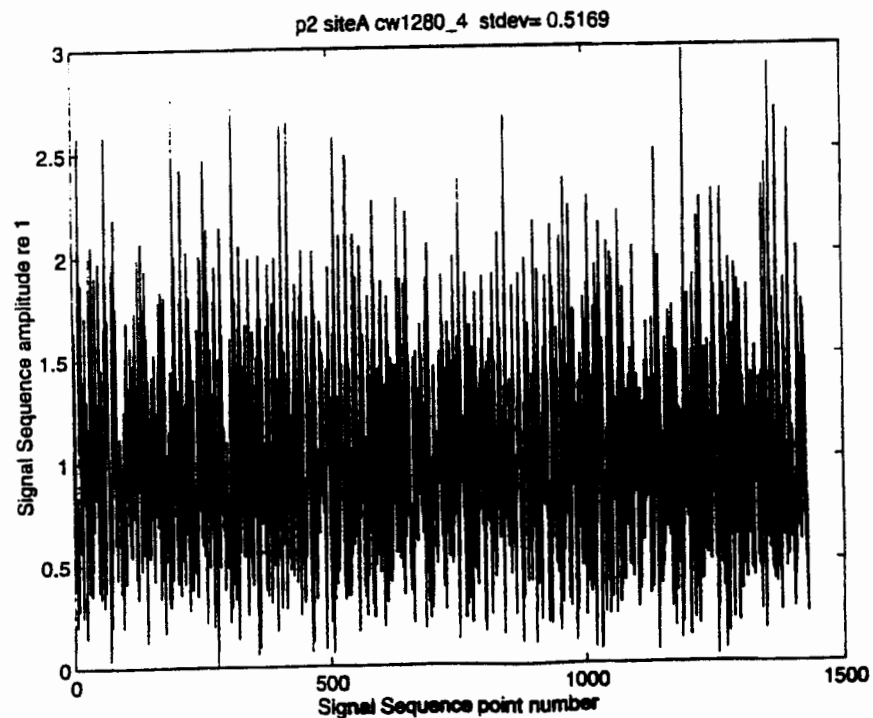


Figure 5-43b: Leg 4 -- Signal sequence (skipping beam 45 which was judged contaminated by local shipping noise), Site A 1280 Hz CW. (Note a vertical scale change.)

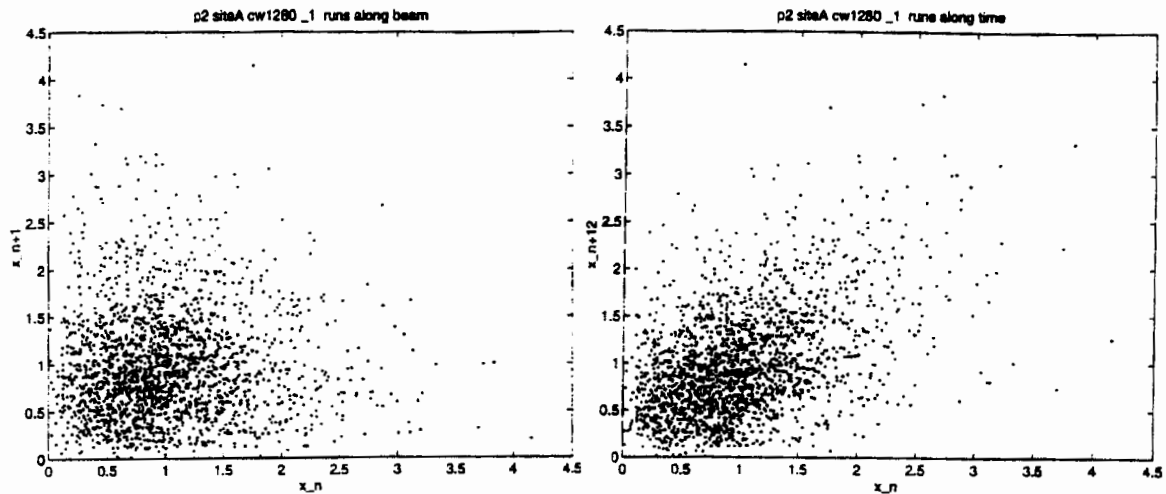


Figure 5-44a: Leg 1 -- Runs test over beam and time, Site A 1280 Hz CW.

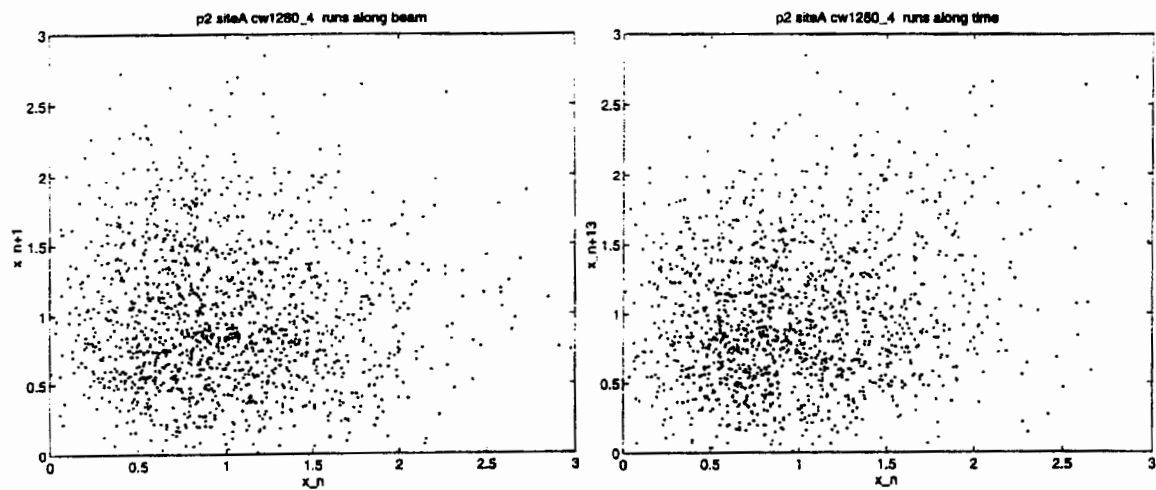


Figure 5-44b: Leg 4 -- Runs test over beam and time, Site A 1280 Hz CW.

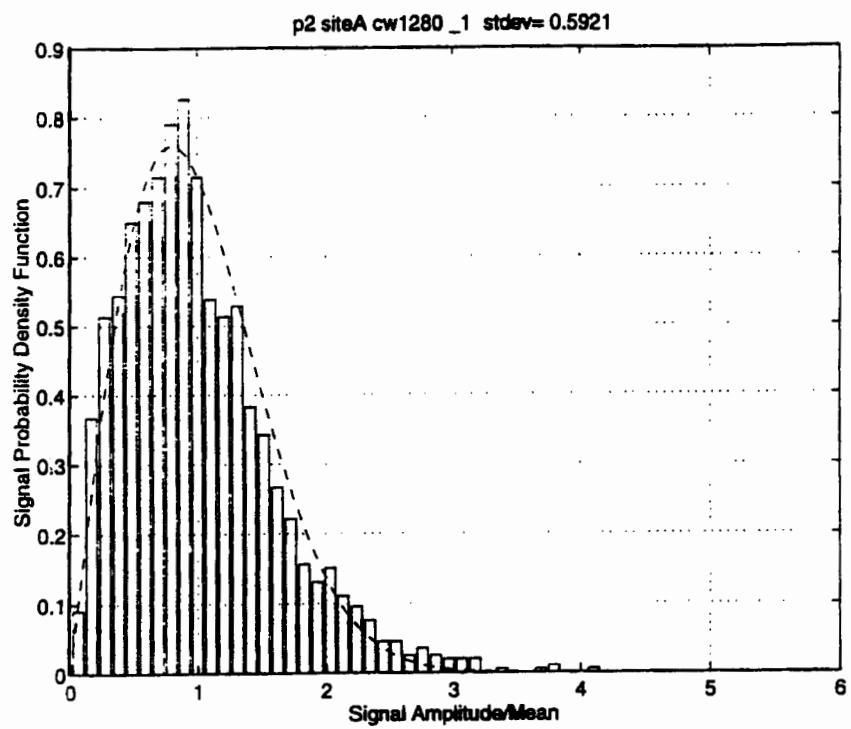


Figure 5-45a: Leg 1 -- Signal histogram of fluctuations, Site A 1280 Hz CW.

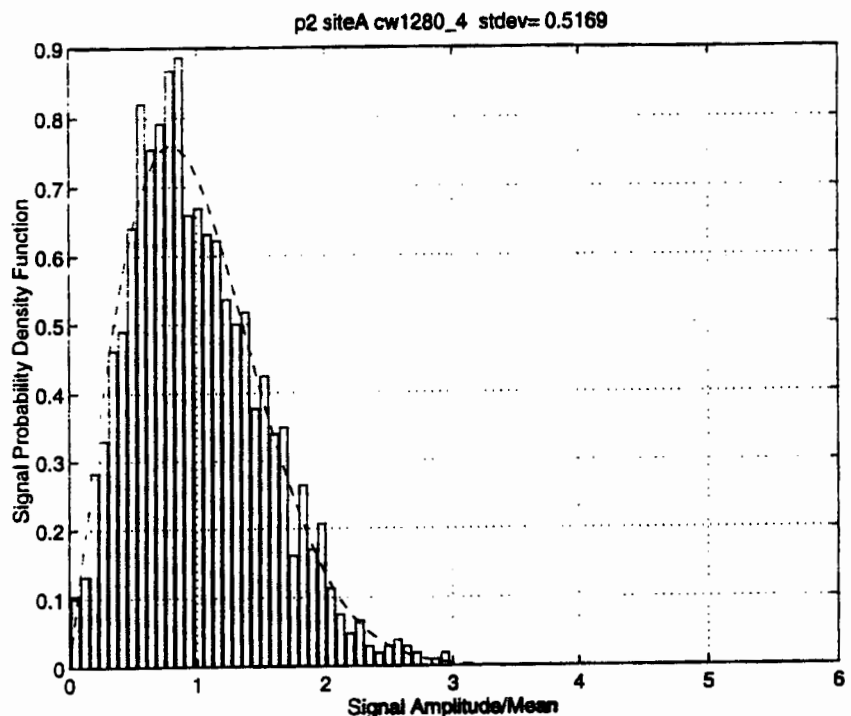


Figure 5-45b: Leg 4 -- Signal histogram of fluctuations, Site A 1280 Hz CW.

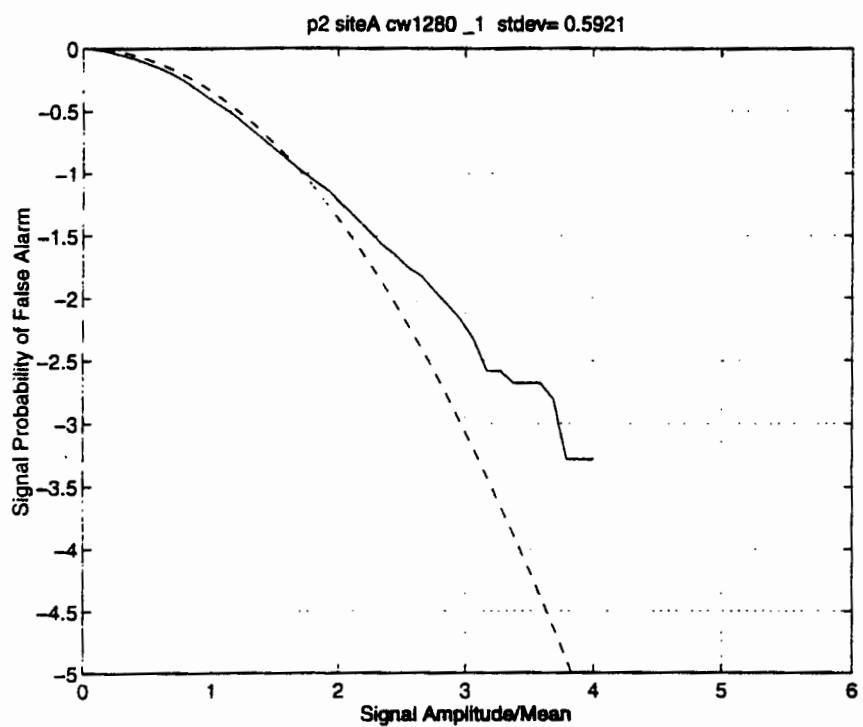


Figure 5-46a: Leg 1 -- Signal log PFA, Site A 1280 Hz CW.

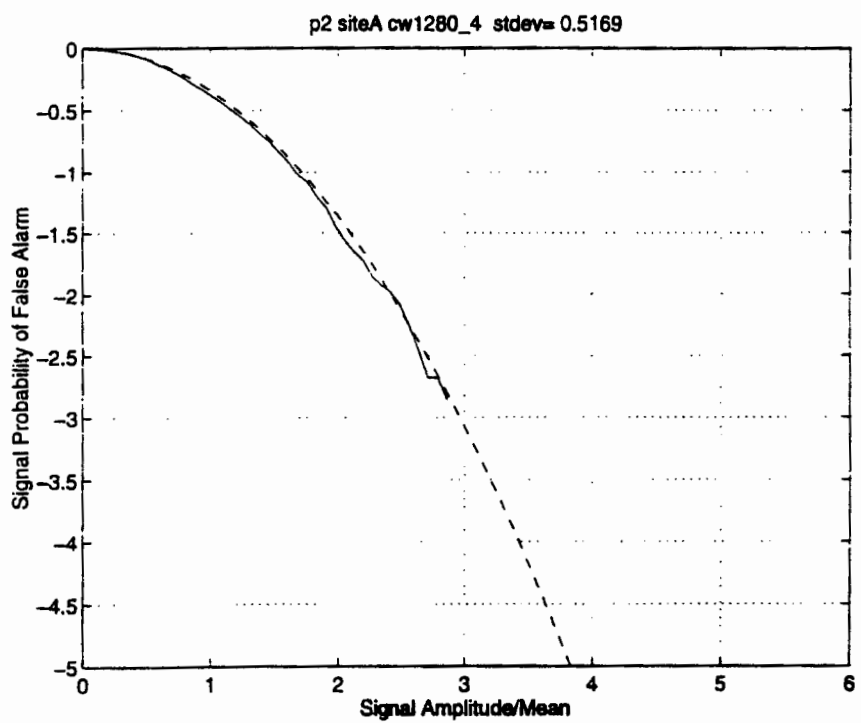


Figure 5-46a: Leg 4 -- Signal log PFA, Site A 1280 Hz CW.

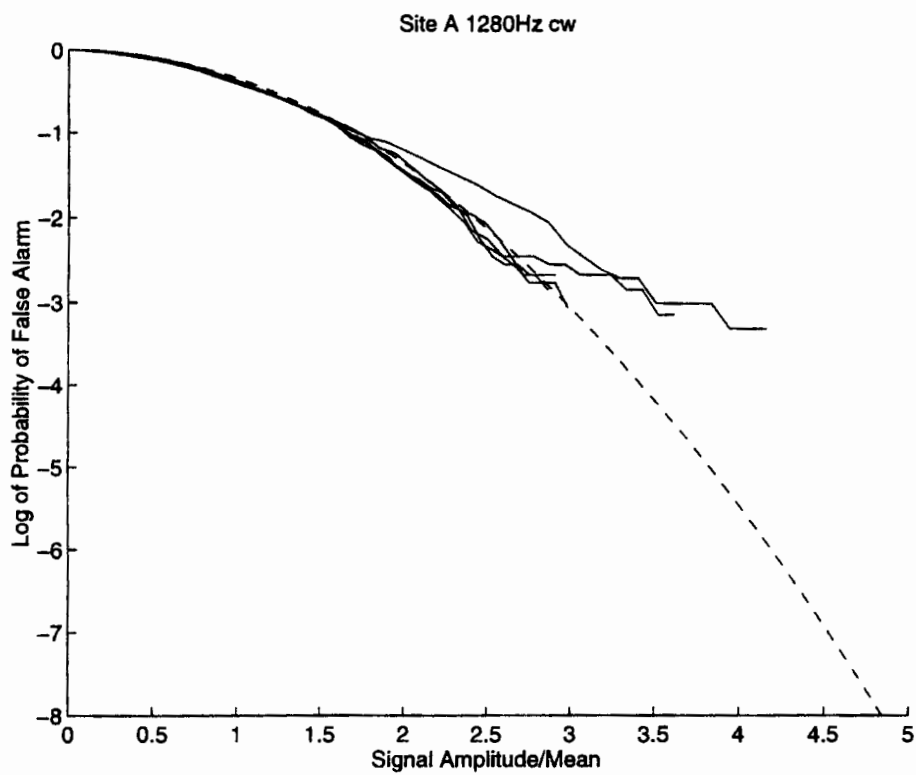


Figure 5-47: Signal log PFA for pulses from 5 legs, Site A 1280 Hz CW.

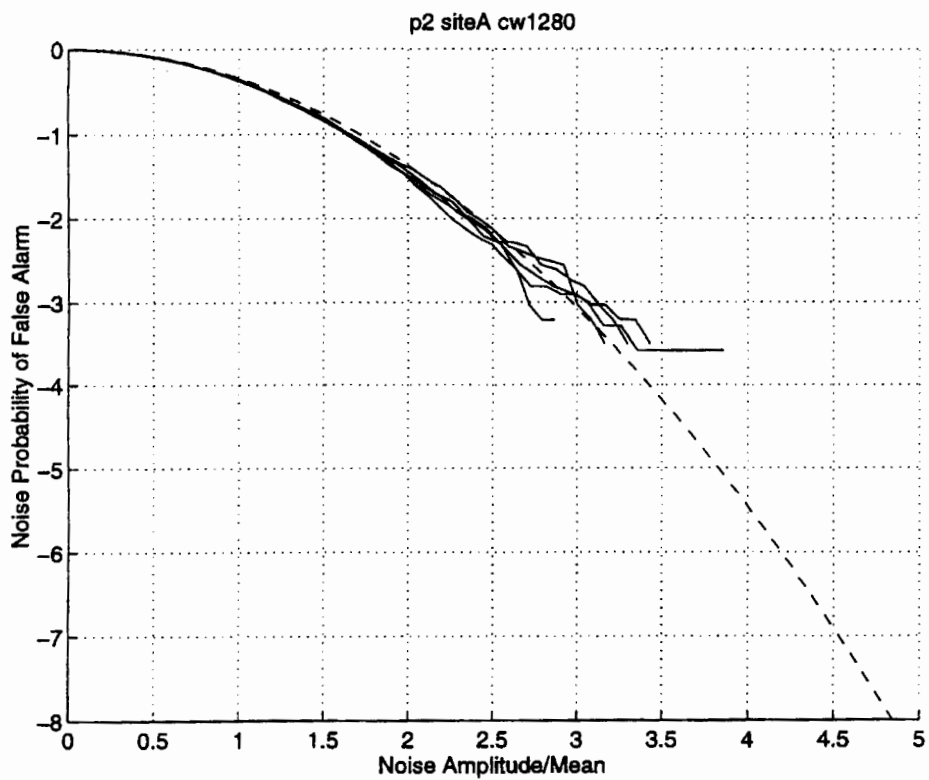


Figure 5-48: Noise log PFA for pulses from 5 legs, Site A 1280 Hz CW.

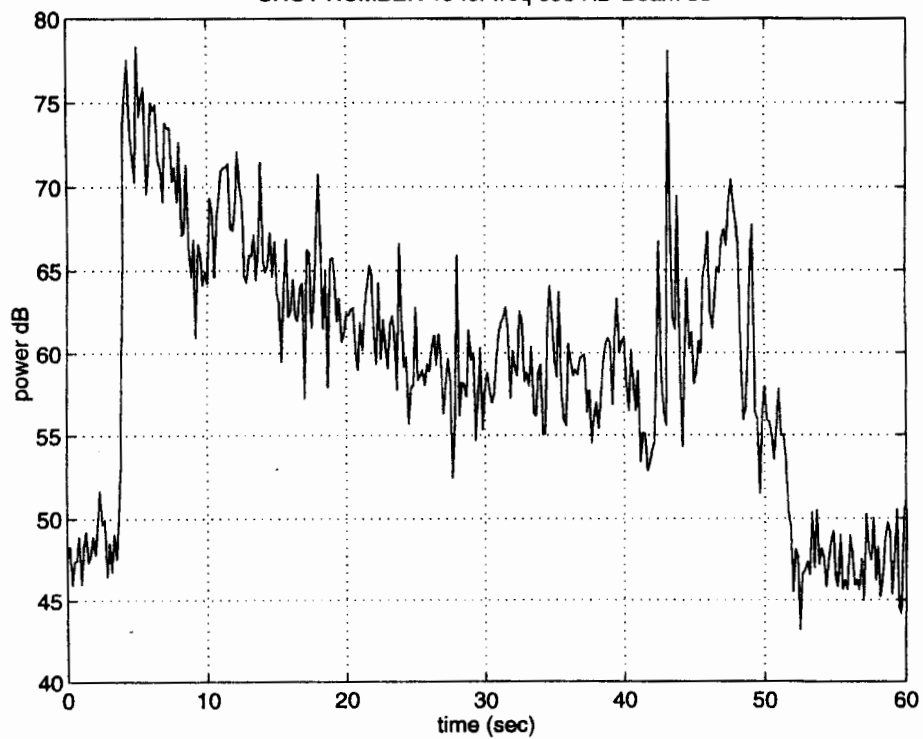


Figure 5-49: A typical Ogopogo time series at 398 Hz from beam 33 of explosive shot.

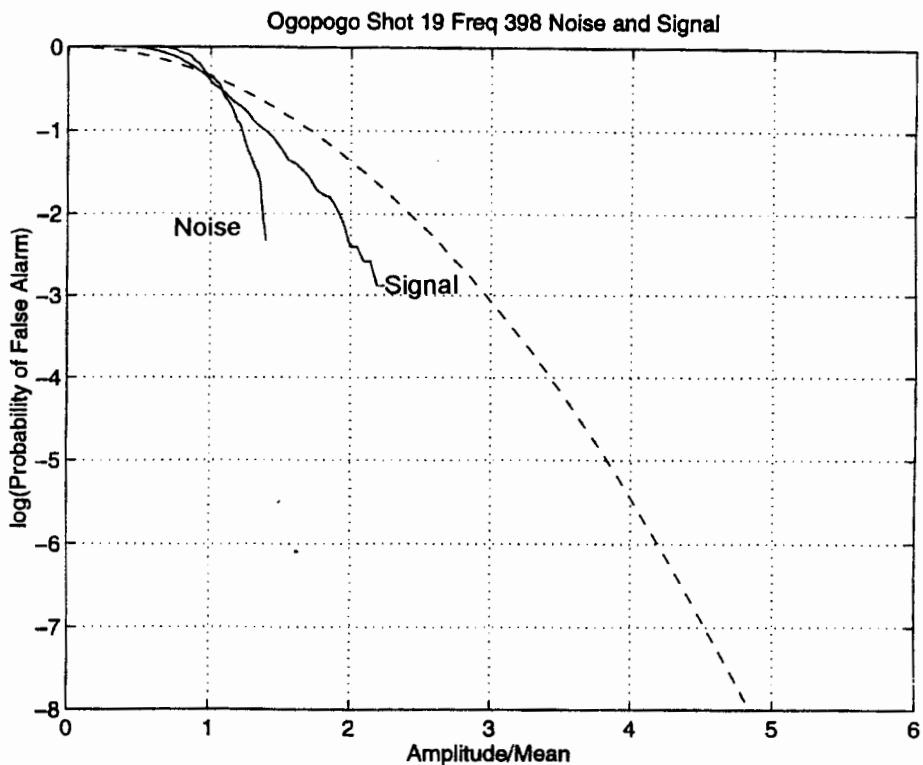


Figure 5-50: Typical log of the PFA curves for signal and noise sections of the Ogopogo data set.

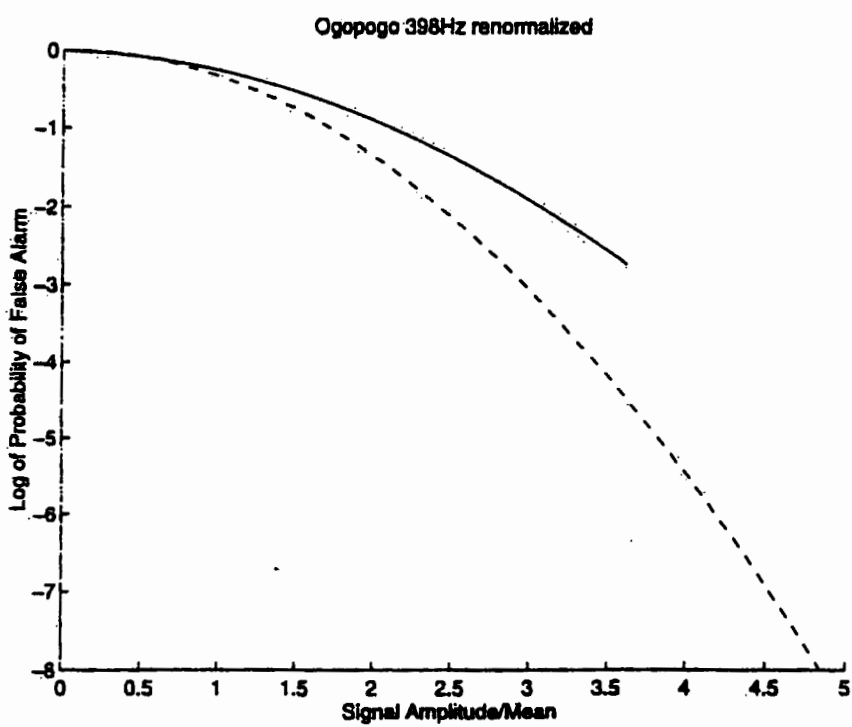
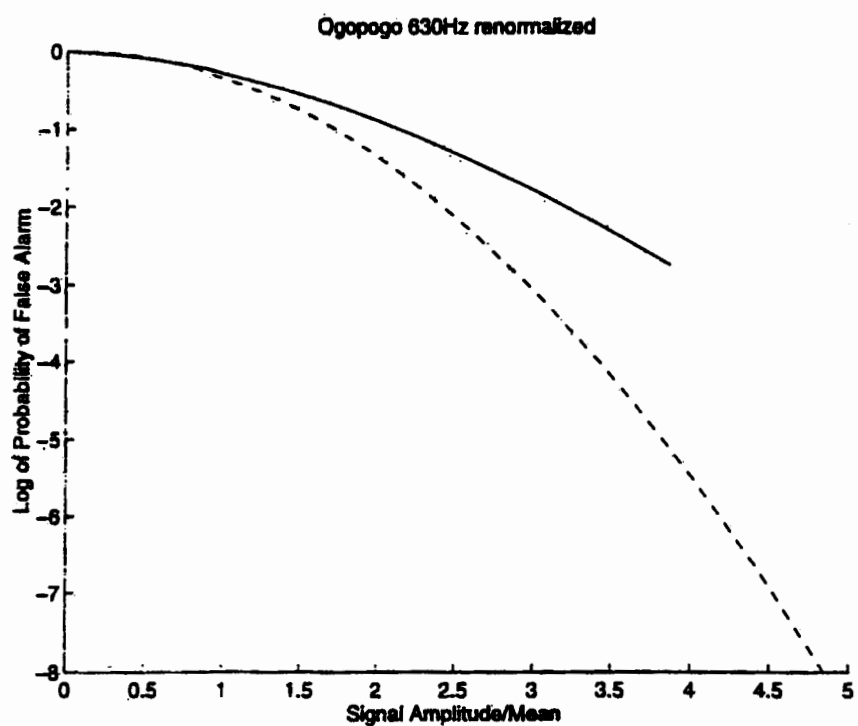


Figure 5-51: Ogopogo explosive signal, 630 Hz and 398 Hz, showing the log PFA renormalized to show the difference between the signal and noise portions relative to the theoretical Rayleigh curve.

## Chapter 6

### SIMULATION STUDIES

In-water measurements do not provide sufficient information to quantify the factors influencing fluctuation statistics of bottom reverberation or to determine if these factors can be related to bottom roughness or a system parameter or the sound velocity profile. Therefore, extensive simulation studies have been performed to isolate and better study the causes of the statistical changes. The purpose of this chapter is to describe the details of the simulation and to present the objectives and conclusions of the studies. The objectives and conclusions are in direct response to the theories postulated in *Table 4-2* of Chapter 4.

#### 6.1 Development of the Simulation

The simulation was developed by generating low frequency (400 Hertz) bottom backscattering strengths with Mourad and Jackson's model [6] and supplying them as inputs to a propagation model called the Fast Multipath Expansion (FAME) model [78] to produce monostatic, narrowband reverberation time series. The propagation model parameters were selected so that bottom reverberation dominated the reverberation time series. To generate the fluctuation statistics, the time series are processed by a MATLAB® [79] program similar to the program presented in Chapter 5.

### 6.1.1 Generating time series

By controlling the distribution of the input parameters to the backscatter model, multiple realizations of the time series can be generated. Each realization has a slightly different acoustic intensity at any given time slice if you vary one of the input parameters to Mourad and Jackson's backscatter model. An input parameter was varied in accordance to a Gaussian distribution around its published mean value with its typical variance. These slight variations to the scattering strength caused by randomly varying an input parameter produced the intensity fluctuations in the time series.

### 6.1.2 Processing the time series

Intensities at each time slice are used to form pressure amplitudes by first taking the square root of the intensities, splitting them into an in-phase  $x$  component and an in-quadrature  $y$  component, and subtracting from each component its mean to form zero mean Gaussian components. The pressure amplitudes  $A$  are then formed by taking the square root of the sum of the squares of the zero mean Gaussian components so that  $A = \sqrt{x^2 + y^2}$ . From this point, the processing is the same as was described in Section 5.1 for forming the histograms, cumulative distributions, and false alarm rates.

### 6.1.3 Verification of the simulation

To verify that the simulation was working correctly and to obtain a thorough understanding of the results, several tests were performed with the simulation before starting the

studies. The first test involved using a random number generator to generate pure Gaussian distributions to form the pressure amplitudes instead of using the intensities generated by the FAME propagation model. The objective of this test was to determine if the procedures written in MATLAB<sup>®</sup> to form the normalized fluctuation sequences and to calculate the fluctuation statistics were correct. Gaussian distributions were injected in the simulation both as intensities and as the  $x$  and  $y$  quadrature components of the pressure amplitudes. *Figure 6-1* shows an example of the results obtained by injecting zero mean Gaussian distributions for the  $x$  and  $y$  quadrature components. The PFA of the simulated sequence closely follows the Rayleigh distribution. This test produced PFAs that were Rayleigh when Gaussian distributions were injected as either intensities or as the  $x$  and  $y$  components and therefore, verified that the simulation was producing the desired statistics.

The objective of the next test was to determine the number of realizations (or beams) at each time slice required to form a valid statistical representation of the data's distribution. Reverberation was simulated for 12 seconds and sampled at 1/6 second intervals producing 72 time slices. The question was, "How many amplitudes (or beams) must be simulated at each time slice in order to obtain a consistent mean amplitude?" A consistent mean amplitude at each time slice is required for the normalization process that removes the propagation effects at each time slice. To perform this test, zero mean Gaussian distributions were injected for the  $x$  and  $y$  components and the number of beams at each time sample were varied between 8 and 16 beams by steps of 2. For each variation, the simulation was used to generate and process approximately twenty different sequences. The PFA curves were visually inspected to determine if Rayleigh statistics were consistently obtained. This test indicated that to consistently yield Rayleigh statistics a minimum of twelve amplitudes (or beams) are required at each time slice when zero

mean Gaussian  $x$  and  $y$  components are used to form the pressure amplitudes. This result was used to choose the minimum number of amplitudes or beams required at each time slice for processing the in-water data presented in Chapter 5 and the simulated data presented below.

As stated in Section 6.1.1, the fluctuations in the time series were produced by varying an input parameter to Mourad and Jackson's backscatter model in accordance to a Gaussian distribution around its published mean and variance. However, the input distribution was not a pure Gaussian distribution. It was slightly skewed because, when generating a Gaussian distribution around the parameter's published mean with its typical variance, negative numbers were generated. Since the input parameters must always be positive, only the positive values of the parameters were used in the input distribution. This technique causes a skewed Gaussian distribution. A test was performed with the simulation to determine if a skewed Gaussian distribution for an input parameter biased the PFAs when compared to a pure Gaussian distribution generated with a smaller variance. Rayleigh statistics (the step-by-step statistical processing will be illustrated in Section 6.2.1) resulted for both the skewed Gaussian and the pure Gaussian distributed input parameters; in other words, the skewed distribution did not bias the PFA. Becker [10] arrived at a similar result. In his thesis, he stated that fluctuation statistics do not show a dependence on the shape of the surface height distribution. He noted that changing the form of the underlying probability distribution function of the surface height spectrum had little effect on the shape of the PFA. The surface height spectral strength input parameter  $w_2$  was the input parameter varied in each of the following simulation studies in order to produce the fluctuations in the time series. (The spectral strength parameter  $w_2$  is defined in Section 2.2.1).

## **6.2 Simulation Studies**

The overall objective of the simulation studies is to define the key factors causing bottom reverberation amplitude fluctuations to be non-Rayleigh. The studies were tailored to address the theories postulated in *Table 4-2*.

### **6.2.1 Sediment parameter study**

Addressing the first two hypotheses listed in *Table 4-2*, the objective of the sediment parameter study was to determine if non-Rayleigh statistics can be caused by variations in the surface reflected rays, the volume penetrated rays, or a combination of both. The assumption for this study is that the fluctuations are caused by changes in sediment properties and that the variations in the sediment surface reflected path are independent of the variations in the transmitted volume scattered path.

The variations in these paths were created by altering the bottom properties to create the fluctuations. These alterations caused *stationary* variability in the sediment properties. The term stationary variability means that the average values of the sediment properties remain constant over the ensonified area for the duration of the received reverberation signal.

The bottom properties of the sediment were altered by assuming the surface roughness spectral strength  $w_2$  and the volume parameter  $\sigma_2$  input to the backscatter model [6] are random quantities with skewed Gaussian distributions. (The eight input parameters for Mourad and Jackson's model are listed in Table 2-1). Varying the spectral strength  $w_2$  varies only the surface reflected path and varying the volume parameter  $\sigma_2$  varies only the volume penetrated path. The

typical mean values and standard deviations for sand, gravel, and muddy clay sediments were obtained from data published by Hamilton [83, 84, 85], Jackson [86], and Fox [87].

Time series and statistics were generated for sand, gravel, and mud/clay sediments by first varying only the surface roughness parameter  $w_2$ , followed by varying only the sediment volume parameter  $\sigma_2$ , and, finally, by varying the two parameters simultaneously. The results for all nine variations produced similar Rayleigh statistics. *Figure 6-2* shows the skewed Gaussian distributions generated for the spectral strength parameter  $w_2$  and the sediment volume parameter  $\sigma_2$  for sand. The published means and standard deviations are printed on the plots along with the skewness and kurtosis. (A Gaussian distribution should have a skewness of zero and a kurtosis of three when defined by Equation 3.5.) The units for the spectral strength are meters raised to the fourth power ( $m^4$ ) and the volume parameter is dimensionless. Plots depicting each step in the simulation process are now presented; the plots are from the sand sediment with both the spectral strength and the volume parameter varied simultaneously. *Figure 6-3* shows the backscatter curves for 5 to 85 degree grazing angles and the corresponding normalized histogram. Each curve on the backscatter plot is generated by selecting as input to the backscatter model a different value for the spectral strength and volume parameter from their respective distributions shown in *Figure 6-2*. The histogram is normalized to have zero mean and unity standard deviation by subtracting the mean value and dividing by the standard deviation at each 5 degree increment in grazing angle.

The next step in the simulation is to input a single backscatter curve from *Figure 6-3* into the propagation model for each realization at each time bin. Twenty four realizations were generated for each of the 72 time bins. The propagation model generates intensities. The intensities at each time slice are then used to form twelve pressure amplitudes as described in Section 6.1.2. *Figure 6-4* shows an example of the normalized histograms of the intensities and

the  $x$  and  $y$  components, along with the twelve Rayleigh amplitudes formed at each of the 72 time bins.

The fluctuation sequence is then generated by normalizing the amplitudes at each time bin by the mean amplitude for that bin. This normalization causes the mean of the fluctuations to be unity. *Figure 6-5* shows the fluctuation sequence, its histogram, and the runs tests. The signal sequence shows random fluctuations with a standard deviation of 0.5218; a Rayleigh distribution has a standard deviation of 0.5227. The histogram nicely fills in the Rayleigh density function. The runs tests over beam and over time are randomly distributed. The cumulative distribution (cdf) for sand and the PFAs for sand, gravel, and mud/clay bottoms are shown in *Figure 6-6*. The three test statistics, Kolmogorov-Smirnov (KS), Kuiper's (Kuiper), and Anderson-Darling (A-D), are printed on all four plots in *Figure 6-6*. As a reminder, these test statistics are performed on the cdf and not the PFA (see Section 3.3); however, they have been printed on the PFA because, in the following studies, the PFA, and not the cdf, will be shown.

The small values of all three test statistics on the plots in *Figure 6-6* indicate that the null hypothesis can not be rejected. The null hypothesis states that the fluctuation sequence is drawn from the theoretical Rayleigh distribution. A large value of the test statistics indicates a large discrepancy between the data and the theoretical distribution. As can be seen in *Figure 3-9*, the KS test statistic  $D$  increases as the difference between the observed data and the theoretical distribution increases; the Kuiper and Anderson-Darling statistics work on the same principle and increase as the difference between the distributions increase. Therefore, a small value of the statistic indicates there is little difference between the two distributions.

To determine the level of significance indicated by the value of the test statistics, lookup tables published in the open literature are normally used. However, the KS test and Kuiper's test

have simple formulas for the distribution of the test statistics that are used to determine the significance level of any observed non-zero value of D. The functions that enter into the calculation of the significance are [57]

$$Q_{KS}(\lambda) = 2 \sum_{j=1}^{\infty} (-1)^{j-1} e^{-2j^2\lambda^2}$$

$$Q_{Kuiper}(\lambda) = 2 \sum_{j=1}^{\infty} (4j^2\lambda^2 - 1) e^{-2j^2\lambda^2}$$

which are monotonic functions with the limiting values

$$Q(0) = 1 \quad \text{and} \quad Q(\infty) = 0$$

where for the KS test,  $\lambda = [\sqrt{N} + 0.12 + 0.11/\sqrt{N}] D$  and for Kuiper's test,  $\lambda = [\sqrt{N} + 0.155 + 0.24/\sqrt{N}] V$ . N is the number of data points in the sequence, D is the KS test statistic and V is the Kuiper's test statistic as given in Sections 3.3.1.2 and 3.3.1.4 respectively.

This level of significance is labeled "Prob" on the plots in *Figure 6-6*. Small values (close to zero) of "Prob" indicate that the cumulative distribution functions are significantly different and the values close to unity indicate a high acceptance level. The values of "Prob" on the plots in *Figure 6-6* all indicate a 100% acceptance level. Keep in mind that accepting the null hypothesis does not *prove* that the fluctuation sequence was drawn from a Rayleigh distribution but only that *gross* disagreement between the data and the theoretical distribution was not detected by the test statistic.

The main conclusion of the parameter study is that stationary variations in the surface reflected rays, volume penetrated rays and, most importantly, a combination of both did not cause

non-Rayleigh statistics. Realistic variations in sediment properties were not sufficient to produce the “patchiness” property (which was discussed in Section 4.2.3 and implies that there are a few - more than one, less than many- different mean levels contributing to the randomness) required to yield non-Rayleigh fluctuations. Even when the variations in surface roughness and sediment volume scattering were combined, the mixture of these two random processes did not cause non-Rayleigh fluctuations.

### **6.2.2 Sediment mixture study**

Addressing the third hypothesis listed in *Table 4-2*, the objective of the sediment mixture study was to determine if non-Rayleigh statistics can be caused by *non-stationary* variations of the sediment surface. The non-stationary variations (or spatial inhomogeneity) were created by adding controlled patches of gravel to a mud/clay sediment. (Due to the lack of separation between the generated intensities for gravel and for mud/clay, it was noted that the scattering strengths are effectively drawn only from 0 to 30 degree grazing angles with the larger grazing angles being highly attenuated due to the propagation geometry. Therefore, for this study, the volume parameter  $\sigma_2$  for the mud/clay sediment was chosen to be slightly lower than the mean value obtained from the open literature but was still within the published variance. This lower value gave a larger separation between the scattering strengths and therefore, intensities of the gravel and mud in the 0 to 30 degree grazing angle range.)

The amount of the gravel added to the mud sediment was varied both in the down-range and cross-range directions. Increasing the down-range extent of the patch size means adding gravel to more consecutive time slices, while increasing the cross-range extent of the patch size means

adding gravel to more consecutive amplitudes per time slice. The down-range extent of the gravel patch can be calculated as the product of the time interval of the reverberation signal containing gravel and the speed of sound. However, the cross-range patch size can not yet be calculated because there are no beampattern effects accounted for in this study; each amplitude in a given time slice is an independent look at the bottom without an associated beamwidth. This study addresses the effect of having some amplitudes see gravel while others see mud. Beampattern effects are investigated in the beampattern study covered in Section 6.1.3.

To extend the range of the PFAs, twenty four amplitudes were generated at each time slice instead of twelve. *Figure 6-7a* shows the PFA for the mud sediment before adding any gravel and *Figure 6-7b* shows the PFA for the gravel sediment without any mud when 24 amplitudes are used to form the fluctuation sequences. The reason for the gravel PFA falling below the Rayleigh curve was investigated and determined to be caused by a smaller coefficient of variation *cv* for gravel than was calculated for mud. This was a surprise since the gravel time series had a larger spread than the mud time series. However, the amplitudes of the gravel and therefore, the mean values were also larger than the mud values, causing the *cv* to be smaller. The test statistics still indicate that the acceptance level of the gravel curve belonging to the Rayleigh distribution is 100%.

To start the study, the effect of varying the number of time slices containing gravel (increasing the down-range extent of the gravel patch) while holding the number of gravel amplitudes in each slice constant (constant cross-range extent) was investigated. *Figure 6-8* shows an example of the results when 12 gravel amplitudes are combined with 12 mud amplitudes in 1, 18, 36, and 54 of the 72 time slices, respectively. Note that as the number of time slices containing gravel increases, the PFAs get further away from the Rayleigh curve. *Figure 6-9* is an overlay of the PFAs obtained in the study when 12 gravel amplitudes are mixed with 12 mud amplitudes for

1, 9, 18, 27, 36, 45, 54, 63, and 72 time slices along with a plot of the three test statistics for the PFAs. The test statistics are plotted against the number of time slices containing the 12 gravel amplitudes. As the number of time slices increases so do the test statistics, indicating that the level of acceptance is decreasing. The trend of all three statistics are similar; therefore, for the remaining examples, only Kuiper's statistic will be displayed.

Next, the number of gravel amplitudes out of a total of 24 amplitudes in each time slice was varied (the cross-range extent of the gravel patch was varied). *Figure 6-10* shows the combined PFA plots when 15, 18, 21, and 24 gravel amplitudes are added, respectively, to 1, 9, 18, 27, 36, 45, 54, 63, and 72 time slices. For 15 and 18 amplitudes, the trend is similar to adding 12 gravel amplitudes to the time slices; as the number of time slices containing gravel increases, the PFAs get further away from the Rayleigh curve. However, the entire grouping is getting tighter and moving closer to the all gravel PFA curve shown in *Figure 6-7b*. As the number of gravel amplitudes per time slice increases, the results are more consistently Rayleigh as can be seen by the plots with 21 and 24 gravel amplitudes. *Figure 6-11* shows the corresponding Kuiper's test statistic for each of the plots displayed in *Figure 6-10*. The plots indicate that the test statistic is decreasing as the number of amplitudes per time slice increases and therefore, the acceptance level of the data being Rayleigh distributed is increasing. For the case where all 24 out of 24 amplitudes in any number of time slices are gravel, the acceptance levels were all 100%.

There are two trends in the data. One trend indicates that as the number of time slices containing gravel increases, the PFA becomes more non-Rayleigh. The other trend indicates that as the number of amplitudes in any given time slice increases, the PFA becomes more Rayleigh. The reason for the first trend is that as the down-range extent of the gravel patch increases (more time slices are added); the additional variability added to the sequence in the normalization process

of each time slice can not be averaged-out or overpowered by the amplitudes in the remaining time slices. In the normalization process, each amplitude in a time slice is divided by the mean amplitude of that time slice. If there is a very small patch of gravel added to the mud (meaning that there are only a few time slices each with a few gravel amplitudes), the normalized amplitudes of the remaining time slices will overpower the small amount of variability added by the small patch. However, as the down-range extent of the patch increases, the remaining time slices can not average-out the added variability and therefore, cause the non-Rayleigh results. For the other trend, as the cross-range extent of the gravel patch increases to more than three-fourths the total amplitudes per time slice, the normalization process removes the variability at each of the time slices containing mostly gravel, causing more Rayleigh-like results.

One last point to be made is that it is not just the percentage of gravel ensonified causing the non-Rayleigh results. As shown in *Figure 6-12*, a mixture of 50% mud and 50% gravel or a mixture of 75% mud and 25% gravel may or may not be Rayleigh. The non-Rayleigh results occur when less than three-fourths of the beams see gravel with the tail of the PFA getting higher and higher as the down-range extent of the gravel patch increases. On the other hand, when three-fourths or more of the beams see gravel, the results move towards the Rayleigh distribution.

The conclusion drawn from the mixture study is that spatial inhomogeneity or sediment patchiness does cause non-Rayleigh statistics. This study shows that patchy sediments were sufficient to produce the conditions required for non-Rayleigh statistics. However, it was not simply the percentage of gravel added to a muddy sediment but rather it was a more specific spatial and temporal extent of the gravel patch ensonified that caused the statistics to change.

### **6.2.3 Beampattern study**

Tailored to address the fourth hypothesis listed in *Table 4-2*, the objective of the beampattern study was to determine if non-Rayleigh statistics can be caused by narrow beamwidths. The hypotheses in Chapter 4 [References 8, 16, 17] indicated that the wide beam measurements followed Rayleigh statistics because of the wider field of averaging. The beampattern study looked at the statistics of both wide and narrow beams. Another objective of this study was to determine if the spatial correlation caused by forming the statistical ensemble from samples taken from overlapping beams caused non-Rayleigh results. The purpose of the overlap study was to determine if the in-water results presented in Chapter 5 were affected by the spatial correlation that results when the same area of the sediment is ensonified by more than one beam. And, the final objective of this study was to see how adding patches of gravel to a muddy sediment affected the statistics when there is a clearly defined cross-range extent to the gravel patch. This is a follow on study to the mixture study presented above.

To perform all parts of the study, a Dolph-Chebyshev weighted horizontal array forming 65 beams was implemented with 64 hydrophones spaced one meter apart. This arrangement mimics the SACLANT Centre's array used to collect the data presented in Chapter 5. The sidelobes were located 40 dB down from the main lobe and the width of the main lobe is a function of frequency. Reverberation amplitudes ( $A = \sqrt{x^2 + y^2}$ ) at two degree increments from 0 to 360 degrees were generated with the backscatter model while varying the surface height spectral strength input parameter  $w_2$ . The response in a beam is the sum of the product of the beampattern attenuation coefficient  $c_\theta$  times the complex reverberation pressure  $A_\theta e^{j\theta}$  at two degree increments of the reverberation wavefront arrival angle  $\theta$ :

$$\text{Beam response} = \sum_{\theta} c_{\theta} A_{\theta} e^{j\theta}, \quad \theta = 0, 2, 4, \dots 360 \text{ degrees.}$$

To determine if beamwidth or beam overlap affect the statistics, the first part of this study was performed over a stationary mud sediment. *Figure 6-13* shows the comparison of 33 beams between +30 and -30 degrees centered around the 0 degree broadside beam for both wide beams (400 Hz) and narrow beams (750 Hz) along with the resulting PFAs. The 750 Hz beamwidth was chosen because it is the highest possible frequency for this array configuration before grating lobe problems start to occur for a speed of sound equal to 1500 meters per second. The 400 Hz broadside beam is approximately twice as wide as the 750 Hz broadside beam. The reverberation time series used to form the PFAs for both sets of beams were generated at 400 Hz; only the width of the beams changed between the plot marked 750 Hz and the one marked 400 Hz. The PFA for the wider beams is slightly below the Rayleigh curve while the narrower beams are closer to the Rayleigh curve; however, the test statistics on both plots indicate that the null hypothesis can be accepted with a 100% acceptance level. *Figure 6-14* shows the beam sets and PFAs when every other beam for a total of 17 beams between +30 and -30 degrees are used in the processing. Notice that for the wider beams the adjacent beams overlap at approximately 3 dB down and at approximately 9 dB down on the narrower beams. *Figure 6-15* shows the beam to beam runs test for 17 wide and 17 narrow beams. As a reminder, this runs test is a plot of the fluctuation level of the first beam against the second beam, the second beam against the third beam, and so on at each of the time slices. Both plots show some beam to beam correlation; however, the wider beams show a much stronger 45 degree diagonal pattern. *Figure 6-16* shows the beam sets and PFAs when every second beam for a total of 11 beams between +30 and -30 degrees are used in the processing. Here the adjacent beams of the wider beam set overlap at approximately 5 dB down

and at approximately 25 dB down for the narrower beams. The test statistics on all six PFA plots in *Figures 6-13, 6-14, and 6-16* indicate that the null hypothesis can be accepted with a 100% acceptance level. These results indicate that neither beamwidth nor spatial correlation caused by beam overlap affect the statistics.

The last part of the beampattern study was to see how adding patches of gravel with a defined cross-range extent to a muddy sediment affected the statistics. The PFAs were formed by processing every other beam between +30 and -30 degrees giving a total of 17 beams at 400 Hz. The results match the findings of the mixture study in Section 6.2.2. If the gravel patch was in the mainlobes of all the beams, the PFA was Rayleigh. If the gravel patch was not in the mainlobes of any of the beams, the PFA was Rayleigh. If the gravel patch was in less than three-fourths of the beams, the PFA was non-Rayleigh. *Figure 6-17* shows an example of the results when the gravel patch was in the mainlobes of all 17 beams as the number of time slices containing gravel was varied from 1, 9, 18, 27, 36, 45, 54, 63, and 72 time slices. The Kuiper's test statistic versus the number of time slices with gravel is also shown. All acceptance levels are above 88%. The KS and Anderson-Darling test statistics produced similar results. These results closely match the results shown in the lower right hand corners of *Figure 6-10* and *Figure 6-11* which were obtained when all 24 out of 24 amplitudes were gravel. *Figure 6-18* shows results when the gravel patch was only in the sidelobes of the 17 beams as the number of time slices containing gravel was varied from 1, 9, 18, 27, 36, 45, 54, 63, and 72 along with the corresponding Kuiper's test statistic. All PFAs were identical as were the acceptance levels of 100%. *Figure 6-19* shows example results when the gravel patch was seen in half of the 17 beams as the number of time slices containing gravel was varied from 1, 9, 18, 27, 36, 45, 54, 63, and 72 and the corresponding Kuiper's test statistic. The PFAs and acceptance levels are similar to the results presented on the top portion of

*Figure 6-9* for mixing 12 gravel amplitudes with 12 mud amplitudes. The results are similar for the narrower beams.

The conclusions drawn from the beampattern study is that neither beamwidth nor spatial correlation caused by overlapping beams cause non-Rayleigh statistics. Also, adding beampattern affects to the mixture study did not change the results presented in Section 6.2.2.

#### **6.2.4 Sound velocity profile study**

Stanic and Kennedy's [13, 14] probability of false alarm (PFA) plots do not appear to be consistent with other published PFA plots. Fluctuations in the data from a stationary measurement system are caused by ping to ping variations in the water column refraction that cause the scattering patch to be shifted about the bottom. The objective of this study is to determine whether the sound velocity profile (SVP) provides enough variability in the data that when coupled with the sediment variation, the non-Rayleigh statistics shown in Stanic and Kennedy's data (see *Figures 4-7 and 4-8*) occur.

To perform the study, a baseline ensemble was formed by varying the surface roughness input parameter  $w_2$  to the backscatter model. The SVP was divided into depths of 0, 20, 40, 60, and 80 meters with the source and receiver at 20 meters. For the baseline, the SVP was isovelocity and the source and receiver were omnidirectional. Next, both the surface roughness parameter and the SVP were varied simultaneously. A Gaussian distribution with a mean of 1500 meters/second and a standard deviation of 2 meters/second was generated for sound speeds. (A standard deviation of 2 meters/second is a large variation in sound speed and represents an extreme case of variability.) A new value chosen from this distribution was assigned to each of the five depths for

generating each of the 24 intensities at the 72 time slices. *Figure 6-20* displays the Gaussian histogram of sound speeds and the resulting normalized distribution of the fluctuation in the grazing angle to the bottom caused by varying the SVP. The bottom grazing angles fluctuate around the mean with a standard deviation of approximately 1 degree. *Figure 6-21* compares the baseline PFA generated with the isovelocity SVP to the PFA generated by varying the SVP at each sample point in the ensemble. The acceptance level of the baseline is 100% and the acceptance level with the varied SVP is above 96%.

The conclusion of this study is that the sound velocity profile (SVP) does not provide enough variability in the data to cause the non-Rayleigh statistics shown in Stanic and Kennedy's data.

### **6.3 Summary**

The purpose of the simulation studies was to investigate the hypotheses presented in Chapter 4. The studies indicated that neither stationary surface roughness, volume scattering nor a combination of both caused non-Rayleigh statistics. However, non-stationary surface roughness caused by adding patches of gravel to a mud sediment did cause non-Rayleigh results. Wide beams gave similar statistics as narrow beams indicating that beamwidth is not a factor in affecting the statistics. Also, like temporal correlation discussed in Chapter 5, spatial correlation caused by overlapping beams ensonifying portions of the same area on the bottom did not affect the statistics. And, finally, variations in the sound velocity profile did not provide enough variability in the data even when coupled with the sediment variation to produce non-Rayleigh statistics.

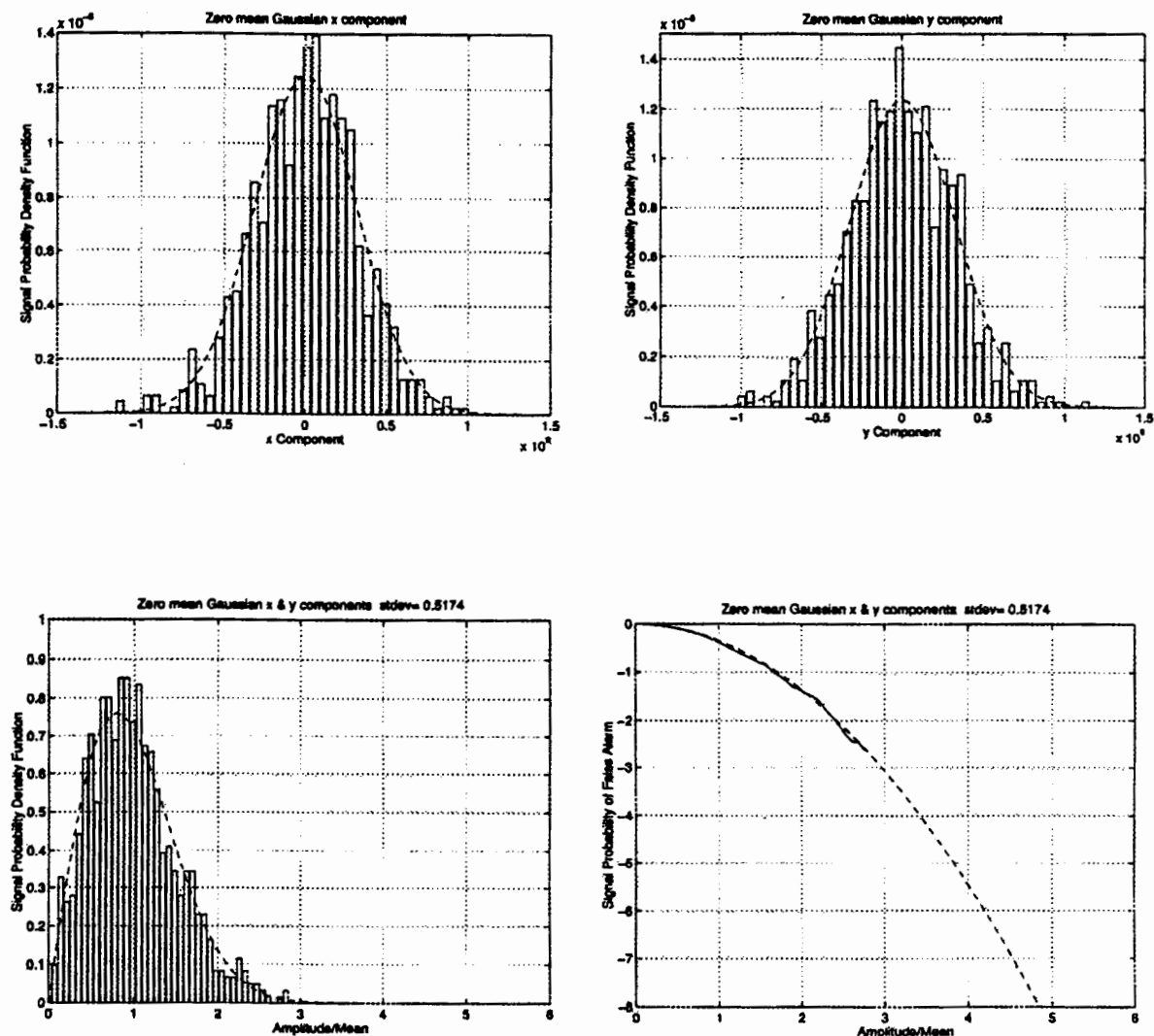


Figure 6-1: Example of simulation verification test where zero mean Gaussian distributions are used to generate the  $x$  and  $y$  components of the pressure amplitude. The top two plots are histograms of the  $x$  and  $y$  components with the dashed line being the Gaussian distribution. The bottom two plots are the histogram and PFA of the simulated reverberation with the dashed line being the Rayleigh distribution.

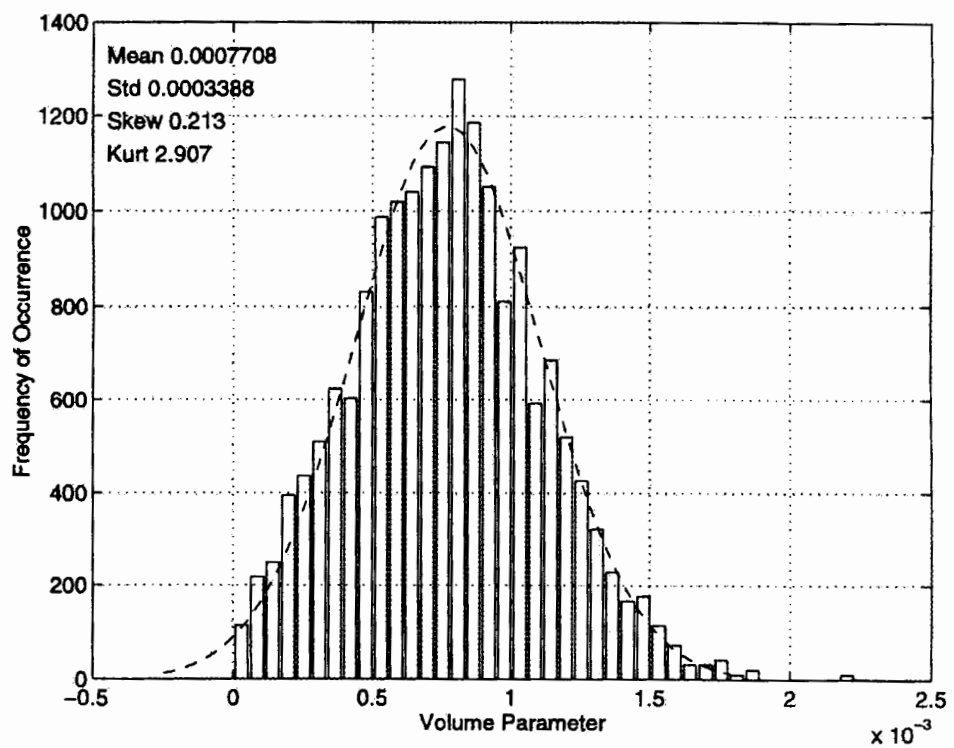
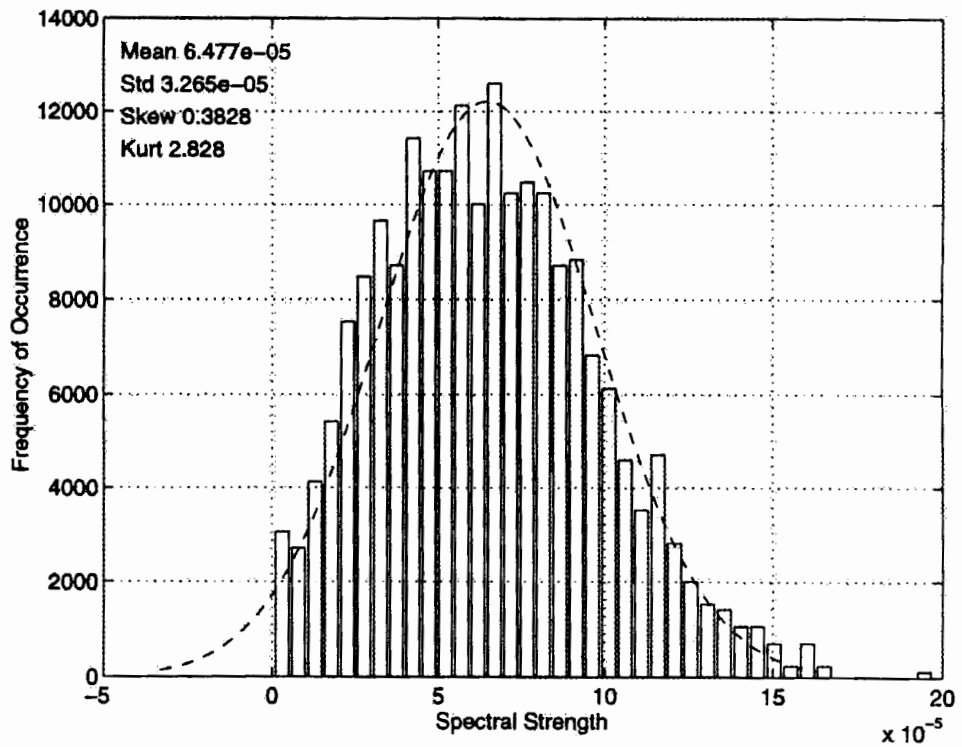


Figure 6-2: Skewed Gaussian distributions for the spectral strength parameter  $w_2$  and the sediment volume parameter  $\sigma_2$  input to the backscatter model. The mean, standard deviation, skewness, and kurtosis are given in units of  $m^4$  for the spectral strength and are dimensionless for the volume parameter.

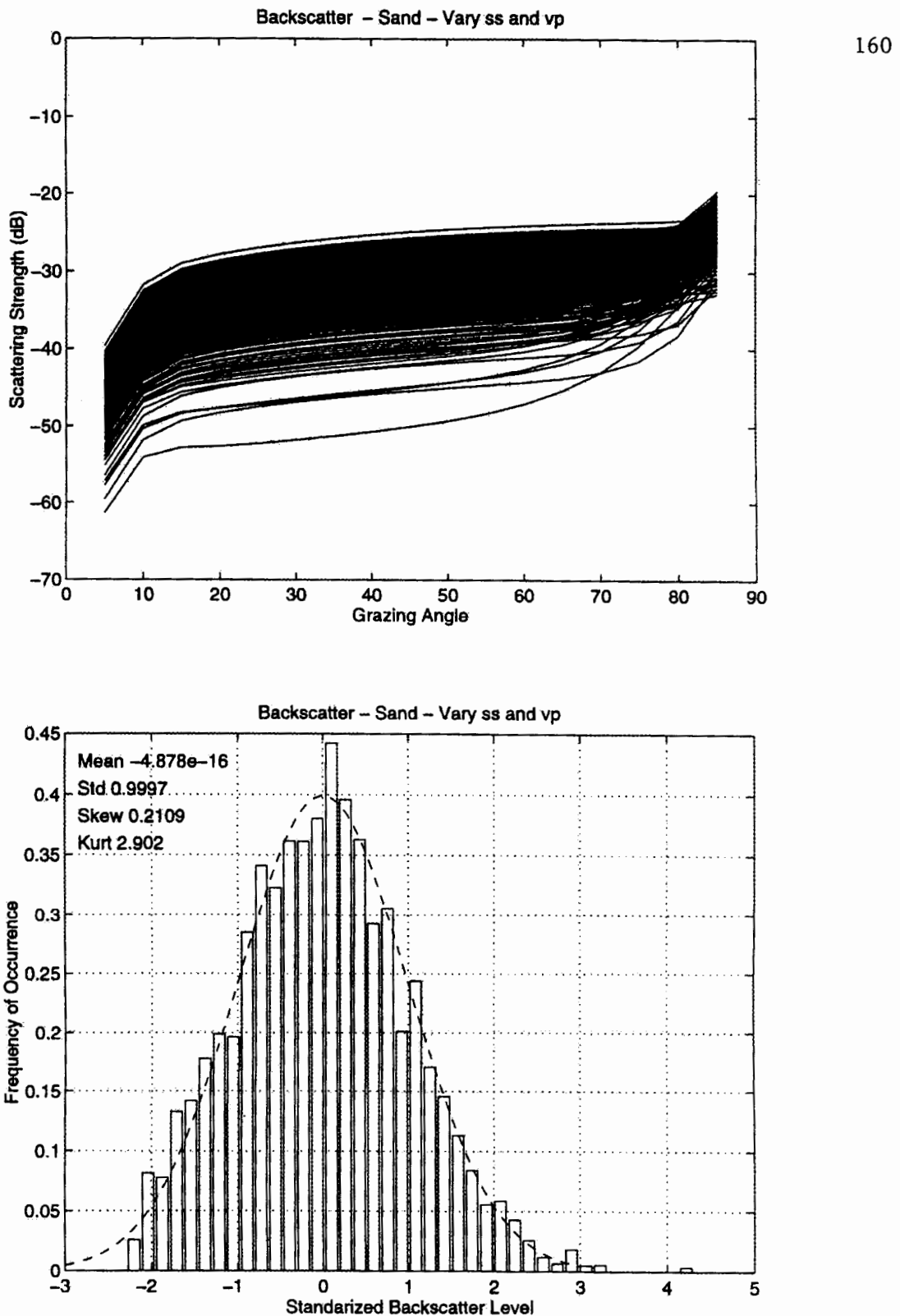


Figure 6-3: Backscatter curves for 5 to 85 degree grazing angles and the corresponding normalized histogram when the spectral strength (labeled ss on plots) and volume parameter (labeled vp on the plots) are varied simultaneously.

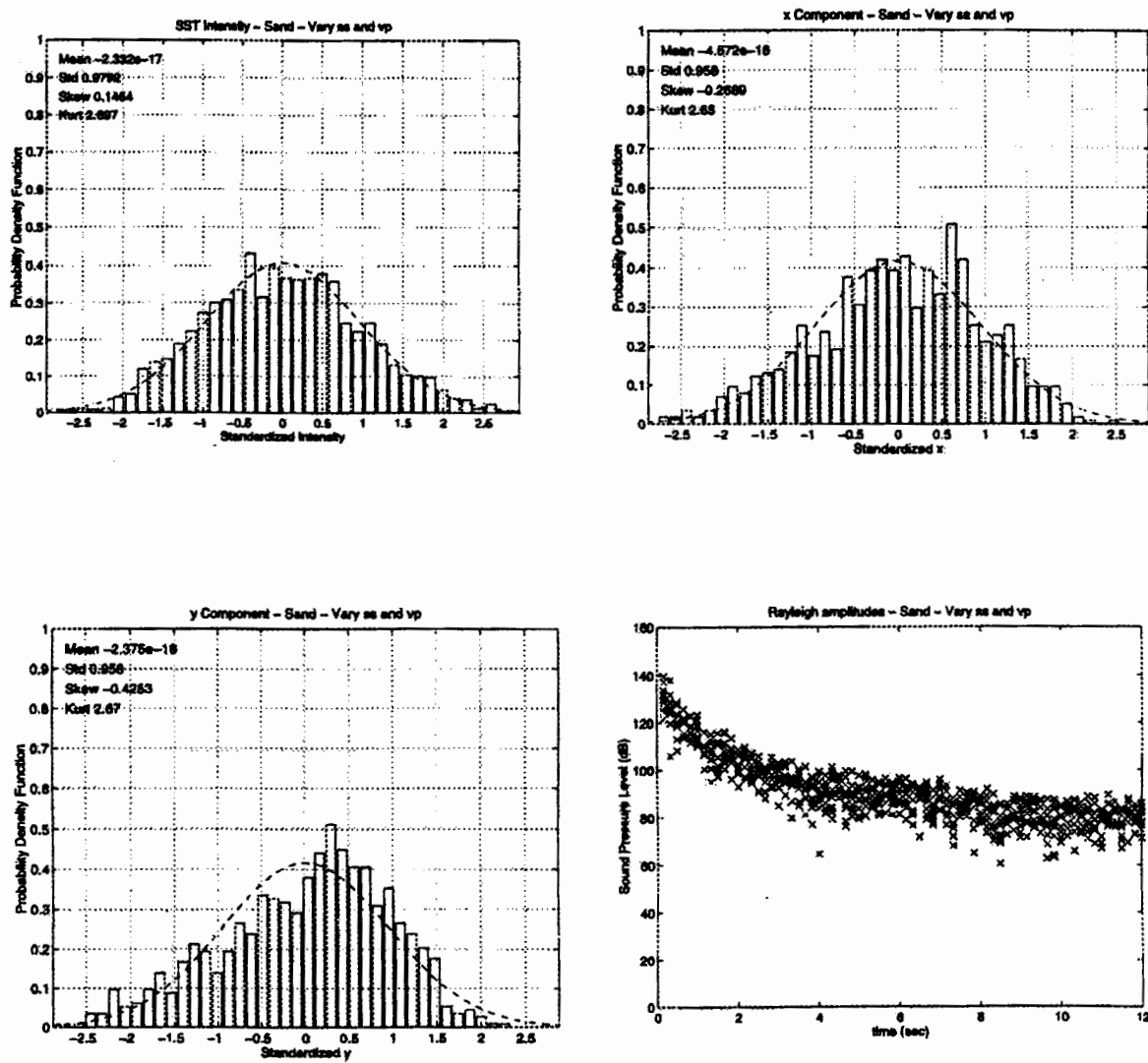


Figure 6-4: Standardized histograms of intensities, zero mean Gaussian  $x$  and  $y$  components, and amplitude time series generated by the simulation.

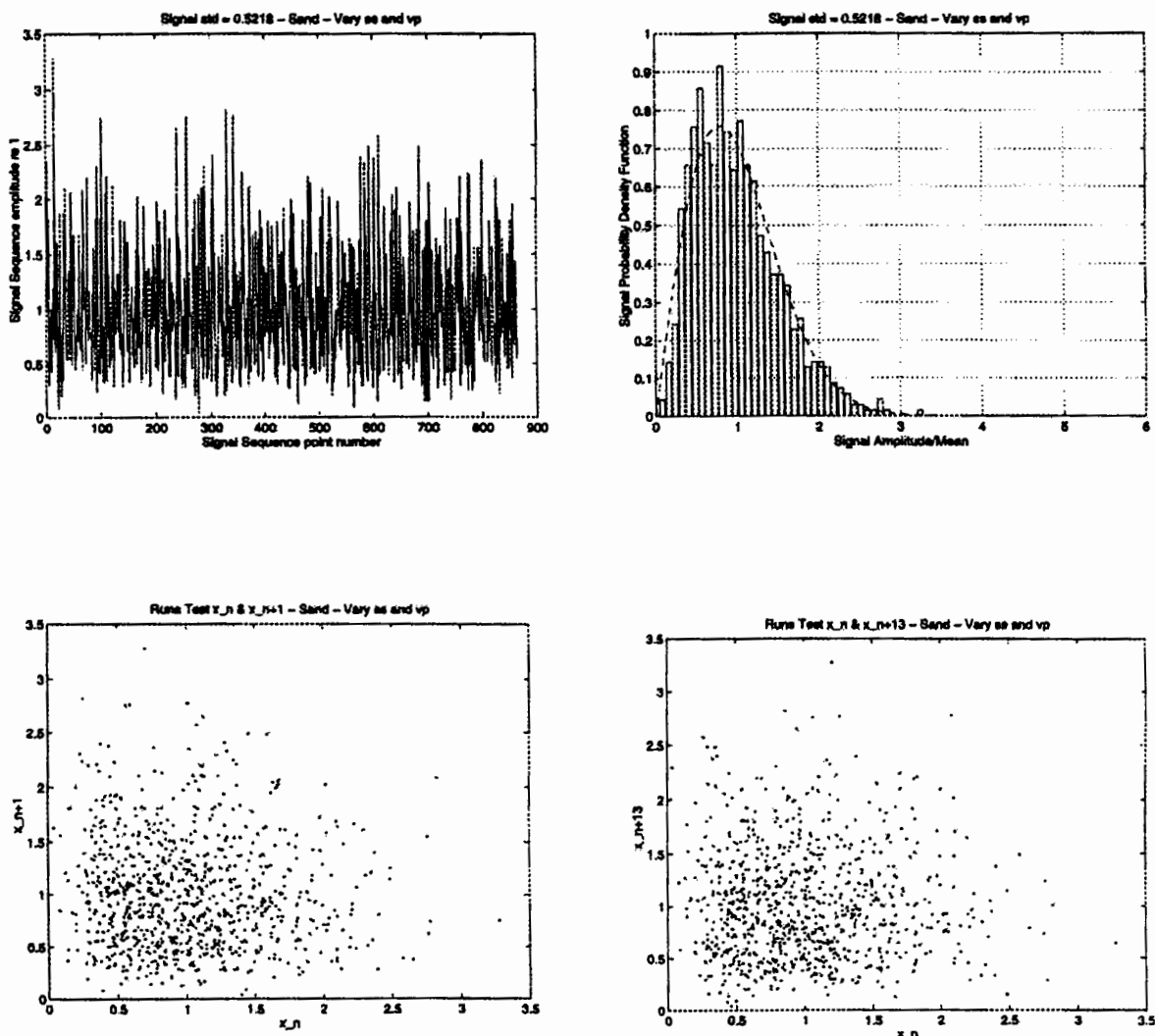


Figure 6-5: Normalized fluctuation sequence, its histogram, and the runs tests for the twelve amplitude reverberation time series shown in the lower right corner of Figure 6-4.

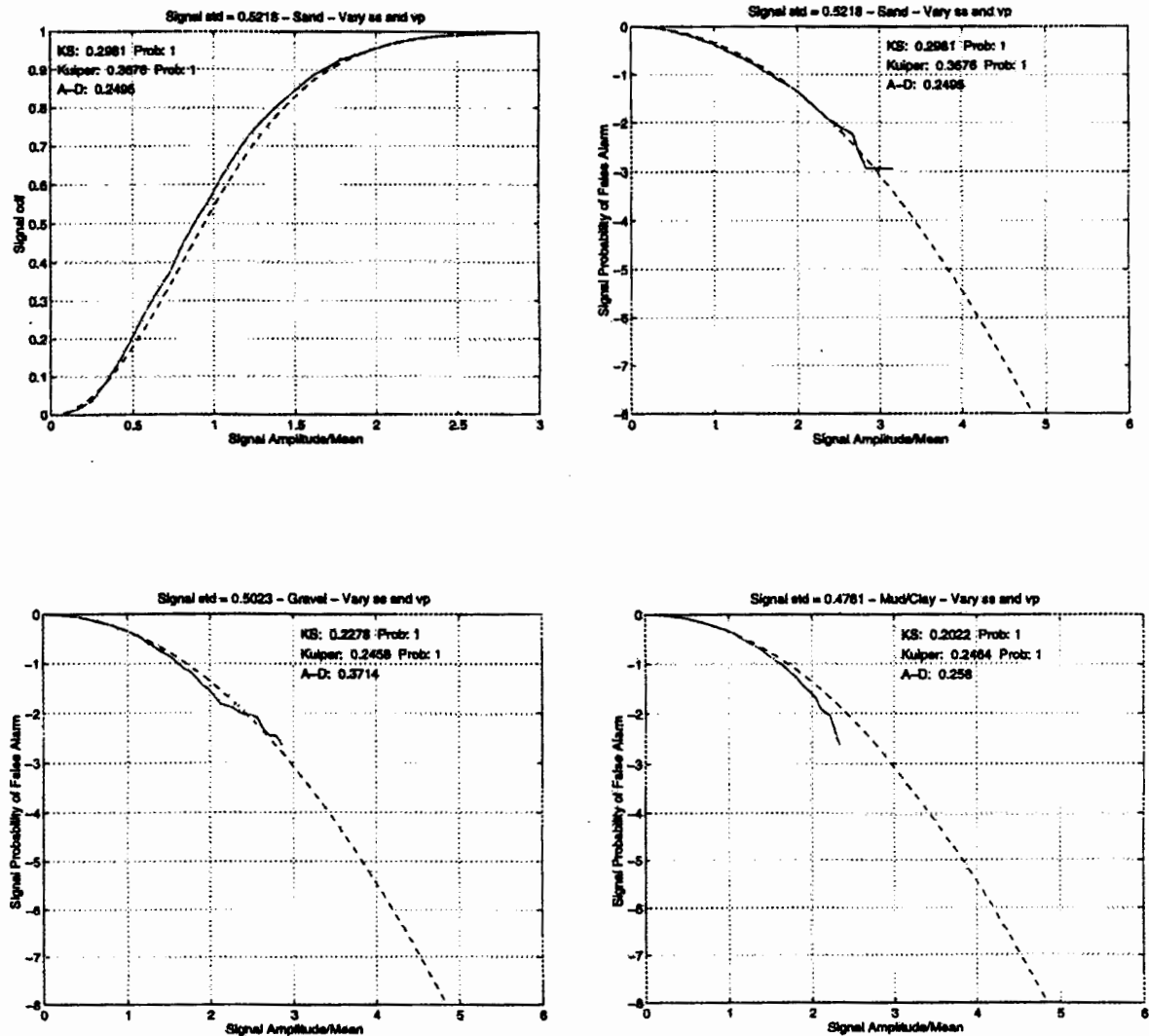


Figure 6-6: The cumulative distribution (cdf) of sand and the PFAs for all three bottoms (sand, gravel, and mud/clay) are presented with the test statistics printed on the plots. The test statistics indicate that the null hypothesis cannot be rejected.

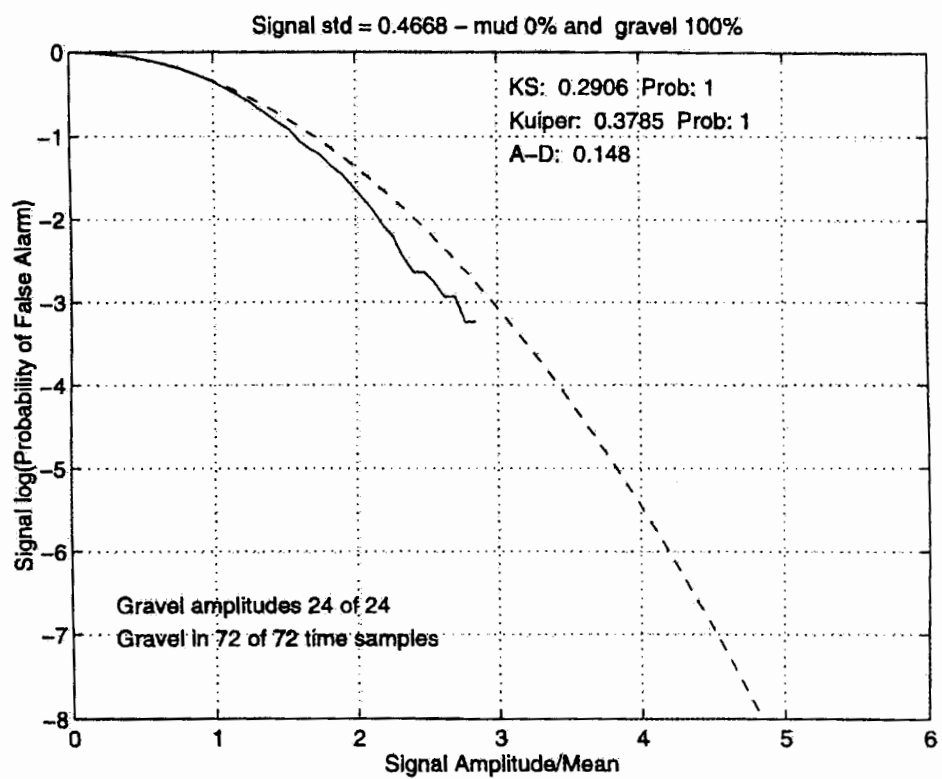
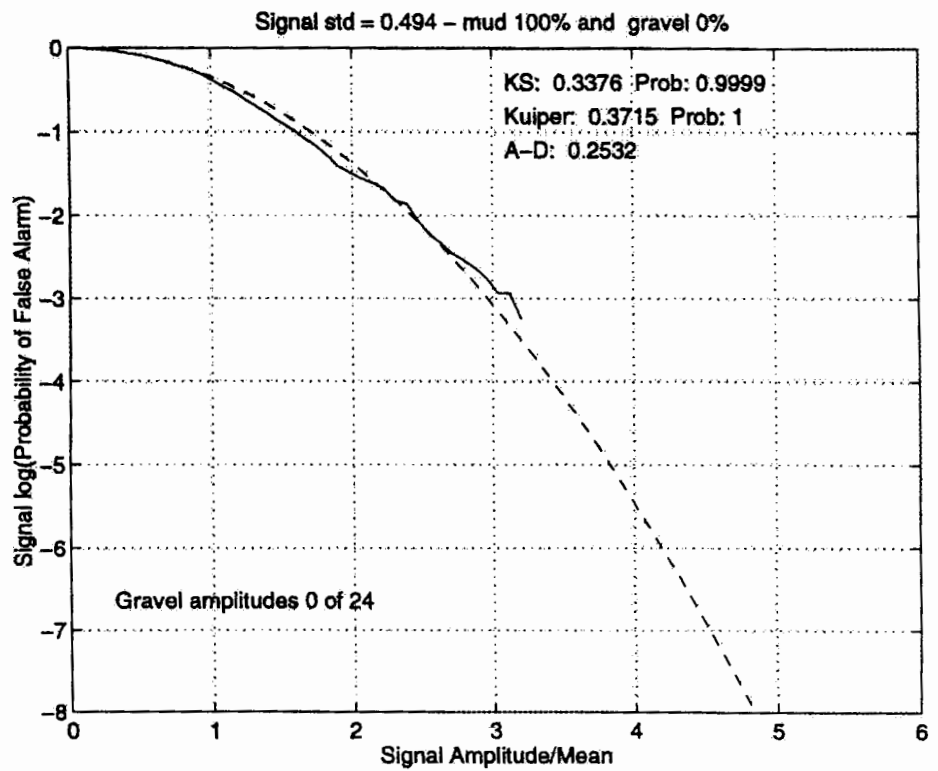


Figure 6-7: a) The top plot is the PFA for the all mud sediment. b) The bottom plot is the PFA for the all gravel sediment.

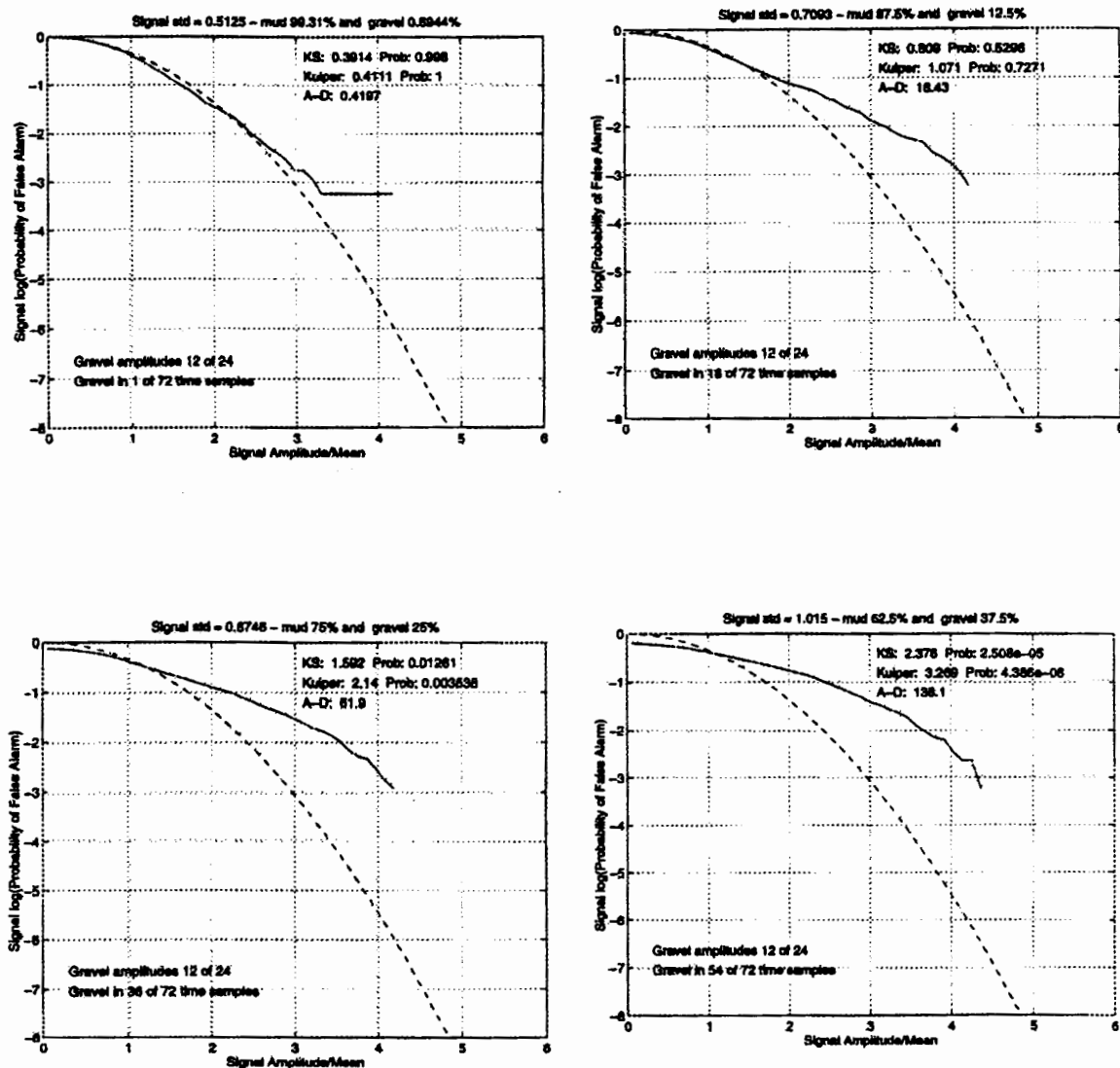


Figure 6-8: PFAs when 12 gravel amplitudes out of 24 are added to 1, 18, 36, and 54 time slices.

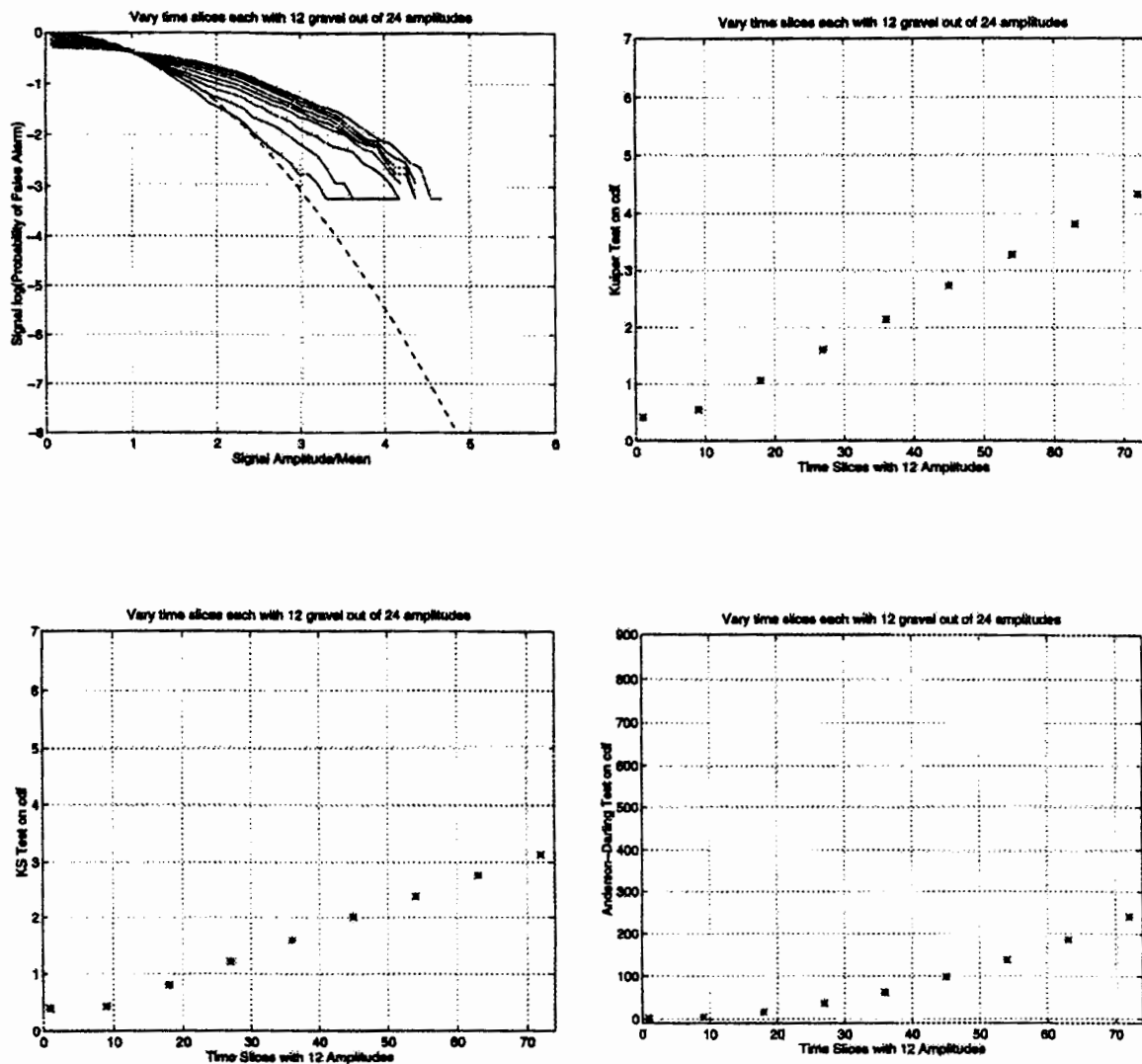


Figure 6-9: An overlay of PFAs from mixing 12 gravel amplitudes with 12 mud amplitudes for 1, 9, 18, 27, 36, 45, 54, 63, and 72 time slices and the three test statistics for each of the PFAs. The test statistics are plotted against the number of time slices containing the 12 gravel amplitudes.

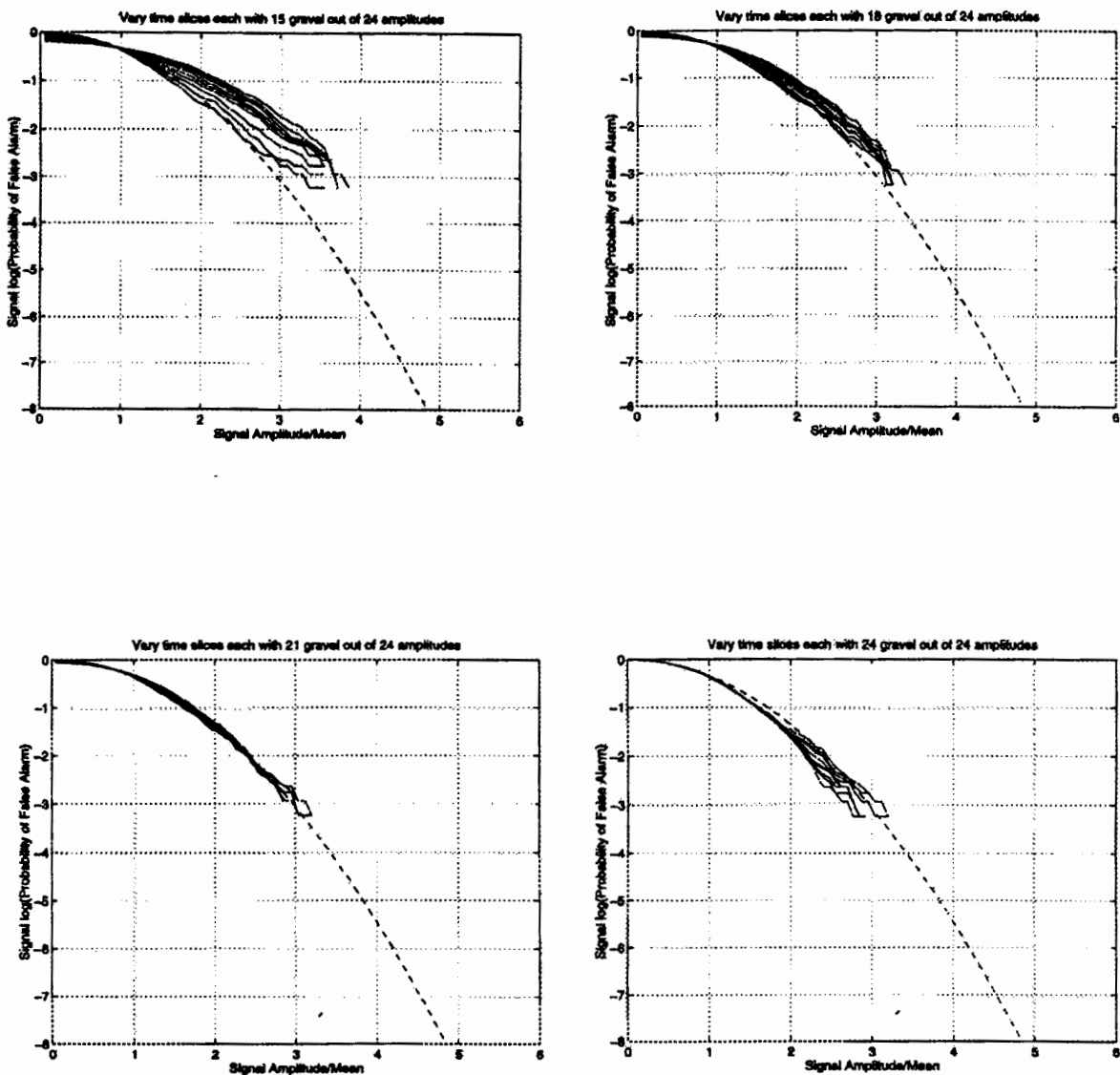


Figure 6-10: The combined PFA plots when 15, 18, 21, and 24 gravel amplitudes are added, respectively, to 1, 9, 18, 27, 36, 45, 54, 62, and 72 time slices.

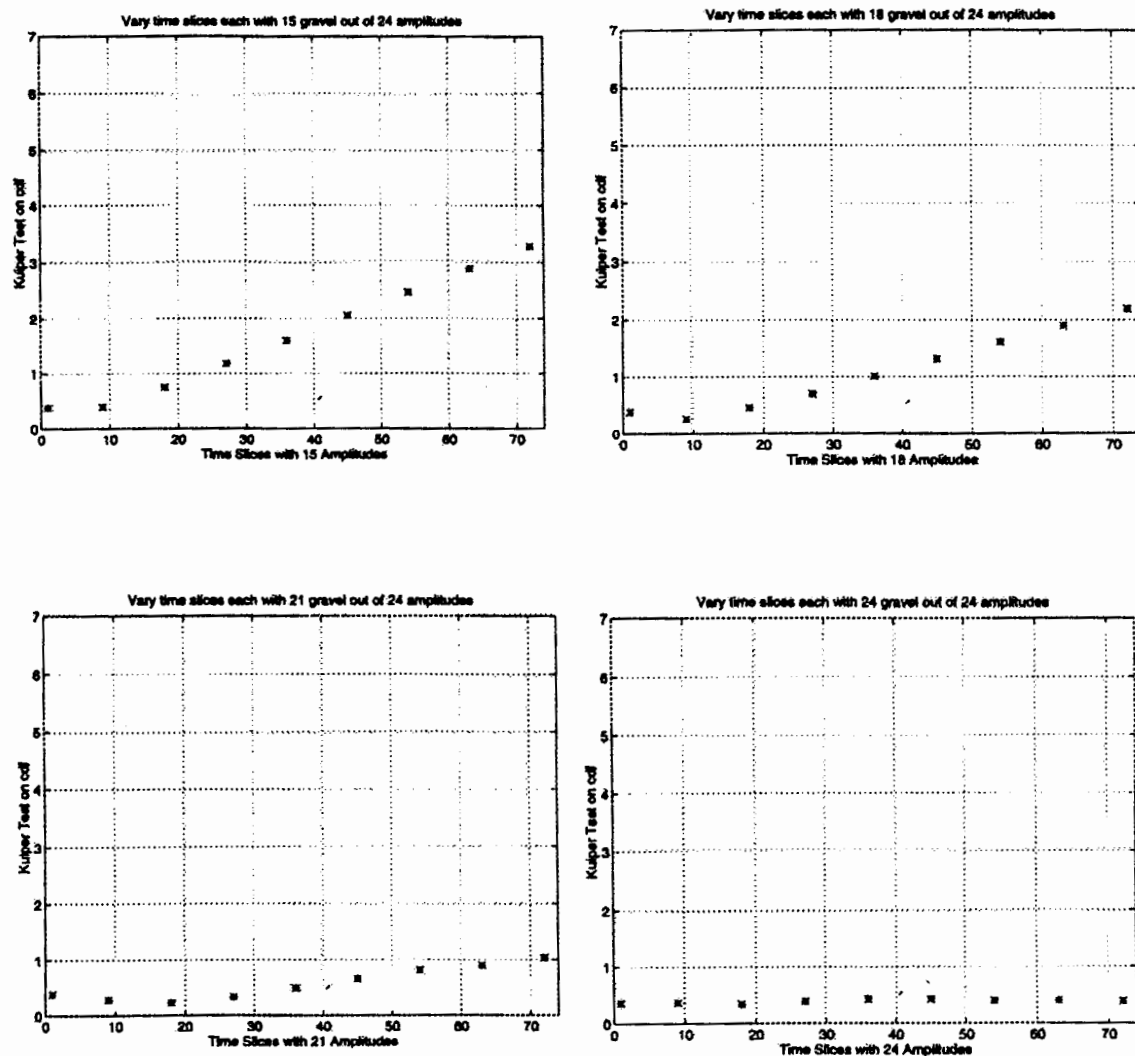


Figure 6-11: The corresponding Kuiper's test statistic for each of the plots shown in Figure 6-10.

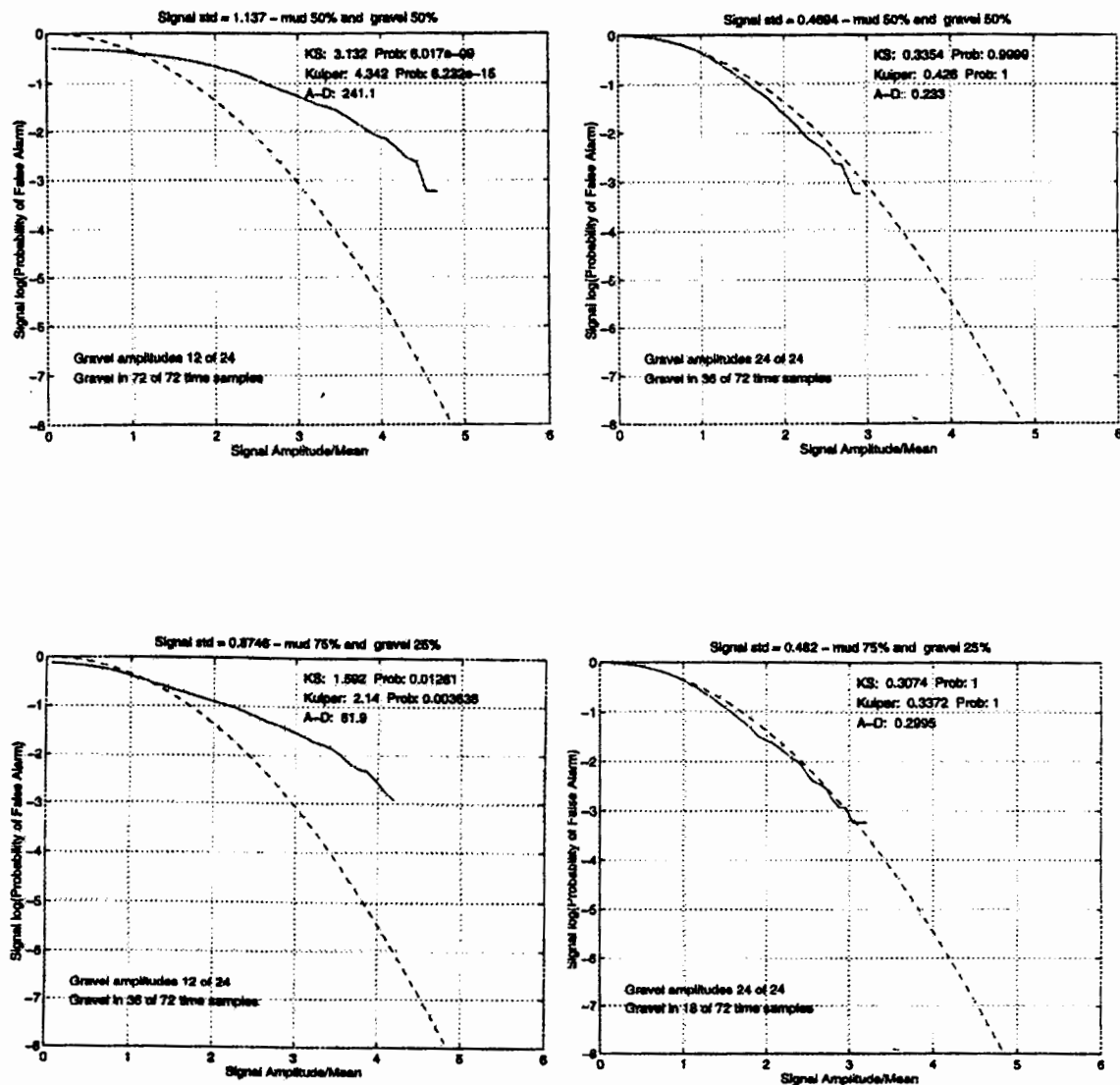
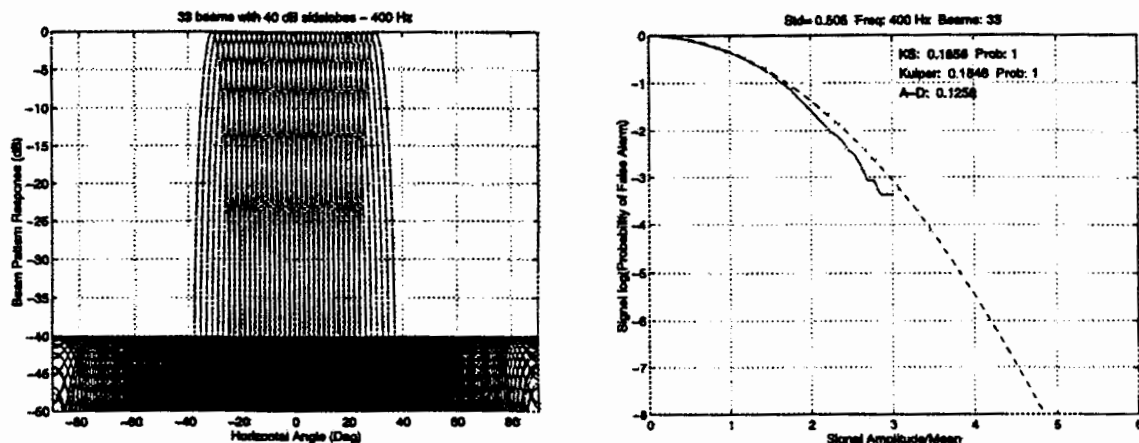


Figure 6-12: The top two PFAs compare two different mixes of 50% mud and 50 % gravel — one is Rayleigh and one is not. The bottom two PFAs compare two different mixes of 75% mud and 25% gravel — again, one is Rayleigh and one is not.

### Wide Beams (400 Hz)



### Narrow Beams (750 Hz)

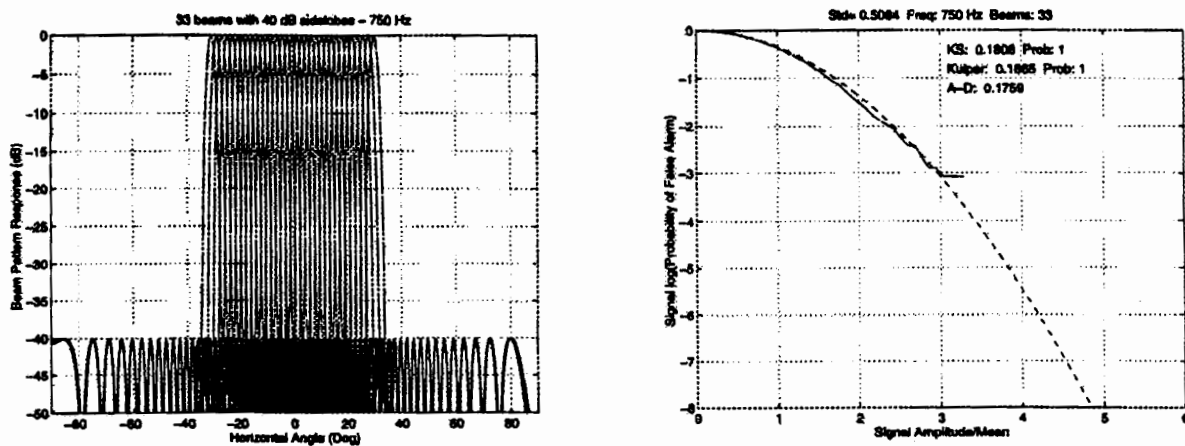
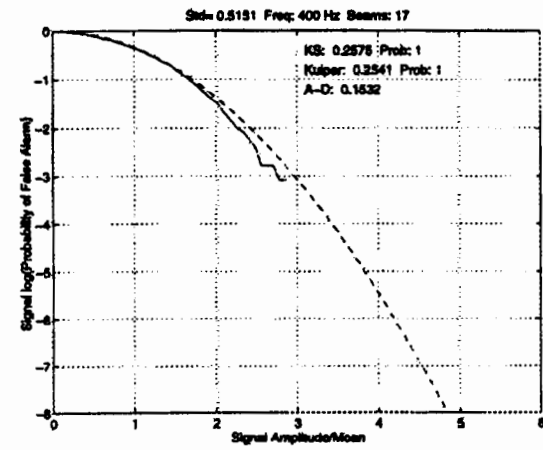
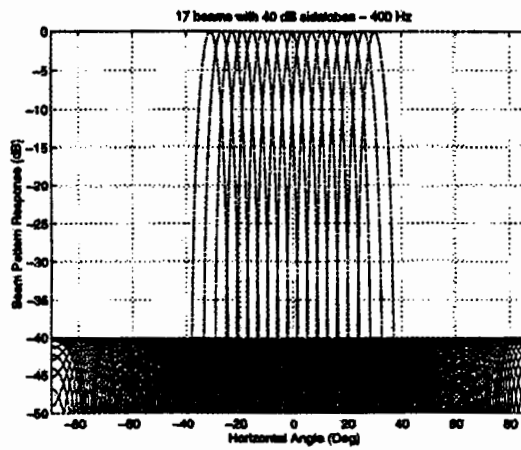


Figure 6-13: Comparison of PFAs processed with 33 beams between +30 and -30 degrees centered around the broadside beam for wide beams (400 Hz) and narrow beams (750 Hz).

### Wide Beams (400 Hz)



### Narrow Beams (750 Hz)

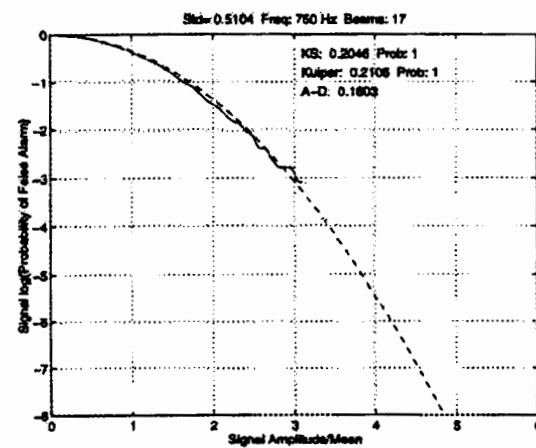
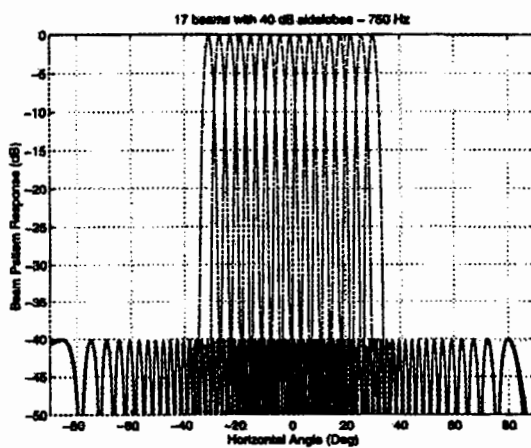
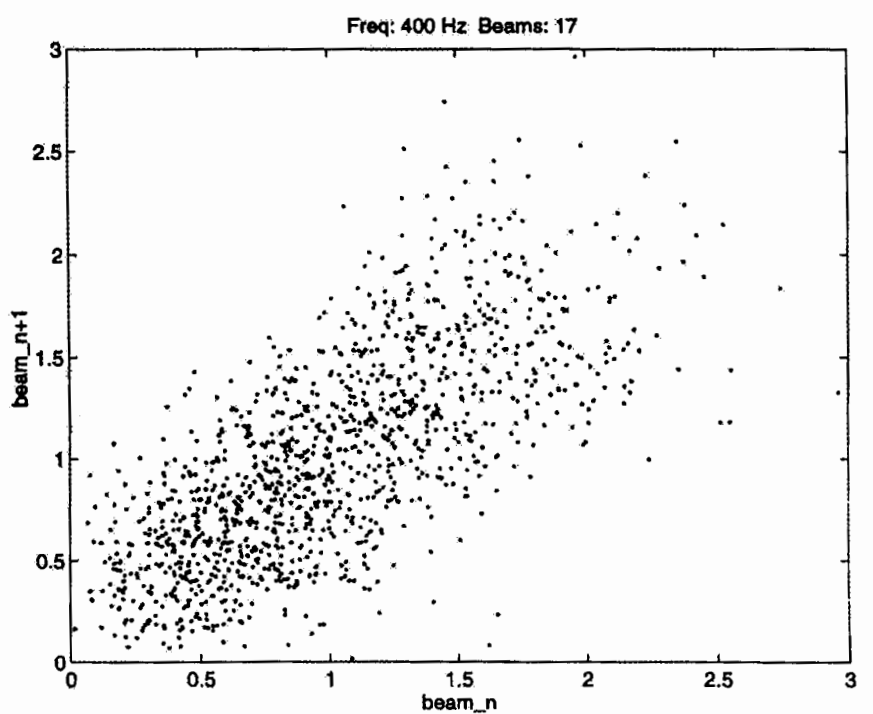


Figure 6-14: Comparison of PFAs processed with every other beam between +30 and -30 degrees giving a total of 17 beams for wide beams (400 Hz) and narrow beams (750 Hz).

### Wide Beams (400 Hz)

172



### Narrow Beams (750 Hz)

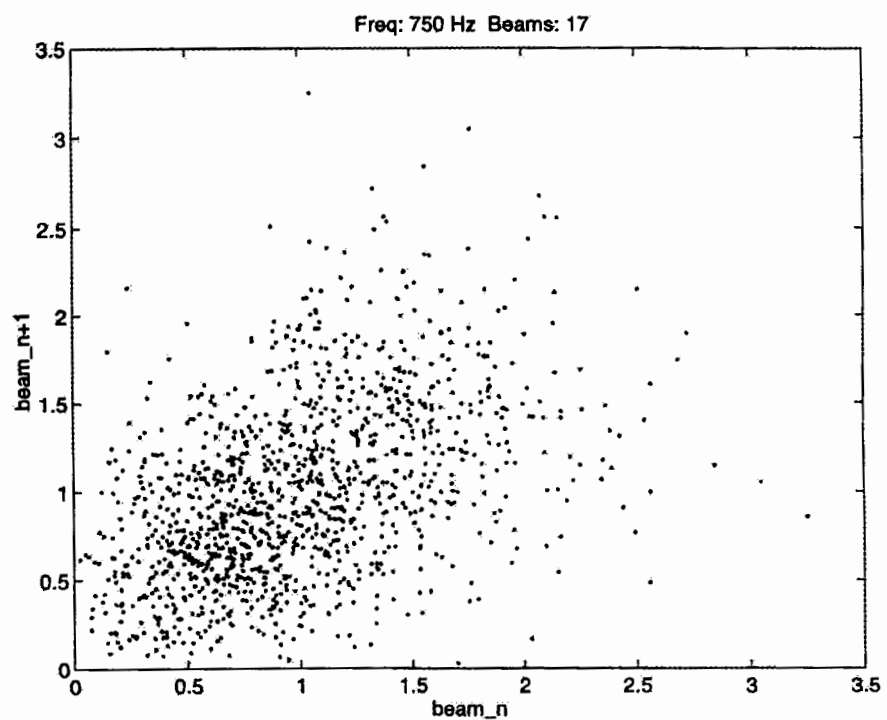
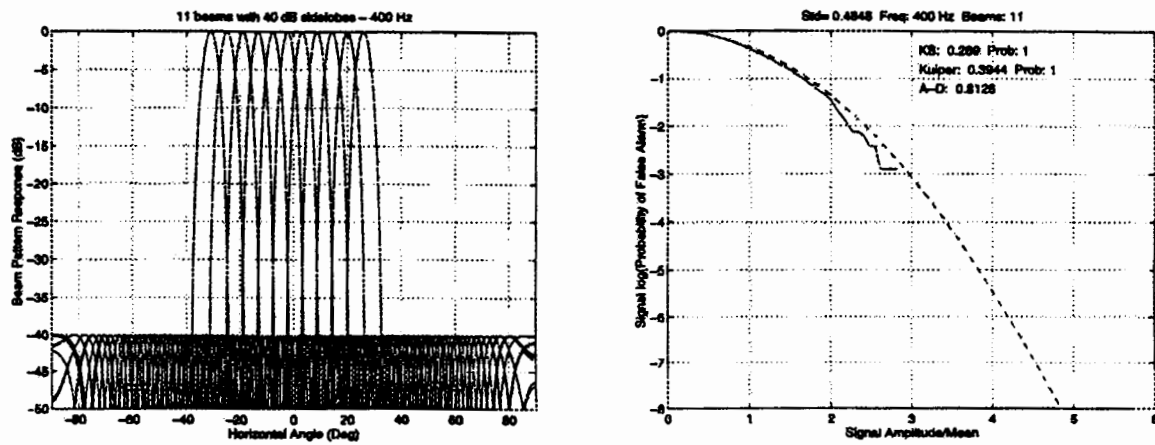


Figure 6-15: The beam to beam runs test for the 17 wide (400 Hz) and narrow (750 Hz) beams.

### Wide Beams (400 Hz)



### Narrow Beams (750 Hz)

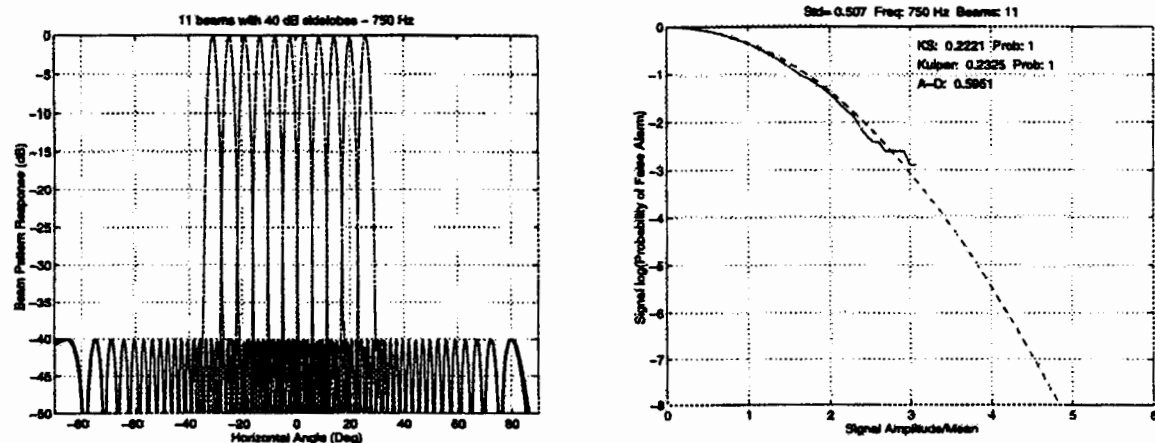


Figure 6-16: Comparison of PFAs processed with every second beam between +30 and -30 degrees giving a total of 11 beams for wide beams (400 Hz) and narrow beams (750 Hz).

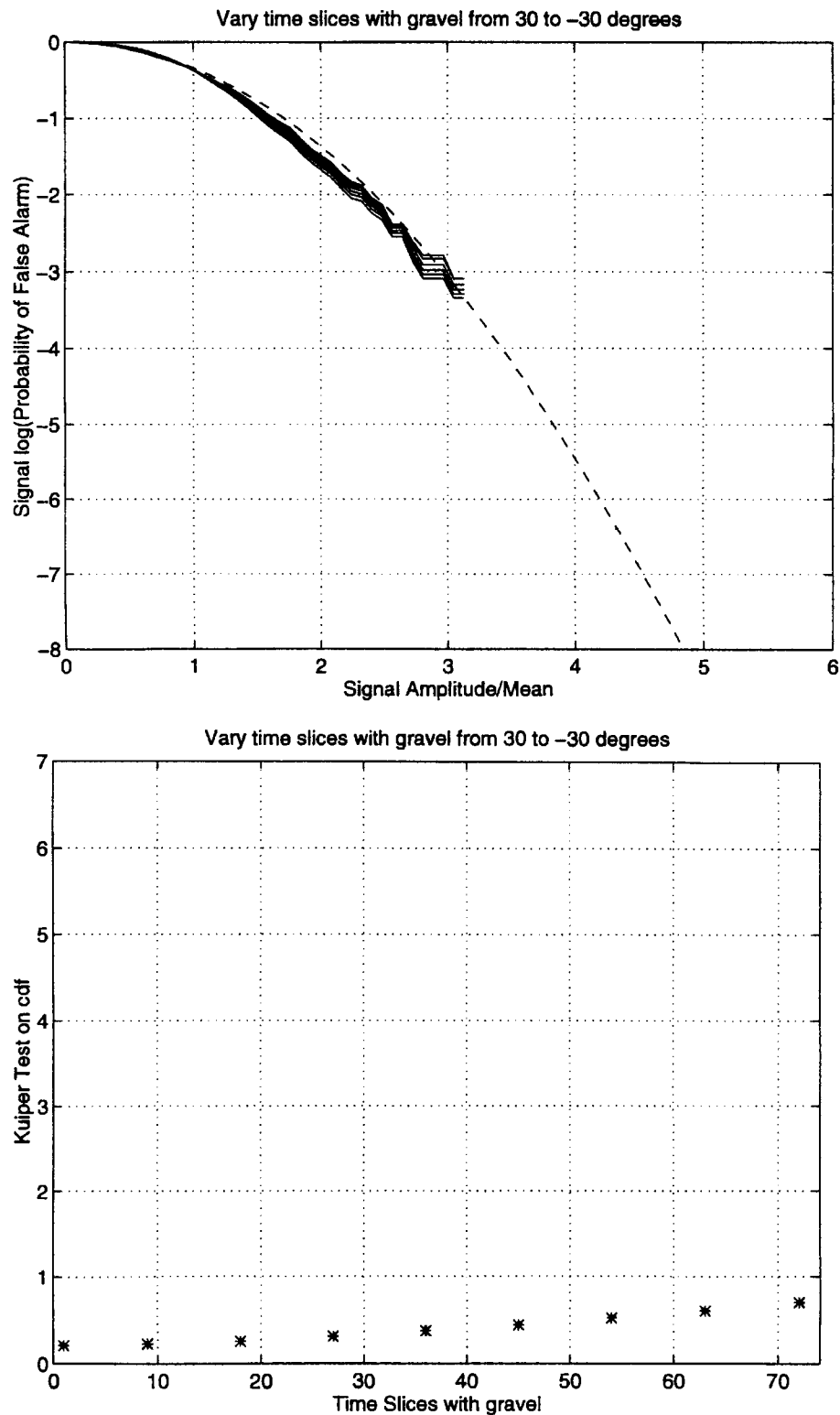


Figure 6-17: Example results when the gravel patch was seen in the mainlobes of all 17 beams as the number of time slices containing gravel was varied. The PFAs were formed by processing every other beam between +30 and -30 degrees giving a total of 17 beams at 400 Hz. The Kuiper's test statistic versus the number of time slices with gravel is also shown. All acceptance levels were above 88%.

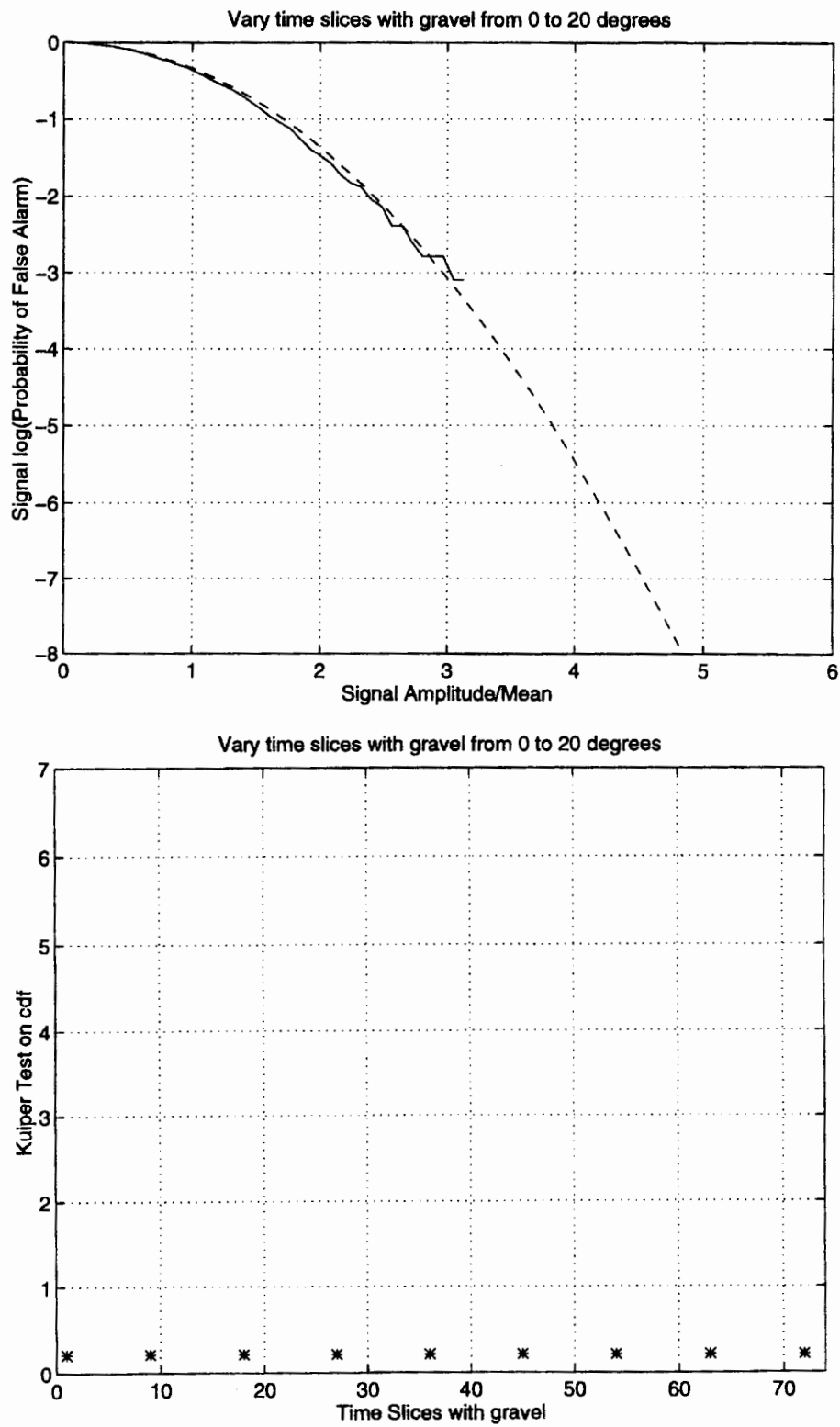


Figure 6-18: Example results when the gravel patch was seen only in the sidelobes of the 17 beams as the number of time slices containing gravel was varied and the corresponding Kuiper's test statistic versus the number of time slices containing gravel. All PFAs were identical and the acceptance levels were all 100%.

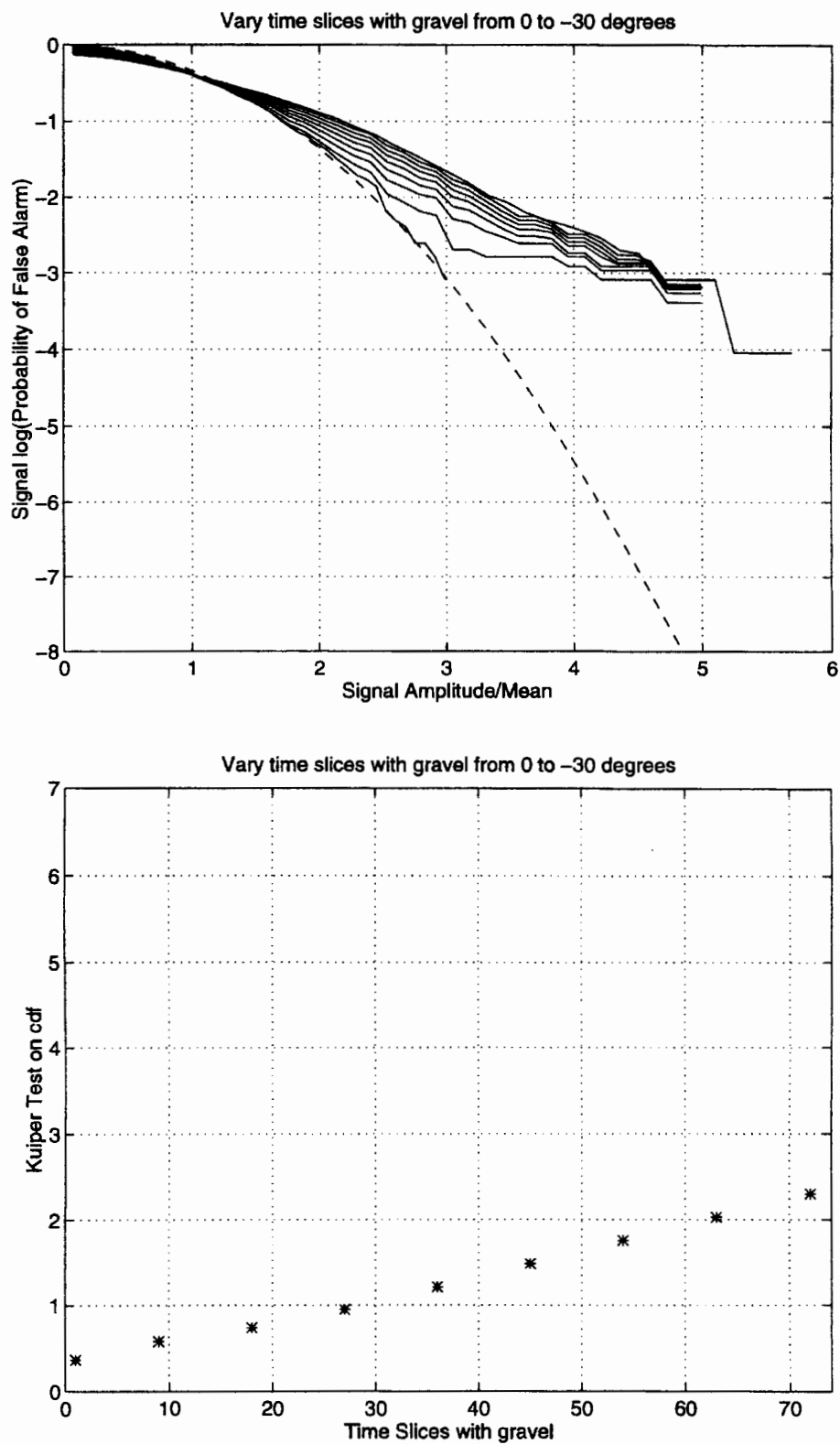


Figure 6-19: Example results when the gravel patch was seen by half of the 17 beams as the number of time slices containing gravel was varied and the corresponding Kuiper's test statistic versus the number of time slices containing gravel. The PFAs and acceptance levels get further away from Rayleigh as the number of time slices containing gravel increases.

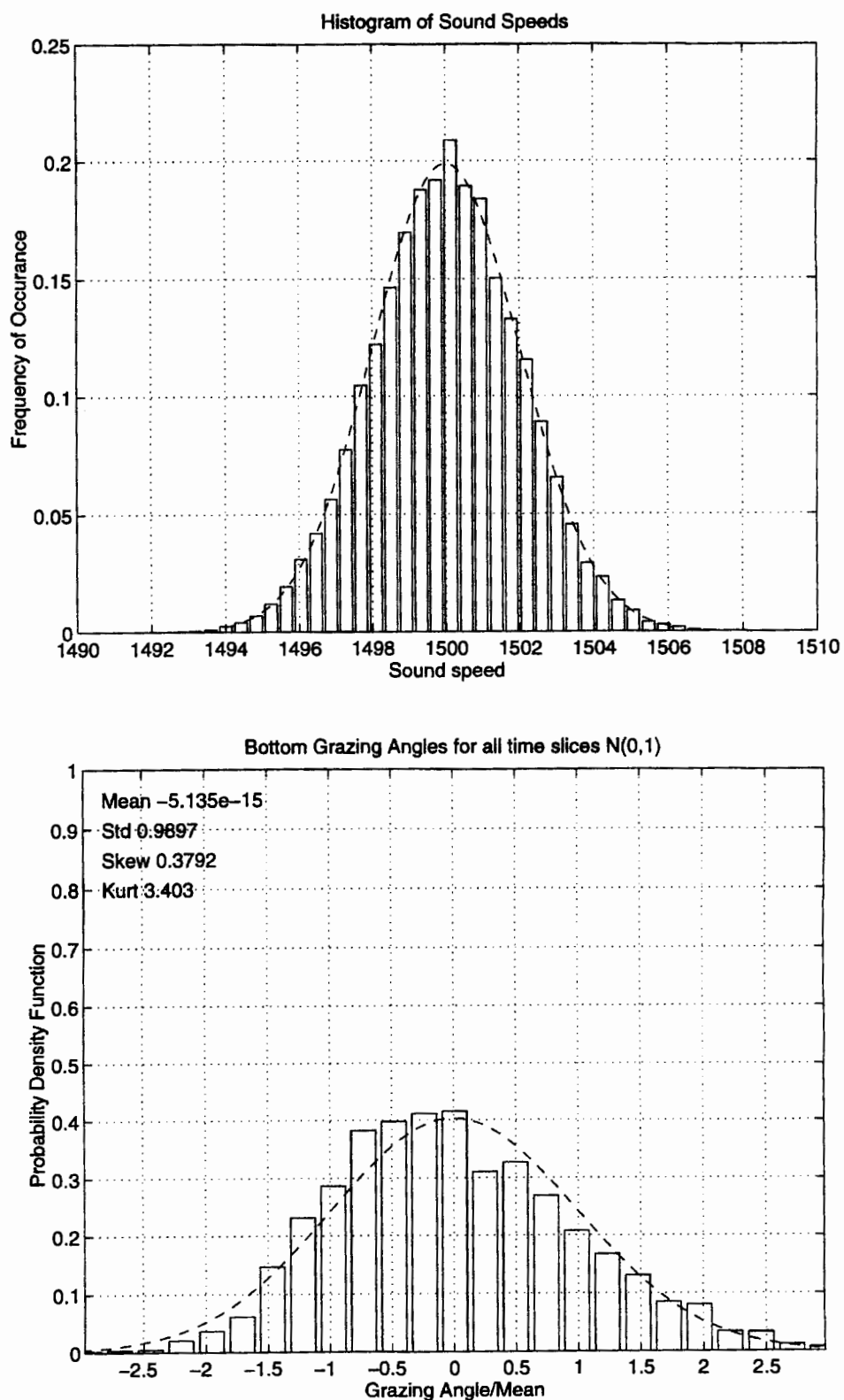


Figure 6-20: Gaussian histogram of sound speeds and the resulting normalized distribution of the fluctuation in bottom grazing angle caused by varying the SVP.

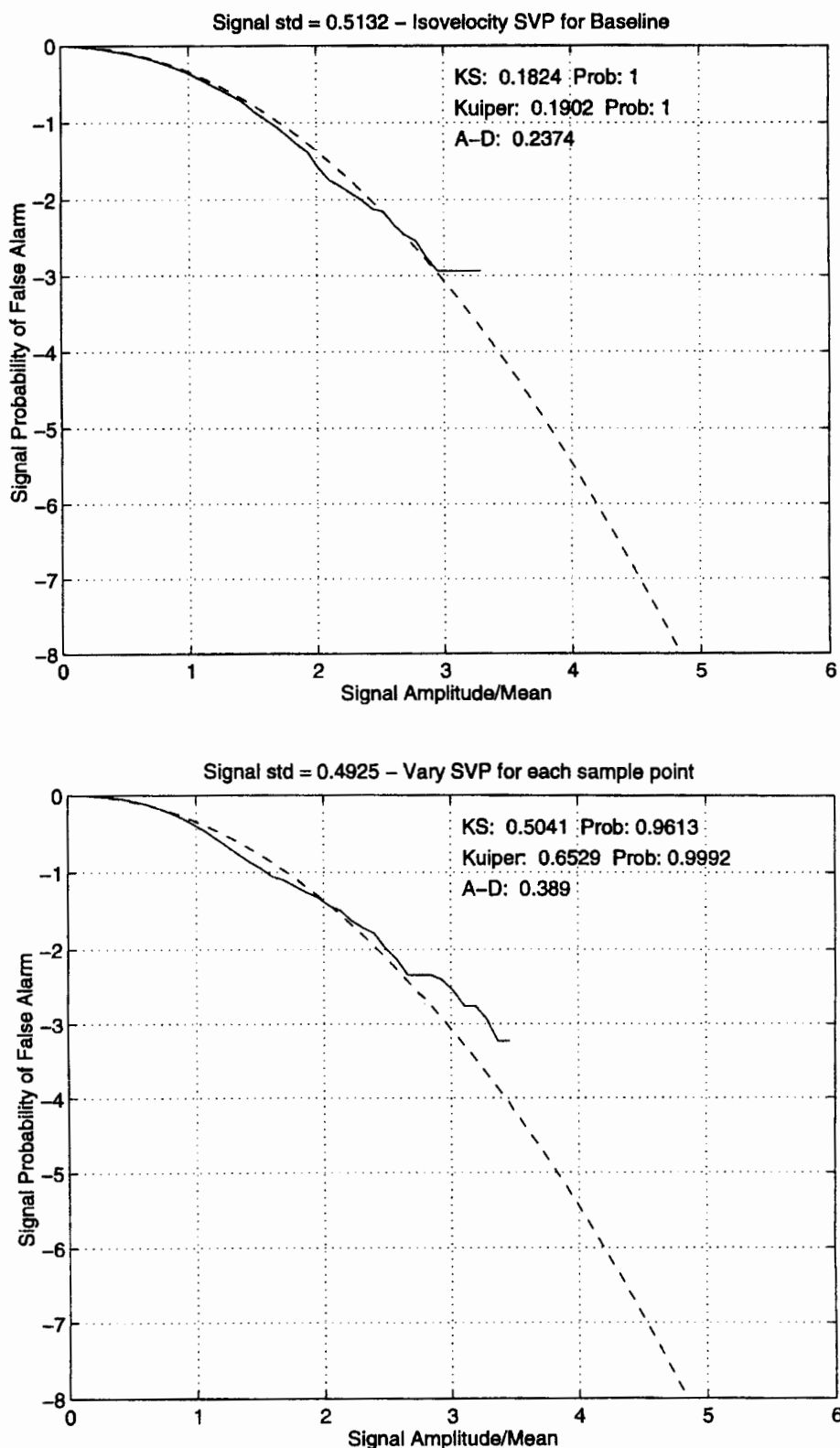


Figure 6-21: The baseline PFA generated with the isovelocity SVP compared to the PFA generated by varying the SVP at each sample point in the ensemble. The acceptance level of the baseline is 100% and the acceptance level with the varied SVP is above 96%.

## Chapter 7

### CONCLUSIONS

#### 7.1 Thesis Summary

This thesis documented measured fluctuation statistics for a variety of environments and frequencies. The probability of false alarm PFA curves were displayed in *Figures 4-4* through *4-8* for high frequency (20 to 180 kiloHertz), shallow water sediment reverberation. The curves were obtained by electronically digitizing the fluctuation statistics published in five articles and converting the independent axes to the normalized amplitude. *Table 4-1* list the titles and references for the articles, as well as frequencies used in the experiments and the sediment bottom types. Chapter 5 presented low frequency (365 to 1280 Hertz) data obtained from two different shallow water experiments conducted by the SACLANT Centre and analyzed as part of this research. The analysis provided PFAs for continuous wave and hyperbolic frequency modulated pulses and explosive charges with sediment types being mainly chalk, limestone, and clay.

More importantly, this thesis determined through simulation the sensitivity of the fluctuation statistics to changes in the distributions of sediment parameters and to small scale variability in the sound speed profile; determined the effect of stationary and non-stationary realizations of the bottom with and without beampattern effects; and, postulated a theory that non-Rayleigh statistics occur when sediment “patchiness” is present. The main objective of the simulation studies were to investigate hypotheses postulated in the open literature and listed in

*Table 4-2.* These hypotheses and the conclusions drawn from the research in this thesis on these hypotheses are as follows:

1. Hypothesis: Non-Rayleigh bottom reverberation fluctuation statistics are caused by scattering from interface roughness [68] or by a non-random combination of interface scattering with sediment volume scattering [74, 75]. The conclusion drawn from the simulation study indicated that even with the largest published variability in surface roughness and volume scattering for sand, muddy clay, and gravel, neither interface roughness nor a combination of both interface scattering and volume scattering caused the statistics to become non-Rayleigh.
2. Hypothesis: Non-Rayleigh bottom reverberation fluctuation statistics are caused by spatial inhomogeneity or patchiness of the surface interface [10, 70, 75]. The conclusion drawn from the simulation study indicated that patchy sediments were sufficient to produce non-Rayleigh statistics and that the spatial and temporal extent of the patch are key factors in producing the non-Rayleigh statistics.
3. Hypothesis: Non-Rayleigh bottom reverberation fluctuation statistics are affected by the receiving beamwidth [8, 16, 17]. The conclusion drawn from the simulation study indicated that beamwidth had little or no effect on the statistics and therefore, was not a major factor in contributing to non-Rayleigh statistics.
4. Hypothesis: Non-Rayleigh bottom reverberation fluctuation statistics [13, 14] were caused by the combined variability of the sound velocity profile SVP and the sediment scattering. The conclusion drawn from the simulation study indicated that the combined variability in the SVP and sediment parameter were not enough to cause the large variability in the data displayed in *Figures 4-7 and 4-8.*

The overall results of this research indicated that sediment type, frequency, pulse type, and pulse length are not a factor *per se* in the deviations of the statistics from Rayleigh. These factors produced both Rayleigh and non-Rayleigh results. However, sediment “patchiness” defined as an ensonified area containing patches which contribute largely different backscattering strengths within the area, did cause the statistics to deviate from Rayleigh. The simulated data reinforced these conclusions and provided insight into the spatial and temporal extent of the “patchiness” required to cause a deviation in the statistics.

## **7.2 Future Research**

Although this thesis investigated many of the postulated theories in the open literature, much work remains on providing a thorough understanding of the complex physical nature of bottom reverberation. Other areas of recommended work include investigating the effect of wind speed variability to determine if the injection of this second random component is enough to cause the fluctuation statistics to be Rayleigh as indicated by the statistics presented for Site C in Section 5.2.3. Additional research needs to be performed to determine the relationship between frequency, patchiness, and the statistics; and to determine if non-stationary volume scatterers produce the same “patchiness” found for non-stationary surface scatterers and to determine what role frequency plays in both these types of non-stationary scattering. Also, understanding the effect of bistatic geometries and broadband transmission on the fluctuation statistics remains to be investigated.

## REFERENCES

1. R. J. Urick, Principles of Underwater Sound, Third edition, McGraw-Hill Book Company, New York, 1983.
2. D. R. Jackson and K. B. Briggs, "High-frequency bottom backscattering: Roughness versus sediment volume scattering," *J. Acoust. Soc. Am.* 92, p 963-977 (1992).
3. J. A. Ogilvy, Theory of Wave Scattering from Random Rough Surfaces, Institute of Physics Publishing, Bristol and Philadelphia, 1991.
4. W. S. Burdic, Underwater Acoustic System Analysis, Second edition, Prentice Hall Signal Processing Series, Prentice Hall, New Jersey, 1991.
5. A. D. Whalen, Detection of Signals in Noise, Electrical Science Series, Academic Press, Inc., 1971.
6. P. D. Mourad and D. R. Jackson, "A model/data comparison for low-frequency bottom backscatter," *J. Acoust. Soc. Am.* 94 (1), p 344-358 (1993).
7. P. A. Crowther, "Fluctuation statistics of sea-bed acoustic backscatter" in Bottom Interacting Ocean Acoustics, Ed. W. A. Kuperman and F. B. Jensen, Plenum, New York, (1980).
8. N. P. Chotiros, H. Boehme, T. G. Goldsberry, S. P. Pitt, R. A. Lamb, A. L. Garcia, and R. A. Altenburg, "Acoustic backscatter at low grazing angles from the ocean bottom, Part II. Statistical characteristics of bottom backscatter at a shallow water site," *J. Acoust. Soc. Am.* 77, p 975-982 (1985).
9. T. K. Staton, "Sonar estimates of seafloor microroughness," *J. Acoust. Soc. Am.* 75 (3), p 809-818 (1984).
10. K. M. Becker, "Effect of Various Surface Height Distribution Properties on Acoustic Backscattering Statistics," Master's Thesis, Acoustic Dept., The Penn. State Univ., Univ. Park, PA, 1995.
11. J. A. Ogilvy, "Computer simulation of acoustic wave scattering from rough surfaces," *J. Phys. D: Appl. Phys.* 21, p 260-277 (1988).
12. P. D. Mourad and D. R. Jackson, "High Frequency Sonar Equation Models for Bottom Backscatter and Forward Loss," *Proc. OCEANS 89, IEEE Publication Number 89CH2780-5*, p 1168-1175 (1989).

13. S. Stanic and E. Kennedy, "Reverberation fluctuations from a smooth seafloor," *IEEE Journal of Oceanic Eng* 18 No.2, p 95-99 (1993).
14. S. Stanic and E. Kennedy, "Fluctuations of high-frequency shallow-water seafloor reverberation," *J. Acoust. Soc. Am.* 91 (4) Pt.1, p 1967-1973 (1992).
15. D. R. Jackson, D. P. Winebrenner, and A. Ishimaru, "Application of the composite roughness model to high-frequency bottom backscattering," *J. Acoust. Soc. Am.* 79, p 1410-1422 (1986).
16. H. Boehme and N. P. Chotiros, "Acoustic backscatter at low grazing angles from the ocean bottom," *J. Acoust. Soc. Am.* 84, p 1018-1029 (1988).
17. S. T. McDaniel, "Seafloor reverberation fluctuations," *J. Acoust. Soc. Am.* 88, p 1530-1535 (1990).
18. S. T. McDaniel, "Effect of surficial sediment layering on high-frequency seafloor reverberation," *J. Acoust. Soc. Am.* 88, p 1530-1535 (1990).
19. C. S. Clay and H. Medwin, Acoustical Oceanography: Principles and Applications, Wiley-Interscience Publication, New York, 1977.
20. E. G. Liszka, "Scattering from randomly rough surfaces (some numerical experiments)," Ph. D. Thesis, The Catholic University of America, Washington, D. C., 1977.
21. E. Y. Kuo, "Wave scattering and transmission at irregular surfaces," *J. Acoust. Soc. Am.* 36, p 2135-2142 (1964).
22. A. N. Ivakin and Y. P. Lysanov, "Theory of underwater sound scattering by random inhomogeneities of the bottom," *Sov. Phys. Acoust.* 27(1), p 61-64 (1981).
23. D. J. Tang, "Acoustic wave scattering from a random ocean bottom," Ph. D. Thesis, Massachusetts Institute of Technology and Woods Hole Oceanographic Institution, 1991.
24. P. C. Hines, "Theoretical model of acoustic backscatter from smooth seabed," *J. Acoust. Soc. Am.* 88, p 324-334 (1990).
25. S. T. McDaniel and A. D. Gorman, "An examination of the composite-roughness scattering model," *J. Acoust. Soc. Am.* 73 (5), p 1476-1486 (1983).
26. S. T. McDaniel and A. D. Gorman, "Acoustic and radar sea surface backscatter," *J. Geophysical Research*, 87, p 4127-4136 (1982).
27. C. A. Boyles and A. C. Biondo, "Modeling acoustic propagation and scattering in littoral areas," *Johns Hopkins APL Technical Digest*, 14 (2), p 162-172 (1993).
28. L. E. Kinsler, A. R. Frey, A. B. Coppens, and J. V. Sanders, Fundamentals of Acoustics, Third edition, John Wiley & Sons, New York, 1982.

29. R. J. Urick, "The backscattering of sound from a harbor bottom," *J. Acoust. Soc. Am.* 26 (2), p 231-235 (1954).
30. F. G. Bass and I. M. Fuks, Wave Scattering from Statistically Rough Surfaces, Pergamon, New York, 1979.
31. D. Tang, G. V. Frisk, C. J. Sellers, and D. Li, "Low-frequency acoustic backscattering by volume inhomogeneities in deep-ocean sediments," *J. Acoust. Soc. Am.* 98, p 508-516 (1995).
32. D. Tang, D. R. Jackson, and K. L. Williams, "Analyses of high-frequency bottom and sub-bottom backscattering for two distinct shallow water environments," *J. Acoust. Soc. Am.* 96, p 2930-2936 (1994).
33. A. W. Nolle, W. A. Hoyer, J. F. Mifsud, W. R. Runyan, and M. B. Ward, "Acoustic properties of water-filled sands," *J. Acoust. Soc. Am.* 35, p 1394-1408 (1963).
34. D. Tang, "A note on scattering by a stack of rough interfaces," *J. Acoust. Soc. Am.* 99 (3), p 1414-1418 (1996).
35. P. C. Hines, "Theoretical model of in-plane scatter from a smooth sediment seabed," *J. Acoust. Soc. Am.* 99 (2), p 836-844 (1996).
36. D. F. McCammon, "Fundamental relationships between geoacoustic parameters and predicted bottom loss using a thin layer model," *J. Geophysical Research* 93 (C3), p 2363-2369 (1988).
37. T. Yamamoto, "Acoustic scattering in the ocean from velocity and density fluctuations in the sediments," *J. Acoust. Soc. Am.* 99 (2), p 866-879 (1996).
38. F. A. Boyle and N. P. Chotiros, "Bistatic scattering and depth dependant gas fractions in the acoustic modeling of gassy sediment," Technical Report ARL-TR-95-25, Applied Research Laboratories, The University of Texas at Austin, (1995).
39. D. J. Yelton, M. Stern, and N. P. Chotiros, "New multiple scatter model of the ocean sediment," Technical Report ARL-TR-95-26, Applied Research Laboratories, The University of Texas at Austin, (1995).
40. M. Gensane, "Sea-bottom reverberation: The role of volume inhomogeneities of the sediment," D. D. Ellis et al (eds.), Ocean Reverberation, Kluwer Academic Publishers, Netherlands, p 59-64 (1993).
41. A. D. Pierce, Acoustics - An Introduction to Its Physical Principles and Applications, Acoustical Society of America, New York, 1989.
42. A. N. Ivakin, "Sound scattering by random inhomogeneities in stratified ocean sediments," *Sov. Phys. Acoust.* 32, p 492-496 (1986).
43. K. B. Smith, W. S. Hodgkiss, and F. D. Tappert, "Propagation and analysis issues in the prediction of long-range reverberation," *J. Acoust. Soc. Am.* 99 (3), p 1387-1404 (1996).

44. P. G. Bergmann, "Intensity Fluctuations," in Physics of Sound in the Sea, NDRC Summary Technical Report Division 6, Chap. 7, (1946).
45. I. Dyer, "Statistics of sound propagation in the ocean," *J. Acoust. Soc. Am.* 48 (1), p 337-345 (1970).
46. B. F. Cron and W. R. Schumacher, "Theoretical and experimental study of underwater sound reverberation," *J. Acoust. Soc. Am.* 33 (7), p 881-888 (1961).
47. G. V. Frisk, "Intensity statistics for long-range acoustic propagation in the ocean," *J. Acoust. Soc. Am.* 64 (1), p 257-259 (1978).
48. M. Gensane, "A statistical study of acoustic signals backscattered from the sea bottom," *IEEE J. of Ocean. Eng.* 14 (1), p 84-93 (1989).
49. G. R. Wilson and D. R. Powell, "Probability density estimates of surface and bottom reverberation," *J. Acoust. Soc. Am.* 73 (1), p 195-200 (1983).
50. G. R. Wilson, "A statistical analysis of surface reverberation," *J. Acoust. Soc. Am.* 74 (1), p 249-255 (1983).
51. D. B. Creamer, "Scintillating shallow-water waveguides," *J. Acoust. Soc. Am.* 99 (5), p 2825-2838 (1996).
52. R. J. Urick, "Models for the amplitude fluctuations of narrow-band signals and noise in the sea," *J. Acoust. Soc. Am.* 62 (4), p 878-887 (1977).
53. D. Alexandrou, C. de Moustier, and G. Haralabus, "Evaluation and verification of bottom acoustic reverberation statistics predicted by the point scattering model," *J. Acoust. Soc. Am.* 91 (3), p 1403-1413 (1992).
54. S. O. Rice, "Mathematical Analysis of Random Noise," *Bell Syst. Tech J.* 24, 46 Art. 3.10 (1945).
55. J. S. Bendat and A. G. Piersol, Random Data - Analysis and Measurement Procedures, Second edition, Wiley-Interscience Publication, New York, 1986.
56. A. M. Law and W. D. Kelton, Simulation Modeling and Analysis, McGraw-Hill Book Company, New York, 1982.
57. W. H. Press, S. A. Teukolsky, W. T. Vetterling, and B. P. Flannery, Numerical Recipes in C, The Art of Scientific Computing, Second edition, Cambridge University Press, New York, 1992.
58. W. D. Kelley, T. A. Ratliff, Jr, and C. Nenadic, Basic Statistics for Laboratories, A Primer for Laboratory Workers, Van Nostrand Reinhold, New York, 1992.

59. D. A. Darling, "The Kolmogorov-Smirnov, Cramer-von Mises Tests," *Annals of Math. Stat.* 28, p823-838 (1957).
60. T. W. Anderson and D. A. Darling, "Asymptotic Theory of Certain "Goodness of Fit" Criteria Based on Stochastic Processes," *Annals of Math. Stat.* 23, p193-212 (1952).
61. F. J. Massey, Jr., "The Kolmogorov-Smirnov Test for Goodness of Fit," *Amer. Stat. Assoc. J. March*, p70-77 (1951).
62. S. S. Shapiro, M. B. Wilk, and H. J. Chen, "A Comparative Study of Various Tests for Normality," *Amer. Stat. Assoc. J. December*, p1343-1372 (1968).
63. A. Naiman, R. Rosenfeld, and G. Zirkel, Understanding Statistics, Second edition, McGraw-Hill Book Company, New York, 1977.
64. E. A. Maxwell, Introduction to Statistical Thinking, Prentice-Hall, Inc, New Jersey, 1983.
65. A. V. Oppenheim and R. W. Schafer, Discrete-Time Signal Processing, Prentice-Hall Signal Processing Series, Prentice-Hall, Inc, New Jersey, 1989.
66. F. D. Tappert and X. Tang, "Effects of internal waves on sound pulse propagation in the Straits of Florida," *IEEE J. Ocean. Eng.* 22 (n2), p245-255 (1997).
67. T. K. Staton, "Echo fluctuations from the rough seafloor: Predictions based on acoustically measured mircorelief properties," *J. Acoust. Soc. Am.* 78 (2), p 715-721 (1985).
68. L. R. LeBlanc, S. G. Schock, D. L. DeBruin, M. Jenkins, and L. Munro, "High-resolution sonar volume scattering measurements in marine sediments," *J. Acoust. Soc. Am.* 97 (5), pt.1, p 2979-2986 (1995).
69. D. M. Drumhellar, "General expressions for Rician density and distribution functions," *IEEE Trans. on Areosp. Electron Systm.* 29 (2), p580-588 (1993).
70. D. M. Drumhellar and M. L. Glasser, "Detection of chi-square fluctuating targets in arbitrary clutter," accepted for publication in *IEEE Trans. on Areosp. Electron Systm.* 33 (2) (1997).
71. E. Conte and G. Ricci, "Performance prediction in compound-Gaussian clutter," *IEEE Trans. on Areosp. Electron Systm.* 30 (2), p611-616 (1994).
72. A. A. Nilsson and T. H. Glisson, "On the derivation and numerical evaluation of the Weibull-Rician Distribution," *IEEE Trans. on Areosp. Electron Systm.* AES-16 (6), p864-867 (1980).
73. X. Hou, N. Morinaga, and T. Namekawa, "Direct evaluation of radar detection probabilities," *IEEE Trans. on Areosp. Electron Systm.* AES-23 (4), p418-423 (1987).
74. D. F. McCammon, Applied Research Laboratory, The Pennsylvania State University, private communications.

75. D. R. Jackson, A. M. Baird, and P. A. G. Thomson, private communications, May (1985).
76. D. F. McCammon, R. L. Culver, and G. Mills, "The underlying causes of changes in reverberation fluctuation statistics," presented at the Symposium on Shallow Water Undersea Warfare, Feb 25-27, 1992, Stennis Space Center, Mississippi.
77. R. V. Hogg and J. Ledalter, Applied Statistics for Engineers and Physical Scientists, Macmillan Publishing Company, New York, 1992.
78. H. Weinberg, "Effective range derivative for acoustic propagation loss in a horizontally stratified ocean," *J. Acoust. Soc. Am.* 70 (6), p 1736-1742 (1981).
79. MATLAB® High-Performance Numeric Computation and Visualization Software is furnished by The MathWorks, Inc, Cochituate Place, 24 Prime Park Way, Natick, Mass. 01760, phone: (508) 653-1415.
80. D. D. Ellis, F. Desharnais, R. H. Clarke, R. Hollett, E. Baglioni, and A. Legner, private communications.
81. A. Caiti, F. Ingenito, A. Kristensen, and M. D. Max, private communications, (December, 1995).
82. T. Akal, C. Gehin, B. Matteucci, and B. Tonarelli, private communications, (December, 1972).
83. E. L. Hamilton, "Compressional-wave attenuation in marine sediments," *Geophysic* 37 (4), p 620-646 (1972).
84. E. L. Hamilton, "Acoustic and related properties of the sea floor: Density and porosity profiles and gradients," Distributed by: National Technical Information Service, U. S. Dept. of Commerce, AD-A016 (1975).
85. E. L. Hamilton, "Prediction of in-situ acoustic and elastic properties of marine sediments," *Geophysic* 36 (2), p 266-284 (1971).
86. D. R. Jackson, "Third Report on TTCP Bottom Scattering Measurements:Model Development," Applied Physics Laboratory, University of Washington APL-UW 8708 September (1987).
87. C. G. Fox, "Description, Analysis, and Prediction of Sea-floor Roughness Using Spectral Models," Distributed by: Defense Technical Information Center, Defense Logistics Agency, Alexandria, Virginia TR 279 (1985).